From the Institute of Biomedical Optics
of the University of Lübeck
Director: Prof. Dr. Alfred Vogel

Quantitative Measurement of Cellular Dynamics using Spectral Domain Optical Coherence Phase Microscopy

Dissertation for Fulfillment of Requirements
for the Doctoral Degree
of the University of Lübeck
from the Department of Natural Sciences

Submitted by

Rehman Ansari M. Abdul
from Hyderabad, India.

Lübeck 2013

First referee: P.D. Dr. Gereon Hüttmann

Second referee: Prof. Dr. Achim Schweikard

Date of oral examination: 20th August 2013

Approved for printing. Lübeck, 20th August 2013

Dedicated to mom and dad
for their unconditional love and support

Acknowledgments

I would like to thank my thesis supervisor Dr. Gereon Hüttmann for the opportunity to work in his lab and pursue my research interests. His expertise and breadth of knowledge has been invaluable in completion of this thesis. I would like to thank my second supervisor, Dr. Achim Schweikard for his inspiring ideas, support and encouragement through out my research work. His crucial advice and guidance have shaped the outcome of this thesis. I would also like to thank my advisor Dr. Alexander Schlaefer for his valuable feedback and critique on my research work.

I would like thank all of my colleagues at Institute for Biomedical Optics for their kind help in setting up the experimental hardware. Many thanks to Dr. Jeanette Erdmann, Dr. Zouhair Aherrahrou, and Redouane Aherrahrou from the department of Cardiovascular Genetics, for providing the cardiomycocyte samples for the experiments.

I would also like to thank Dr. Peter König from Institute of Anatomy for providing the trachea samples for experiments, and Dr. Mario Pieper and Christian Myrtus for their kind help in performing the experiments.

Lastly, I would like to extend my deepest gratitude and appreciation to my family for their love, support and patience through out my graduate studies.

Abstract

Optical coherence microscopy (OCM) combines OCT with high numerical aperture scanning optics, and improves the transverse spatial resolution for visualization of single cells. Most of the OCM implementations reported in literature so far, had depth of focus larger than the coherence length of the light source, suboptimal transverse spatial resolution, and maximum sampling speed in the range of $25,000 - 75,000$ A-scans/sec, which does not allow high-speed volumetric acquisition of morphological structures and functional contrast from dynamic tissue samples. Optical coherence phase microscopy (OCPM) is an extension of OCM, which utilizes the phase contrast for quantitative measurement of functional properties of tissue. OCPM has been implemented using common-path interferometer as it provides the best phase sensitivity, but it also limits the transverse spatial resolution, and offers poor control on reference arm power which decreases the detection sensitivity.

This thesis presents an implementation of optical coherence phase microscopy (SDOCPM) system that overcomes the limitations of common-path interferometer topologies, and combines sub-micrometer transverse spatial resolution with sub-nanometer axial pathlength sensitivity. The implemented system has a maximum sampling speed of $217,000$ A-scans/sec, which allows for high-speed volumetric acquisitions, up to 108 sub-volumes/sec with sub-nanometer axial pathlength sensitivity. Shorter depth of focus, combined with point illumination of sample reduces the effect of speckle noise in the obtained images.

Given that most of the biological tissues are inherently dynamic in nature, where host of physiological processes sustain life at cellular level, imaging of morphological structures alone is not sufficient to completely understand the function of biological tissues and their various pathologies. This thesis demonstrates the optical sectioning capability of Implemented SDOCPM, by imaging subcellular structures in anterior and posterior segments of *ex vivo* porcine eyes. Furthermore, the capability of SDOCPM to combine morphological and functional imaging at subcellular level is demonstrated by imaging subcellular dynamics of spontaneously active cardiomyocytes, and by quantitatively measuring the dynamics of ciliary beating in mouse trachea.

Contents

List of Figures

List of Tables

Chapter 1

Introduction

Optical coherence tomography (OCT) is a non-invasive imaging technique that enables cross-sectional tomographic imaging of materials and tissue on micron-scale [1]. OCT has found many applications in biology and medicine. However, lack of cellular resolution in OCT makes it difficult to identify different cell types and their fine processes. OCT images also suffer from speckle noise which degrades the contrast, and obscures the boundaries of tissue morphology.

OCT combined with high numerical aperture scanning optics, known as optical coherence microscopy (OCM) [2], improves the transverse spatial resolution when compared with OCT, and enables visualization of single cells. Most of the OCM implementations [3, 4, 5] reported in the literature, have larger depth of focus than the coherence length of the light source and suboptimal transverse spatial resolution. Also, most of the OCM implementations have maximum sampling speed in the range of $25,000 - 75,000$ A-scans/sec, which does not allow high-speed volumetric acquisition of morphological structures and functional contrast from dynamic tissue samples.

Optical coherence phase microscopy (OCPM) is an extension of OCM, which utilizes the phase component of the measured interferograms to characterize dynamic properties of tissue [6, 7]. Almost all of the OCPM implementations that have been reported in literature so far, have used common-path interferometer as it provides the best phase stability [6, 7, 8, 9, 10, 11, 12, 13]. However, common-path topologies have significant drawbacks such as limited transverse spatial resolution, poor control on reference intensity which decreases the detection sensitivity, and limited depth scanning capability.

This thesis presents an implementation of spectral domain optical coherence phase microscopy (SDOCPM) system that overcomes the limitations of common-path interferometer topologies, and combines sub-micrometer transverse spatial resolution with sub-nanometer axial pathlength sensitivity. The implemented system has a maximum sampling speed of $217,000$ A-scans/sec, which allows for high-speed volumetric acquisitions, up to 108 sub-volumes/sec with sub-nanometer axial pathlength sensitivity. Because of the shorter depth of focus, illumination of the sample is limited to a very narrow focal volume and the measured backscattered signal is not subject to statistical variations that generate speckle noise [14, 15, p. 33]. Therefore, fine morphological structures of biological tissue such as collagen fibers and single red blood cells are clearly visualized. This thesis demonstrates the optical sectioning capability of Implemented SDOCPM, by imaging subcellular structures in anterior and posterior segments of *ex vivo* porcine eyes. Furthermore, the capability of SDOCPM to combine morphological and functional imaging at subcellular level is demonstrated by imaging subcellular dynamics of spontaneously active cardiomyocytes, and by quantitatively measuring the dynamics of ciliary beating in mouse trachea.

1.1 Background and Motivation

Most of the biological tissues, especially the ones that make up sensing organs, are inherently dynamic in nature. There are host of physiological processes such as molecular diffusion, muscle contraction, respiration, perfusion, and mucuciliary clearance, among others that support and sustain life in the biological systems. Therefore, imaging of morphological structures alone is not sufficient to completely understand the function and pathologies of various biological tissues. It is critical to have an additional contrast that provides functional information about the physiological processes at cellular level. Given that the specific changes in physiological processes precede morphological changes in biological tissues, functional imaging could potentially help in early diagnosis of diseases.

The particular appeal of OCPM with respect to functional imaging is that, it measures both amplitude and phase of the light backscattered from tissue samples, through coherent detection. The amplitude of backscattered light provides images with morphological structures of biological tissue. The phase component of the backscattered light, which is sensitive to sub-nanometer changes in scatterers pathlength, provides a functional contrast in relation to the physiology of biological tissue. Furthermore, OCPM does not require any extraneous contrast agents to provide anatomical and functional assessment of biological tissues.

1.2 Contributions of This Thesis

The original contributions of the research work presented in this thesis are as follows:

- Implementation of spectral domain optical coherence phase microscopy system that overcomes the limitations of conventional common-path interferometer topologies, and combines sub-micron transverse spatial resolution with sub-nanometer axial pathlength sensitivity.
- High-speed implementation of spectral domain OCPM system capable of acquiring $217,000$ A-scans/sec, and up to 108 sub-volumes/sec.
- Capability of implemented system to acquire and display 4D data from dynamic tissues, i.e., 3D morphological structures along with functional contrast over time.
- Demonstrate the optical sectioning capability of OCM by imaging sub-cellular morphological structures of biological tissues, and elucidate the advantages of OCM over confocal scanning optical microscopy.
- Quantitative measurement of contraction dynamics in spontaneously active cardiomyocytes, at sub-cellular level.
- Utilization of phase contrast for quantitative measurement of ciliary dynamics in mouse tracheal epithelium.

- Development of a new approach and algorithm for calculation and compensation of dispersion in OCM images

1.3 Thesis Outline

The thesis is structured as follows:

Chapter 2 describe the theory of optical coherence tomography, and its axial resolution through coherence gating.

Chapter 3 describes the theory of confocal scanning microscopy, and its depth and transverse response for point and planar reflectors. Origin of amplitude and phase contrast in optical microscopes and their distinctive characteristics are also presented

Chapter 4 describes the implementation of spectral domain optical coherence microscopy system. Procedures and methods in signal processing and image reconstruction are also presented.

Chapter 5 presents the performance evaluation of implemented system with key parameters such as signal-to-noise ratio, spatial resolution, phase sensitivity, maximum field of view, and temporal resolution.

Chapter 6 presents microanatomical images and reconstructed 3D structures of different cell layers in cornea and neural retina from an *ex vivo* porcine eye.

Chapter 7 presents images and reconstructed 3D structures of cardiomyocytes. Quantitative measurements of cell membrane displacement associated with contraction are also presented.

Chapter 8 presents the microanatomical images reconstructed 3D structure of mouse trachea, where ciliated cells in the epithelium and single blood cells in the capillaries below the epithelium are clearly visualized. Results of quantitative measurement of ciliary dynamics using the phase contrast are also presented.

Finally, Chapter 9 summarizes the overall research work of this thesis and its conclusion.

Chapter 2

Principles of Optical Coherence Tomography

2.1 Introduction

Optical coherence tomography (OCT) is a non-invasive imaging technique that provides cross-sectional images of tissue by detecting round trip delay time of the back scattered light waves. OCT was invented in the laboratory of Professor James G. Fujimoto at Massachusetts Institute of Technology in 1991 [1]. Subsequently, potential diagnostic capability of OCT was demonstrated by imaging posterior and anterior segments of the eye on micron-scale [16]. OCT is particularly well suited for imaging micro-structures in eyes, as they are transparent in near infrared region. In ophthalmology, OCT has become an indispensable tool for non-invasive diagnosis and monitoring of glaucoma [17, 18], diabetic retinopathy [19] and macular edema [20], among others. More applications of OCT are actively being explored in imaging of pancreatobiliary tissues [21], hard and soft tissues in oral dental cavity [22], dermatology [23, 24], etc.

There are several extensions of OCT that enable depth-resolved imaging of intrinsic tissue properties such as birefringence, Doppler flow, and spectroscopic absorption. Polarization-sensitive OCT (PS-OCT) measures the polarization states of back-reflected light to estimate the degree of birefringence in biological tissues [25], which can be utilized to measure the thickness of RPE cell layer [26]. Doppler OCT [27, 28] utilizes the phase component of the detected cross-spectral interferogram to measure the velocity of blood flow in human skin [29], and in human retina *in vivo* [30]. Spectroscopic OCT has been demonstrated in quantitative assessment of blood oxygen saturation level [31].

OCT is based on low coherence interferometry, a classic optical measurement technique which is described in this chapter. The fundamental distinction between OCT and all other optical imaging techniques is coherence gating, a mechanism that discriminates backscattered light from different depths inside the sample is also described in detail. Physical principles that guide the axial and transverse spatial resolutions are also discussed.

2.2 Low Coherence Interferometry

Interference is a wave phenomenon, based on the principle of superposition of waves, which states that two or more waves can propagate independent of each other in a medium at the same time, and when they overlap, amplitude of the superimposed wave is the vector sum of individual amplitudes. Interference occurs when two electromagnetic waves superimpose on each other and produce a resultant wave whose amplitude is greater or lower than the individual amplitudes.

The prerequisite to observing an interference fringe pattern is that the superimposing waves should be coherent. The word “coherence” is derived from a Latin word “cohaerentia” which means logical connection or consistency. Time duration during which a wavelet from light source maintains consistent or fixed phase relation among its waves is known as coherence time. Thus, to observe an interference between two waves, relative delay between them should be less than or equal to the coherence time of light source. The coherence time of a light source is inversely proportional to its bandwidth, i.e., larger the bandwidth of a light source shorter is its coherence time or length [32].

Low coherence interferometry (LCI) is a type of interferometry that uses low coherence light source to detect time delays (or equivalent pathlength difference) smaller than or equal to the coherence time (or length) of the light source. The principle of LCI using a free space Michelson interferometer is illustrated in Figure 2.1. A source emits light beam that hits a 50/50 beamsplitter, and get splits into two arms of an interferometer, reference and sample arm. Reference arm light reflects off a mirror, and the sample arm light reflects off a sample surface, and both of them recombine at the beamsplitter. If the optical pathlength difference between the sample and reference arms is less than or equal to the coherence length of the light source, an interference fringe pattern is formed at the beamsplitter. The detector at the output of the interferometer measures the interference fringe pattern which encodes the magnitude and echo delay of reflected fields from sample and reference arms.

$$|\mathbf{E}_r|^2 + |\mathbf{E}_s|^2 + 2\mathbf{E}_r\mathbf{E}_s\cos(2k(z_r - z_s))$$

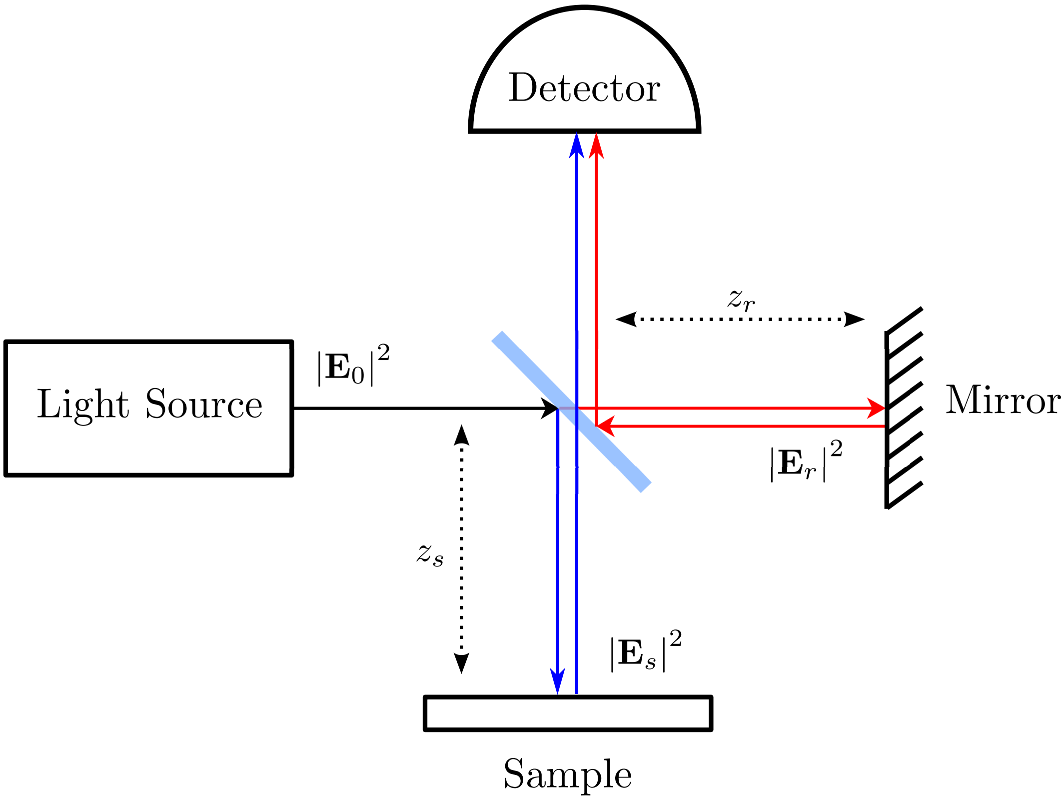

Figure 2.1: A schematic illustrating principle of low coherence interferometry using a Michelson interferometer.

Interference between two monochromatic plane waves

A linearly polarized electromagnetic plane wave can be represented as [33]:

$$\mathbf{E}(\mathbf{r},t) = \mathbf{E}_o e^{i(\mathbf{k}.\mathbf{r}-\omega t)} \tag{2.1}$$

Where $\mathbf{E}_o$ is the amplitude of the electromagnetic wave. ω is the angular frequency, and related to frequency v, by $\omega = 2\pi v$. $\mathbf{k}$ is the wave vector pointing in the direction of propagation, and its magnitude is the wave number $k = 2\pi/\lambda_\circ$, where $\lambda_\circ$ is the wavelength in free space. $\mathbf{r}$ is the position vector in polar coordinates which is equivalent to $\sqrt{x^2+y^2+z^2}$, where x, y and z are coordinates in three spatial dimensions.

Let $\mathbf{E}_s$ and $\mathbf{E}_r$ be the reflected fields from sample and reference arm of a Michelson interferometer, as shown in Figure 2.1. $\mathbf{E}_s$ and $\mathbf{E}_r$, after traveling a distance of $2z_s$ and $2z_r$ respectively, can be written as

$$\mathbf{E}_s = \mathbf{E}_{os} e^{(2\mathbf{k}z_s-\omega t)}$$
$$\mathbf{E}_r = \mathbf{E}_{or} e^{(2\mathbf{k}z_r-\omega t)}$$

Where $\mathbf{E}_{os}$ and $\mathbf{E}_{or}$ are the amplitude of the reflected fields from sample and reference arm, respectively. The reflected fields recombine at the beamsplitter, and are superimposed on each other. Using the superposition principle, the resultant electric field can be obtained by taking the sum of individual fields:

$$\mathbf{E} = \mathbf{E}_s + \mathbf{E}_r$$

The photodetector at the output of the interferometer measures the intensity, which can be represented in terms of electric field as [34]:

$$\mathrm{I}_D \approx cn\varepsilon_0 \frac{|\mathbf{E}_s + \mathbf{E}_r|^2}{2} \tag{2.2}$$

Where c is the speed of light in vacuum, n is the refractive index, and ε_0 is the vacuum permittivity.

To obtain an equation for measured intensity as a function of optical pathlengths, Equation 2.2 can be expanded as

$$\begin{aligned}\mathrm{I}_D &= \frac{cn\varepsilon_0}{2}[(\mathbf{E}_s+\mathbf{E}_r).(\mathbf{E}_s^*+\mathbf{E}_r^*)]\\ \mathrm{I}_D &= \frac{cn\varepsilon_0}{2}[\mathbf{E}_s.\mathbf{E}_s^*+\mathbf{E}_r.\mathbf{E}_r^*+\mathbf{E}_s^*.\mathbf{E}_r+\mathbf{E}_s.\mathbf{E}_r^*] \qquad (2.3)\end{aligned}$$

The product terms in Equation 2.3 can be simplified as follows:

$$\begin{aligned}\mathbf{E}_s.\mathbf{E}_s^* &= \mathbf{E}_{os}^2 e^{i(2\mathbf{k}z_s-\omega t)}e^{-i(2\mathbf{k}z_s-\omega t)}\\ &= \mathbf{E}_{os}^2\\ \text{Similarly}\quad \mathbf{E}_r.\mathbf{E}_r^* &= \mathbf{E}_{or}^2\\ \mathbf{E}_s^*.\mathbf{E}_r &= \mathbf{E}_{os}\mathbf{E}_{or}e^{-i(2\mathbf{k}z_s-\omega t)}e^{i(2\mathbf{k}z_r-\omega t)}\\ &= \mathbf{E}_{os}\mathbf{E}_{or}e^{i2\mathbf{k}(z_r-z_s)}\\ &= \mathbf{E}_{os}\mathbf{E}_{or}e^{i2\mathbf{k}\Delta z}\\ \text{Similarly}\quad \mathbf{E}_s.\mathbf{E}_r^* &= \mathbf{E}_{os}\mathbf{E}_{or}e^{-i2\mathbf{k}\Delta z}\end{aligned}$$

Where $\Delta z = z_r - z_s$ is the optical pathlength difference between sample and reference arms. The sum of the products can be further simplified as follows:

$$\begin{aligned}\mathbf{E}_s^*.\mathbf{E}_r+\mathbf{E}_s.\mathbf{E}_r^* &= \mathbf{E}_{os}\mathbf{E}_{or}(e^{i2\mathbf{k}\Delta z}+e^{-i2\mathbf{k}\Delta z})\\ &= \mathbf{E}_{os}\mathbf{E}_{or}(\cos(2\mathbf{k}\Delta z)+i\sin(2\mathbf{k}\Delta z)+\cos(2\mathbf{k}\Delta z)-i\sin(2\mathbf{k}\Delta z))]\\ &= 2\mathbf{E}_{os}\mathbf{E}_{or}\cos(2\mathbf{k}\Delta z)\end{aligned}$$

Substituting the obtained product values in to Equation 2.3 yields:

$$\mathrm{I}_D = \frac{cn\varepsilon_0}{2}[\mathbf{E}_{os}^2+\mathbf{E}_{or}^2+2\mathbf{E}_{os}.\mathbf{E}_{or}\cos(2\mathbf{k}\Delta z)] \qquad (2.4)$$

Therefore, superposition of two linearly polarized and monochromatic electromagnetic plane waves, after having traveled optical pathlength difference of Δz between them, creates a fringe pattern whose amplitude is proportional to the product of individual field strengths, and whose frequency is proportional to the optical pathlength difference, as given by Equation 2.4. The interference fringe pattern in terms of measured intensity at the output of interferometer can be represented as:

$$\mathrm{I}_D = \mathrm{I}_s + \mathrm{I}_r + 2\sqrt{\mathrm{I}_s\mathrm{I}_r}\cos(2\mathbf{k}\Delta z) \tag{2.5}$$

where I_D is the detected intensity at the output of interferometer, I_s and I_r are the intensities of sample and reference arm reflectance, respectively.

2.3 Optical Coherence Tomography

The concept of interference between two monochromatic electromagnetic plane waves, as described above, can be extended to a case where polychromatic electromagnetic plane waves illuminate multiple discrete reflectors in the sample arm and a single reflector in the reference arm, which forms the basis of OCT.

The backscattered light from a sample can be measured sequentially in time from different depths by translating the coherence window into the sample, or it can be measured simultaneously from all depths in Fourier domain as a function of wavenumbers. Based on these two detection schemes, OCT systems are broadly classified into time-domain or Fourier-domain, respectively. Time-domain OCT (TDOCT) is the first generation of OCT systems that requires axial scanning in the reference arm to scan in depth [1]. The mechanical scanning of the reference arm not only slows down the image acquisition speed, but also provides very poor phase stability. Fourier domain OCT systems [35, 36] does not require reference arm scanning, provide faster image acquisition, and also have a sensitivity advantage over time-domain OCT [37, 38, 39].

Fourier domain OCT systems are further classified into spectral (spectrometer based) domain and swept source OCT systems. In spectral domain OCT (SDOCT), the interference fringe pattern is measured by spectrally resolving the back reflected light [35], where as in swept source OCT systems, interference fringe pattern is measured by a point detector while a swept laser source sweeps across the wavelength bandwidth [40, 41, 42].

The experimental setup constructed as part of this thesis uses a spectral domain OCT system to measure the back scattered light from samples, and as such only SDOCT is described in considerable detail.

2.3.1 Spectral Domain Optical Coherence Tomography

In spectral domain OCT (SDOCT), light reflected back from different depths of a sample and a single reflector in reference arm is spectrally resolved and detected using a spectrometer. A schematic illustrating the principle of SDOCT with Michelson interferometer is as shown in Figure 2.2.

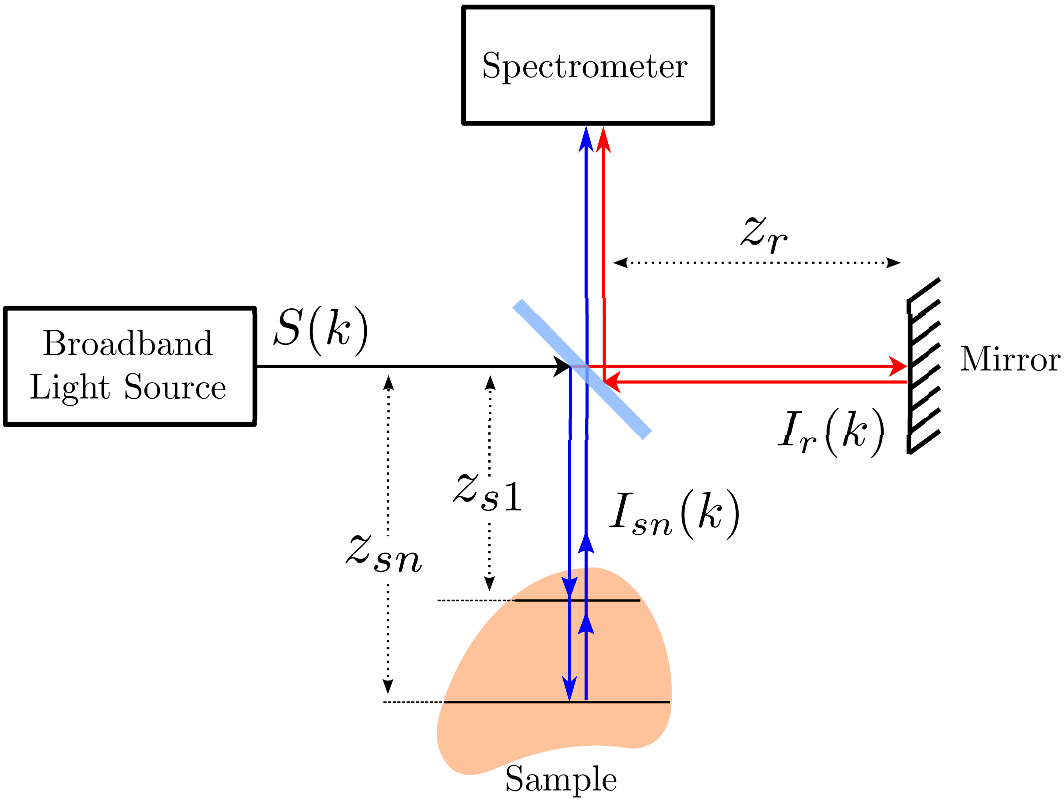

Figure 2.2: Schematic representation of Spectral domain OCT with Michelson interferometer.

Light beam from a broadband source is split into sample and reference arm using a beamsplitter. Backscattered light from all depths of the sample and reflected light from the reference arm mirror recombine at the beamsplitter and superimpose on each other. The spectrometer at the output of Michelson interferometer spectrally resolves the superimposed field, and measures intensity as a function of wavelength. The backscattered reflectance from different depths of the sample are encoded by their respective time delays, which modulate the spectrum with frequencies that increase linearly with time delay (or equivalent pathlength). The inverse Fourier transform of the measured spectral interferogram provides reflectivity profile of the sample or an A-scan.

SDOCT was demonstrated to have sensitivity advantage over TDOCT, as it collects the backscattered light from all depths of the sample using a detector array [37, 38, 39]. SDOCT also provides faster image acquisition as the back-scattered light from all depths of sample is collected simultaneously, as opposed to sequentially in TDOCT.

In TDOCT, any sample movements during the acquisition of A-scan severely distorts the images, which cannot be corrected retrospectively. Whereas in SDOCT, movement artifacts during an A-scan acquisition leads to fringe washout, which decreases the signal-to-noise ratio. However, with high-speed linescan cameras in SDOCT, where an integration time is on the order of tens of microseconds, sample movement during an A-scan acquisition becomes almost negligible. Furthermore, movement artifacts between A-scans or B-scans can be corrected retrospectively by cross correlating the neighboring A-scans or B-scans [43, 44].

Let $S(k)$ be the output of a polychromatic or broadband light source, which represents amplitude of electric fields at different wavenumbers, k. Let $[z_{s1} \ldots z_{sn}]$ be the axial position of discrete reflectors in the sample, and let $[\mathrm{I}_{s1} \ldots \mathrm{I}_{sn}]$ be the reflected intensities from each of these discrete reflectors. Let z_r and I_r be the axial position and reflected intensity of the only reflector in the reference arm. For a generalized OCT system, the detector current measured at the output of an interferometer as a function of wavenumber, can be represented as [45]:

$$\begin{aligned}
\mathrm{I}_D(k) =& S(k)[\mathrm{I}_r + \mathrm{I}_{s1} + \mathrm{I}_{s2} \ldots \mathrm{I}_{sn}] \quad \text{“DC Terms”} \\
&+ 2S(k) \sum_{n=1}^{N} \sqrt{\mathrm{I}_r \mathrm{I}_{sn}} (\cos[2k(z_r - z_{sn})]) \quad \text{“Cross-Correlation Terms”} \\
&+ 2S(k) \sum_{n \neq m = 1}^{N} \sqrt{\mathrm{I}_{sm} \mathrm{I}_{sn}} (\cos[2k(z_{sm} - z_{sn})]) \quad \text{“Auto-Correlation Terms”}
\end{aligned} \tag{2.6}$$

The “cross-correlation” terms in the Equation 2.6 represent the modulation or fringe pattern in the measured intensity, resulting from the superposition of reference field and the reflected fields from discrete reflectors in the sample. This term gives OCT its axial ranging capability, where each discrete reflector modulates the spectrum with a frequency in relation to its depth position in the sample, i.e., the higher the pathlength difference between a reflector and reference mirror, the higher is the modulation frequency. The amplitude of the modulation terms are proportional to the product of square root of reflected intensities from reference and sample reflectors. The constant reference arm reflectance, $\sqrt{\mathrm{I}_r}$, is the homodyne gain factor that enables weakly backscattered light to be detected.

The “DC Terms” in the Equation 2.6 represent offset in the measured intensity, and are optical pathlength independent. Generally, the largest component of “DC Terms” is the reference arm intensity, I_r, which helps in shot-noise limited detection of the interference fringe pattern. Shot-noise limited detection is the performance region of a photodetector, where the overall readout noise is negligible compared with the photon shot-noise [46].

The “auto-correlation” terms in the Equation 2.6 represents interference between different scatterers within the sample. In common-path interferometer based OCT systems, this term provides the axial ranging information, where as in all other interferometer types, this term appears as an artifact in the OCT images. Under the condition $\mathrm{I}_r >> \mathrm{I}_s$, this term is usually negligible.

Sample Depth Profile or an A-scan

The Fourier transform links the spectral amplitude of back reflected light, measured at the output of interferometer, to the sample depth structure. Therefore, a sample depth profile or A-scan is calculated by taking the inverse Fourier transform of the measured spectral interferogram, given by Equation 2.6. The Fourier transform of Gaussian shaped function $S(k)$, is Gaussian function itself in conjugate domain, i.e.,

$$S(k) \overset{\mathfrak{F}}{\longleftrightarrow} \gamma(z) \tag{2.7}$$

and the Fourier transform of cosine function can be given as

$$\begin{aligned} \cos(kz_o) &\overset{\mathfrak{F}}{\longleftrightarrow} \frac{1}{2}[\delta(z+z_o)+\delta(z-z_o)] \\ \cos[2k(z_r-z_{sn})] &\overset{\mathfrak{F}}{\longleftrightarrow} \frac{1}{2}[\delta(z+2k(z_r-z_{sn}))+\delta(z+2k(z_r+z_{sn}))] \\ &\overset{\mathfrak{F}}{\longleftrightarrow} \frac{1}{2}[\delta(z\pm 2k(z_r-z_{sn}))] \\ \text{Similarly, } \cos[2k(z_{sm}-z_{sn})] &\overset{\mathfrak{F}}{\longleftrightarrow} \frac{1}{2}[\delta(z\pm 2k(z_{sm}-z_{sn}))] \end{aligned}$$

Therefore, making use of the above derived Fourier pairs, and the convolution property of Fourier transforms, $x(z)\otimes y(z) \overset{\mathfrak{F}}{\longleftrightarrow} X(k)Y(k)$, the inverse Fourier transform of Equation 2.6 can be written as [45]:

$$\begin{aligned} i_D(z) =& \gamma(z)[\mathrm{I}_r+\mathrm{I}_{s1}+\mathrm{I}_{s2}\ldots\mathrm{I}_{sn}] \quad \text{“DC Terms”} \\ &+\left[\gamma(z)\otimes\sum_{n=1}^{N}\sqrt{\mathrm{I}_r\mathrm{I}_{sn}}(\delta(z\pm 2(z_r-z_{sn})))\right] \quad \text{“Cross-Correlation Terms”} \\ &+\left[\gamma(z)\otimes\sum_{n\neq m=1}^{N}\sqrt{\mathrm{I}_{sm}\mathrm{I}_{sn}}(\delta(z\pm 2(z_{sm}-z_{sn})))\right] \quad \text{“Auto-Correlation Terms”} \end{aligned} \tag{2.8}$$

Where $i_D(z)$ is the inverse Fourier transform of $\mathrm{I}_D(k)$. Utilizing the sifting property of delta functions, $f(x)\otimes\delta(x-x_o) = f(x_o)$, convolutions of Gaussian and delta function in Equation 2.8 can be simplified as

$$
\begin{aligned}
\gamma(z) \otimes \delta(z \pm 2(z_r - z_{sn})) = \gamma(\pm 2(z_r - z_{sn})) \\
\gamma(z) \otimes \delta(z \pm 2(z_{sm} - z_{sn})) = \gamma(\pm 2(z_{sm} - z_{sn}))
\end{aligned}
$$

Substituting the above simplified convolutions in Equation 2.8, gives an A-scan

$$
\begin{aligned}
i_D(z) = &\gamma(z)[\mathrm{I}_r + \mathrm{I}_{s1} + \mathrm{I}_{s2} \ldots \mathrm{I}_{sn}] \\
&+ \left[\sum_{n=1}^{N} \sqrt{\mathrm{I}_r \mathrm{I}_{sn}} [\gamma[2(z_r - z_{sn})] + \gamma[-2(z_r - z_{sn})]]\right] \\
&+ \left[\sum_{n \neq m=1}^{N} \sqrt{\mathrm{I}_{sm} \mathrm{I}_{sn}} [\gamma[2(z_{sm} - z_{sn})] + \gamma[-2(z_{sm} - z_{sn})]]\right]
\end{aligned} \tag{2.9}
$$

The A-scan consists of DC, cross-correlation, and auto-correlation parts whose origins and implications are already discussed. It is important to note that the delta peaks caused by the reflectors in the sample are broadened to a width of light source coherence length, after convolving with the Gaussian function, $\gamma(z)$, which sets the limit on axial resolution. Therefore, the shorter the coherence length of a light source, the higher is the axial resolution.

The terms in Equation 2.9 are further elucidated by simulated response of SDOCT system for a sample with two delta reflectors at different depths, as shown in Figure 2.3. The top panel shows the spectral interferogram as a function of wavenumbers, obtained by interference between sample and reference fields. The inverse Fourier transform of the spectral interferogram provides the depth profile or an A-scan of the sample, as shown in second panel. The third panel shows the position of two reflecting layers in the sample, which are at a distance of z_{s1} and z_{s2} from the virtual position of reference mirror.

The position of peaks in the A-scan correspond to the depth position of delta reflectors in the sample. The amplitude of the peaks are proportional to $\sqrt{I_r I_{sn}}$, i.e., back reflectance from each reflector in the sample is multiplied by a constant reference arm intensity, $\sqrt{I_r}$, which serves as the homodyne gain factor, and makes it possible to detect very weak back scattered light from samples.

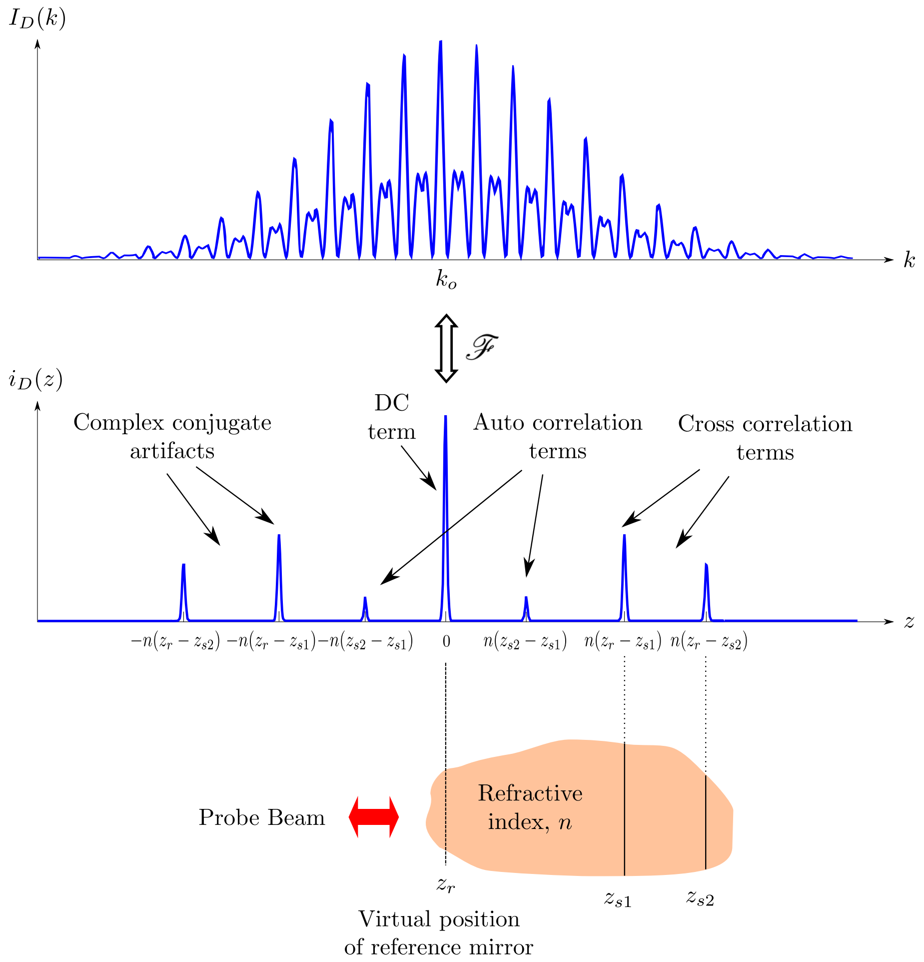

Figure 2.3: Simulated response of SDOCT system for a sample with two reflecting layers at different depths. The first panel shows the measured spectral interferogram, second panel shows the reconstructed A-scan obtained by taking the inverse Fourier transform of spectral interferogram. The third panel shows the position of delta reflectors in the sample. n is the average refractive index of the sample.

The complex conjugate artifacts or the mirror image of an A-scan across the zero delay is because of Hermitian symmetry, which is a necessary condition for real valued signals. These artifacts limit the depth measurement range, and can be eliminated by recording complex interferograms. A variation of OCT system, known as full-range OCT employs phase shifting techniques to reconstruct the complex interferograms, and doubles the depth measurement range [47, 48, 49].

The DC term near the zero optical pathlength difference position can be eliminated by a high pass filter before taking the inverse Fourier transform, and the auto-correlation artifacts can be suppressed by higher reference arm intensity.

It is important to note that, to obtain high sensitivity and Fourier transform limited axial resolution, measured spectral interferogram needs to be corrected for offset errors, fixed pattern noise, dispersion mismatch, and the interferogram must be linearly spaced in wavenumbers. Signal processing and calculation of A-scans are described in detail in Chapter 4.

Linear Wavenumber Spectrometer

Spectrometer essentially measures light intensity with respect to wavelength. In SDOCT, the spectral interferograms are modulated as a function of wavenumbers, which are in inverse relation to the wavelengths. Therefore, measured spectral interferograms needs to be linearly sampled in wavenumbers or k-space before Fourier transform, for accurate ranging of reflectors from different depths inside the sample. Generally, the spectrum is linear or spline interpolated for uniform sampling in k-space. However, interpolation of each spectrum can be computationally intensive and increases the time it takes to reconstruct a volumetric image.

An alternate solution for uniform sampling of spectrum in k-space is to use an optical glass prism right after the diffraction grating to compensate for the down-chirping of the spectrum [50]. A simplified schematic in Figure 2.4 depicts light path through different components of a linear wavenumber spectrometer. Light entering into spectrometer is first collimated and then passes through a transmission grating, which separates light by the wavelength. Diffracted light passes through a prism and a lens images the point sources from diffraction grating onto the line scan camera. The quadratic dependence of the deviation angle around the angle of minimal deviation of a prism compensates the chirp in wavenumbers. The measured spectrum is nearly uniformly spaced in k-space, does not require further re-sampling, which decreases the volumetric image reconstruction time.

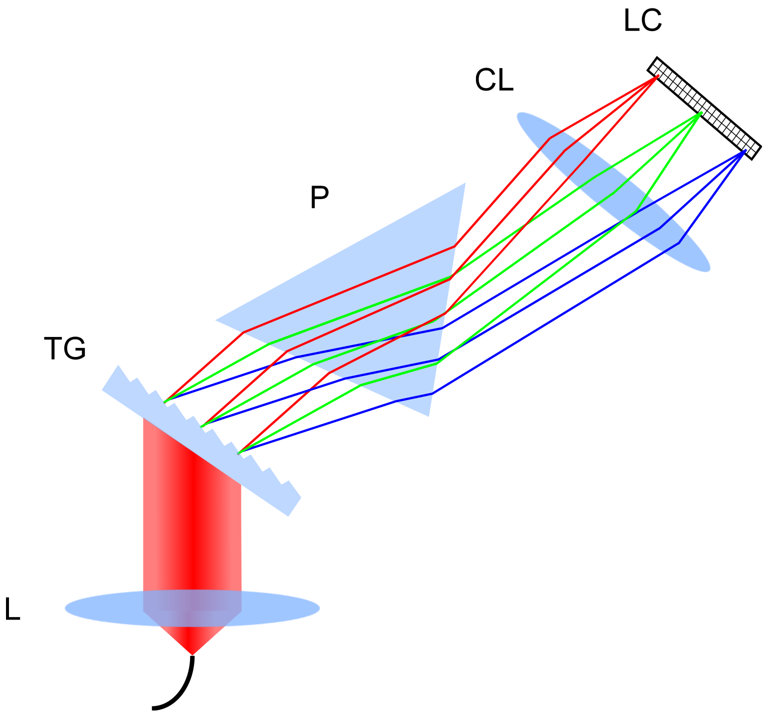

Figure 2.4: Schematic of linear wavenumber spectrometer. L, collimator lens; TG, transmission grating; P, optical glass prism; CL, cylindrical lens; LC, line scan camera

2.3.2 Axial Resolution Through Coherence Gating

The main distinction between OCT and other optical imaging techniques is that, the axial resolution in OCT is determined by the coherence length of the light source, which is inversely proportional to its bandwidth. The coherence length of a light source can be determined by taking the Fourier transform of its auto-correlation function as shown in Figure 2.5.

For a Gaussian shaped source spectrum, coherence length in free space is given as [32, p. 180]

$$l_{c(air)} = \frac{4ln(2)}{\pi} \frac{\lambda_\circ^2}{\Delta\lambda} \tag{2.10}$$

Where $\lambda_\circ$ is the center wavelength of light source in free space and $\Delta\lambda$ is its FWHM bandwidth.

The axial resolution in OCT is half the coherence length, as the light beam traverses the sample arm twice. Therefore, axial resolution in air is given as

$$\delta z_{(air)} = \frac{2ln(2)}{\pi}\frac{\lambda_\circ^2}{\Delta\lambda} \tag{2.11}$$

Because the wavelength in a medium is reduced by a factor of medium's refractive index, axial resolution in tissue is given as

$$\delta z_{(tissue)} = \frac{1}{n_{tissue}}\left[\frac{2ln(2)}{\pi}\frac{\lambda_\circ^2}{\Delta\lambda}\right] \tag{2.12}$$

Where n_{tissue} is the average refractive index of the tissue. Generally, axial resolution in OCT can be increased by using light sources with shorter wavelengths and broad bandwidth.

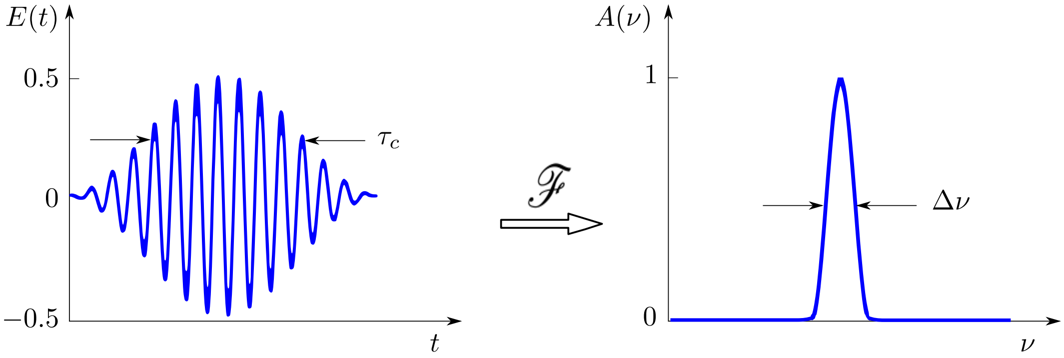

Figure 2.5: Auto-correlation function of a low coherence light source (left) and its coherence length obtained by taking the Fourier transform (right).

2.3.3 Transverse Resolution

In OCT, the axial and transverse resolution are decoupled from each other as they manifest from completely different physical principles. The axial resolution, as discussed above, is determined by the coherence length of the light source, and the transverse resolution is determined by the diffraction limited spot size of the focused light beam. For a Gaussian beam, minimum focal spot size or beam waist is given as:

$$w_\circ = 0.4\frac{\lambda_o}{\mathrm{NA}} \tag{2.13}$$

Where λ_o is the center wavelength of the light source and NA is the numerical aperture.

The numerical aperture of the sample scanning optics also effects the confocal parameter or depth of focus. The confocal parameter defines the axial range along which the transverse resolution is considered to be relatively constant. In OCT, numerical aperture of the scanning optics is chosen based on the axial range desired, so that the transverse resolution at all depths is relatively constant. The confocal parameter is given as:

$$b = 2z_r = 2\frac{\pi w_\circ^2}{\lambda_\circ} \tag{2.14}$$

Where z_r is the Rayleigh length.

It can be noted that, there is a trade off between transverse resolution and the axial field of view, i.e., if one choses to have higher transverse resolution with high numerical aperture optics, it will also result in a limited depth of focus. If the depth of focus is equal to or smaller than the coherence length of the light source, then a combination of confocal and coherence gating can be used to reject multiple scattered light, which provides sharp images from highly scattering samples. This mode of operation is known as optical coherence microscopy, which is described in the next chapter.

Chapter 3

Principles of Optical Coherence Microscopy

3.1 Introduction

The limited transverse spatial resolution of OCT does not allow visualization of single cells in biological tissues. For applications where cellular imaging is desired, the transverse spatial resolution of OCT has to be improved by increasing the numerical aperture (N.A.) of scanning optics. An implementation of OCT with high N.A. objective lens in the sample arm is known as optical coherence microscopy (OCM) [2]. OCM combines the high spatial resolution of confocal microscopy with axial ranging capability of OCT, and enables sharp optical sectioning of highly scattering samples such as biological tissue.

This chapter describes the principles of confocal microscopy, and its depth and transverse response. Physical principles underlying OCM, and its several advantages over confocal microscopy such as improved axial response, and higher penetration depth in scattering samples are described.

Optical coherence phase microscopy (OCPM) is an extension of OCM that quantitatively measures the phase of cross-spectral density function, which is sensitive to sub-nanometer displacements of scatterers in depth. This chapter describes how the phase contrast is obtained in OCM, theoretical limit of phase sensitivity, and its utilization as a functional contrast in dynamic tissue samples. The origin of amplitude and phase contrast in optical microscopes, and their characteristic differences are also discussed.

3.2 Confocal Microscopy

To overcome some of the limitations of traditional widefield microscopes, the concept of confocal microscopy was developed by Marvin Minsky in 1957 [51]. In traditional widefield microscopes, condenser lens illuminates the whole sample uniformly, and a microscope objective forms the image of illuminated plane onto a detector along with unfocused background light which blurs the image. Confocal microscope illuminates and images the object, one point at a time, to eliminate the unfocused background light. A pair of confocal pinhole apertures, each on illumination and detection side, filters out the background light. This spatial filtering of light along with point illumination and detection, enables optical sectioning of highly scattering samples, and provides sharp images. Optical sectioning refers to virtual slicing of sample using light.

A schematic in Figure 3.1 illustrates the basic principle of confocal microscopy. Light from a laser source passes through illumination pinhole aperture, reflects off a partial mirror and a microscope objective focuses it to a point inside the object. From all of the light scattered back from the object, only light originated from the focal volume passes through the detection pinhole to form an image. The out-of-focus or background light gets blocked by the detection pinhole aperture.

As a consequence of the confocal arrangement of the illumination and detection point, the spatial resolution also improves over traditional widefield microscopes. The spatial resolution of confocal microscope can be quantified by measuring the axial and transverse response to a point object. The sections below describe the axial and transverse response of a confocal imaging system to a point and planar reflector. The theoretical principles and derivations presented here are based on the theory of confocal scanning microscopy, developed by Gordon S. Kino et al. [15].

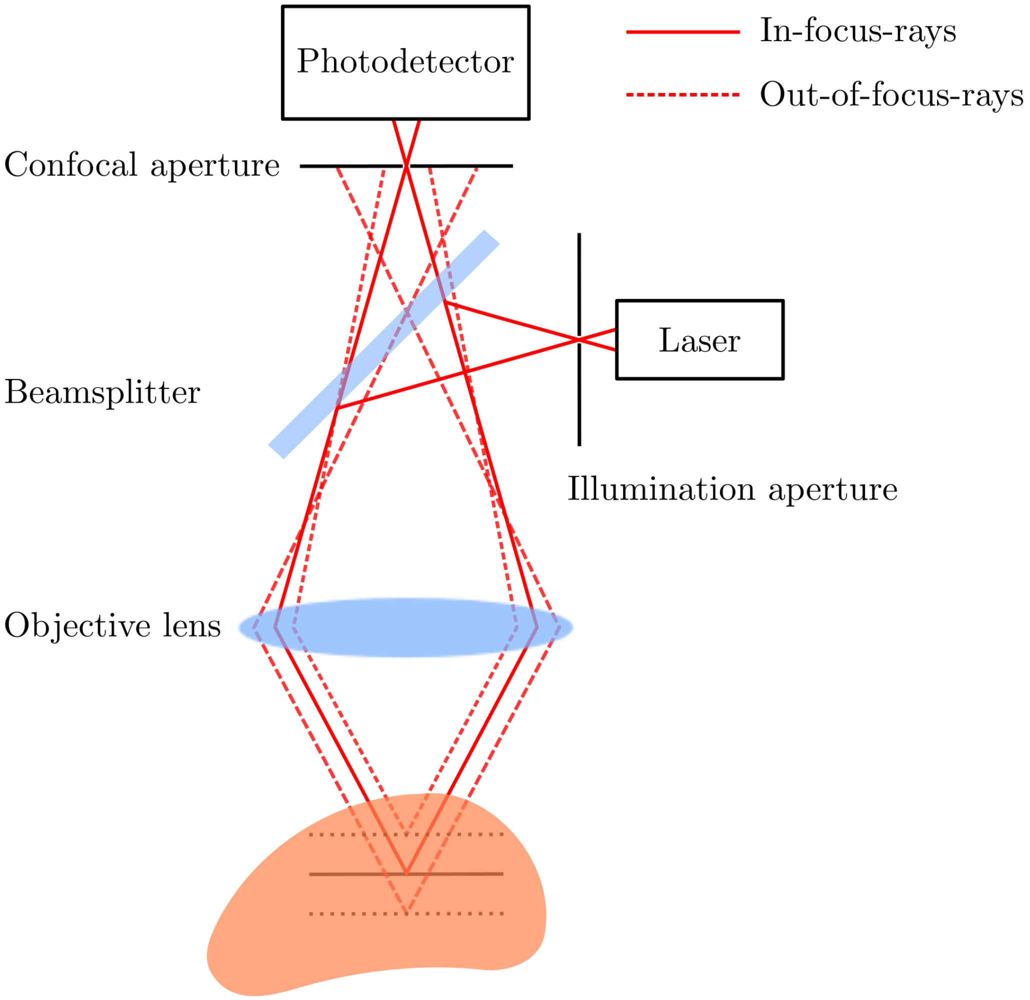

Figure 3.1: Simplified schematic showing principle of confocal microscopy.

3.2.1 Depth Response of Confocal Microscope

The depth response of a confocal microscope is characterized by the variations in intensity of an image received at the detector plane as a planar or point reflector moves away from the focus position, along the optical axis. The intensity response for planar and point reflector is different, because a planar reflector at defocus position results in a cone of light at the pinhole aperture, whose area varies with the square of defocus distance, i.e., z^2. Hence the intensity at the detector varies as $1/z^2$. Illumination intensity at a point reflector falls off as $1/z^2$ and the intensity measured at the detection pinhole, for a point reflector, varies as $1/z^4$. Depth response of confocal microscope for both planar and point reflector is derived below.

For an ordinary microscope, assuming that an objective lens is illuminated with a collimated beam, the amplitude variation of light passing through the detection plane, in response to a planar reflector at distance z away from the focus can be written as

$$V(z)_{planar\ (widefield)} = \frac{\sin(u/2)}{u/2} = \frac{\sin[nkz(1-\cos\theta)]}{nkz(1-\cos\theta)} \tag{3.1}$$

Where $u = 2nkz(1-\cos\theta)$ is the normalized optical coordinate, $k = \frac{2\pi}{\lambda_\circ}$ is the wave number, with $\lambda_\circ$ as the wavelength in free space. n is the refractive index of material between sample and objective lens, and θ is half the angle subtended by the focused beam at the objective lens.

In confocal imaging system, same objective lens is used for illumination and detection. Therefore, the amplitude response is squared and given as

$$V(z)_{planar\ (confocal)} = \left(\frac{\sin(u/2)}{u/2}\right)^2 = \left(\frac{\sin[nkz(1-\cos\theta)]}{nkz(1-\cos\theta)}\right)^2 \tag{3.2}$$

The intensity measured by a detector is square of the amplitude given by Equation 3.2, and can be written as

$$I(z)_{planar\ (confocal)} = \left|V(z)_{planar\ (confocal)}\right|^2 = \left|\frac{\sin knz(1-\cos\theta)}{knz(1-\cos\theta)}\right|^4 \tag{3.3}$$

Where $\left|V(z)_{planar\ (confocal)}\right|$ is the normalized electric field amplitude in response to a planar reflector in confocal imaging system, as a function of defocus distance z.

The axial resolution of confocal microscope is defined as the half-power width (3 dB point) of the main lobe of the intensity response from Equation 3.3, which is given as

$$\Delta z_{planar} = \frac{0.45\lambda_\circ}{n(1-\cos\theta)} \tag{3.4}$$

For numerical apertures smaller than $\frac{1}{\sqrt{(2)}}$, paraxial approximation sufficiently describes the axial response [52], and Equation 3.4 can further be simplified by using the identities

$$\sin\theta \approx \theta$$
$$\cos\theta \approx 1 - \frac{\theta^2}{2}$$

to a more frequently described formula in the literature

$$\Delta z_{planar} = \frac{0.9n\lambda_\circ}{NA^2} \tag{3.5}$$

Where $NA = n\sin\theta$ represents the numerical aperture of objective lens.

For point reflector, the intensity at the detector plane of confocal imaging system can be written as:

$$I(z)_{point} = |V(z)_{point}|^2 = \left| \frac{\sin\frac{knz}{2}(1-\cos\theta)}{\frac{knz}{2}(1-\cos\theta)} \right|^4 \tag{3.6}$$

It can be noted that the normalized optical coordinate for point reflector is half of the normalized optical coordinate from planar reflector. This is because, the intensity response of point reflector is approximately square of the intensity response from planar reflector.

The half-width point of the intensity response to a point reflector, From Equation 3.6, is given as

$$\Delta z_{point} = \frac{0.62\lambda_\circ}{n(1-\cos\theta)} \tag{3.7}$$

For numerical apertures smaller than $1/\sqrt{2}$, Equation 3.7 is simplified to

$$\Delta z_{point} = \frac{1.24 n \lambda_{\circ}}{NA^2} \tag{3.8}$$

The effectiveness of confocal gating in both improving the axial resolution and enhancing the image contrast, when compared with conventional widefield microscope, is demonstrated by plotting a simulated point spread function (PSF) in Figure 3.2. The improvement in the axial resolution of confocal microscope is because of using the microscope objective twice, for point illumination and detection, as opposed to once in widefield. Therefore, the confocal response is simply the squared response of widefield, and hence the resolution improvement. Image contrast, on the other hand, is also improved in confocal detection, because the squared response flattens the side lobes present in widefield PSF. The side lobes in widefield PSF are caused by the diffraction property of the light waves and finite aperture size of the lens.

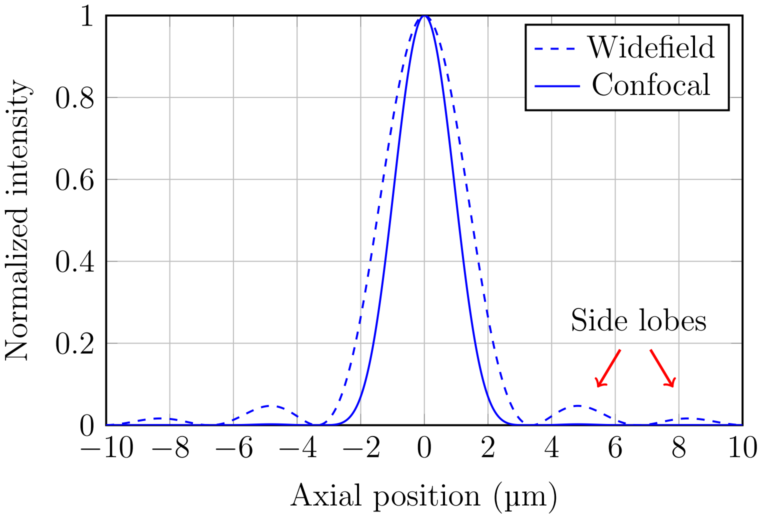

Figure 3.2: Simulated depth response of widefield and confocal microscope for a point reflector along the optical axis, imaged with 0.8 NA microscope objective and 835 nm wavelength. There are no side lobes in confocal PSF which signify the fact that, confocal imaging systems measure light from a limited and contiguous axial section and hence enables optical sectioning of samples.

The presence of one main lobe in confocal response, as shown in Figure 3.2, signifies the fact that detector measures the only light that originated from a limited and contiguous axial section, hence images obtained with confocal microscope are referred to as optical sections.

3.2.2 Transverse Response of Confocal Microscope

The transverse response of confocal microscope is characterized by spatial variation of the intensity of the image received at the detector plane when the objective lens is illuminated by a perfect point source.

In an ordinary microscope, image of a perfect point source through an aberration free spherical lens is an airy function [53]

$$h(r)_{widefield} = \frac{2J_1(v)}{v} = \frac{2J_1(krn\sin\theta)}{krn\sin\theta} \tag{3.9}$$

Where $J_1(v)$ is the Bessel function of the first order and the first kind, $v = krn\sin\theta$ is the normalized radial distance from the optical axis, $k = \frac{2\pi}{\lambda_\circ}$ is the wave number with $\lambda_\circ$ as the wavelength in free space. n is the refractive index, and r is the distance from the center point of image.

For a confocal imaging system, the response is squared as the same objective lens is used for illumination and detection, given as

$$h(r)_{confocal} = \left(\frac{2J_1(v)}{v}\right)^2 = \left(\frac{2J_1(krn\sin\theta)}{krn\sin\theta}\right)^2 \tag{3.10}$$

The intensity measured by a detector can be written as

$$I(r)_{confocal} = |h(r)_{confocal}|^2 = \left|\frac{2J_1(krn\sin\theta)}{krn\sin\theta}\right|^4 \tag{3.11}$$

For a given intensity response in confocal imaging system, resolution can be defined using different criterion, resulting in slightly different formulae. Half-power width criteria defines transverse resolution as the distance along which intensity response from a point reflector falls to its half power, given as:

$$\Delta x_{3dB} = \frac{0.37\lambda_\circ}{\mathrm{NA}} \tag{3.12}$$

Rayleigh criteria defines transverse resolution as the distance between two closely spaced point reflectors, when maxima of one point reflector's response coincides with the minima of other, given as:

$$\Delta x_{Rayleigh} = \frac{0.44\lambda_\circ}{\mathrm{NA}} \tag{3.13}$$

The Sparrow criteria considers two closely spaced point reflectors to be resolved, if their joint intensity response has a vanishing minima, given as:

$$\Delta x_{Sparrow} = \frac{0.51\lambda_\circ}{\mathrm{NA}} \tag{3.14}$$

where $\lambda_\circ$ is the wavelength of light in free space, and $NA = n \sin\theta$ represents the numerical aperture of the objective lens.

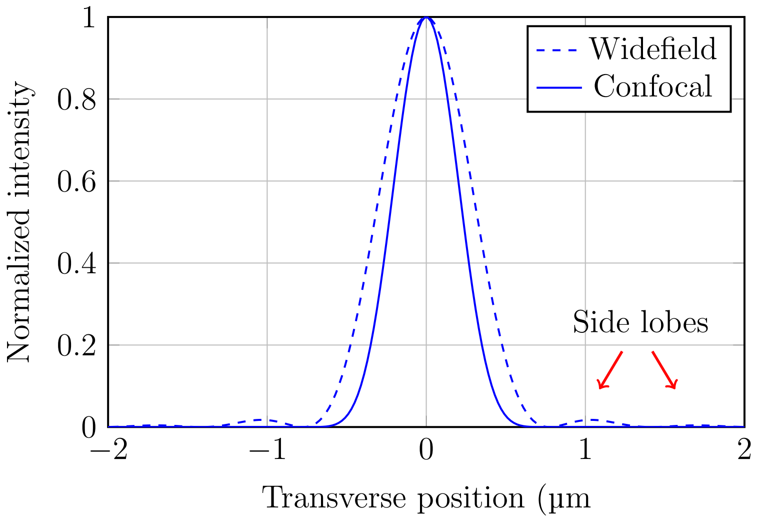

Figure 3.3: Simulated transverse response of widefield and confocal microscopes for a point reflector, imaged with 0.8NA objective lens at 835nm wavelength. The intensity fall off is more rapid in confocal response, which improves the resolution. The side lobes present in widefield response are flattened by the confocal response.

Simulated transverse response of confocal and widefield microscope with 0.8

NA, and 835 nm wavelength is plotted in Figure 3.3. The effectiveness of confocal detection is demonstrated by the suppressed side lobes and rapid intensity fall off, as compared with widefield PSF. Therefore, confocal detection improves the transverse spatial resolution in comparison with widefield microscopes.

3.3 Optical Coherence Microscopy

Optical coherence microscopy (OCM) is a powerful imaging technique that combines characteristics of low coherence interferometry with confocal microscopy, and enables optical sectioning of highly scattering samples. OCM was first introduced in time domain detection scheme [2, 3], where a moving mirror in the reference arm was used for depth scanning, and galvanometer scanners for lateral scanning, to obtain cross sectional images from scattering samples. Another implementation of OCM reported in the literature, known as full-field OCM (FFOCM) involves full-field illumination of the sample, which does not require lateral scanning [54, 55, 56]. However, the main disadvantage with both of these approaches is the poor phase sensitivity, because of scanning mirror in the reference arm. Phase sensitivity was improved with spectral domain implementation of OCM [7, 6], which does not require scanning of the reference arm.

The main distinction between OCT and OCM is that, the later employs high numerical aperture (NA) optics in the sample arm to increase the transverse spatial resolution. Since the depth of focus varies with inverse square of NA, high transverse resolution trades off the depth of focus. The effect of NA on transverse resolution and depth of focus is illustrated in Figure 3.4. In spectral domain OCT, lower NA and larger depth of focus is used to acquire the complete depth profile of a sample in one exposure. Where as in OCM, higher NA and shorter depth of focus limits the amount of depth information that can be acquired in one exposure, and the sample or the beam is translated axially to cover the entire imaging depth possible for a given tissue type and probing wavelength. Therefore, with high NA objective in the sample arm, 3D scanning mechanism is required in spectral domain OCM, which also increases the system complexity. *En face* images are acquired at consecutive depths to reconstruct the 3D structure of samples.

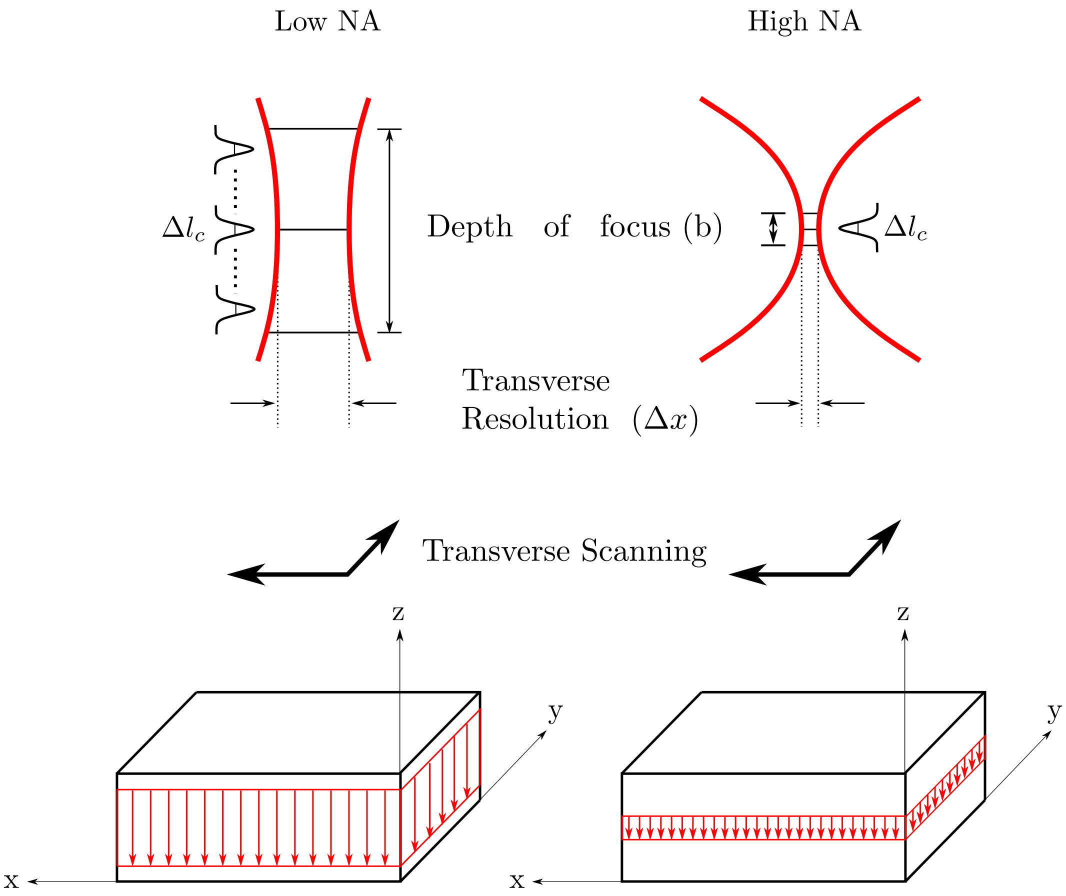

Figure 3.4: Illustration of how numerical aperture affects the depth of focus. With low NA, SDOCT has limited transverse resolution but extended depth of focus, which allows for measurement of complete depth profile of a sample in one exposure. With high NA, OCM has high transverse resolution but limited depth of focus, and acquired *en face* or C-scans at different depths to reconstruct 3D structure of a sample.

3.3.1 Depth Response of OCM

The axial resolution of OCM is influenced by the numerical aperture of objective lens, only if the resulting depth of focus or confocal parameter is equal to or shorter than the coherence length of the light source. Under this condition, the axial resolution of OCM can be defined as the half-power width (or 3dB point) of convolved confocal and coherence responses of the system. In fiber-optic based confocal scanning systems, aperture of the single mode fiber functions as a pinhole that spatially filters the light, and therefore axial resolution is determined by the principles of confocal microscopy.

The depth response of confocal imaging systems is already described in previous section. The depth response of coherence detection is equivalent to the envelope of the self-coherence function, and is given as [57]:

$$\mathrm{PSF}(\Delta z) \propto \left| \int S(\lambda) \exp \left[i \frac{2\pi}{\lambda_\circ^2} (\lambda - \lambda_\circ) 2\Delta z \right] d\lambda \right| \tag{3.15}$$

Where $S(\lambda)$ represents power spectrum of the light source, and $\lambda_\circ$ its center wavelength. The intensity of coherence gated PSF falls off exponentially as the optical pathlength difference Δz increases. Therefore, combination of confocal and coherence gating attenuates out-of-focus light much more effectively than confocal gating alone.

Maximum OCM signal and sharp image contrast is achieved only when both confocal and coherence gating functions are perfectly aligned along the optical axis [58]. In time-domain OCM, the position of the mirror in reference arm is adjusted to perfectly overlap the confocal and coherence window. However, this alignment is not straightforward because the position of focus inside the tissue depends on its refractive index, and moves deeper inside the tissue with an increase in refractive index. Whereas, the position of coherence window gets shallower with an increase in refractive index. Therefore, in time-domain OCM systems manual alignment between confocal and coherence functions is necessary, and generally realized with passive or active auto-focusing implementations [59].

In spectral domain OCM systems, alignment between confocal and coherence functions is not an issue, because the cross-correlation function or the measured spectral interferogram is encoded with frequencies that increases linearly with depth. Therefore in spectral domain OCM, confocal function can be positioned anywhere within the axial range of the spectrometer, as the coherence functions are uniformly distributed.

3.4 Optical Coherence Phase Microscopy

Optical coherence phase microscopy (OCPM) is an extension of OCM, which utilizes the phase component of coherent signal as an additional contrast to characterize dynamic properties of the sample. The important advantage of phase contrast in OCM is that, it is quantitatively measured and it is sensitive to sub-nanometer changes in optical pathlength. This is in contrast with Zernike and Nomarski phase contrasts in traditional widefield microscopy, which are qualitative phase measurement techniques. Another important advantage of phase contrast in OCM is that it is depth resolved, i.e., it can resolve sub-nanometer optical pathlength changes at different depths inside a tissue.

In order to consider the origin of phase contrast, lets recall the equation that represents measured detector current for a spectral interferogram, from Equation 2.6:

$$\begin{aligned}\mathrm{I}_D(k) =& S(k)[\mathrm{I}_r + \mathrm{I}_{s1} + \mathrm{I}_{s2} \dots \mathrm{I}_{sn}] \quad \text{“DC Terms”} \\ &+ S(k) \sum_{n=1}^{N} \sqrt{\mathrm{I}_r \mathrm{I}_{sn}} (\cos[2k(z_r - z_{sn})]) \quad \text{“Cross-Correlation Terms”} \\ &+ S(k) \sum_{n \neq m=1}^{N} \sqrt{\mathrm{I}_{sm} \mathrm{I}_{sn}} (\cos[2k(z_{sm} - z_{sn})]) \quad \text{“Auto-Correlation Terms”}\end{aligned} \tag{3.16}$$

For simplicity sake, DC, auto-correlation and complex conjugate terms can be ignored, then detector current can be written as

$$\mathrm{I}_D(k) = S(k) \sum_{n=1}^{N} \sqrt{\mathrm{I}_r \mathrm{I}_{sn}} (\cos[2k\Delta z_n])$$

$$or$$

$$\mathrm{I}_D(k) = S(k) \sum_{n=1}^{N} \sqrt{\mathrm{I}_r \mathrm{I}_{sn}} (\cos[2k(\Delta z_n + \delta z_n)]) \tag{3.17}$$

Where $(\Delta z_n + \delta z_n)$ is the position of n^{th} reflector in the sample. Δz_n is an integer multiple of sampling interval in z-space or the index of elements in an A-scan. δz_n is the sub-coherence-length fluctuations in the position of reflectors in depth. The detector current at successive instances of time can be written as

$$\mathrm{I}_D(k,t) = S(k)\sum_{n=1}^{N}\sqrt{\mathrm{I}_r\mathrm{I}_{sn}}(\cos\left[2k(\Delta z_n + \delta z_n(t))\right]) \tag{3.18}$$

Where $\delta z_n(t)$ represents sub-coherence length fluctuations in the position of reflector over time, which can be recovered by taking the phase angle difference over time

$$\begin{aligned}\angle\mathrm{I}_D(k,t_m) - \angle\mathrm{I}_D(k,t_{m-1}) &= 2nk(\delta z(t_m) - \delta z(t_{m-1}))\\ &= \frac{4\pi n}{\lambda_\circ}[\delta z(t_m) - \delta z(t_{m-1})]\end{aligned} \tag{3.19}$$

Where n is the refractive index of the medium. Therefore, sub-coherence-length fluctuations of reflectors position in depth is calculated by taking the difference of phase angles, $\Delta\phi$, and is given as:

$$\delta z = \frac{\Delta\phi}{4n\pi}\lambda_\circ \tag{3.20}$$

The term δz appears in the phase of the complex A-scan, and can resolve the position of depth scatterers beyond the axial resolution limit set by the coherence length of light source. It can be noted that the phase angle has a principal range of $[-\pi,\pi]$, and gets wrapped for fluctuations larger than half of the center wavelength, and gives rise to 2π ambiguity, which can be avoided with high temporal resolution.

Simulated response in Figure 3.5 illustrates how the phase component determines the sub-coherence-length changes in the position of depth scatterers. For the shown simulated example, center wavelength and bandwidth is 835 nm and 50 nm respectively, which provides a coherence length of $\approx 6\,\mu\mathrm{m}$. The panel (a) shows two spectral interferograms measured from a sample with two delta reflectors. First delta reflector has moved an axial distance of $\delta z_1 = 20$ nm between the two measurements. Because δz_1 is a distance much smaller than the coherence length of the light source, respective modulation frequency stays the same, albeit phase shifted.

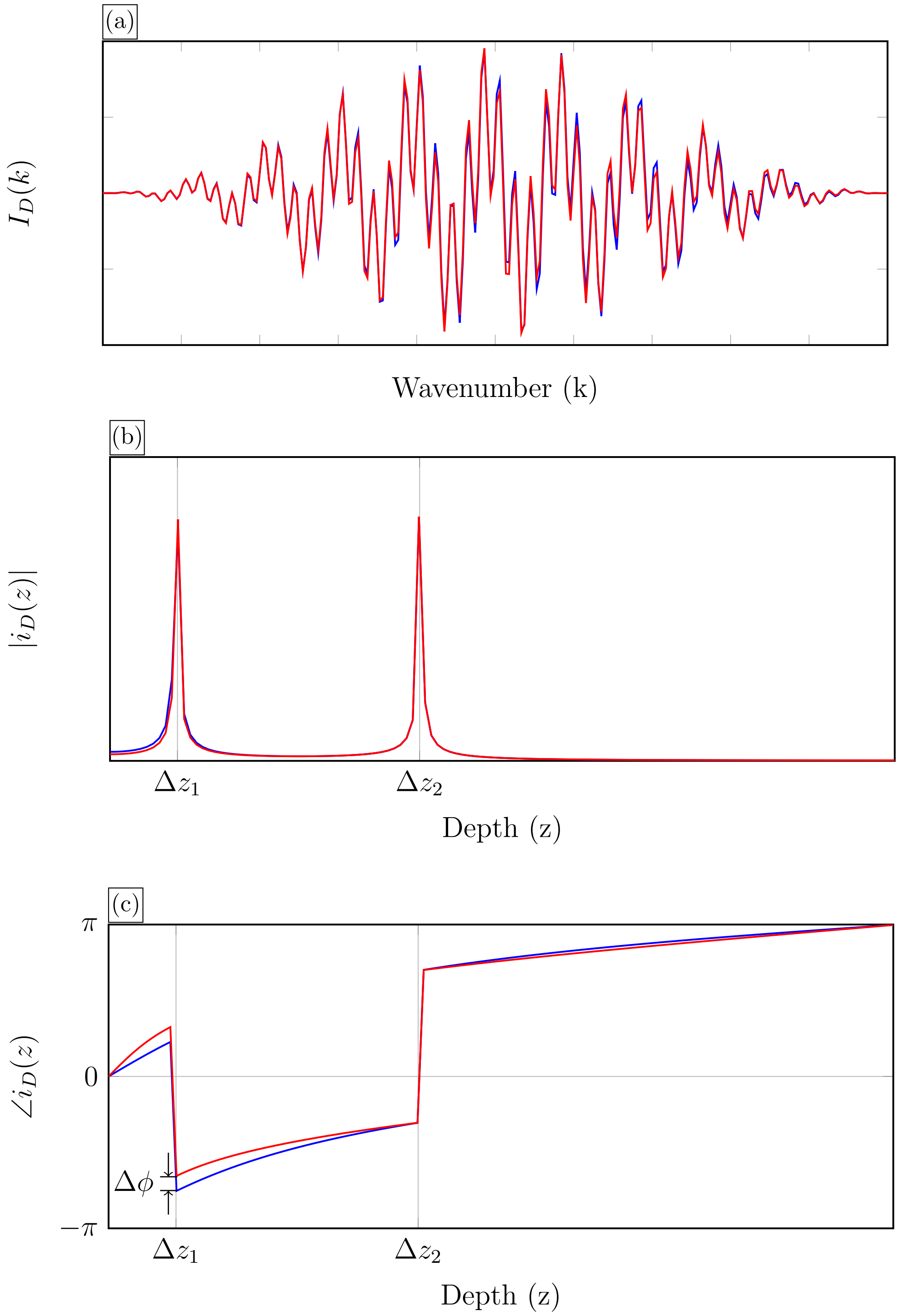

Figure 3.5: Simulated relationship between sub-coherence-length displacement of depth scatterers and phase values of complex A-scans. (a) Two spectral interferograms acquired before (blue) and after (red) the displacement of first delta reflector by $\delta z_1 = 20$ nm. (b) The amplitude of complex A-scans, whose peak positions have not changed significantly. (c) The phase of complex A-scans, where $\delta z_1 = 20$ nm manifests as $\Delta\phi_1 = 0.3$ radians between the two measurements.

The panel (b) in the figure shows the amplitude of the complex A-scans where the scatterers position between the two measurements have not changed significantly. The panel (c) shows the phase values of two complex A-scans, which have changed for first delta reflector, in response to it sub-coherence-length movement. The difference of the phase values between two A-scans, $\Delta\phi$, provides the axial displacement of scatterer, δz, as given by Equation 3.20.

The minimum axial displacement δz that can be detected is determined by the phase sensitivity of the system, which in turn is determined by signal-to-noise ratio (SNR). For a shot-noise limited detection system standard deviation of phase noise or the phase sensitivity is given as [32, p.768]:

$$\delta\phi_{sens} = \frac{2}{\pi}\sqrt{\frac{1}{SNR}} \tag{3.21}$$

3.5 Phase Component as Functional Contrast

Phase contrast in optical microscopy has long been utilized, as it enables visualization of subcellular structures that are obscured in traditional widefield microscope images. However, traditional phase contrast techniques such as Zernike [60] and Nomarsky [61] contrasts provide qualitative measurement of phase variations, as they convert phase changes into image brightness. SDOCPM provides quantitative measurement of phase that is sensitive to sub-nanometer axial displacements of scatterers. This phase contrast can be utilized to characterize dynamic properties of the tissue, and for surface topographic measurement of reflecting samples.

In optical microscopy, contrast of an image can arise from variations in both amplitude and phase of the probing light. Illustration of how amplitude and phase contrast originates in optical microscopy is as shown in Figure 3.6. Absorption and scattering of photons in tissue are caused by inhomogeneities in optical index, and leads to loss of amplitude. These relative losses are measured across the sample to form an amplitude image, which reveals the morphological structure of sample. Phase contrast on the other hand, is generated by

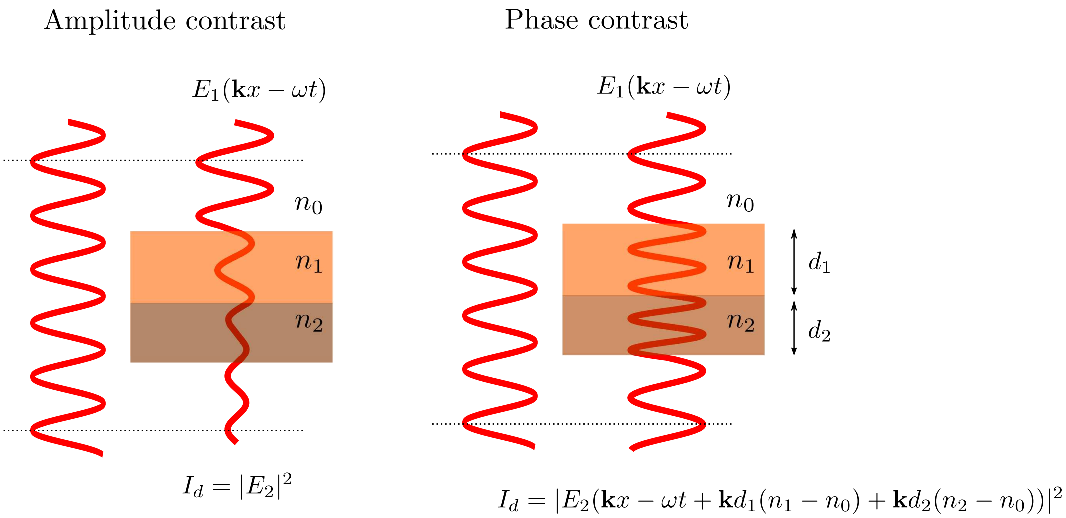

Figure 3.6: Generation of amplitude and phase contrast in optical microscopes. Amplitude contrast is generated by loss in the amplitude of incident light due to absorption and scattering, and is measured by a simple incoherent detector. Phase contrast is generated by propagation delay of light waves, introduced by the sample refractive index in relation to the wavelength of light. Interference is required for phase contrast measurements.

variations in optical pathlength across a sample. Optical pathlength is the product of sample length and its refractive index, which is $n_1d_1 + n_2d_2$ for the sample shown in Figure 3.6. As the light passes through the tissue, structures with different refractive index introduce different path delays, also known as phase retardation, and these relative path delays across the sample reveals its optical density. Amplitude contrast can be measured with a simple incoherent photodetector, whereas interference is required for quantitative phase measurements.

Phase contrast measurements are quantitative in nature as phase change depends only on the sample properties such as change in physical dimensions or change in its optical index. Phase contrast is insensitive to amplitude variations, which can be caused by any number of reasons such as source instability, angle of incidence, etc.

Different physiological processes in tissue such as homeostasis, respiration, perfusion, cellular signaling, etc., cause spatio-temporal changes in optical pathlength. These physiological processes also underpin the functioning of senses such as vision, smell, hearing, etc. Most of these physiological processes cannot be understood from the morphological structures alone, and require an additional dynamic contrast. Therefore, phase contrast of OCM could potentially be used to measure spatio-temporal changes in optical pathlength, in relation to physiological processes and provide a functional contrast.

3.6 Advantages of OCM Over Confocal Microscopy

Confocal scanning microscopy itself has revolutionized many disciplines in biological sciences with its optical sectioning and 3D imaging capability. However, it also has some limitations that can be improved upon by optical coherence microscopy.

- Combined confocal and coherence gating attenuates out of focus and multiple scattered light much more effectively than confocal gating alone, and enables thin optical sectioning of scattering samples.
- The confocal axial response is broadened in scattering samples because of spherical aberrations [62], which degrades image resolution and contrast. Coherence gating with its narrow response can effectively flatten the spread out wings of aberrated confocal response, and restore the image resolution and contrast.
- Combined confocal and coherence gating extends the penetration depth in scattering samples compared with confocal gating alone [63], as it can detect very weak back scattered light through its homodyne gain factor.
- The quantitative phase contrast of OCM can potentially be used to characterize dynamic properties of the samples.
- OCM could also provide depth-resolved spectroscopic contrast [64] that can be utilized for assessment of oxygen saturation level [31], and localization of melanocytes [65] in tissues.

Chapter 4

Implementation of SDOCPM System

4.1 Introduction

Spectral domain optical coherence phase microscopy (SDOCPM) is a phase sensitive implementation of optical coherence microscopy, where phase contrast of the coherent signal is used to measure nano-scale displacements of scatterers in tissue. Almost all of the SDOCPM implementations so far have used common-path interferometer to achieve high phase sensitivity. However, the significant drawbacks of common-path topology are limited transverse spatial resolution, limited depth scanning capability, and poor control on reference reflectance which reduces the detection sensitivity. This chapter describes an implementation of SDOCPM that overcomes these drawbacks and provides very high phase sensitivity.

This chapter provides a detail overview of the hardware and software of the implemented SDOCPM system. High transverse spatial resolution is achieved by using a water immersion microscope objective with 0.8 NA. High phase sensitivity is achieved by splitting the laser beam into sample and reference paths, after the galvanometer scanners, so as to keep the phase noise originating from scanners into common mode. The optical setup was further isolated from other stray noise sources by a passively damped optical table.

A widefield microscope is integrated into the SDOCPM system for better visualization of sample under focus, and to elucidate the differences between

SDOCPM and conventional widefield images. The sampling speed of widefield microscope is up to 400 frames/sec with a pixel resolution of 1280×1024.

In the next section, a brief overview of the state of the art and its limitations are presented, and in following sections, detailed overview of the implemented SDOCPM system including methods and procedures developed for image acquisition and signal processing are presented. A procedure for calculation and compensation of dispersion is also presented.

4.2 State of The Art

To achieve high phase sensitivity almost all implementations of SDOCPM reported in the literature so far, have used a common-path interferometer [6, 7, 8, 9, 10, 11, 12, 13]. In common-path interferometer setup, specular reflections from a surface near the sample provides the reference electric field with which scattered light from the sample combines, and generates an interference fringe pattern. It provides high phase sensitivity because sample and reference light traverse the same optical path, and any noise incurred by mechanical perturbations along the way to the detector, will remain in common mode and cancel out with homodyne mixing. However, common-path topology requires relatively large depth of focus to get reflections from both the reference surface, generally a glass coverslip, and the sample. Larger depth of focus are generally possible with low numerical apertures, which in turn limits the transverse spatial resolution.

Figure 4.1 illustrates the limited transverse spatial resolution in common-path topology. The other drawbacks of common-path topology are limited axial field of view, and poor control on reference reflectance power which lowers the sensitivity. The field of view is effected by the fixed reference position which does not allow translation of focused beam spot further into the sample. The image acquisition speed of SDOCPM systems reported in the literature so far is in the range of $25,000$ to $75,000$ A-scans/sec, which is not sufficient for fast volumetric recording of specimens.

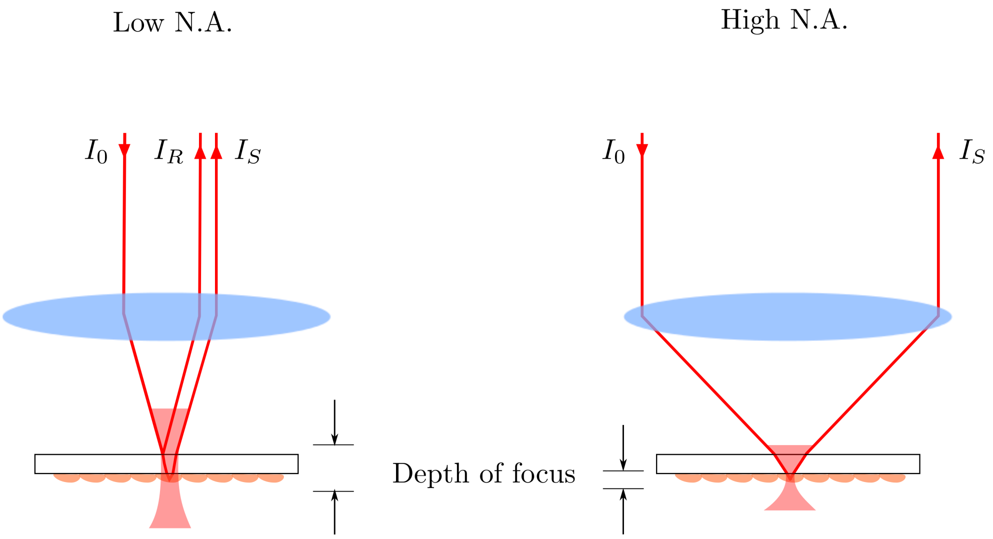

Figure 4.1: Illustration of limited transverse spatial resolution in common-path interferometer setups. With low N.A. and larger depth of focus (left), reflections from the surface of glass coverslip, I_r, serves as reference intensity to the sample reflectance intensity, I_s. With high N.A. and shorter depth of focus (right), it isn't possible to get reflections from both the glass coverslip and the sample, which makes high transverse spatial resolution impractical with common-path interferometer topology. $I_\circ$ represents incident light.

4.3 Optical Setup

Implemented SDOCPM system is integrated into a widefield microscope for combining visualization of sample under focus, and comparison between OCM and conventional widefield images. A simplified schematic of the integrated widefield and SDOCPM system is as shown in Figure 4.2. The light source for SDOCPM is a high power superlumeniscent light diode (BLM-S-840-B-I-20, Superlum Inc., Ireland) with 835 nm center wavelength, 53.6 nm bandwidth, and 29 mW output power. The light from SLD is coupled into the optical setup with a 50/50 fiber coupler and collimated with an achromat of 20.1 mm effective focal length (60FC-4-M20-10, Schäfter + Kirchhoff GmbH), resulting in a $1/e^2$ beam diameter of 3.61 mm. The collimated beam goes through galvanometer based X-Y optical scanners and then through a pair of achromats with 50 and 100 mm focal length respectively, setup in a $4f$ configuration. The pair of achromats, L2 and L3, form a $1:2$ telescopic relay, and increase the beam diameter to 7.22 mm.

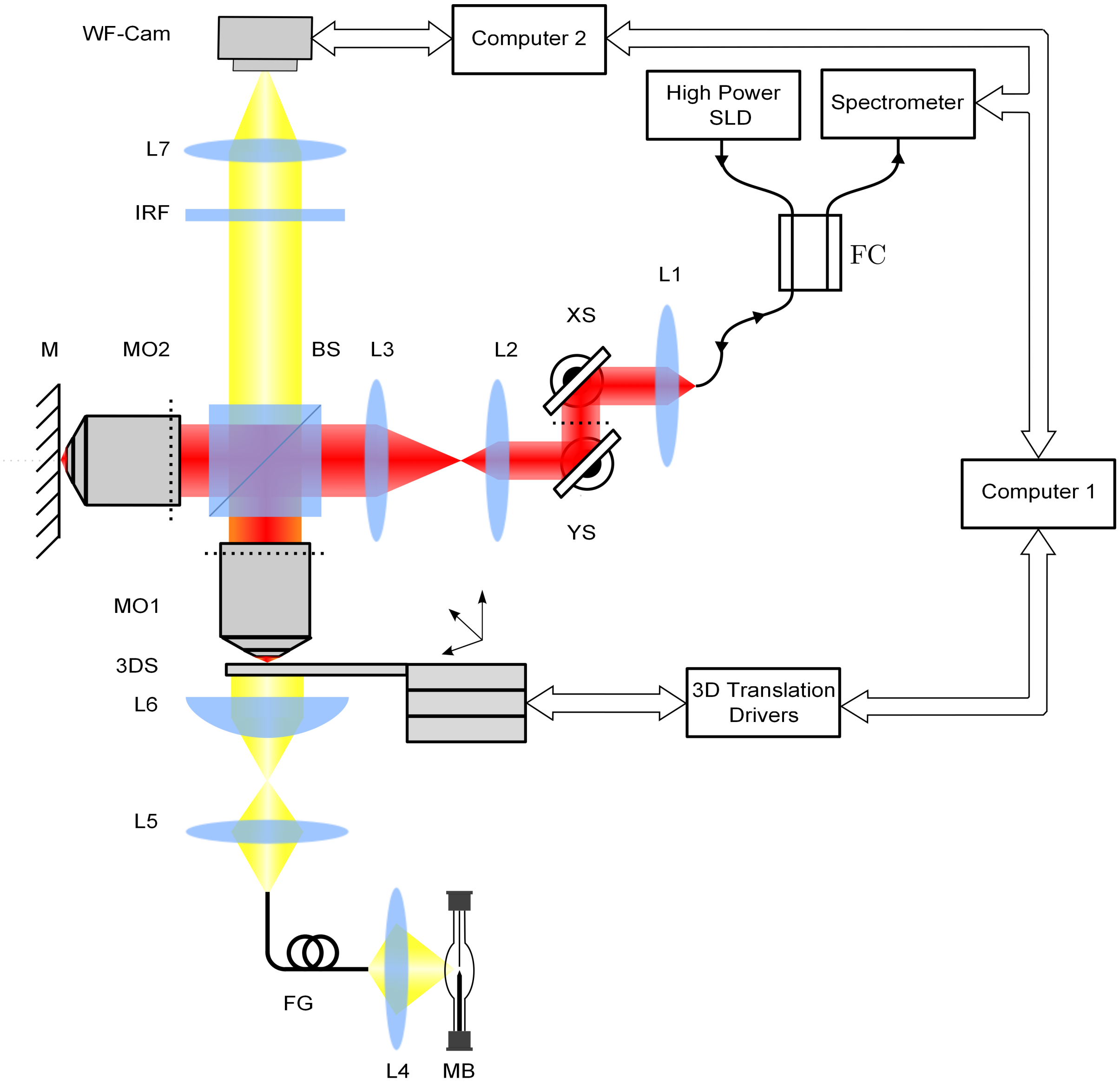

Figure 4.2: Schematic of integrated widefield microscope and SDOCPM system. SLD, super-luminescent diode; FC, 50:50 fiber coupler; L1, collimator lens; XS & YS, X and Y axis galvanometer scanners; L2 & L3, achromats arranged in 1 : 2 telescopic relay; BS, 50:50 beamsplitter cube; MO1 & MO2, identical infinity corrected microscope objectives with 0.8 NA; M, gold mirror; MB, high pressure mercury burner; FG, fiber guide; L4 & L5, collector lens; L6, condenser lens; 3DS, three-dimensional sample translation stage; IRF, near-infrared filter; L7, tube lens; WF-Cam, high speed camera for widefield microscopy.

The pair of achromats, L2 and L3, also image the midpoint of the X-Y scanners pivot points onto the exit pupil planes of two identical microscope objectives. The identical pair of water immersion microscope objectives with 0.8 NA (model # 440095, Carl Zeiss Microimaging GmbH), each in sample and reference arm along with a non-polarizing 50/50 beam splitter cube form a symmetric Linnik interferometer. The single-mode fiber functions as a confocal pinhole aperture for both illumination and detection of light from the sample. The dashed lines perpendicular to the optical light path in the shown schematic represent pupil planes of microscope objectives. A gold plated mirror with $\lambda/10$ surface quality was used in the reference arm. A special mirror holder was designed to keep the gold mirror and reference arm microscope objective tip immersed in water. A 3D translation stage was used for positioning of the sample under the microscope. All achromats used in the setup were coated for maximum visible-infrared transmission.

The output power of the SLD was measured to be 29 mW at center wavelength, 835 nm. However, after splitting the optical power into half, twice, and with 65 % efficiency of galvanometer scanners, optical power at pupil plane of each microscope objective was measured to be 4.5 mW. The power incident on the sample, after rated 80 % transmission efficiency of the microscope objective, was approximately 3.6 mW.

It can be noted that, the laser beam splits into reference and sample arm after the galvanometer scanners. This configuration makes interference fringe recording insusceptible to jitter and mechanical vibrations of the galvanometer scanners. Because any noise originating from the scanners will be in common mode for both sample and reference arm intensities, and cancels out with their homodyne mixing at the beamsplitter. To further minimize the mechanical vibrations and improve the phase sensitivity, the Linnik interferometer was isolated from the rest of the setup, and stationed on a passively damped optical table.

A picture of the integrated widefield and SDOCPM system is as shown in Figure 4.3. Critical components of the optical setup are discussed in the subsections below.

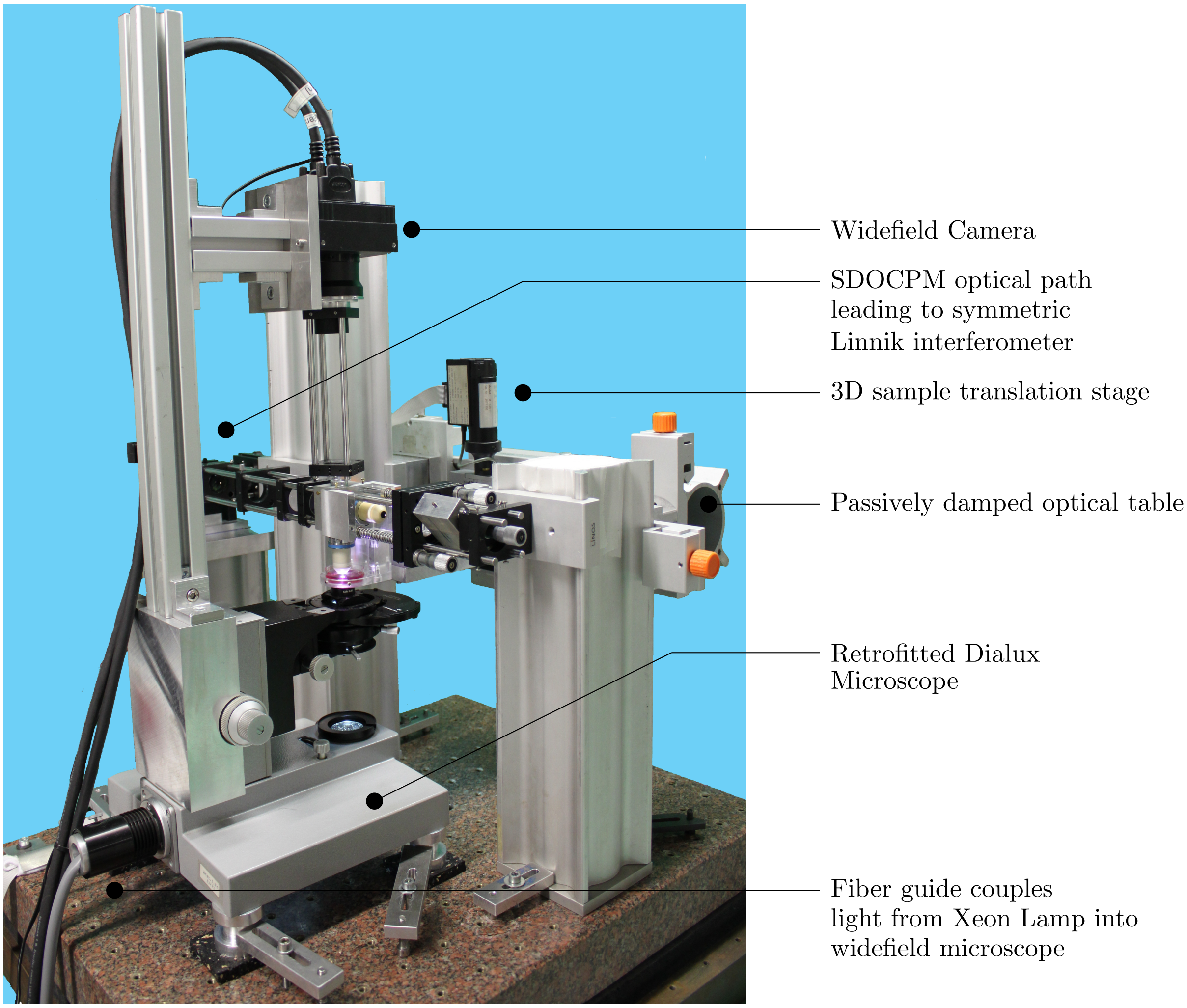

Figure 4.3: Picture of the integrated widefield microscope and SDOCPM system.

4.3.1 Spectrometer

Implemented SDOCPM system uses a linear wavenumber spectrometer from a commercially available OCT imaging system (model # Hyperion, Thorlabs Inc.). A linear wavenumber spectrometer measures light intensity as a function of equispaced wavenumbers ($2\pi/\lambda_\circ$). Measured spectral interferograms does not require computationally intensive data interpolation, and thus significantly increase the image processing speed.

The high-speed line scan camera (spl4096-140k, Basler AG) in the spectrometer has a read out speed of 217, 000 lines/sec. Custom software was developed in LabVIEW (National Instruments, U.S.A) to read out the spectral interferograms, and synchronize it with the galvanometer scanners and sample translation stage.

4.3.2 X-Y Galvanometer Scanners

A pair of closely spaced X-Y galvanometer scanners (6200H, Cambridge Technology) are used to steer the focused beam spot in raster manner. The X-Y galvanometer scanners were adapted into a 30 mm Linos optical cage system, as shown in Figure 4.4. The galvanometer scanners have a total range of ±20°, and are driven by control voltage applied through a multifunction data acquisition board (USB-6251, National Instruments, U.S.A.). A graphical user interface was developed in LabVIEW (National Instruments, U.S.A), which generates a sawtooth scan pattern for X-Y scanners for a range of image field sizes.

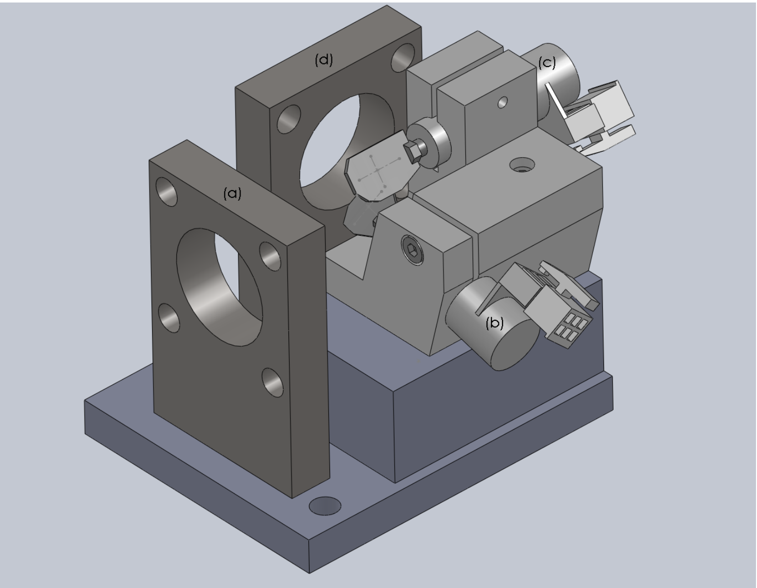

Figure 4.4: 3D Solidworks model depicting XY galvanometer scanners and its adaptation into standard 30 mm Linos optical cage system. (a) 30 mm optical cage plate that aligns the beam with X scanner. (b) Fast axis, X galvanometer scanner, (c) Slow axis, Y galvanometer scanner. (d) 30 mm cage plate that aligns the beam with 1 : 2 telescopic relay.

To avoid fringe washout during the exposure time of the camera, scanners movement is hardware timed with a digital clock from the line scan camera, which sends a pulse after each line read out and advances the scanner position. This timing scheme makes sure that the focused beam spot does not travel more than half the transverse resolution during each exposure time. Furthermore, this synchronization allows for exposure time to be varied anywhere from 2 µs to 100 ms, and the scanners speed would adjust accordingly.

4.3.3 3D Sample Stage

3D translation sample stage is constructed with a pair of piezomotors (M-663, Physik Instrumente GmbH) for XY translation and a linear motor (M-125, Physik Instrumente GmbH) for Z translation. 3D model of the sample translation stage, rendered using Solidworks (Dassault Systèmes SolidWorks Corp., USA) is as shown in Figure 4.5. XY Translation stages have a range of 20 mm with 0.2 µm step resolution, and Z translation stage have a range of 50 mm with 0.1 µm step resolution. A graphical user interface was developed in LabVIEW (National Instruments, USA) to control the 3D motion of the translation stage.

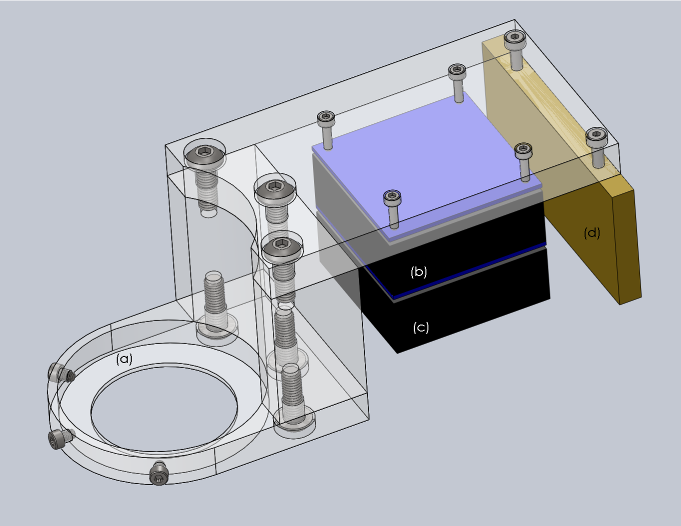

Figure 4.5: Mechanical stage for three-dimensional translation of sample. (a), Light weight acrylic frame for stable mounting of 35 mm petri dish on XY motors. (b), Piezo motor for X translation. (c), Piezo motor for Y translation. (d), Counter-weight to keep the center of mass axis perpendicular to the plane of motion.

For larger field of view than possible with galvanometer scanners and when the temporal resolution isn't critical, a sample can be scanned by translating the XY stage while a static beam fills the back aperture of the microscope objective. The advantage of sample translation is that, focused beam spot diameter remains constant through out the image field and produces uniform optical sections.

4.3.4 Widefield Imaging

To facilitate better visualization of sample under focus, widefield microscope is integrated into SDOCPM system. For optimal Köhler illumination of the sample, composite condenser lens system from Leitz microscope (Dialux 20, Ernst Leitz Wetzlar GmbH) was adapted into the SDOCPM system. The illumination light source for widefield microscope is a high-pressure mercury burner (BH2-RFL-T2, Olympus Optical Co., Ltd.). A fiber optic bundle is used to couple the light from source to the illumination port of Leitz microscope. A water immersion microscope objective (model # 440095, Carl Zeiss Microimaging GmbH) with 40× magnification and 0.8 N.A. collects the transilluminated light from the sample, and a 200 mm focal length tube lens projects the magnified inverted image of the sample on a high-speed CMOS area scan camera (A503k, Basler AG). A near-infrared filter, positioned just before CMOS sensor, blocks the light from high power SLD contributing to the widefield images.

The high-speed area scan camera allows recording of widefield images at 400 frames/sec with 1280 × 1024 pixel resolution. A graphical user interface was developed in LabVIEW for real-time display, and synchronized recording of widefield and SDOCPM images.

4.3.5 Image Acquisition

Two Camera Link image acquisition boards (PCIe-1429, National Instruments) are used to read out OCT spectrometer and widefiled images simultaneously. Because of high data stream rate, 128 and 112 MB/sec for widefield and SDOCPM respectively, acquisition boards were housed in two separate desktop computers and image acquisition was synchronized with a hardware trigger signal.

The timing sequence for one complete OCT volume or OCM *en face* image acquisition is as shown in Figure 4.6. A master digital clock signal, generated by the linescan camera controls the movements of X-Y galvanometer scanners and triggers the acquisition of widefield images. Frequency of the digital clock signal is determined by the exposure time (t_{exp}) of linescan camera, and goes up to 217 kHz. Analog control voltage values for X-Y galvanometer scanners are stored in the on-board memory of data acquisition board (USB-6251, National Instruments, USA), and read out sequentially by the digital clock signal.

The fast axis of the scanning system, X-axis galvanometer scanner, requires a settling time after each B-scan as the scanner reverses the trajectory for raster scan pattern. The settling time of the scanners is calibrated for different scan angles and taken into account for scanning different image field sizes.

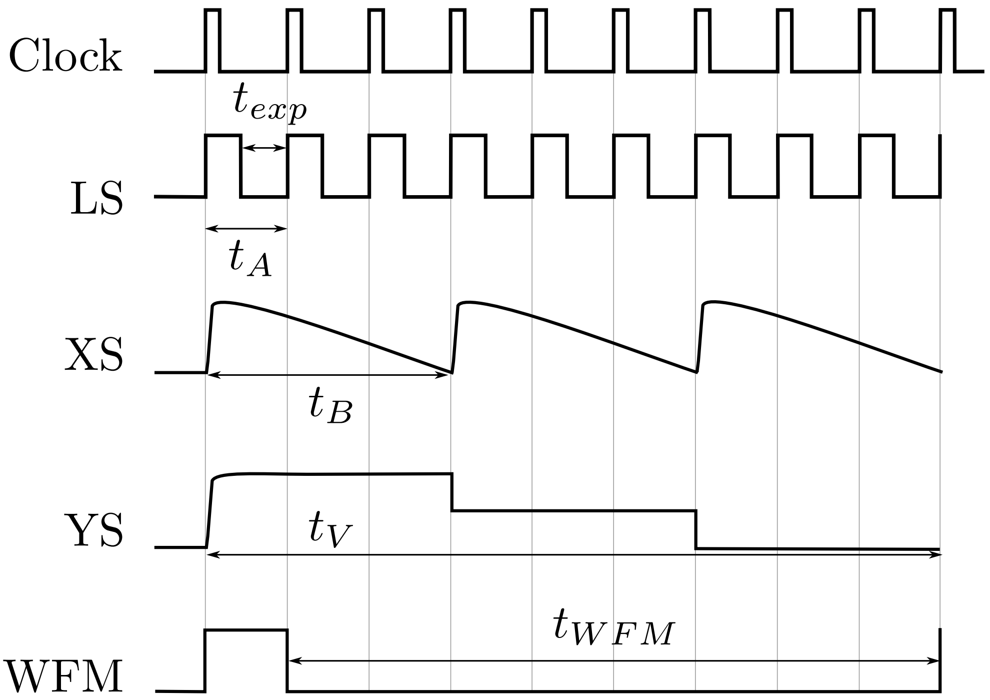

Figure 4.6: Timing sequence of SDOCPM and widefield image acquisition. Clock, master digital clock signal generated by linescan camera; LS, digital control voltage for the linescan camera; XS & YS, analog control voltage for X and Y-axis galvanometer scanners; WFM, digital control voltage for widefield microscope; t_{exp}, exposure time for an A-scan; t_A, t_B, and t_V, time for acquisition of A-scan, B-scan, and a complete SDOCPM volume, respectively; t_{WFM}, exposure time for widefield image.

4.4 Signal Processing

Signal processing and computation of OCM images was done with Matlab (Mathworks, USA). A simplified block diagram in Figure 4.7 shows various computational steps in signal processing and image reconstruction process. Because of high transverse spatial resolution and shorter depth of focus, the sample was *en face* or C-scanned at different depths, to reconstruct its 3D structure. Volumetric apodization corrects for fixed pattern noise in the spectral interferograms before taking the Fourier transform to calculate the complex A-scans. Complex *en face* image plane is extracted from calculated A-scans, by determining the orientation of two-dimensional focal plane. *En face* optical sections with thickness equivalent to axial resolution are obtained by taking the magnitude of complex *en face* image planes. The three dimensional structure of a sample is reconstructed by combining the *en face* optical sections acquired from consecutive depths.

The corresponding phase values along the focal plane are unwrapped over two spatial dimensions and time, and converted into changes in axial optical pathlength. For dynamic samples, spatio-temporal changes in optical pathlengths are caused by physiological processes and is converted into either axial displacement, group refractive index, or optical dispersion, etc., depending on the tissue type. Spatio-temporal changes in optical pathlengths are used as a functional contrast, which is measured with sub-nanometer accuracy using the implemented SDOCPM system.

4D display of the reconstructed sample, i.e., three dimensions of structural data and another dimension of functional contrast over time, is also done with Matlab.

Critical steps in signal processing and image reconstruction are further discussed in subsections below:

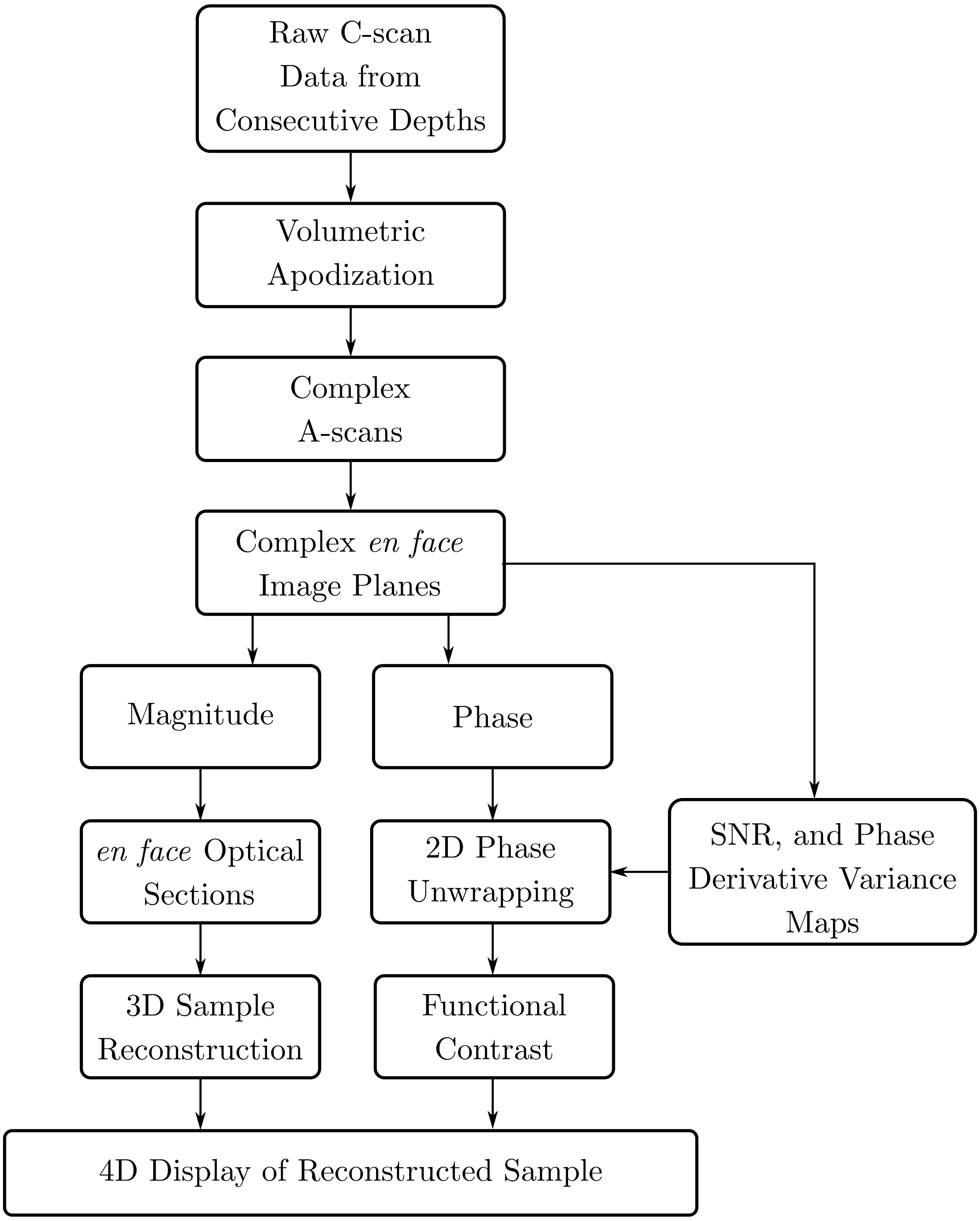

Figure 4.7: Simplified block diagram showing various steps in signal processing, image reconstruction and display of the SDOCPM data. All of the computational steps, algorithms and 4D display were implemented in Matlab.

4.4.1 Calculation of A-scans

In optical coherence tomography, depth profile or A-scan is obtained by taking the Fourier transform of measured cross-spectral density function, i.e., a spectral interferogram between sample and reference arm reflectance. In order to obtain Fourier transform limited axial resolution for a given light source, measured interferogram needs to be corrected for various noise sources. Block diagram in Figure 4.8 depicts various computational steps in calculation of an A-scan. It can be noted that the raw spectrum obtained from spectrometer is already linearly spaced in wavenumbers or k-space, and does not require further resampling.

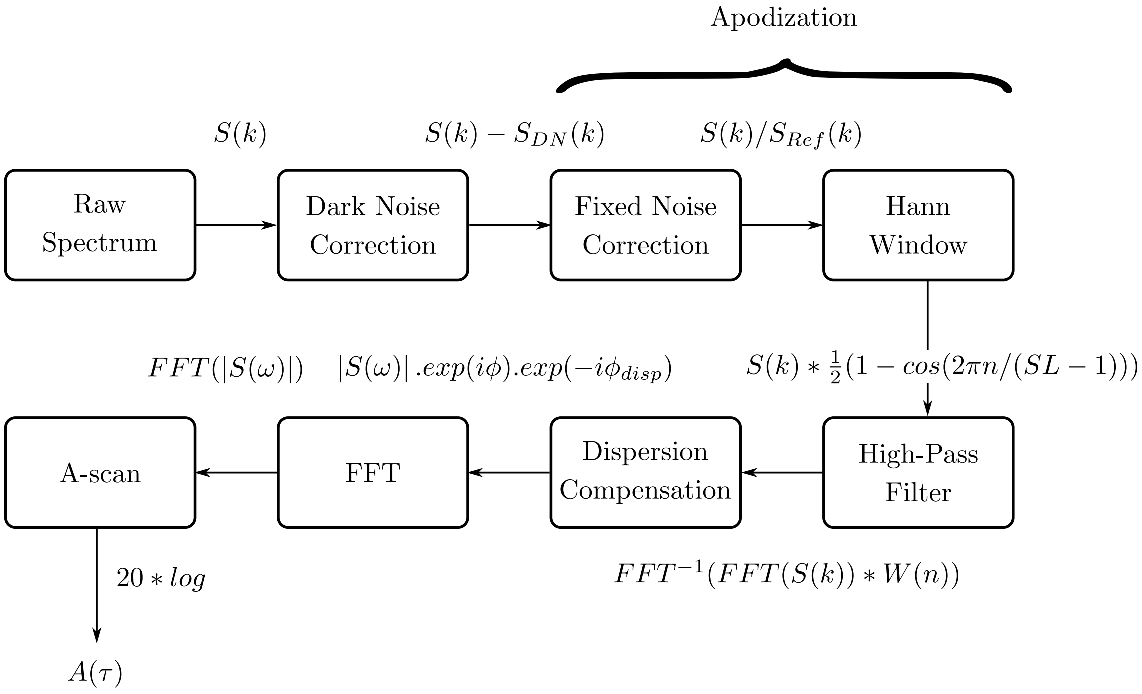

Figure 4.8: A block diagram depicting various computational steps in calculation of an A-scan in SDOCT

Dark Noise Correction

Measured raw spectrum is first corrected for dark noise, which is the temporal random noise of CMOS linescan camera with no illumination. The dark noise, $S_{DN}(\lambda)$, also referred to as thermal noise is obtained by taking the average of 3000 line readouts with SLD powered off, and subtracted from all subsequent measurements.

Apodization

Apodization refers to reshaping of the measured spectrum to avoid spectral leakage. Spectral leakage results from finite spectrum length and could be minimized by smoothing the discontinuities on the edges of measured interference spectrum. Hann window is chosen for smoothing the discontinuities, as it provides a good balance between frequency resolution and spectral leakage [66].

Apodization step also includes correction of fixed pattern noise, which is variation in individual pixel response for uniform illumination. A reference spectrum for fixed pattern noise is obtained by blocking the sample arm, and recording the reference arm intensity. Fixed pattern noise is corrected by dividing all subsequent spectral interferograms with the reference spectrum.

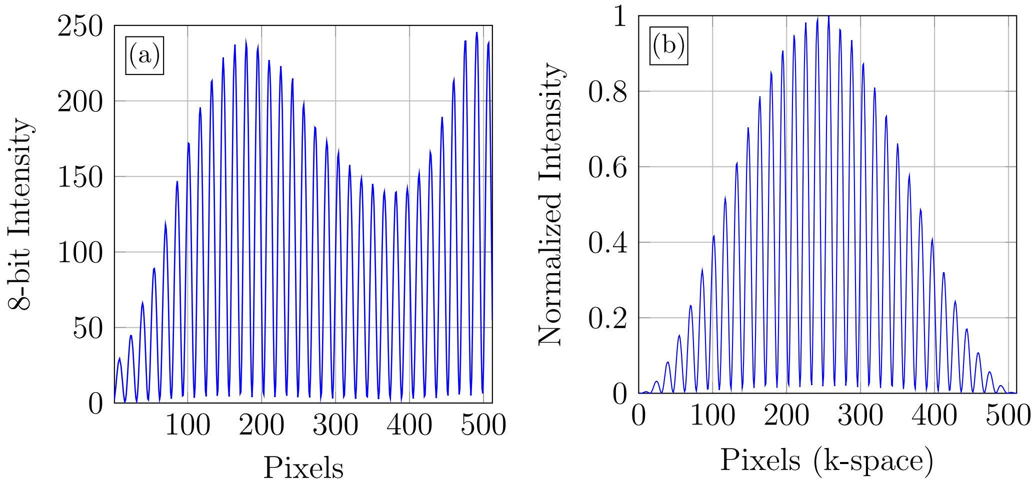

Figure 4.9: Spectral interferogram measured from two surfaces of a coverslip. (a) Raw spectrum, (b) Apodized spectrum.

In the implemented SDOCPM system, reference arm is also being scanned with a symmetric Linnik interferometer, and as a consequence of lateral scanning, the spectral shape might not be uniform through out the image field. Therefore, a volumetric apodization is done to correct for any slight changes in spectral shape.

The apodizing volume, $S_{Apod}(k, x, y)$, is calculated using the equation below:

$$S_{Apod}(k, x, y) = \left[\frac{1}{S_{Ref}(k, x, y)}\right] \cdot \left[\frac{1}{2}(1 - cos(2\pi n/(SL - 1)))\right] \tag{4.1}$$

Where $S_{Ref}(k, x, y)$ is the reference arm intensity for entire image field, and the second bracketed term is the hann window with SL as the spectrum length, and $n = 1, 2, 3 \; ... \; SL$.

Figure 4.9 shows an interference spectrum before and after apodization.

High-Pass Filter

The measured spectral interferogram includes a relatively large DC component along with a modulated AC signal, as given below:

$$I_D(k) = S(k)[I_r + I_s + 2\sqrt{I_r I_s} cos(2k\Delta l)] \tag{4.2}$$

The cosine term in the measured interferogram is the only relevant term for axial ranging of scatterers in tissue, where as the DC components does not carry any information about the sample, and simply yield higher amplitude near zero frequency after the Fourier transform. Apodized spectrum is high-pass filtered before FFT to suppress the higher amplitudes near zero frequency. High-pass filter implementation in frequency domain, can be represented as:

$$S(k)_{HP} = \mathfrak{F}^{-1}[\mathfrak{F}(S(k)) * W(n)] \tag{4.3}$$

Where $W(n)$ is the filter function. The apodized spectrum from Figure 4.9, after high pass filtering is can be seen in Figure 4.10.

Dispersion Compensation

Dispersion mismatch between sample and reference arm broadens the FWHM of cross-correlation function, which means it degrades the axial resolution by broadening the peaks in an A-scan and also decreases the sensitivity. Mismatched dispersion between sample and reference arm is numerically compen-

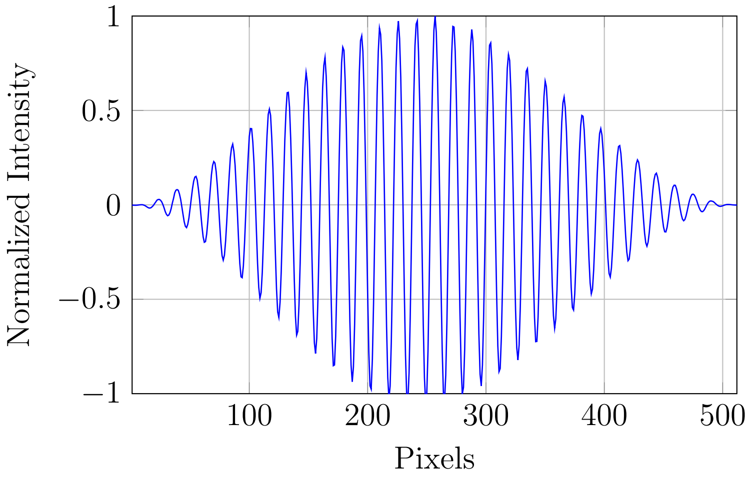

Figure 4.10: Apodized spectrum in Figure 4.9 after high-pass filtering.

sated by subtracting dispersive phase term, ϕ_{Disp}, from the measured spectrum, before performing the Fourier transform.

Although, two identical objectives are used in Linnik configuration in the implemented SDOCPM system, and they themselves do not cause any significant mismatched dispersion. But, acquiring images from 100 µm below the surface of thick specimens does introduce dispersion and is numerically compensated when necessary. An algorithm developed for calculation and compensation of dispersion is described in section 4.4.2.

A-scan

The FFT of the apodized and high-pass filtered spectral interferogram yields a complex A-scan. Because intensity of light falls off exponentially with increasing depth inside the tissues, reflectivity profiles or A-scans are displayed on a log scale. The magnitude of the complex A-scan is converted into decibels (dB) by taking the $10 * \log_{10}$ of the squared detector current, as given below:

$$A(\tau) = 10 * \log_{10} |\mathfrak{F}(S(\omega))|^2$$

or

$$A(\tau) = 20 * \log_{10} |\mathfrak{F}(S(\omega))| \tag{4.4}$$

A-scan as a function of time delay, τ, provides the cross-sectional depth reflectivity profile of the sample. Time delay, τ, is scaled into physical distance in air or tissue by detecting the index of peak position in a reflectivity profile of a glass coverslip with known thickness. The depth range of an A-scan inside the tissue can be calculated as

$$\text{Depth Range} = \frac{(Coverslip\ Thickness) * SL}{2 * n_{tissue} * (Peak\ Index)} \tag{4.5}$$

Where, SL is the spectrum length, and n_{tissue} is the refractive index of the tissue. Figure 4.11 shows a sample A-scan obtained by interference from two surfaces of a glass coverslip.

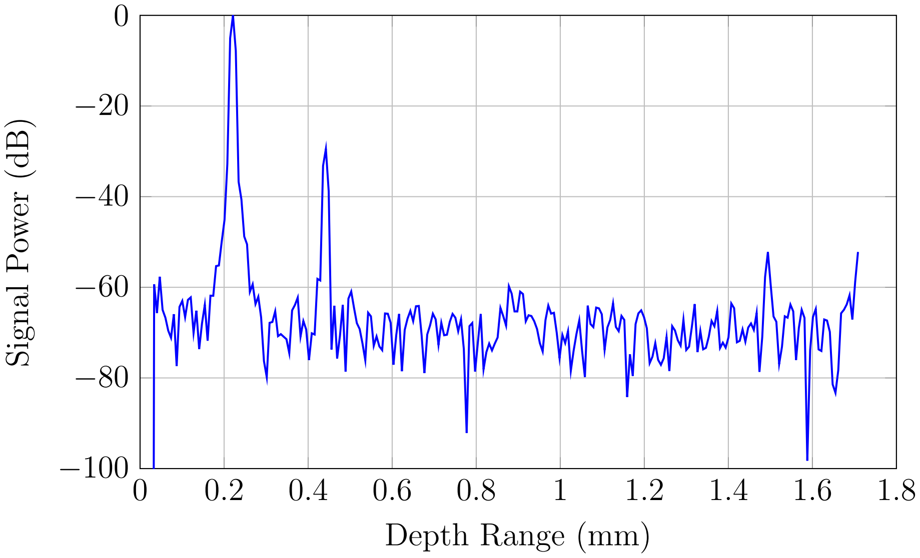

Figure 4.11: Sample A-scan obtained by taking the FFT of apodized and high-pass filtered spectrum, shown in Figure 4.10.

4.4.2 Dispersion Compensation

Dispersion originates because different wavelengths of light travel with different velocity in certain mediums, including glass and tissue. Optical coherence tomography is based on low coherence or broadband light sources, therefore dispersion is inevitable. However, it is the mismatched amount of dispersive media in the sample and reference arm that causes the problem. Mismatched dispersion broadens the FWHM of cross-correlation function, and the axial resolution would not be Fourier transform limited. This degrades the axial resolution, and decreases the sensitivity of OCT signal.

Difference in dispersion between sample and reference arm introduces wavenumber dependent phase shifts in the spectral interferogram. Differential dispersion can be compensated by either matching the amount of dispersive material in sample and reference arm or it can be compensated numerically. The advantage of numerical compensation is that, it can be corrected offline, after the data has already been acquired. Here, an algorithm for calculation of dispersion is described in detail.

In optical coherence tomography, cosine angle of the measured cross-spectral density spectrum can be written as:

$$\phi = 2k(\omega)\Delta l \tag{4.6}$$

Where $k(\omega)$ and Δl are propagation constant and pathlength difference between sample and reference arm, respectively.

In case of perfectly matched dispersive material between sample and reference arm, propagation constant $k(\omega)$, will be a linear function of wavenumber. However, in case of mismatched dispersive material between sample and reference arm, the propagation constant will have non-linear components. As a consequence of non-linear components in propagation constant, the cosine angle term will not be equidistant in k-space, and as such it broadens the peaks in measured A-scans. The propagation constant as a function of wavenumber, can be approximated by expanding in a Taylor series:

$$k(\omega) = k_\circ + \left.\frac{dk}{d\omega}\right|_{\omega_\circ} (\omega - \omega_\circ) + \left.\frac{d^2k}{d\omega^2}\right|_{\omega_\circ} (\omega - \omega_\circ)^2 + \left.\frac{d^3k}{d\omega^3}\right|_{\omega_\circ} (\omega - \omega_\circ)^3 + ... \tag{4.7}$$

The constant term, $k_\circ$, simply adds an offset to the cosine angle and does not effect the cross-correlation function of the light source. The first order derivative term, $\frac{dk}{d\omega}$, equivalent to group delay, linearly shifts the propagation constant of all wavenumbers, but does not effect the periodicity of the cross-correlation function. The second order derivative term, $\frac{d^2k}{d\omega^2}$, equivalent to group velocity dispersion, alters the periodicity of the cross-correlation function quadratically, and causes the broadening of peaks in measured A-scan. The third order derivative term, $\frac{d^3k}{d\omega^3}$, also known as third order delay, alters the periodicity of the cross-correlation function in cubic relation with wavenumbers.

Therefore second and third order derivative terms of propagation constant cause the dispersion of cross-correlation function, and this dispersion can be numerically compensated by subtracting the non-linear components of propagation constant from the measured interferogram.

In order to calculate non-linear propagation constant terms, Equation 4.7 can be rewritten in polynomial form as:

$$k(\omega) = p_0 + p_1(\omega - \omega_\circ) + p_2(\omega - \omega_\circ)^2 + p_3(\omega - \omega_\circ)^3 + ... \tag{4.8}$$

Where p_0, p_1, p_2, p_3 are polynomial coefficients of function $k(\omega)$, evaluated at central wavenumber, $\omega_\circ$. To obtain the non-linear component of propagation constant, cosine angle term of the measured cross-spectral density spectrum is extracted, and also modeled into a polynomial function, as shown in Equation 4.8.

Algorithm for calculation of non-linear dispersion components is schematized in Figure 4.12. Raw interferogram from a mismatched interferometer is acquired with a single specular reflection from the sample arm. After correcting for background and fixed pattern noise, the interferogram is high pass filtered and linearly sampled in wavenumbers. An analytic representation of interferogram is obtained by using Hilbert transform, which provides an imaginary part with a 90° phase shift to the real signal. The phase angle of the analytic signal is calculated and unwrapped. A third degree polynomial regression fit is applied to the unwrapped phase, and non-linear component of the phase values are extracted. In order to compensate for the dispersion, dispersed spectral interferogram is multiplied with a phase term $e^{-i\phi_{Disp}(\omega)}$, before taking the Fourier transform.

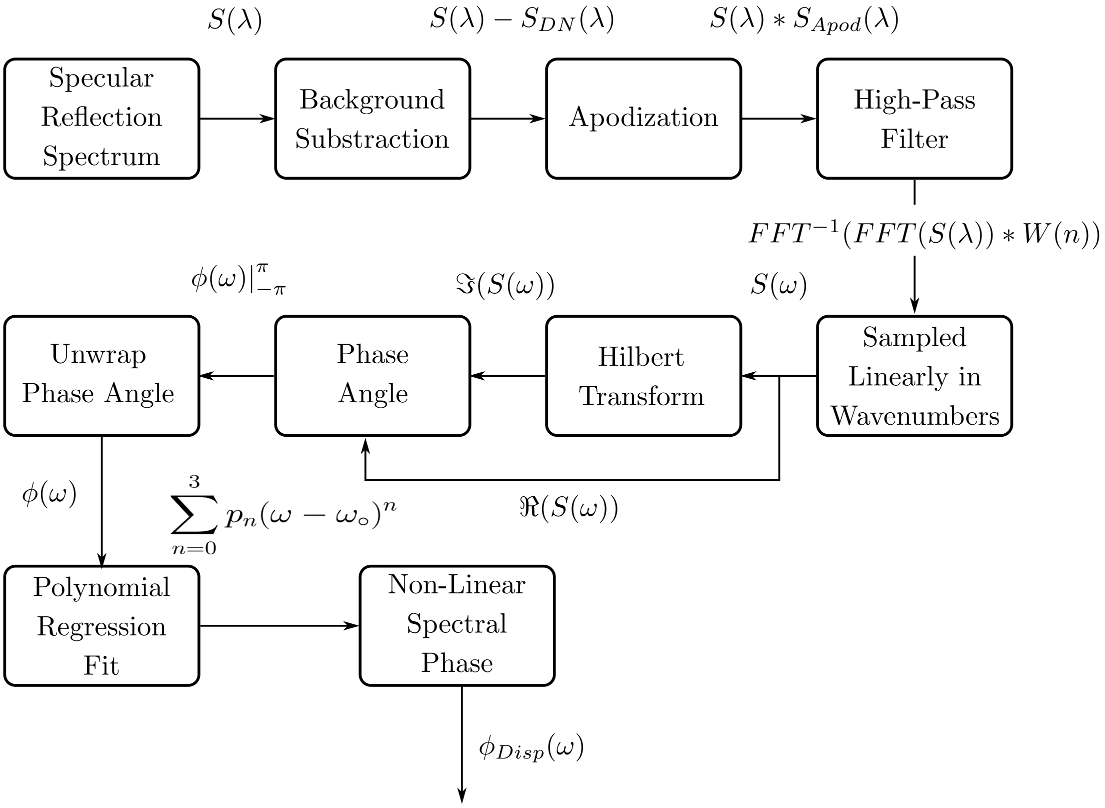

Figure 4.12: Block diagram depicting various computational steps in an algorithm for calculation of dispersion

To demonstrate the performance of algorithm, an interferogram was acquired by introducing a 5 mm of N-SF57 (refractive index = 1.8) substrate into sample arm. Reconstructed A-scans, at two different depths with broadened peaks are as shown in Figure 4.13a. Using the algorithm described above, non-linear components of propagation constant terms were calculated and subtracted from the interferogram. A-scans obtained after numerically compensating the dispersion are as shown in Figure 4.13b.

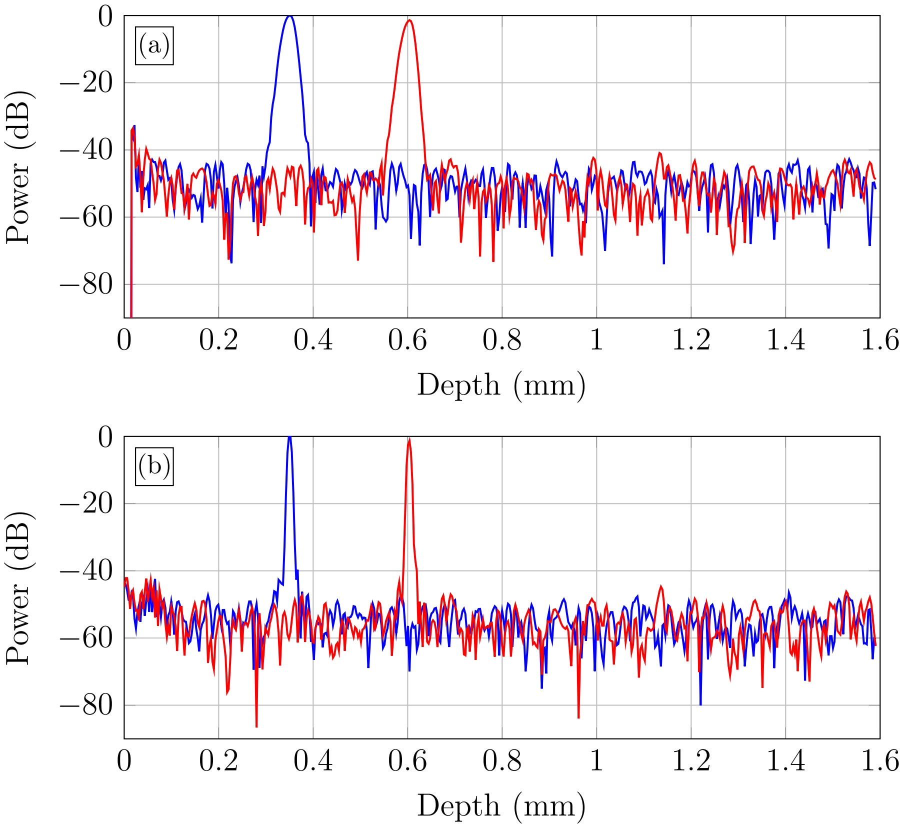

Figure 4.13: A-scans before (a) and after (b) numerical compensation of dispersion. Interference spectrums were acquired by introducing 5mm of N-SF57 substrate (Refractive index = 1.8) in sample arm.

4.4.3 Extraction of En-face OCM Images

In spectral domain optical coherence microscopy, depth of focus is much shorter than the total axial range of the spectrometer and as such, relevant information about the sample is limited to few pixels in an A-scan. Specifically, the OCM signal in an A-scan appears at an index

$$OCM_{Ind} = \frac{\Delta OPL}{\delta z} \tag{4.9}$$

Where ΔOPL is the optical pathlength difference between sample and reference arm, and δz is the pixel spacing in an A-scan.

In order for OCM signal to appear at the same index of an A-scan through out the image field, one requires a perfect telecentric scanning system that provides a flat image field. Generally, for a scanning system to be telecentric, two pivot points of the X and Y scanners should be individually imaged onto the pupil plane of the objective. However, the implemented SDOCPM system is quasi-telecentric, because it uses closely spaced X and Y scanners, and only the midpoint between their respective pivot points is imaged onto the pupil plane of the objective. This results in a slight curvature of the image field, which means the optical pathlength from the center of the beamsplitter to the focal spot would vary with the scanning angle. Therefore, the axial index of OCM signal in a laterally scanned volume also moves with ΔOPL.

The optical pathlength from center of beam splitter cube to the focal spot, as a function of transverse scanning angle can be represented as:

$$OPL(x, y) \propto OPL_{\circ} \left[\frac{1}{cos(\theta_x)} + \frac{1}{cos(\theta_x)} \right] \tag{4.10}$$

Where $OPL(x, y)$ is the optical pathlength at spatial coordinates (x, y), $OPL_{\circ}$ is the optical pathlength along the optical axis. θ_x and θ_y are the angle of X and Y scanners.

In the implemented SDOCPM system, both reference and sample arms are scanned for high phase stability. The optical pathlength variation with scanning angle in reference and sample arm are modeled in Figure 4.14a & b, respectively. It can be noticed that, slight misalignment of optical axis in sample arm is taken into account for realistic simulation. The OCM image plane is then, the difference of optical pathlengths between sample and reference arm, as shown in Figure 4.14c. Therefore OCM image plane is quadratic, and simple indexing or maximum projection of A-scans would not provide sharp images. An automated procedure to extract sharp OCM images by quadratically slicing the interpolated volume is described below.

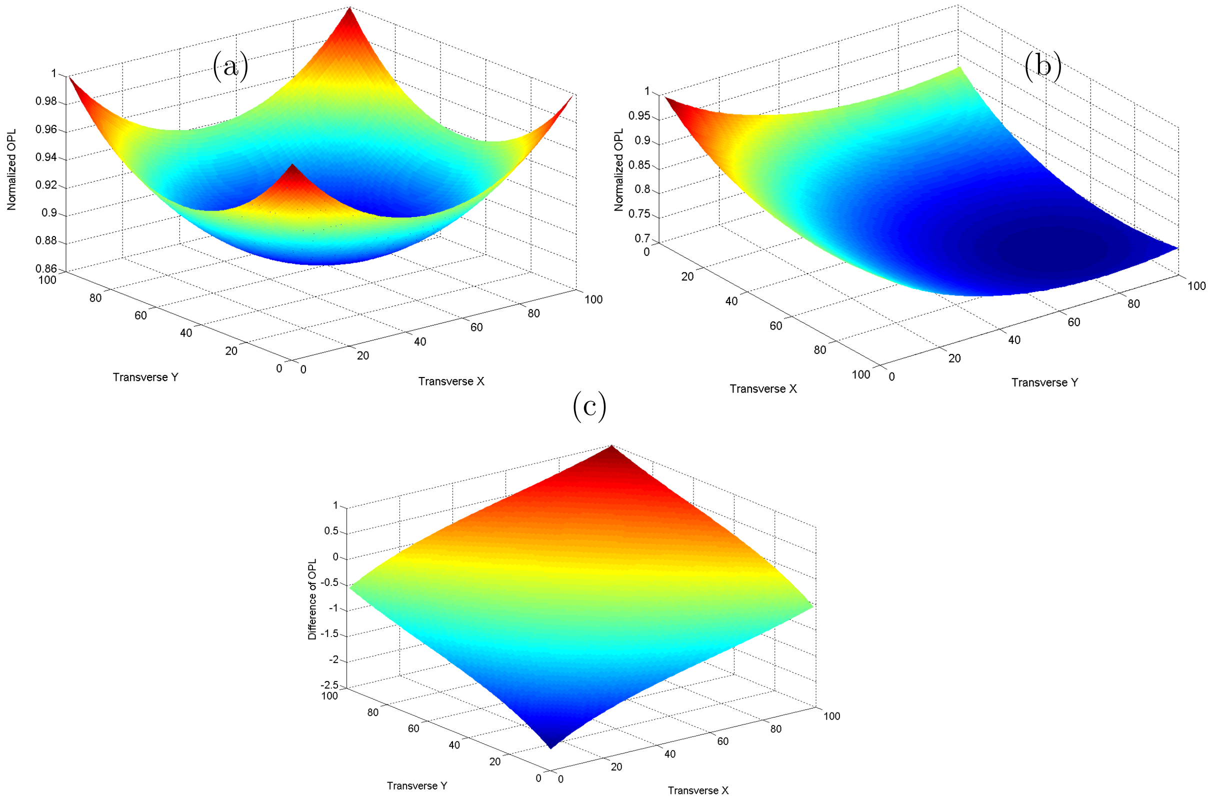

Figure 4.14: Simulated change in optical pathlength across the image field as a function of lateral scanning angles, in sample arm (a), and reference arm (b). Difference of the optical pathlengths in (a) and (b) produce a quadratic focal plane (c).

Algorithm for *en face* OCM Image Extraction

An algorithm has been developed to automate the extraction of *en face* OCM images from the laterally scanned volumes. Shannon entropy is used as a criteria to track the focal plane in 3D volumetric data. Shannon entropy, in the scope of information theory, essentially estimates amount of bits required to represent given information. Number of bits required to represent random noise is always higher compared to structured information. Therefore, location of focal spot or sharp features in a 3D volume is estimated by calculating the Shannon entropy of small blocks inside a volume.

The entropy of an image plane $I(x, y)$ is calculated using

$$E = \sum p * \log_2(p) \tag{4.11}$$

Where p is the histogram count of a grayscale image of $I(x, y)$. Various computational steps in the extraction of *en face* OCM image is schematized in Figure 4.15.

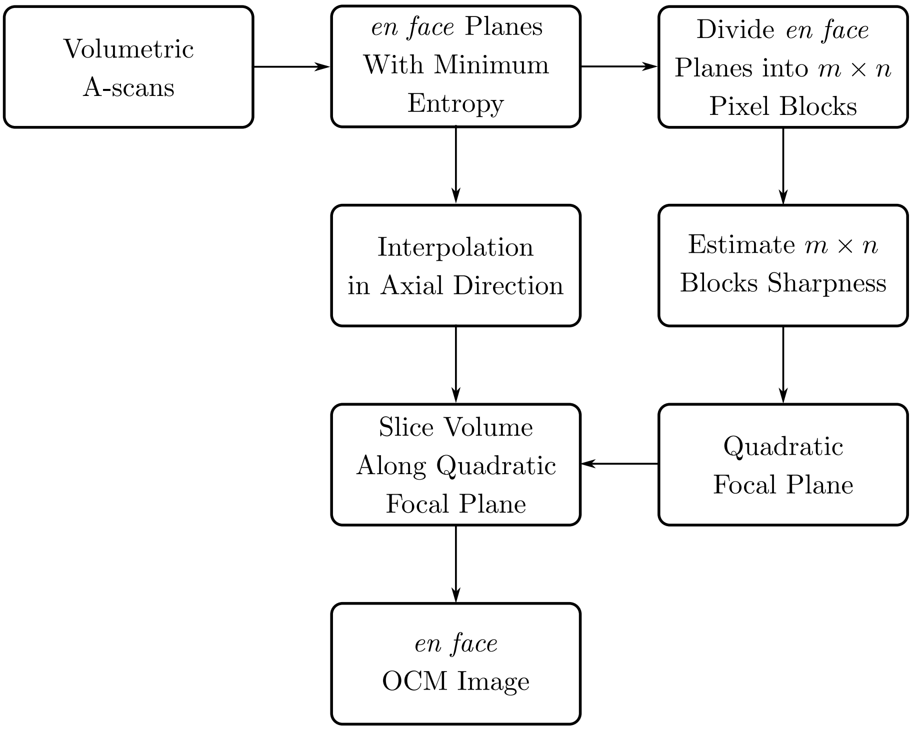

Figure 4.15: A block diagram representing various computational steps in extraction of *en face* OCM image.

Example of *en face* OCM Image Extraction

The effect of quadratic image plane is can be seen in Figure 4.16, which shows a laterally scanned onion epidermal cell layer. Images shown are *en face*, 400 µm × 400 µm, and at consecutive indices of laterally scanned A-scans. Because of quadratic OCM image plane, each image has sharp features of the sample limited to a small sub-area within the image. For the shown example, sharp features of the sample span 9 consecutive pixels of laterally scanned A-scans. Because, the optical path length difference increases with lateral scanning angles, images covering smaller lateral area will have OCM image plane limited to fewer indices of laterally scanned A-scans.

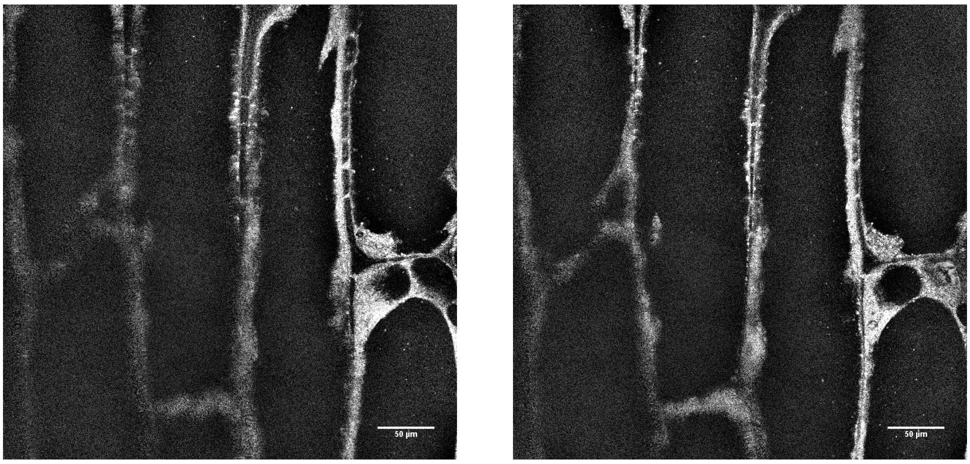

A-scan index = 52 A-scan index = 53

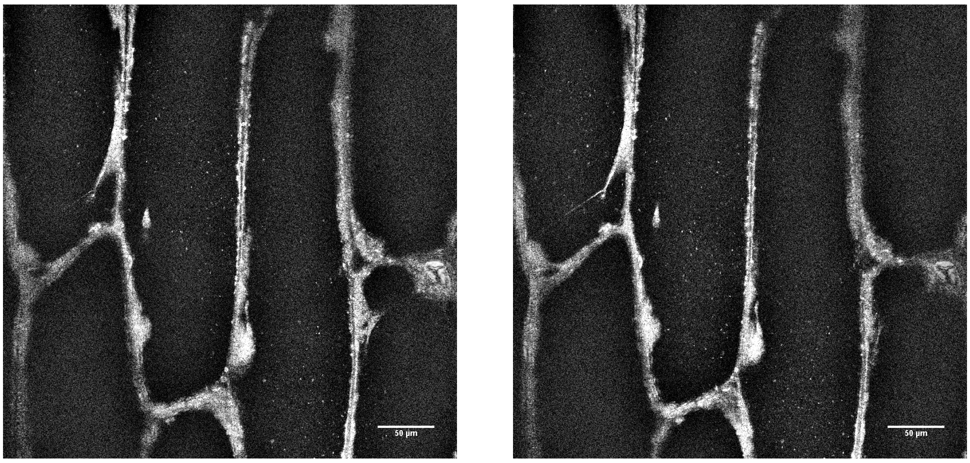

A-scan index = 54 A-scan index = 55

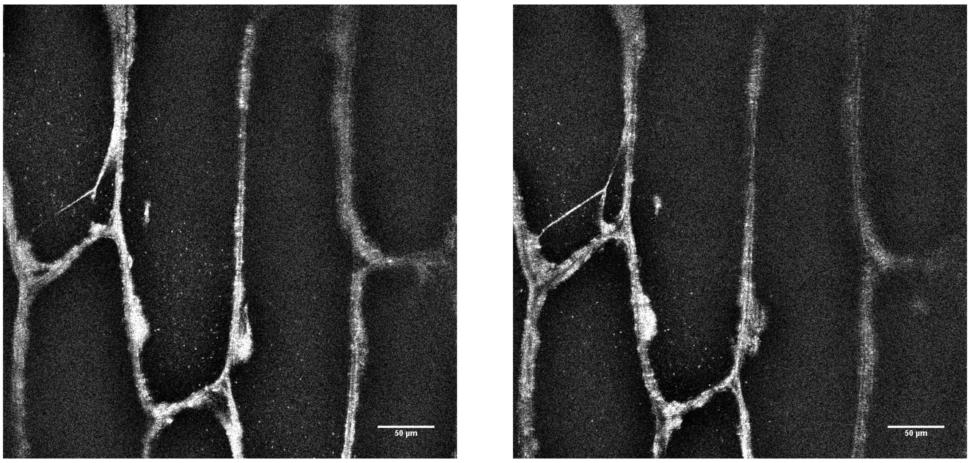

A-scan index = 56 A-scan index = 57

Figure 4.16: *en face* image planes from an onion epidermis cell layer. Image planes are at consecutive index of laterally scanned A-scans. Notice that different features of the sample are sharp in different images, because of quadratic focal plane. Scale bar represents 50 µm.

The automated OCM image extraction procedure was applied to the image planes shown in Figure 4.16. After estimating the quadratic focal plane using Shannon entropy, criteria, volume composed of the image planes was interpolated and sliced quadratically. The extracted *en face* OCM image is as shown in Figure 4.17, which has sharp features through out the image field.

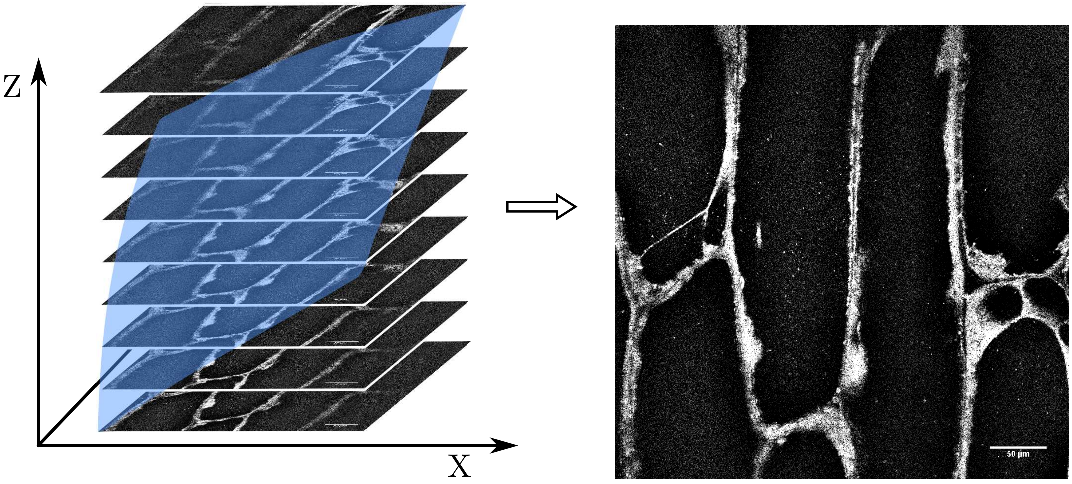

Figure 4.17: (Left) Illustration of OCM image quadratically spanning 9 consecutive pixels of laterally scanned A-scans. (Right) Extracted *en face* OCM Image using automated procedure, which is sharp across the image field in comparison with images in Figure 4.16.

4.4.4 Phase Unwrapping

In optical coherence tomography, phase component of the cross-spectral density signal increases linearly with optical pathlength difference between sample and reference arm. However, the principle range of phase component is $-\pi$ to π, and as such optical pathlength differences greater than 2π gets wrapped in the principle range, giving rise to the so called 2π ambiguity. The phase component can resolve the axial position of scatterers beyond the axial resolution imposed by the coherence length of light source. Here, a simple approach for unwrapping of two-dimensional phase is described.

For a complex *en face* image, $\hat{I}(x,y)$, phase image can be obtained by taking arctangent of ratio between imaginary and real values:

$$\phi(x,y) = Tan^{-1}\left[\frac{\Im(\hat{I}(x,y))}{\Re(\hat{I}(x,y))}\right] \tag{4.12}$$

where $\phi(x, y)$ is the phase angle at spatial locations x and y in 2D plane. Because of the 2π ambiguity, calculated $\phi(x, y)$ is wrapped between $-\pi$ and $+\pi$. The relationship between wrapped and unwrapped phase can be represented as:

$$\phi(x, y) = \psi(x, y) - 2\pi k(x, y) \tag{4.13}$$

Where $\psi(x, y)$ is the unwrapped phase, and $k(x, y)$ is a two-dimensional integer function limiting $\phi(x, y)$ in the principle range $[-\pi, \pi]$. Now, the problem of phase unwrapping is reformulated into finding a two-dimensional integer function $k(x, y)$, which has integer values in spatial locations where the phase is wrapped and zero everywhere else. Therefore, unwrapped phase can be given as

$$\psi(x, y) = \phi(x, y) + 2\pi k(x, y) \tag{4.14}$$

A modified version of quality map guided algorithm [67] is used for phase unwrapping. A block diagram in Figure 4.18 shows various computational steps in two-dimensional phase unwrapping. Because the phase noise varies with signal-to-noise ratio (SNR), a phase quality map is derived from the SNR values. However, it is possible for some pixels to have high SNR and yet the phase cannot be unwrapped because of phase jumps or undersampling. Phase derivative variance map, a measure of rate of change of phase, helps in identifying areas with phase jumps, and is used as a quality map along with SNR map. Using the composite quality maps, pixels with higher SNR and lower phase derivative variance are unwrapped first, and then continue through a path of decreasing SNR until the whole 2D plane is covered.

Figure 4.19a shows an example of wrapped phase image obtained by scanning group 7 of an Air Force resolution target. The two-dimensional phase was unwrapped using the quality map guided algorithm described above, and the unwrapped phase image is as shown in Figure 4.19.

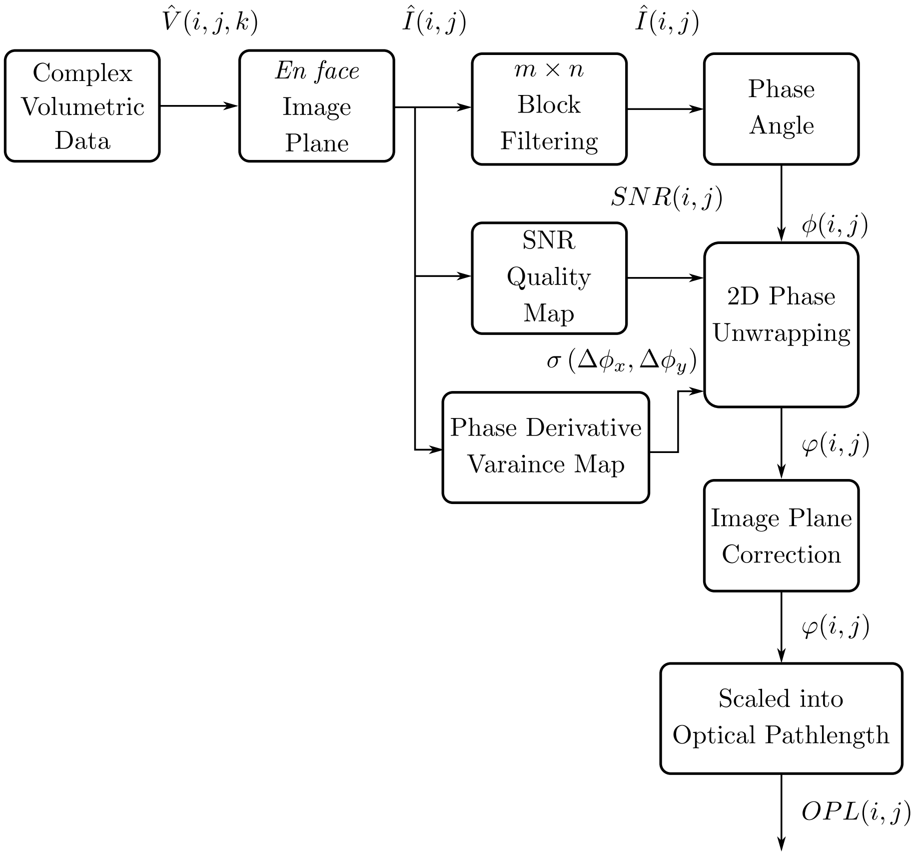

Figure 4.18: Block diagram depicting various steps in unwrapping of two-dimensional phase

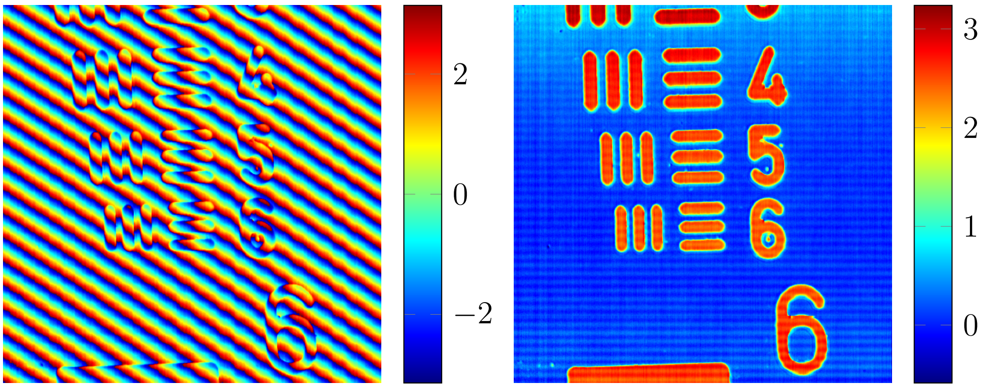

Figure 4.19: (Left) Wrapped OCM phase image obtained by scanning group 7 of an Air Force Resolution Target. (Right) Unwrapped phase image Same image as in (a), after unwrapping the two-dimensional phase.

4.5 Software

The software for controlling hardware, image acquisition and real-time display of SDOCM images was developed in LabVIEW (National Instruments, USA), where as the software for offline signal processing and display was developed in Matlab (Mathworks, USA).

Real-time Display of SDOCM Images

A graphical user interface was developed in LabVIEW for real-time acquisition and display of SDOCM images, as shown in Figure 4.20. The GUI can be configured to acquire range of image field sizes on the fly, and it also allows for calibration of galvanometer scanners.

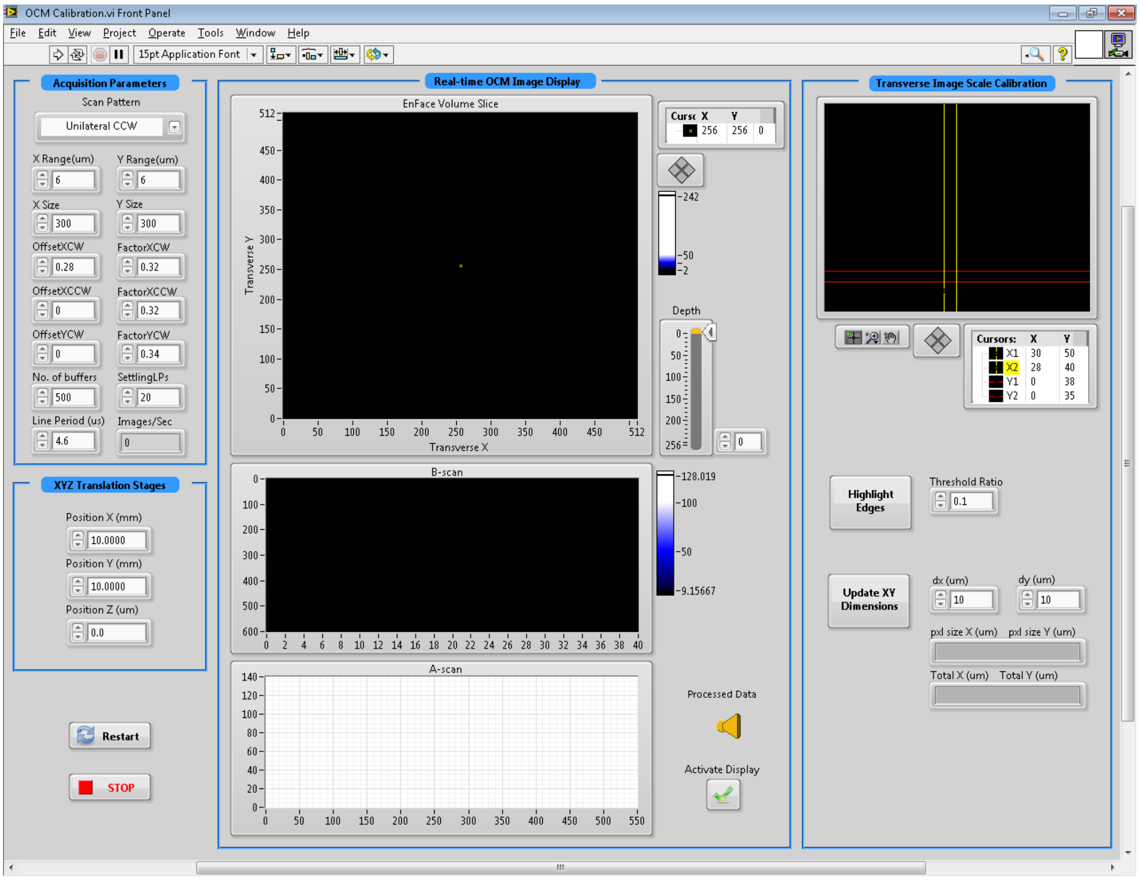

Scan Pattern: Unilateral CCW
X Range(um): 6
Y Range(um): 6
X Size: 300
Y Size: 300
OffsetXCW: 0.28
FactorXCW: 0.32
OffsetXCCW: 0
FactorXCCW: 0.32
OffsetYCW: 0
FactorYCW: 0.34
No. of buffers: 500
SettlingLPs: 20
Line Period (us): 4.6
Images/Sec: 0
Position X (mm): 10.0000
Position Y (mm): 10.0000
Position Z (um): 0.0

Cursc	X	Y
	256	256

Cursors:	X	Y
X1	30	50
X2	28	40
Y1	0	38
Y2	0	35

Threshold Ratio: 0.1
dx (um): 10
dy (um): 10
pxl size X (um) pxl size Y (um)
Total X (um) Total Y (um)

Figure 4.20: Graphical user interface developed in LabVIEW for real-time display of SDOCM images, and calibration of galvanometer scanners.

Simultaneous SDOCPM and Widefield Z-stack Acquisition

A graphical user interface was developed in LabVIEW, for simultaneous acquisition and saving of binary data from SDOCPM spectrometer and widefield camera. Screenshot of the GUI is as shown in Figure 4.21. The GUI also automates the acquisition of Z-stack, where the sample is translated axially and volumes are recorded at each step.

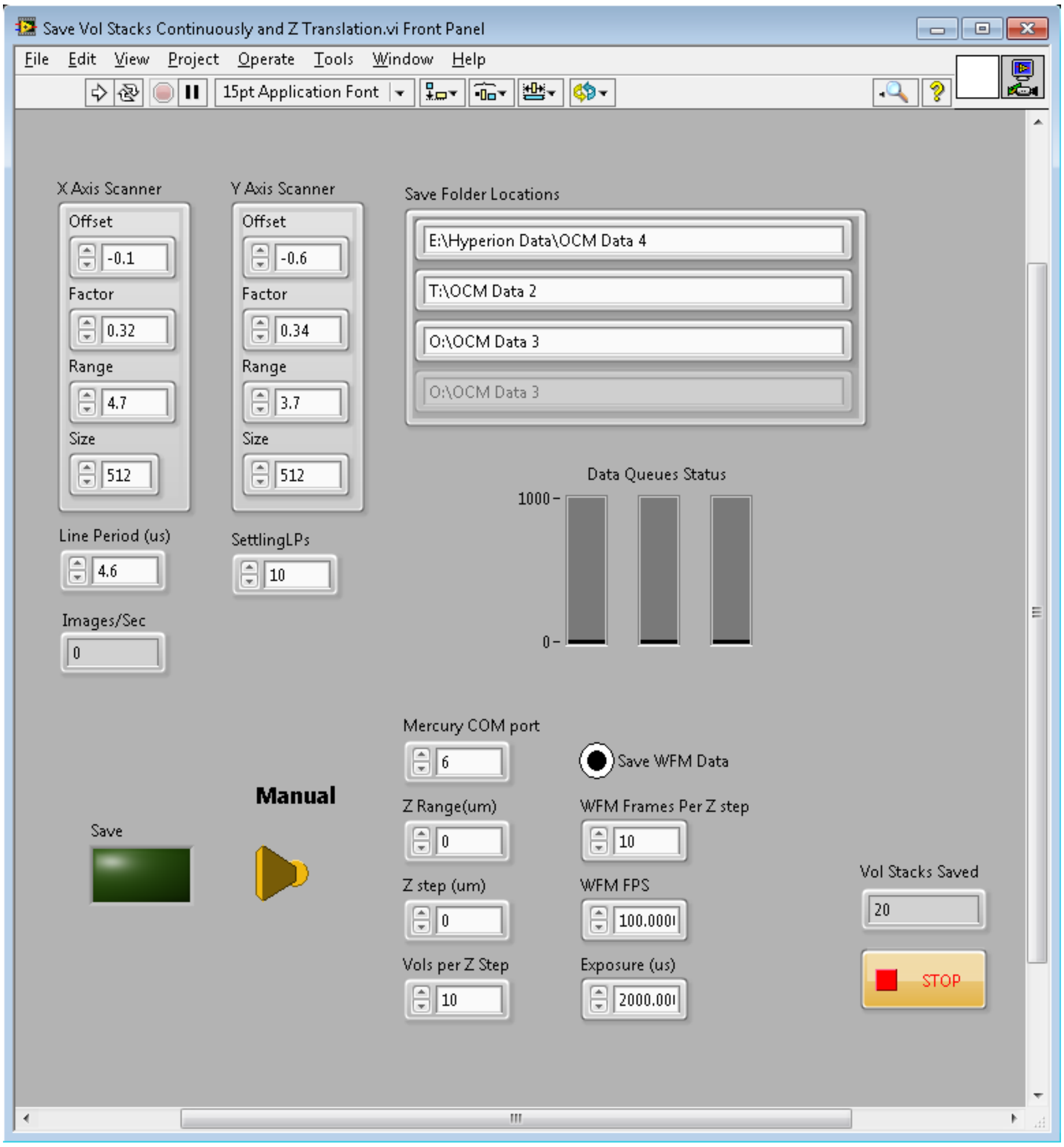

X Axis Scanner

Offset: -0.1
Factor: 0.32
Range: 4.7
Size: 512

Y Axis Scanner

Offset: -0.6
Factor: 0.34
Range: 3.7
Size: 512

Line Period (us): 4.6
SettlingLPs: 10
Images/Sec: 0

Save Folder Locations

E:\Hyperion Data\OCM Data 4
T:\OCM Data 2
O:\OCM Data 3
O:\OCM Data 3

Mercury COM port: 6
● Save WFM Data
Z Range(um): 0
WFM Frames Per Z step: 10
Z step (um): 0
WFM FPS: 100.0001
Vols per Z Step: 10
Exposure (us): 2000.001
Vol Stacks Saved: 20

Figure 4.21: Graphical user interface developed in LabVIEW for synchronized recording of widefield and SDOCPM images. The GUI also allows for automated acquisition of Z-stack.

3D Sample Translation Stage

For precise movement of sample under the microscope, 3D translation stage was assembled using two piezomotors for X-Y axis, and a linear motor for Z axis. The graphical user interface for controlling of the 3D sample translation stage was developed in LabVIEW, as shown in Figure 4.22. As an alternative to the galvanometer scanners, 3D translation stage can be used to scan the sample, and Z-stack acquisition can be automated by setting few parameters on the GUI.

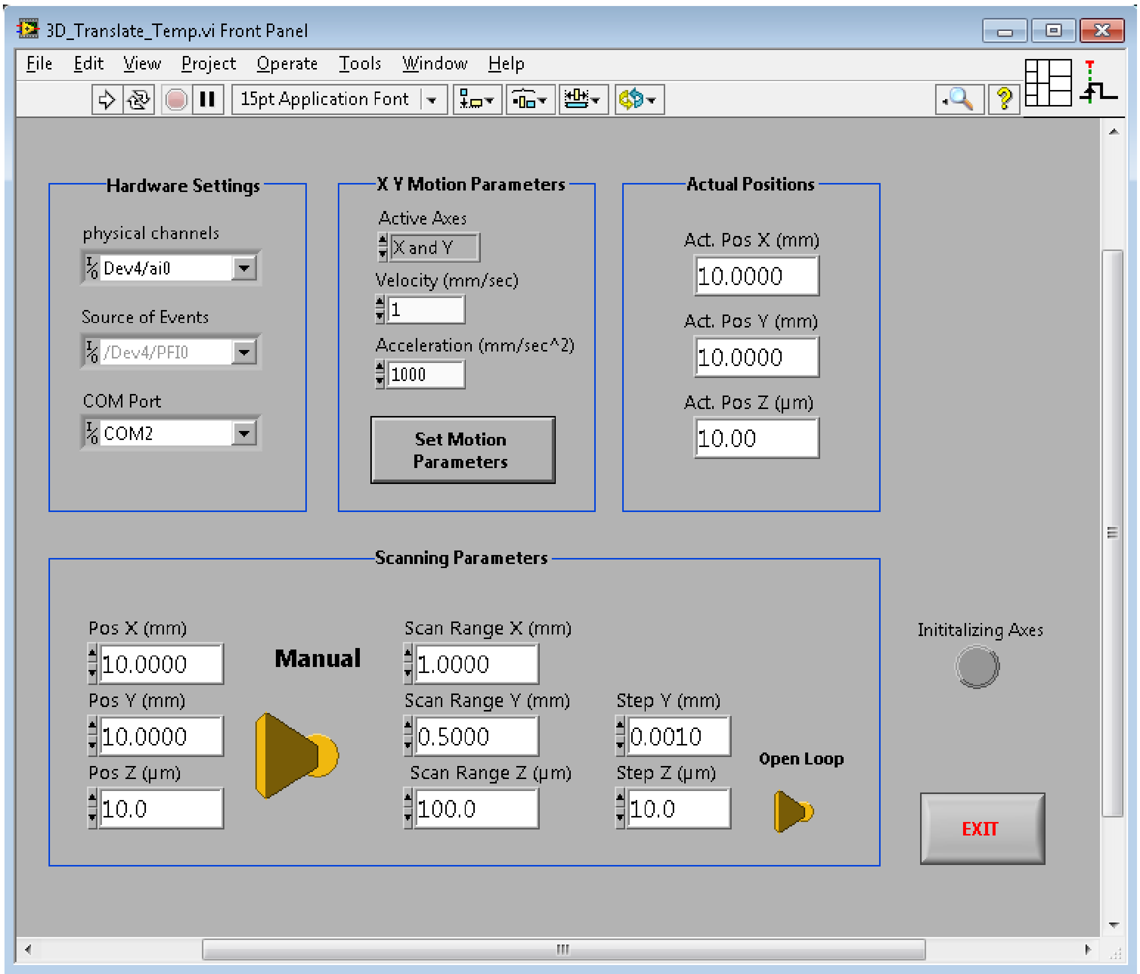

Hardware Settings

physical channels: Dev4/ai0

Source of Events: /Dev4/PFI0

COM Port: COM2

X Y Motion Parameters

Active Axes: X and Y

Velocity (mm/sec): 1

Acceleration (mm/sec^2): 1000

Actual Positions

Act. Pos X (mm): 10.0000

Act. Pos Y (mm): 10.0000

Act. Pos Z (µm): 10.00

Scanning Parameters

Pos X (mm): 10.0000

Pos Y (mm): 10.0000

Pos Z (µm): 10.0

Scan Range X (mm): 1.0000

Scan Range Y (mm): 0.5000

Scan Range Z (µm): 100.0

Step Y (mm): 0.0010

Step Z (µm): 10.0

Figure 4.22: GUI developed in LabVIEW for precise 3D movement of sample under the microscope.

4D Display and Analysis of SDOCPM Data

A graphical user interface was developed in Matlab for displaying four-dimensional SDOCPM data, i.e., reconstructed volumetric data and its functional contrast over time. The sliders in the lower bottom of the GUI are used to update the *en face* images, and functional contrast associated with each pixel in the image. GUI also allows for frequency analysis, and rate of change of the functional contrast over time.

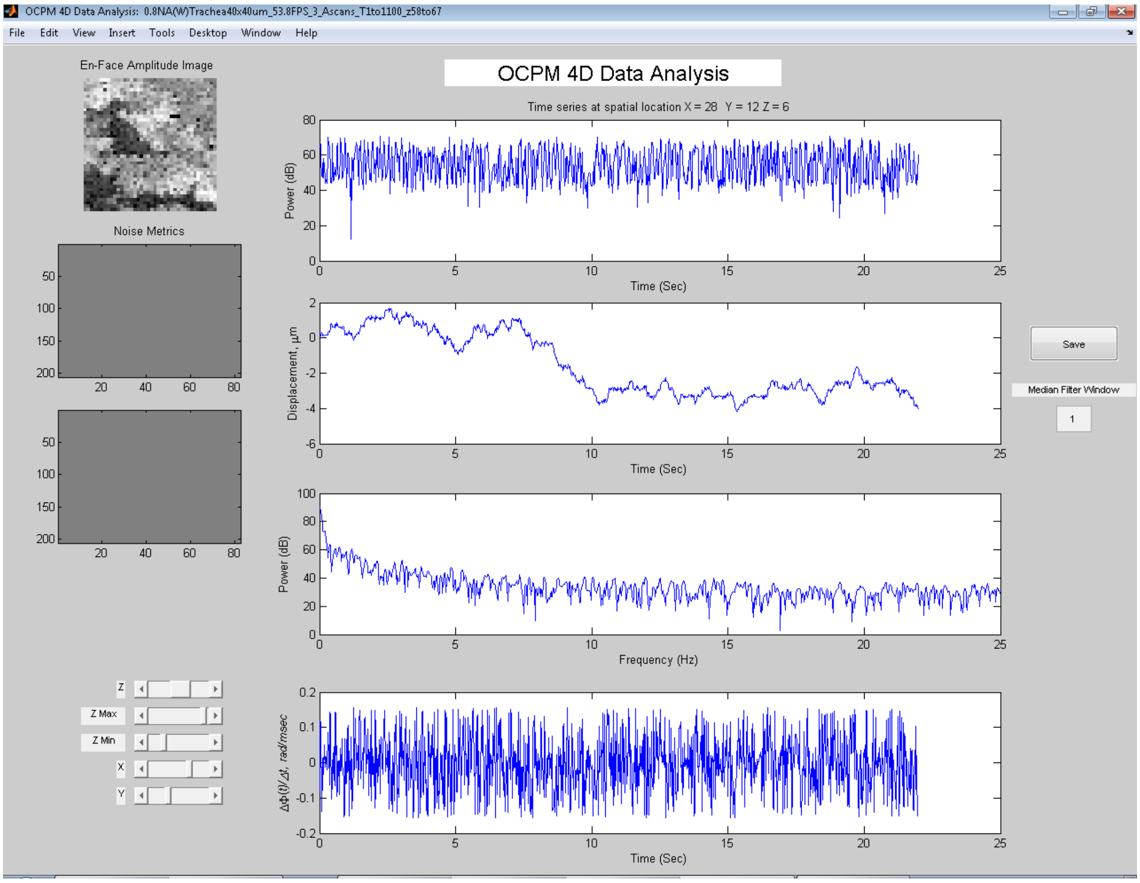

Figure 4.23: GUI developed in Matlab for displaying volumetric data and its functional contrast over time.

4.6 Test Sample

To demonstrate the imaging performance of the implemented SDOCPM system, this section presents OCM *en face* images and three-dimensional structure of an onion epidermis cell layer obtained using the SDOCPM system.

Preparation of an Onion Epidermis Cell Layer

A square piece of scale was cut from a fresh red onion (binomial name : Allium cepa), and a cell layer from the inner epidermis was extracted using a forcep. The cell layer was attached to a glass coverslip using a double-sided adhesive tape. The coverslip was then secured on 3D sample translation stage, and distilled water was used as the immersion media. A list of parameters and their values used in image acquisition are as shown in Table 4.1.

Imaging Parameters	**Value**	**Units**
Axial resolution	2.5	µm
Transverse resolution	0.5	µm
Image area	400 × 400	µm
No. of pixels	1024 × 1024	
No. of images in Z-stack	60	
Z-step	0.75	µm
Frame rate	0.1	Hz

Table 4.1: List of imaging parameters used in the Z-stack acquisition of onion epidermis cell layer.

En Face OCM Images of Onion Epidermis Cell Layer

En face OCM images of an onion epidermis cell layer are as shown in Figure 4.24. Shown images are 400 µm × 400 µm, and at different depths inside the cell layer, indicated by the Z values. The cell membrane of each cell, their nuclei (marked with red arrows), and the gap between difference cell membranes are clearly visualized. The cell-to-cell communication channels, i.e., interconnecting pathways among different cells are also clearly visible.

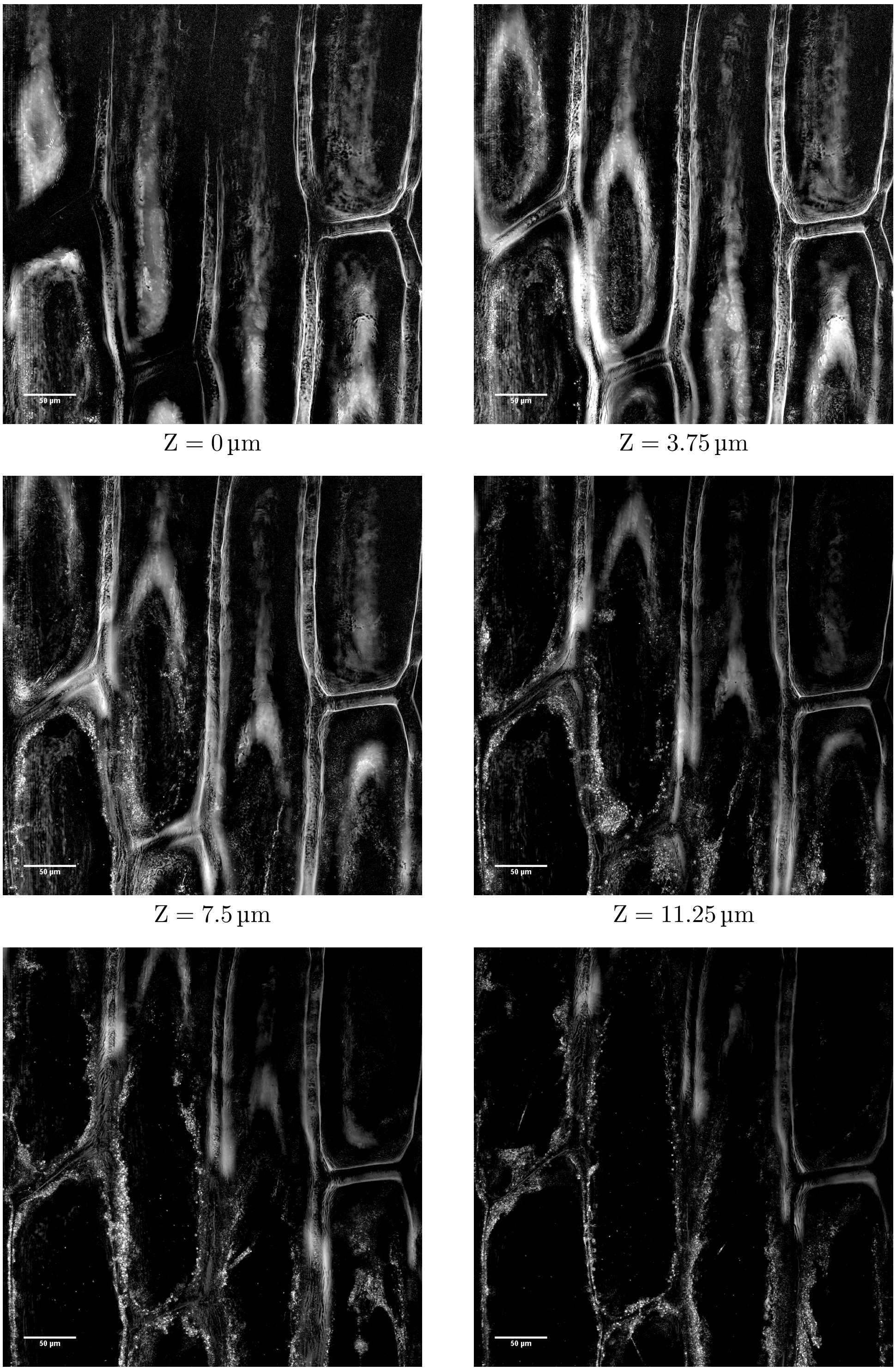

Z = 0 µm

Z = 3.75 µm

Z = 7.5 µm

Z = 11.25 µm

Z = 15 µm

Z = 18.75 µm

Figure 4.24: *En face* OCM images of an onion epidermis cell layer at different depths inside the cell layer, where Z = 0 is the surface of the epidermis. Image size is 400 µm × 400 µm, and the scale bar represents 50 µm.

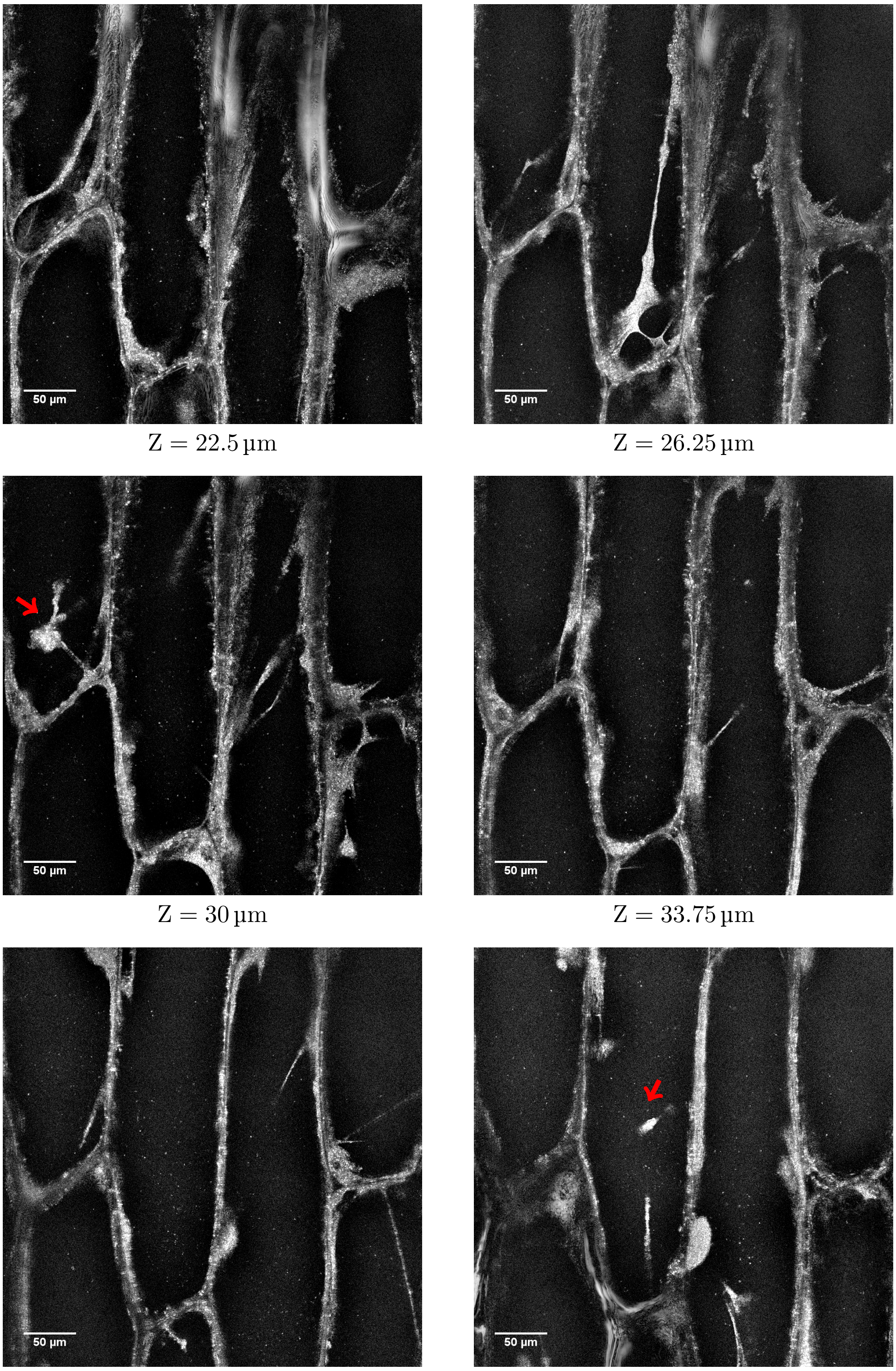

Z = 22.5 µm

Z = 26.25 µm

Z = 30 µm

Z = 33.75 µm

Z = 37.5 µm

Z = 41.25 µm

Figure 4.24: (continued) *en face* OCM images of an onion epidermis cell layer, where nuclei of the cells are clearly visualized, marked by red arrow. Image size is 400 µm × 400 µm, and the scale bar represents 50 µm.

Volumetric Reconstruction of an Onion Epidermis Cell Layer

Three dimensional structure of onion epidermis cell layer was reconstructed by combining 60 *en face* images, acquired at 0.75 µm axial steps. The size of the volume is 400 µm × 400 µm × 45 µm. The Z dimension was enlarged by linear interpolation, for proper visualization of the structures.

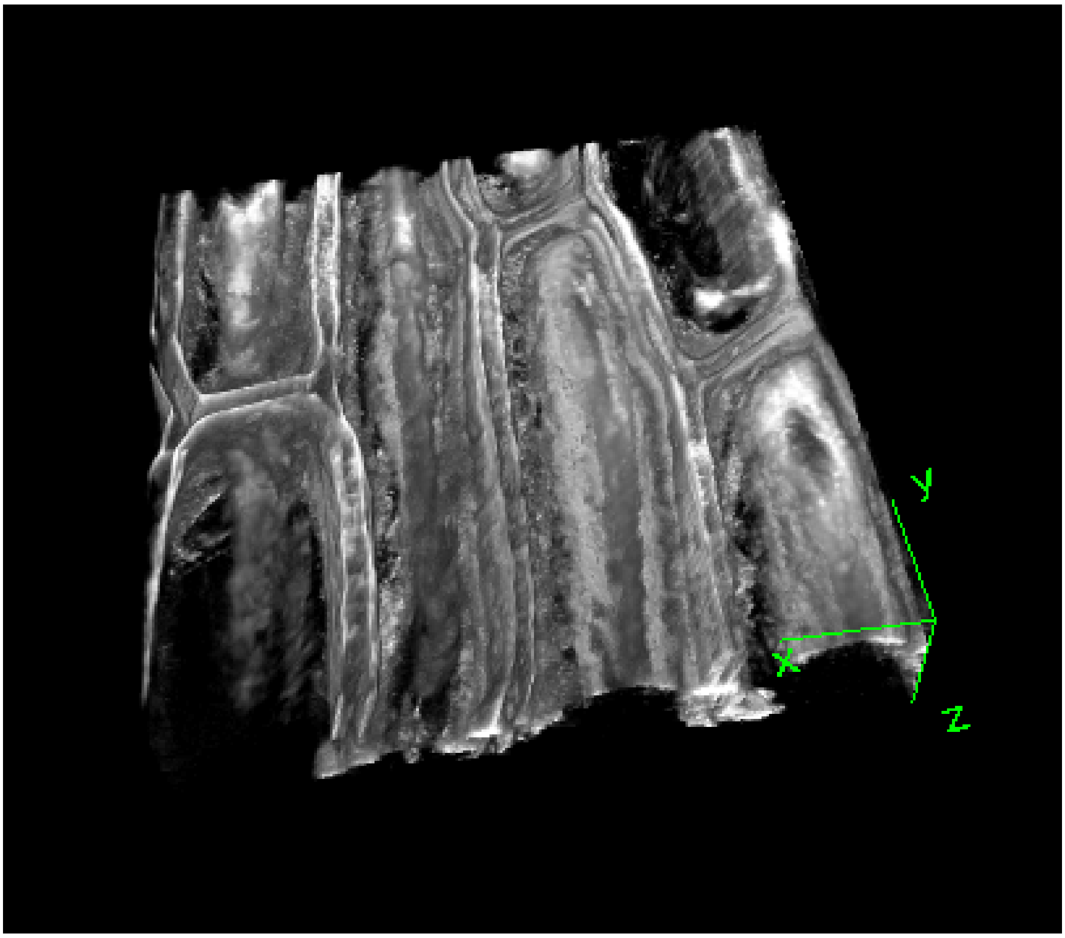

Figure 4.25: (movie) Three dimensional reconstruction of onion epidermis cell layer, obtained using SDOCM. The spatial dimensions are 400 µm × 400 µm × 45 µm.

4.7 Summary

Implementation of an SDOCPM system using symmetric Linnik interferometer is described, where mechanical vibrations and jitter noise of the galvanometer scanners is in common-mode between the sample and reference arm. With this arrangement, interferogram measurements are insusceptible to phase noise originating from galvanometer scanners, which improves the phase stability of the optical setup. Generally, common-path interferometer setups are used to minimize the phase noise originating from the vibrations of galvanometer scanners. However common-path topologies, among other drawbacks, also limits the transverse spatial resolution. The implementation presented in this chapter seeks to overcome the limitations of common-path topologies, and still maintain very high phase sensitivity.

Implemented SDOCPM system uses a linear wavenumber spectrometer, that does not require computationally intensive resampling, and decreases the time it takes to reconstruct three-dimensional structure of the samples. Implemented system has a numerical aperture of 0.8 NA, and maximum sampling speed of $217,000$ Ascans/sec.

Chapter 5

Performance Characteristics of SDOCPM System

This chapter describes the performance evaluation and analysis of implemented spectral domain optical coherence phase microscopy (SDOCPM) system. The performance is characterized by five different parameters, namely

- Signal-to-Noise Ratio
- Spatial Resolution
- Phase Sensitivity
- Field of View
- Temporal Resolution

5.1 Signal-to-Noise Ratio (SNR)

SNR describes the proportion of signal and noise in a measured signal, and is calculated by taking the ratio of signal power to average noise power. First, lets consider the theoretical limit of maximum SNR that could be achieved by an spectral domain optical coherence microscopy (SDOCM) system, and then SNR as a function of detector efficiency and sample arm reflectance power will be discussed.

In SDOCM, light reflected back from sample and reference arm is converted into electric charge by an array of photodector elements, and then subsequently digitized by an analog-to-digital converter (ADC). Fourier transform of the digitized spectrum reconstructs the depth profile of the sample, called as an A-scan. For an ideal ADC, quantization errors are the only source of noise which are caused by rounding or truncation of real signal into its digital representation. Therefore, quantization noise limited SNR of an ADC can be given as [68]:

$$SNR_{ADC} = 6.02 * n + 1.76 \quad \text{dB} \tag{5.1}$$

Where n is the number of bits in an ADC.

Because the output of an ADC is Fourier transformed to obtain an A-scan, SNR is further improved due to processing gain of the FFT. The processing gain is the effect of FFT spreading the input noise over the entire Nyquist bandwidth, whereas the signal is confined to few frequency bins. Increasing the number of processing points in FFT also increases the frequency resolution, and decreases the overall noise floor. Processing gain in FFT is given as [66]:

$$\text{FFT Processing Gain} = 10 \log_{10} \frac{N}{2} \tag{5.2}$$

Where N is the number of processing points in DFT.

Therefore, combining Equations 5.1 & 5.2 gives us the theoretical maximum SNR that can be achieved by a SDOCM system:

$$SNR_{max} = (6.02 * n + 1.76) + \left(10 \log_{10} \frac{N}{2}\right) \tag{5.3}$$

It can be noted that, for time domain OCM systems, FFT processing gain does not apply and maximum theoretical SNR can be approximated as 6 dB per digitization bit.

In practice, SDOCM signal is generated by light reflected back from different depths of a sample, whereas the light reflected back from the reference arm remains constant. Because of the constant reference arm power, usually above 20 % of the saturation value, the linescan camera operates in shot-noise regime. For a shot-noise limited spectral domain system, SNR is given by [38]:

$$SNR_{SDOCM} = \frac{\eta P_{sample} \tau_i}{E_\nu} \tag{5.4}$$

Where η is the spectrometer efficiency, P_{sample} is the light power detected from sample arm, τ_i is detector integration time, and E_ν is the photon energy.

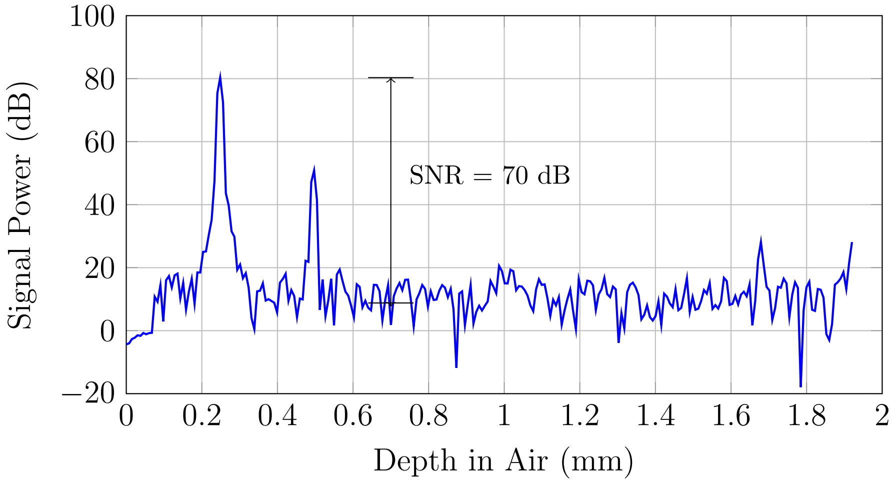

Figure 5.1: A-scan obtained with glass coverslip as sample to demonstrate maximum possible SNR of the implemented SDOCPM system.

The linescan camera (Basler Sprint spl4096-140k) in SDOCPM system has a 12-bit ADC, but is operated in 8-bit mode for maximum possible A-scan rate. To demonstrate the maximum possible SNR that could be obtained by SDOCPM system, full-scale modulated spectrum was measured with a glass coverslip as sample, and reconstructed A-scan is as shown in figure 5.1. The difference between peak signal power and noise floor for measured A-scan is 70 dB, which is close to the theoretical maximum SNR of 74 dB, as predicted by equation 5.3 for 8-bit ADC and 512 FFT bins.

It can be noted that, maximum attainable SNR is also limited by the full-well capacity of a sensor. The full-well capacity defines the maximum number of charge carriers or electrons a sensor can generate and hold for a given integration time. SNR of a sensor can be defined as the ratio of full well capacity to the total read out noise [69, p. 163]. For photon shot-noise limited detection, sensor noise is equivalent to the statistical variations in the number of electrons generated by the signal. Then the standard deviation of shot-noise is the square root of the number of electrons generated by the signal.

If n_e is the full-well capacity of a sensor, then at full scale, the statistical or shot-noise of the sensor is equivalent to $\sqrt{n_e}$. SNR can be given as the ratio of number of signal electrons to number of noise electrons, i.e, $n_e/\sqrt{n_e}$. Therefore, under the condition of shot-noise limited detection, maximum attainable SNR in SDOCM can be given as:

$$SNR = 20\log_{10}(\sqrt{n_e}) + 10log_{10}\frac{N}{2} \tag{5.5}$$

Where n_e is the full-well capacity of the sensor, and N is the number of processing points in FFT.

5.2 Spatial Resolution

This section evaluates the spatial resolution of implemented SDOCM system, which determines the minimum structural details that could be resolved along and perpendicular to the optical axis. The resolution criteria considered here is the half power width (or 3 dB point) of the axial and transverse intensity response. Axial resolution, measured along the optical axis, also determines the thickness of optical sections that could be attained in thick scattering samples.

The axial and transverse response of confocal microscope and SDOCM system are compared. The confocal response was measured by blocking the reference arm in the SDOCM setup. Without the reference arm, the SDOCM system functions like a confocal microscope, except that CMOS linescan camera is not as sensitive compared to the conventional confocal microscopes PMT detectors. This difference in detection sensitivity manifests as higher noise floor for the confocal images but does not influence the confocal FWHM response.

5.2.1 Axial Resolution

The axial resolution in SDOCM is influenced by the numerical aperture of the objective lens, only if the resulting depth of focus is equal to or smaller than the coherence length of the light source. For the implemented system, objective lens depth of focus is much smaller than the coherence length of light source. Therefore, axial resolution is the convolution between coherence gated response of broadband light source and confocal gated response of the microscope objective, as schematized in Figure 5.2.

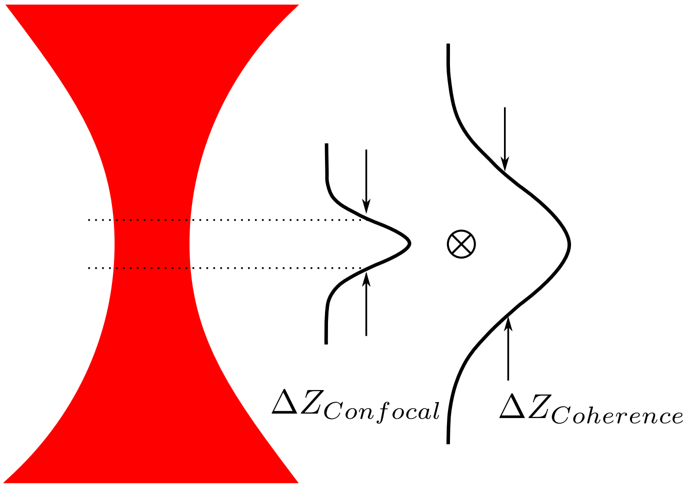

Figure 5.2: Illustration of axial resolution in OCM, which is determined by the convolution of confocal and coherence gated axial responses.

Coherence Gated Axial Resolution

Coherence gating is a mechanism which discriminates light reflected back from different depths of the tissue using its echo delay time . The axial resolution obtained by coherence gating is inversely proportional to the FWHM spectral bandwidth of the light source. For a Gaussian shaped spectral source, coherence gated axial resolution is given by [43]:

$$\Delta z_{coherence} = \frac{2ln2}{\pi}\frac{\lambda_{\circ}^{2}}{\Delta\lambda} \tag{5.6}$$

Where $\lambda_{\circ}$ and $\Delta\lambda$ represent center wavelength of light source and FWHM spectral bandwidth, respectively. The broadband light source of the implemented system has a bandwidth of 53.6 nm and a center wavelength of 835 nm, which gives a theoretical coherence gated axial resolution of 5.7 µm.

Confocal Gated Axial Resolution

The depth of focus or axial resolution in a confocal imaging system is defined as the half power width of the axial response to a planar or point reflector translated along the optical axis. As derived in Section 3.2.1, confocal axial resolution for point and planar reflectors is given as:

$$\Delta z_{confocal\ (planar)} = \frac{0.45 \cdot \lambda_\circ}{n(1 - cos\theta)} \tag{5.7}$$

$$\Delta z_{confocal\ (point)} = \frac{0.62 \cdot \lambda_\circ}{n(1 - cos\theta)} \tag{5.8}$$

$$\theta = sin^{-1}(NA/n)$$

Where $\lambda_\circ, n$ and NA represent center wavelength of light source, refractive index of the medium, and numerical aperture of microscope objective, respectively. θ is half the angle of light cone collected by microscope objective. In the implemented system, numerical aperture of the objective lens is 0.8 NA, which gives a theoretical confocal axial resolution of 1.4 µm and 1.94 µm for planar and point reflectors respectively. For biological samples, axial resolution defined using point reflector is used, as it better represents the tissue samples.

The FWHM width of the confocal depth response for implemented SDOCPM system was measured to be 1.5 µm, which is in good agreement with theoretical value of 1.4 µm, predicted by Equation 5.7.

Confocal + Coherence Gated Axial Resolution

The confocal + coherence gated axial response of the SDOCM system was measured by translating a mirror axially, in steps of 0.75 µm. Obtained result along with confocal response, for comparison, is plotted in Figure 5.3. The

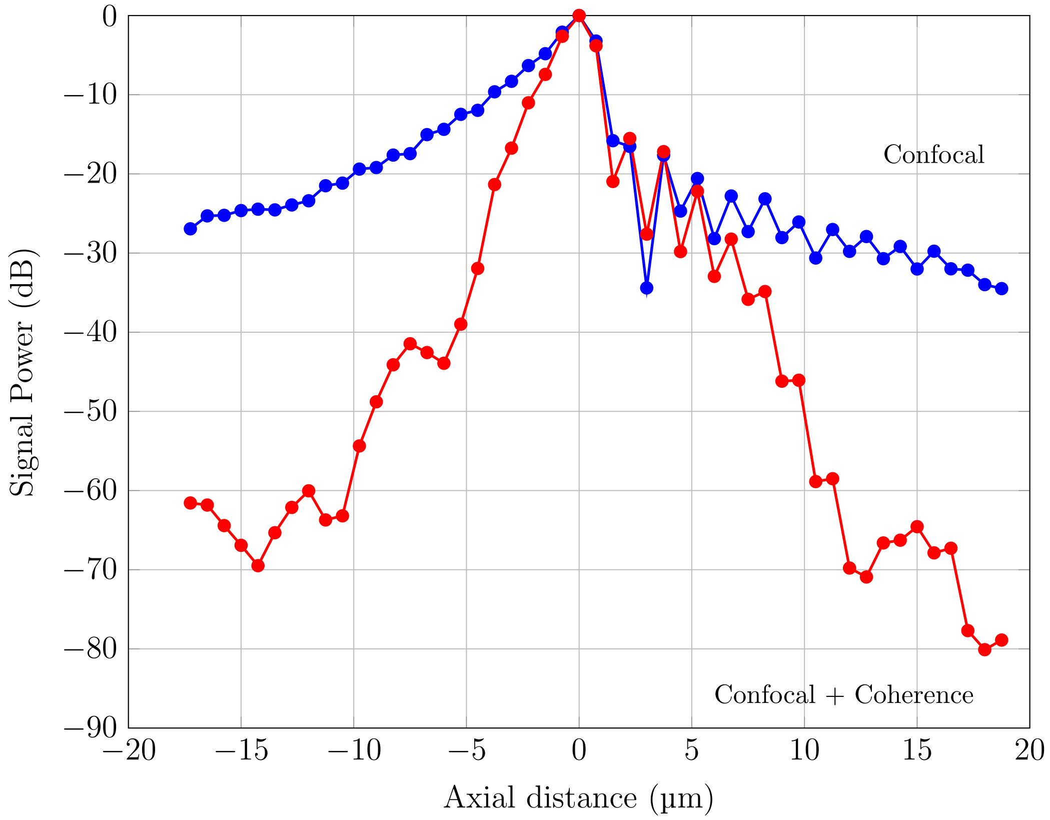

Figure 5.3: Axial response of the implemented SDOCPM system, measured by translating a mirror in the sample arm in 0.75 µm steps. A 40×, 0.8 NA objective was used for confocal detection, and a broadband light source with a FWHM width of 53.5 nm was used for coherence detection. Axial response for $confocal$ gating (blue), and axial response for $confocal + coherence$ gating (red).

axial response was measured using a 40×, 0.8 NA objective lens, and with a broadband light source of coherence length 6 nm. The FWHM of confocal + coherence gated axial response is 2.11 µm, which is higher than the confocal axial response of 1.5 µm. This is because, the amplitude of the modulated fringe pattern in confocal + coherence gating response varies with the square root of the sample reflectivity. Multiplying the confocal FWHM with $\sqrt{2}$, yields 2.12 µm which is equivalent to the FWHM of confocal + coherence response.

From the measured axial response it is apparent that, near the focal plane confocal function dominates the depth response, and with increasing defocus distance coherence function is much more effective in attenuating the out of focus light.

The noise floor in confocal + coherence depth response is −80 dB, which means that it can detect backscattered reflections of up to 10^{-7} times the incident light power. Whereas the noise floor of confocal response is only −35 dB, which corresponds to a minimum detection signal value of 10^{-3} times the incident light power. Therefore, OCM has a sensitivity advantage over confocal microscope, and this is because of the homodyne gain factor, which is the constant reference arm power, that helps detect very weak backscattered light. Increased detection sensitivity in OCM also extends the penetration depth in highly scattering samples, such as tissues.

5.2.2 Transverse Resolution

The transverse spatial resolution is measured on a focal plane perpendicular to the optical axis. The transverse spatial resolution is determined by the diffraction limited spot size of the focused beam, which is inversely proportional to the numerical aperture of microscope objective, as given by [15]:

$$\Delta x = 0.37\left(\frac{\lambda_\circ}{\mathrm{NA}}\right) \tag{5.9}$$

Where $\lambda_\circ$ and NA represent center wavelength of light source and numerical aperture of microscope objective, respectively.

Water immersion microscope objective (model # 440095, Carl Zeiss Microimaging GmbH) with 0.8NA, and a center wavelength of 835 nm provides a theoretical focused beam spot diameter of 0.4 µm. An Air Force resolution target was used to demonstrate the transverse resolution of implemented SDOCPM system. Scanned *en face* image of the group 9 line pairs are as shown in Figure 5.4. The size of the image size is 128 µm × 128 µm, and all line pairs of the group 9 are easily distinguishable. The finest of the line pairs are separated by 0.78 µm.

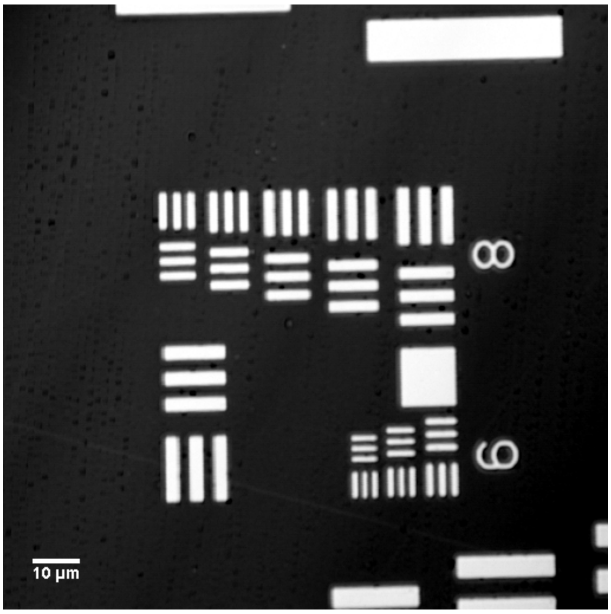

Figure 5.4: SDOCM image of an Air Force resolution target. Finest line pairs of group 9 are separated by 0.78 µm.

5.2.3 3D Point Spread Function

Having described the theoretical axial and transverse resolutions in previous sections, here, results of axial and transverse response of the SDOCM system for a point object are presented. For accurate measurement of 3D point spread function, size of the object has to be smaller than the diffraction limited resolution of the system.

The 3D point spread function of confocal microscope was measured by blocking the reference arm of SDOCPM system.

Point object for PSF Measurement

Microspheres (Fluoresbrite YG Microspheres, Polysciences, Inc.) with 0.2 µm diameter were chosen as the point object for 3D point spread function measurement. The microspheres solution was dissolved in distilled water with 1:100 ratio, to attain suspension of individual microspheres. The dissolved solution was coated on a 0.15 mm thick glass coverslip and convection dried. The glass coverslip with immobilized microspheres was mounted on the 3D translation sample stage of the SDOCM system, and C-scans were collected while translating the glass coverslip in steps of 0.75 µm to measure the 3D response.

3D PSF of Confocal Microscopy

The important characteristic of confocal microscope is that it selectively collects light from the focal volume to form an image, and rejects out-of-focus light. This selective collection of light enables optical sectioning in highly scattering media, such as tissue, and also enhances the contrast.

The transverse confocal response to a point object is shown in Figures 5.5 (a) & 9b. The XY image plane in (a) is 22 µm × 22 µm, and is color coded with normalized intensity values. The point object is can be seen in the center of the plane with the highest intensity. The intensity values along Y-axis, and through the point object is shown in (b). The FWHM width of the intensity line profile is 0.6 µm, which is 50 % larger than the theoretical value of 0.4 µm. This could be because of higher background intensity, as the reflections from the glass coverslip is up to 28 % of the maximum intensity reflected from the point object. Strong reflections from the glass coverslip are caused because of refractive index mismatch between the immersion medium i.e., water and the glass surface. Oil as the immersion medium, could have minimized the strong reflections, however the objective lens used for these experiments is specifically designed to work with water as the immersion medium.

The axial confocal response to a point object is shown in Figures 5.5 (c) & (d). The YZ image plane in (c) is 22 µm × 22 µm, and is also color coded with normalized intensity values. The surface of glass cover slip is can be seen as the horizontal two pixel line in the image plane, along with the point object with highest intensity values. The intensity line profile along Z-axis, and through the point object is plotted in (c). The intensity line profile was interpolated to obtain accurate FWHM width, which is 2.0 µm. Measured confocal axial response is close to the theoretical value of 1.94 µm, predicted by Equation 5.8.

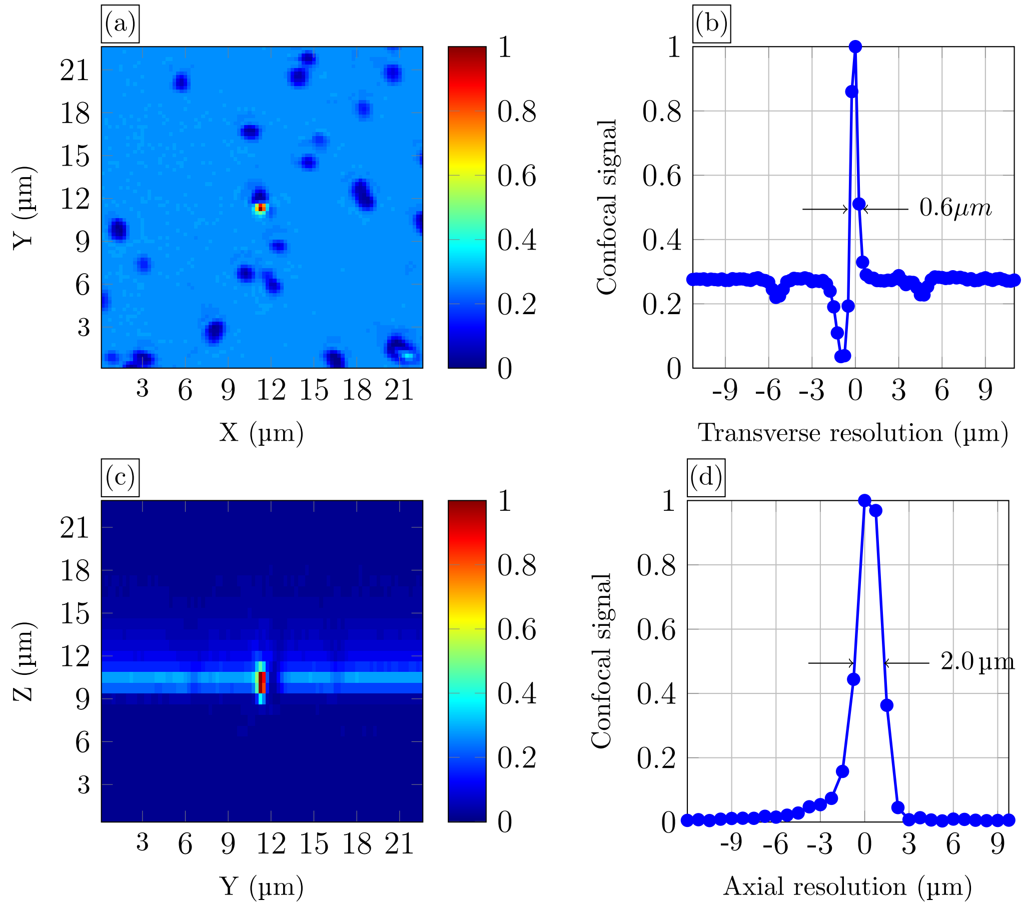

Figure 5.5: Three-dimensional point spread function of confocal scanning microscope. (a) 22 µm × 22 µm image plane along X-Y axis showing measured intensity distribution from a point object, with glass coverslip as the background; (b) Normalized intensity profile through the point object along Y axis from image plane shown in (a); (c) 22 µm × 22 µm image plane along Y-Z axis showing measured intensity distribution from the point object along Z-axis; (d) Normalized intensity profile through the point object along Z axis from image plane shown in (c).

3D PSF of Optical Coherence Microscopy

Results of 3D point spread function measurement of implemented SDOCM system are as shown in Figure 5.6. The transverse XY plane with normalized and color coded intensity values is can be seen in (a). The point object with highest intensity value is in the center of the image plane. It can be noted that the background intensity, i.e., reflections from the surface of glass coverslip are up to 60 % of the reflections from the point object. Compared with confocal response, the background intensity in SDOCM is more than doubled. This is because of the homodyne gain factor, i.e., a constant reference arm power that enables detection of very weak back scattered light from the samples. The FWHM of the transverse SDOCM response is 0.55 µm, which is equivalent to the confocal response.

The axial response of SDOCM system to a point object are as shown in Figures 5.6. The point object with highest intensity values is can be seen in the center of YZ plane, and the glass coverslip appears as the horizontal line with up to 60 % of intensity values. Intensity line profile along Z-axis, and through the point object is plotted in (d), whose FWHM width is 2.4 µm, and about 0.4 µm higher than the confocal response. One would expect the OCM axial response to be narrower than the confocal response alone because of convolution between coherence and confocal gating. However, the axial OCM response has actually broadened. This is because of the fact that, the amplitude of modulation term in the interference signal varies with the square root of the sample reflectivity. Whereas in confocal response, measured intensity varies linearly with the sample reflectivity.

The main advantage of SDOCM over confocal microscopy is the higher sensitivity, i.e., it can detect very weak back scattered light from a sample with the help of homodyne gain factor. Higher sensitivity combined with the improved rejection of multiple scattered light helps extend the penetration depth in scattering samples such as tissues.

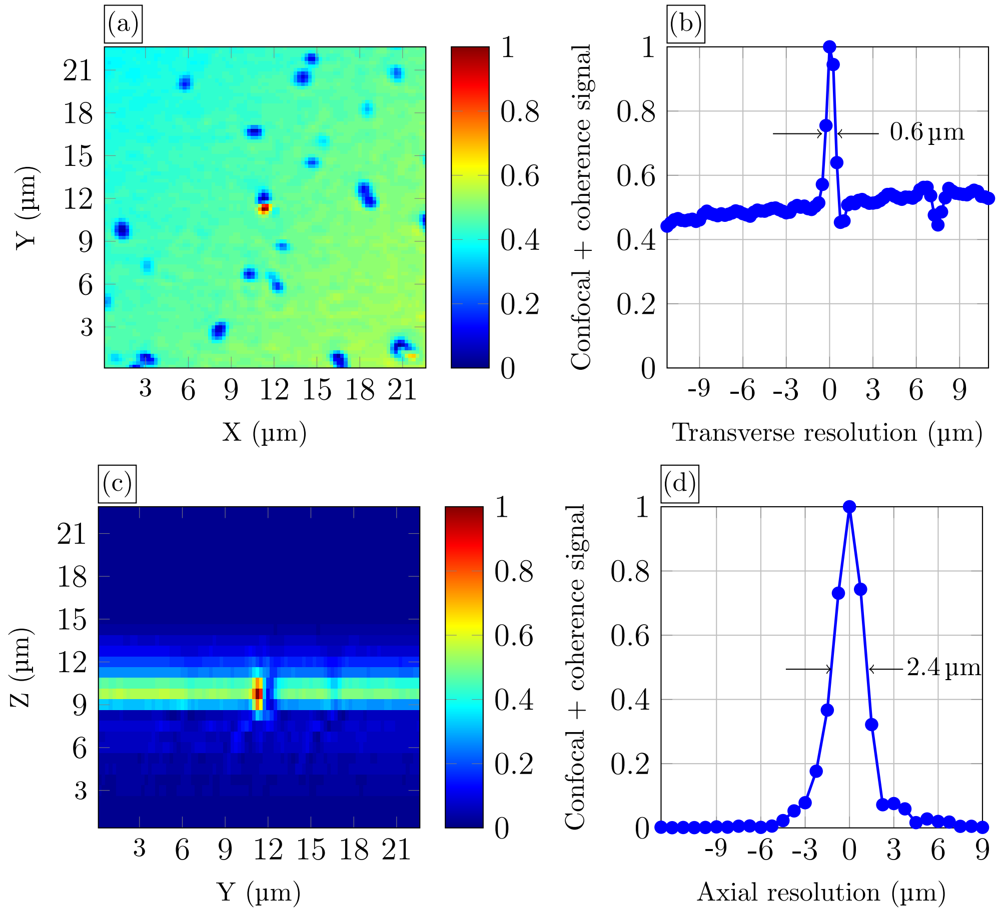

Figure 5.6: Three-dimensional point spread function of SDOCM system. (a) 22 µm × 22 µm image plane along X-Y axis showing measured intensity distribution from a point object, with glass coverslip as the background; (b) Normalized intensity profile through the point object along Y axis from image plane shown in (a); (c) 22 µm × 22 µm image plane along Y-Z axis showing measured intensity distribution from the point object along Z-axis; (d) Normalized intensity profile through the point object along Z axis from image plane shown in (c).

5.3 Phase Sensitivity

Phase sensitivity of SDOCPM system can be defined as the standard deviation of interferometric phase over time, i.e., minimum change in interferometric phase that is measurable by the system. It is limited by the OCT system noise and relative optical path length differences between sample and reference arm, which are often caused by mechanical vibrations. Phase noise is usually specified by the standard deviation of phase differences, $\Delta\phi$, obtained by subtracting the phases of two successive A-scans, measured at same spatial location in a static sample, over time:

$$\Delta\phi = [(\phi_2 - \phi_1), (\phi_3 - \phi_2), \; .... \; (\phi_N - \phi_{N-1})] \tag{5.10}$$

For a shot-noise limited SDOCPM system, the phase sensitivity is determined by signal-to-noise ratio of the interference signal. The standard deviation of phase difference is inversely proportional to the square root of the SNR, as given by [32, p.768]:

$$\delta\phi_{sens} = \frac{2}{\pi}\sqrt{\frac{1}{SNR_{SDOCM}}} \tag{5.11}$$

Where SNR_{SDOCM} represents the signal-to-noise ratio of SDOCM signal obtained from the sample. The phase sensitivity in turn determines the minimum change in optical path length that can be detected axially, as given by:

$$\begin{aligned} \delta Z_{sens} &= \frac{\lambda_\circ}{4n\pi}\delta\phi_{sens} \\ &\text{or} \\ \delta Z_{sens} &= \frac{\lambda_\circ}{2n\pi^2}\sqrt{\frac{1}{SNR_{SDOCM}}} \end{aligned} \tag{5.12}$$

Where $\lambda_\circ$ and n represent center wavelength of the light source and refractive index of the medium, respectively.

The phase sensitivity of the implemented system was measured by varying the SNR, and obtained result along with theoretical values are plotted in Figure 5.7. Measurements were done with glass coverslip as the sample, where the reflections from two glass-air surfaces produce the interference signal in common-path interferometer topology. Measurements were done with a stationary beam i.e., no lateral scanning, and SNR was varied by defocusing the glass coverslip.

In the next sections, phase sensitivity of implemented SDOCPM system for point measurements and volumetric scanning are considered separately, and is compared with phase sensitivity of common path interferometer, as it provides the lowest phase noise floor for homodyne interferometric measurements.

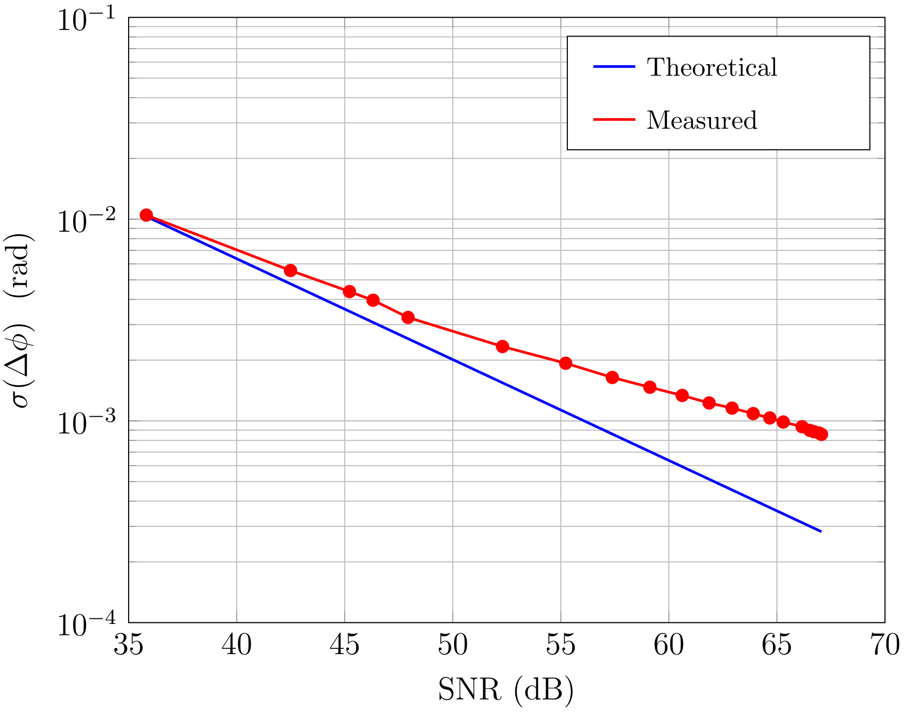

Figure 5.7: Relationship between phase sensitivity and signal to noise ratio of interference signal. Theoretical limit imposed by SNR (blue), and measured with a common-path interferometer (red).

5.3.1 Phase Sensitivity For Point Measurements

Point measurements are A-scans collected from a sample with stationary focused beam. The galvanometer scanners are powered on but the driving voltage is set to zero. For a given detector integration time and sample arm power, phase noise floor is lower when the focused beam spot is stationary, compared with a scanning beam. The apparent reason for low noise floor is that, measured interference fringe pattern generally averages the phases of all sub-resolution reflectors within the focal volume. And when the beam is stationary, there is very little variance in the phases of sub-resolution reflectors and interference fringe is recorded with relatively higher contrast or fringe visi-

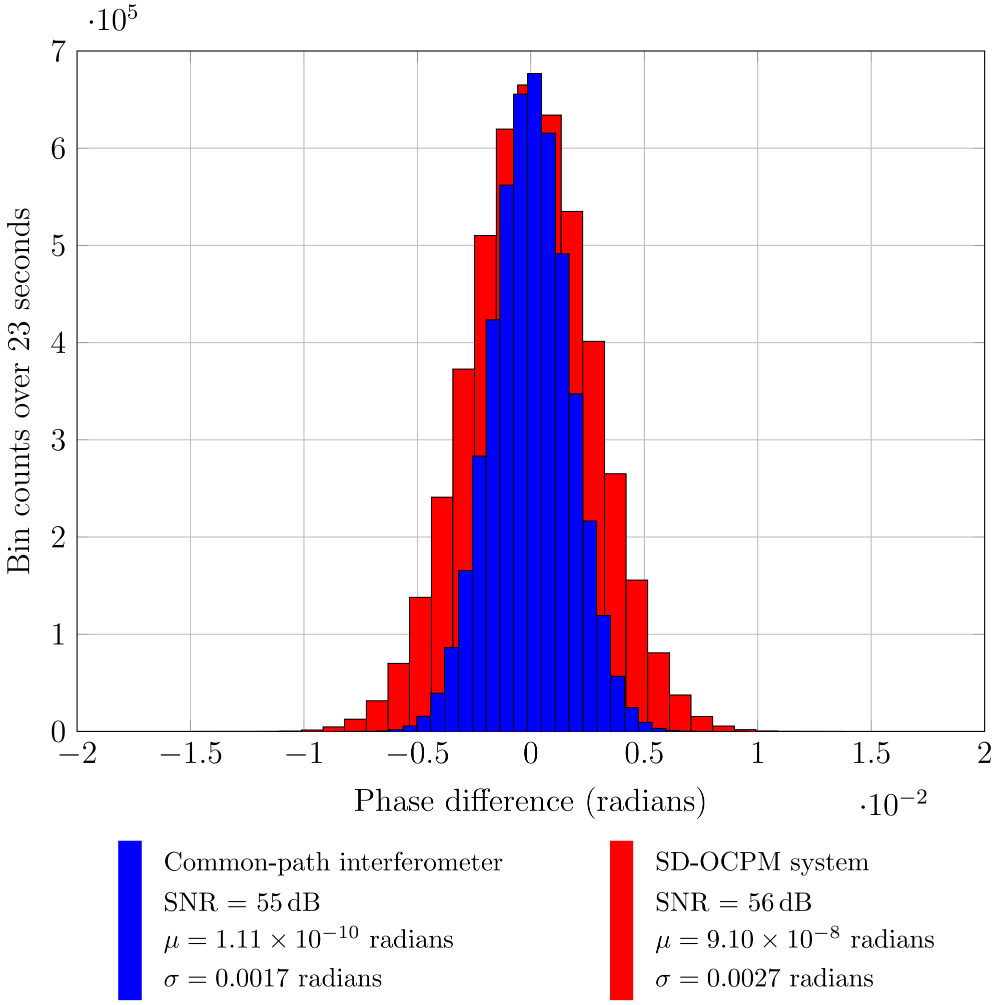

Figure 5.8: Distribution of phase differences measured with a stationary focused beam using common path interferometer (blue), and SDOCPM system (red).

bility. Whereas with a scanning beam, variation in the phase of sub-resolution reflectors is relatively higher, which causes fringe washout and decreases the contrast.

The interferometric phase difference obtained by common path interferometer, and SDOCPM system are plotted as histogram in figure 5.8. The phase sensitivity or the standard deviation of phase differences are 0.0017 and 0.0027 radians for common path interferometer and SDOCPM system, respectively. Equivalent optical pathlength sensitivity is 0.07 and 0.11 nanometers, respectively. Therefore, the optical pathlength sensitivity of the implemented SDOCPM system is comparable to the one obtained from common-path interferometer. This is significant because, common-path topology has many drawbacks including suboptimal transverse spatial resolution, limited depth scanning, and poor control on the reference arm power. Detailed comparison between the optical pathlength sensitivity of common-path interferometer topology and the implemented SDCOPM system with Linnik interferometer setup of the SDOCPM are listed in Table 5.1.

Phase Sensitivity			
	SNR (dB)	Theoretical $\delta\phi_{sens}$(rad)	Measured $\delta\phi_{sens}$(rad)
Common-path	55	0.0011	0.0017
SDOCPM	56	0.001	0.0027
Optical Pathlength Sensitivity			
	SNR (dB)	Theoretical δx_{sens}(nm)	Measured δx_{sens}(nm)
Common-path	55	0.047	0.071
SDOCPM	56	0.042	0.11

Table 5.1: Phase and optical pathlength sensitivity comparison between common-path interferometer and implemented SDOCPM system for point measurements.

5.3.2 Phase Sensitivity For Volumetric Scanning

For volumetric scanning, where focused beam spot is scanned transversely, the phase noise is expected to be higher when compared with point measurements. This increase in phase noise or decrease in phase sensitivity, is caused by the decrease in signal-to-noise ratio with beam movement. It has been demonstrated that the signal-to-noise ratio decreases for scattering samples by logarithm factor of normalized beam displacement [70]:

$$SNR_{decrease} = -5log_{10}\left(1 + 0.5\frac{\Delta x^2}{{\omega_o}^2}\right) \tag{5.13}$$

Where $\frac{\Delta x^2}{\omega_o^2}$ is the squared ratio of beam displacement to FWHM of beam profile, referred to here as normalized beam displacement.

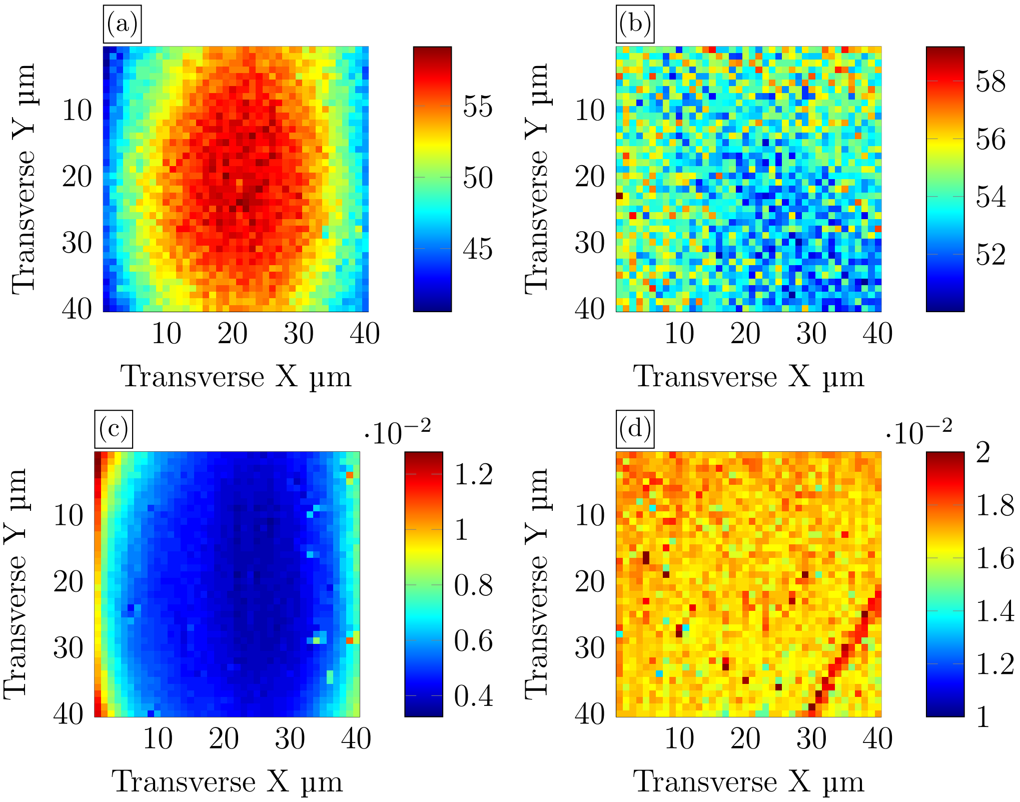

Figure 5.9: SNR and phase sensitivity comparison between common path interferometer and SDOCPM system. All images are *en face*, acquired at 54 volumes/sec, with glass coverslip as the sample. Signal-to-noise ratio measured with common path interferometer (a), and SDOCPM system (b). Standard deviation of phase difference, measured with common path interferometer (c), and SDOCPM system (d).

Phase sensitivity for volumetric scanning was determined by recording a series of 5000 *en face* images (40 µm × 40 µm) at 54 frames/sec, with glass coverslip as the sample. Standard deviation of phase difference over time is computed for each pixel, to estimate the phase noise floor for volumetric scanning.

Figures 5.9 (a) & (c) show the signal-to-noise ratio and phase sensitivity maps of *en face* images obtained with common path interferometer topology. The SNR decreases by 20 dB from center to the periphery of image field. This is caused by lack of telecentricity in scanning optics and also because of lack of constant reference arm power in common path interferometer. The phase sensitivity which is limited by SNR also decreases by three folds from center to the periphery of the image field.

The signal-to-noise ratio and phase sensitivity maps of *en face* images obtained by SDOCPM system are shown in Figures 5.9 (b) & (d). The SNR and phase sensitivity is rather uniform across the image field, because Linnik interferometer topology in SDOCPM system allows for relatively constant reference arm power through out the image field.

Summary of phase sensitivity ($\delta\phi_{sens}$) and axial optical pathlength sensitivity (δx_{sens}) measurements, for volumetric scanning are listed in Table 5.2.

Phase Sensitivity			
	SNR (dB)	Theoretical $\delta\phi_{sens}$(rad)	Measured $\delta\phi_{sens}$(rad)
Common-path	$40 - 60$	$0.0064 - 0.00064$	$0.0072 - 0.0032$
SDOCPM	$50 - 59$	$0.002 - 0.0007$	$0.018 - 0.016$
Optical Pathlength Sensitivity			
	SNR (dB)	Theoretical δx_{sens}(nm)	Measured δx_{sens}(nm)
Common-path	$40 - 60$	$0.28 - 0.028$	0.3
SDOCPM	$50 - 59$	$0.1 - 0.04$	0.9

Table 5.2: Phase and optical pathlength sensitivity comparison between common-path interferometer and implemented SDOCPM system for volumetric scanning.

Measured phase and optical pathlength sensitivities are much higher than the theoretical values, for both common-path interferometer and SDOCPM system. This is because of high-speed scanning, as the *en face* images were acquired at 54 frames/sec. At this frame rate, the fast axis of the galvanometer scanners was operating at a frequency of 2.7 kHz, which is quite high for non-resonant galvo motors, and thus contributing to higher phase noise in the measurements. With resonant galvo scanners or acousto-optic modulators, the phase and optical pathlength sensitivity could be improved.

Implemented SDOCPM system has optical pathlength sensitivity of 0.9 nm for volumetric scanning in comparison with 0.3 nm for common path interferometer, at 54 C-Scans/second. It can be noted that the variation of SNR and optical pathlength sensitivity across the image field in common-path measurements is much higher compared with SDOCPM system. This is because of reference arm power fluctuations with scanning angle, and highlight the poor control of reference arm power in common-path topologies. To further demonstrate that the implemented SDOCPM system combines high phase

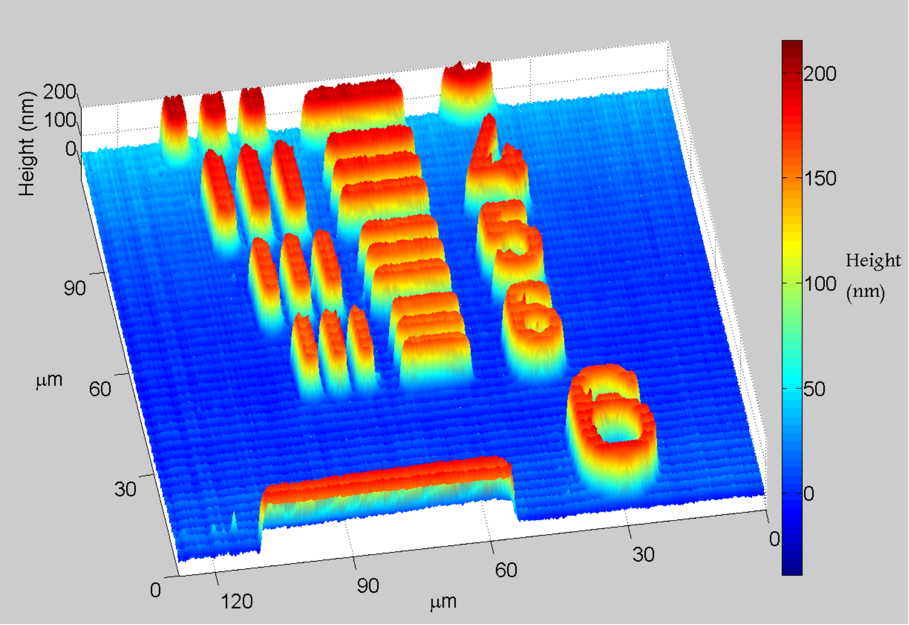

Figure 5.10: 3D topographical image of Air Force Resolution Target obtained by unwrapping the two dimensional phase of transverse scanned focal plane. Horizontal lines shown are from group 7 and #6 Line pairs are separated by 2.2 micrometers, and color bar represents height in nanometers.

sensitivity with high transverse spatial resolution, height of metal deposit on standard Air Force resolution target was determined by unwrapping the two dimensional phase of interference signal, as shown in figure 5.10.

5.4 Field of View

In this section, maximum area that can be imaged both along and perpendicular to optical axis, referred to here as total axial field of view and lateral field of view respectively, is evaluated for the implemented SDOCPM system.

In optical coherence microscopy, because of high N.A. the depth of focus is limited, and does not cover the complete penetrable depth of the sample. So, the depth of focus is translated axially into the sample and C-scans or *en face* images are acquired from consecutive depths to reconstruct the sample 3D structure.

Optical coherence microscopy provides larger penetration depth or total axial field of view into tissue when compared with confocal microscopy because of homodyne gain factor. The homodyne gain factor is the constant reference arm power, that makes it possible to detect very weak back scattered light from deep inside the tissue. The total axial field of view, in OCM, is limited by the penetration depth in scattering samples, which in turn depends on scattering coefficient (μ_s) of the tissue and $1/e^2$ beam diameter of the illumination beam [71].

The lateral field of view in SDOCM primarily depends on the focal length of the objective lens and the maximum angle at which the collimated beam can enter the back aperture of microscope objective, as given by:

$$FOV_{lateral} = 2\mathrm{f}_{objective}\Theta_{max} \tag{5.14}$$

Where $\mathrm{f}_{objective}$ is the focal length of the microscope objective and Θ_{max} is the maximum scanning angle.

Although, the galvanometer based XY scanners have a range of ±20°, maximum scan angle is limited by the diameter of the beam, which completely fills the 11 mm back aperture of the microscope objective. The illustration in Figure 5.11 shows the maximum angle with which scanning beam can enter the back aperture of microscope objective. The magnification and focal length of the microscope objective is 40, and 5 mm respectively. With a tube lens of 100 mm focal length and 11 mm beam diameter, maximum scan angle Θ_{max} was calculated to be 4.12°. Using Equation 5.14, theoretical maximum value for the lateral field of view was calculated to be 0.72 mm.

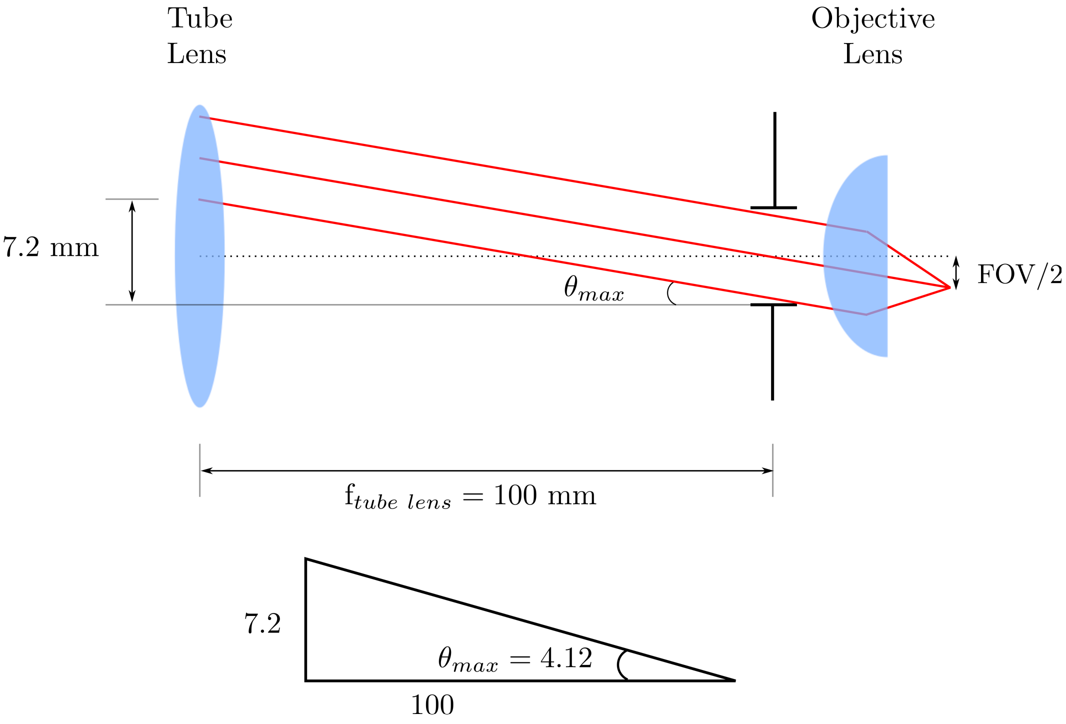

Figure 5.11: Schematic illustration of maximum lateral field of view in implemented SDOCPM system.

To demonstrate the maximum lateral field of view of the implemented SDOCPM system, an Air force resolution target was scanned and the obtained image is as shown in Figure 5.12. Shown image consists of 2048 × 2048 pixels, and took about 19 seconds for the acquisition. The image covers a lateral area of 0.7 mm × 0.7 mm, and is comparable to the theoretical maximum field of view of 0.72 mm.

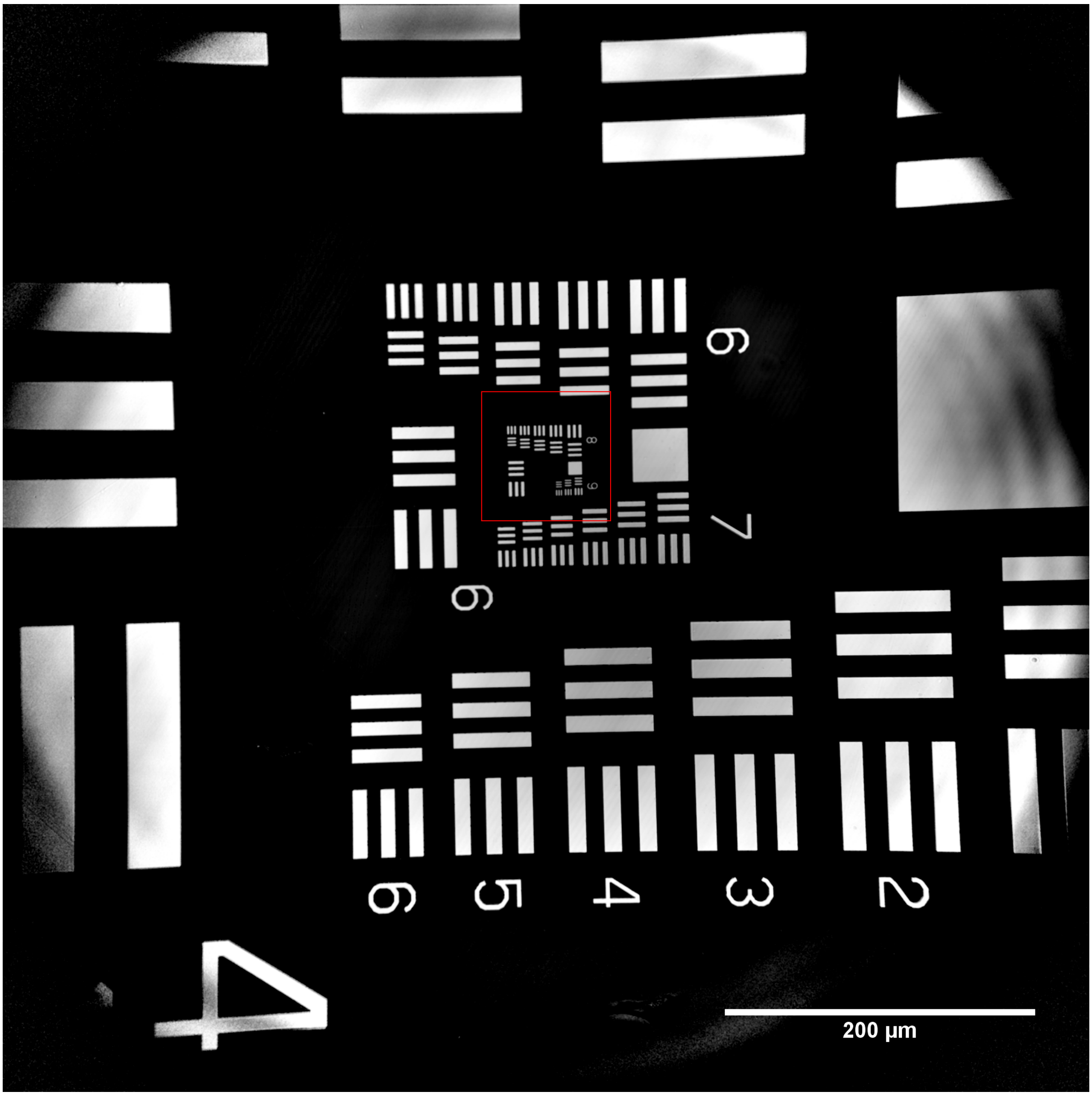

Figure 5.12: Scanned image of Air force resolution target showing maximum lateral field of view of the implemented SDOCPM system. Image consists of 2048 × 2048 pixels, and covers an area of 0.7 mm × 0.7 mm. The area covered by red square in the center of the image field is displayed in Figure 5.13, where line pairs from group 9 of the Air Force resolution target are clearly resolvable.

The area marked by the red square in Figure 5.12 is zoomed in, and is shown in Figure 5.13. Zoomed in image covers an area of 90 µm × 90 µm, where the line pairs of group 9 are clearly resolvable. The finest of the line pairs in group 9 are separated by 0.78 µm.

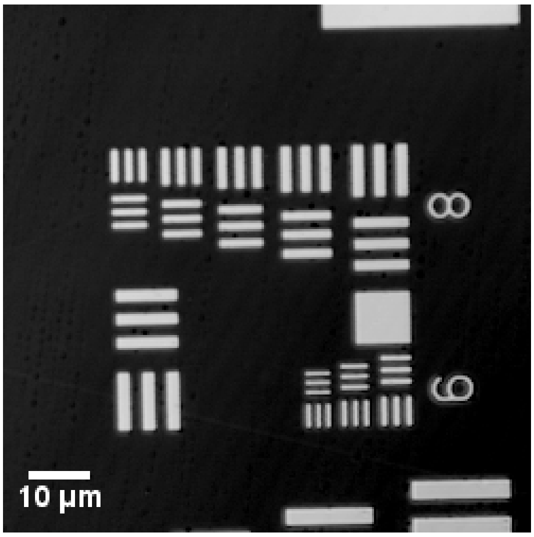

Figure 5.13: Zoomed in image of area covered by red square in Figure 5.12. Image covers an area of90 µm × 90 µm, and the finest lines of group 9 are separated by 0.78 µm.

5.5 Temporal Resolution

Temporal resolution is an important factor in the performance of SDOCPM system, because dynamic samples needs to be sampled sufficiently fast in time and sufficiently dense in space to avoid 2π ambiguity, which is inherent in quantitative phase contrast measurements.

Temporal resolution is usually specified as frames/sec in Hz. The implemented SDOCPM has limited depth of focus because of high numerical aperture, and acquires *en face* or C-scan images at consecutive depths to reconstruct the 3D structure of the sample. So, the temporal resolution is specified in C-scans/sec. For a given maximum linescan rate of the camera, 217, 000 A-scans/sec in the implemented SDOCPM system, temporal resolution is inversely proportional to the image field size, as given below:

$$\text{C-scans/Sec} = \frac{F_s}{N} \tag{5.15}$$

Where F_s and N are linescan rate of the camera and total number of A-scans in the C-scan, respectively.

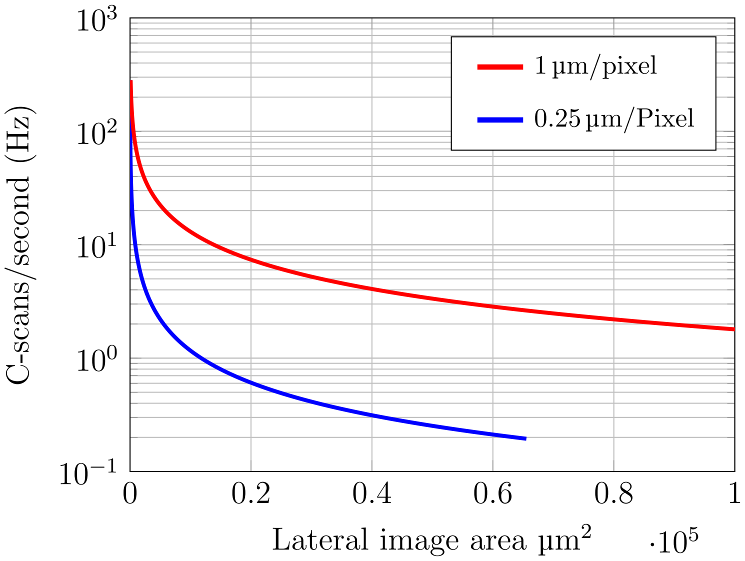

Figure 5.14: Relationship between lateral image field area in µm^2 and C-scans/second, for 0.25 µm and 1 µm square pixels.

Figure 5.14 shows the inverse relationship between C-scans/second and image field size for two different square pixel sizes, 0.25 µm and 1 µm. Implemented SDOCPM system can be configured to operate for any Image field size and its corresponding temporal resolution in Figure 5.14, depending on the type of sample.

5.6 Summary

The performance of the implemented SDOCPM is evaluated for key parameters such as signal-to-noise ratio, spatial resolution, phase sensitivity, field of view, and temporal resolution. The SNR of the implemented system was measured to be 70 dB, which is close to the theoretical maximum of 74 dB.

The transverse and axial spatial resolution of the SDOCPM system was quantified with 3D point spread function measurement. The FWHM width of the transverse and axial response was measured to be 0.6 µm and 2.4 µm, which are comparable to the theoretical values. The advantage of confocal + coherence gating in rejection of multiple scattered light more effectively than confocal gating alone is demonstrated.

The optical pathlength sensitivity of the implemented SDOCPM is 0.11 nanometers or 110 picometers for point measurements, compared with 71 picometers for common-path interferometer. The implemented SDOCPM system overcomes various limitations of common-path interferometer and provides very high optical pathlength sensitivity. Some of the limitations of common-path interferometer setups are limited transverse spatial resolution, limited depth scanning capability, and poor control on the reference arm power. For volumetric scanning, with up to 54 C-scans/sec, optical pathlength sensitivity of the system is 0.9 nanometers.

Implemented SDOCPM can cover a maximum field of view of 0.7 mm × 0.7 mm with sub-micrometer spatial resolution. The temporal resolution of the system can be adjusted in relation with the image field size, with up to 108 sub-volumes/sec for 30 µm × 30 µm image field size.

To summarize, the implemented SDOCPM system combines sub micrometer transverse spatial resolution with sub nanometer optical pathlength sensitivity, and can be used to characterize both morphological and functional properties of dynamic tissue types, simultaneously.

Chapter 6

Microanatomical Images of Ex Vivo Porcine Eye

6.1 Introduction

The most significant clinical application of optical coherence tomography has been in ophthalmology, which is a branch of medicine that deals with anatomy, physiology and diseases of the eye. In human eyes, atypical morphological changes in different cell layers develop into various pathologies and this structure-function correlations are well documented [72, 73, 74]. Because OCT provides morphological assessment of both anterior and posterior segments of the eye on micron scale, *in vivo* and non-invasively, it has become an important tool for diagnosis of various pathologies in ophthalmology. Currently, OCT is being used for diagnosis and monitoring of age-related macula degeneration, diabetic retinopathy, and many other neurodegenerative diseases.

Apart from atypical morphological changes, some pathologies can be triggered by reduced retinal blood flow, resulting in glaucoma. In such cases, Doppler OCT has been used to measure the decrease in retinal blood flow, prior to the loss of visual field [75].

In this chapter, anatomy of the eye is briefly described, and then microanatomical images with subcellular resolution are presented from anterior and posterior segments of an *ex vivo* porcine eye, obtained with spectral domain optical coherence microscopy (SDOCM). Given the structure-function correlation, and single cell morphological details obtained with SDOCM, a strong case is made for its application as diagnostic tool in ophthalmology.

6.2 Anatomy of the eye

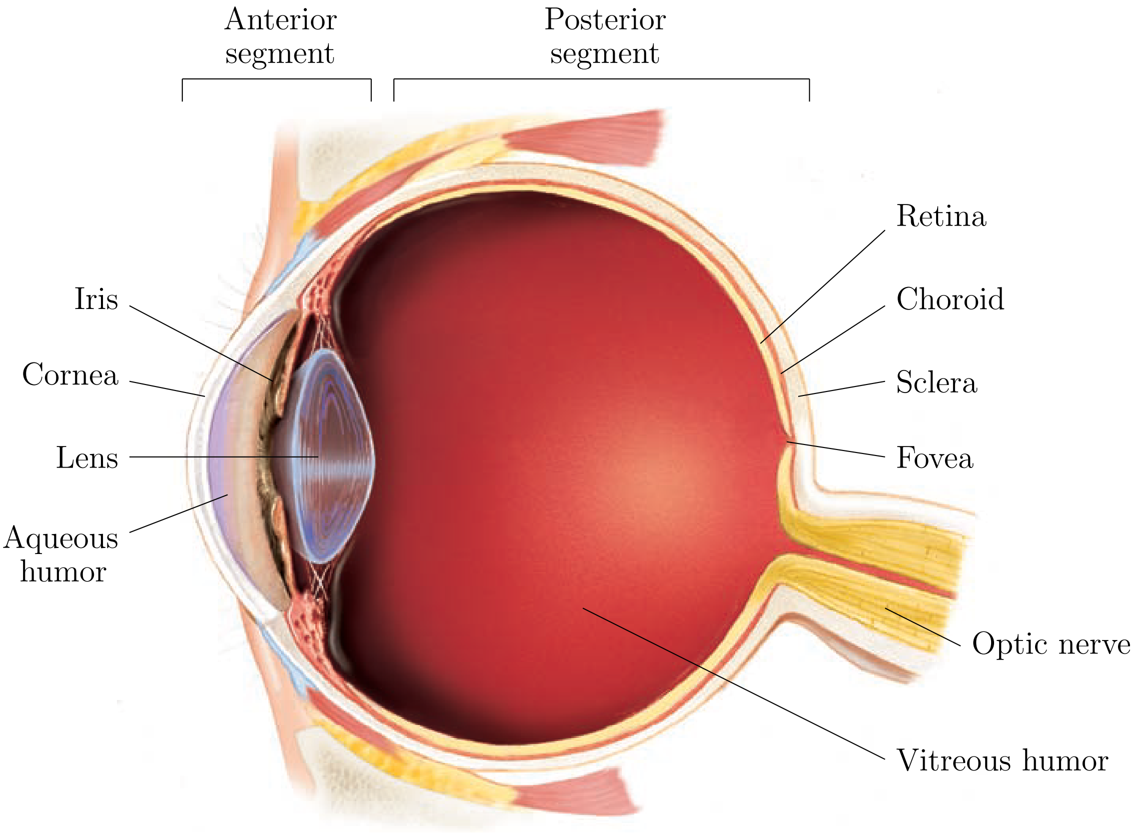

Figure 6.1: Sketch representing transverse section of the human eye [76].

Human eye is a part of complex visual system that regulates the influx of light, converges it to form a sharp image, converts photons into electrical signals, and compresses the aggregated signal before it reaches the brain. As shown in the sketch of a transverse section of eye in Figure 6.1 [76], anatomy of the eye can be subdivided into anterior and posterior segments. The anterior segment of the eye includes cornea, iris, lens and the ciliary body. The anterior segment of the eye regulates the light influx with iris, and converges the incoming light rays onto the retina with the help of curvature of cornea and the lens.

The posterior segment of the eye includes vitreous humor, retina, choroid and the optic nerve. The photoreceptor cells undergoes phototransduction in response to incident light, and the resulting electric impulses are processed by several layers of interconnected neurons, and then the processed signal is relayed to the brain through optic nerve.

Cornea

Cornea is the outermost layer of the eye that covers the iris and pupil. The cornea is largely composed of connective tissue sandwiched between epithelium and endothelium, which are cell layer on the outermost and innermost side of the eye, respectively. The cornea is transparent because it contains no blood vessels, and the cells and collagenous fibers form regular pattern. While the transparency of the cornea ensures minimal scattering of light, its curvature along with the lens helps refract the incoming light rays to form an image on the retina. The amount of light entering into the eye is regulated by iris which decreases the pupil diameter with increasing luminance.

The organization of cell layers in cornea is can be seen from the H&E stained histology section as shown in Figure 6.2 [77]. There are several cell layers in the epithelium with minimal fluctuations in refractive index, and hence the high degree of transparency. The ultrathin fluid layer on the top of the corneal epithelium known as tear film, keeps the surface smooth and hydrated. Any surface irregularities of the cornea causes excessive light scattering by the epithelium and compromises the visual acuity. Stroma is the transparent layer with regularly arranged collagen fibers, which accounts for up to 90 % of cornea thickness.

Most of the corneal pathologies such as corneal ulceration, infectious keratitis, and corneal edema, etc. are currently being diagnosed with scanning slit confocal microscopy [78, 79, 80].

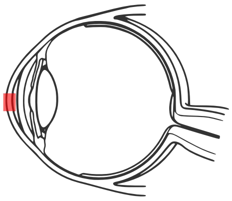

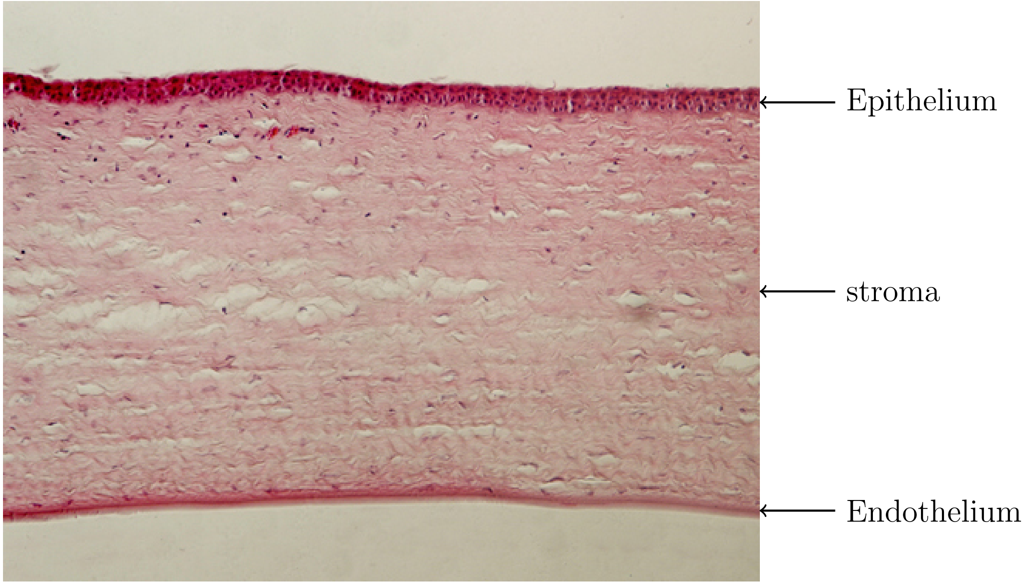

Figure 6.2: H&E stained histology of a longitudinal cross-section of cornea [77].

Neural Retina

Neural retina is a highly organized group of neuronal cell layers between vitreous humor and choroid, that lines the inner orbit of the eye. H&E stained histology section of neural retina is as shown in Figure 6.3 [81]. Neural retina is nearly transparent and contains photoreceptors cells, rods and cones in its outermost region. The bipolar and horizontal cells innervate the projections of rods and cones, and help spatially encode or compress the aggregated signal before it reaches the optic nerve. Compressing of the aggregated signal involves edge and motion detection.

There are host of pathologies associated with retina such as glaucoma, diabetic retinopathy, age-related macular degeneration, arterial or veinal occlusion, etc. Imaging techniques that are currently used in diagnosis of these diseases are fundus photography, intravenous fluorescein angiography, and optical coherence tomography.

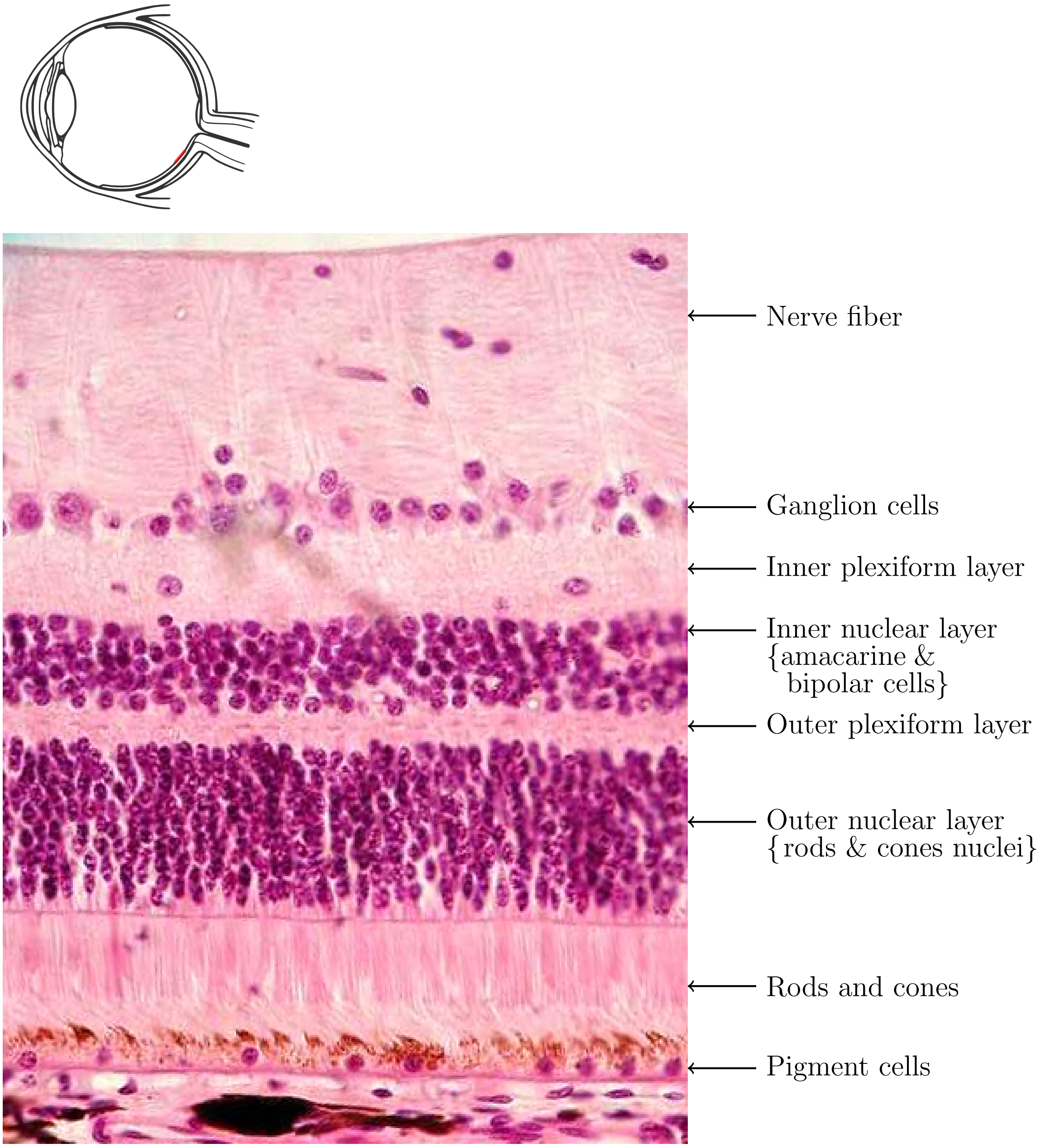

Figure 6.3: H&E stained histology of a longitudinal cross-section of neural retina [81].

6.3 Materials and Methods

6.3.1 Sample Preparation

Cornea

Being the outermost layer of the eye, cornea is easily accessible for imaging, and did not required any dissection. A whole *ex vivo* porcine eye was secured inside a special chamber that can be mounted to 3D sample translation stage. Ringer's solution was used to bathe the whole eye to preserve the morphology.

Neural Retina

Ex vivo porcine eyes were dissected around the cornea circularly, and anterior segment of the eye was completely separated along with lens and vitreous humor. A rectangular area of retina along with sclera was cut out, and the sclera side of the tissue was glued onto a petri dish using a cyanoacrylate based fast-acting glue. Since the transparent layers of neural retina easily peels off from the layer below photoreceptor cells, fast-acting glue was applied on the edges of the tissue to seal the neural retina with choroid and sclera. Fixed neural retina was bathed in Ringer's solution to preserve the tissue.

6.3.2 Image Acquisition

Microanatomical images of neural retina presented in this chapter were obtained by SDOCM system similar to the one described in Chapter 4, except that 3D translation stage was used to scan the sample, instead of galvanometer scanners. The 3D sample translation stage was constructed with a pair of piezomotors (M-663, Physik Instrumente GmbH) for X-Y translation, and a linear motor (M-125, Physik Instrumente GmbH) for Z translation. A commercially available spectrometer (Callisto, Thorlabs GmbH.) was used to read out the broadband interference fringe patterns. A user interface was developed in LabVIEW (National Instruments, USA) to synchronize the spectrometer read out and translation of the sample, for volumetric imaging.

The microanatomical images of cornea presented in this chapter were obtained by SDOCM system as described in Chapter 4, using galvanometer scanners.

Raw data was processed and *en face* optical sections were obtained using the procedure also described in Chapter 4.

6.4 Results

Microanatomical images of both anterior and posterior segments of an *ex vivo* porcine eye with single-cell morphological details, obtained with SDOCM are presented below.

6.4.1 Microanatomical Images of Cornea

There are three prominent cell layers in the cornea, i.e., epithelium, stroma, and endothelium as can be seen in the histology section in Figure 6.2. All of these cell layers can be visualized by SDOCM as they are transparent, here *en face* optical sections from epithelium and stroma are presented.

Corneal epithelium

Microanatomical images (128 µm × 128 µm) of cell layers in the corneal epithelium are as shown in Figure 6.4. Because images were acquired from the whole *ex vivo* porcine eye, vignetting is caused by the natural curvature of cornea. In the center of the image field however, single cells and their nuclei (marked with red arrows) can be clearly visualized.

Characteristic morphological details of corneal epithelium, such as arrangement of cells, their shape and sizes are all well depicted in the shown images. Morphological details obtained from SDOCM are comparable to the one obtained from H&E stained histology sections. Since most of the corneal pathologies interrupt the organization of cell layers and cause turbidity in the epithelium, SDOCM can potentially be used as to carry out an *in vivo* histology examination, non-invasively.

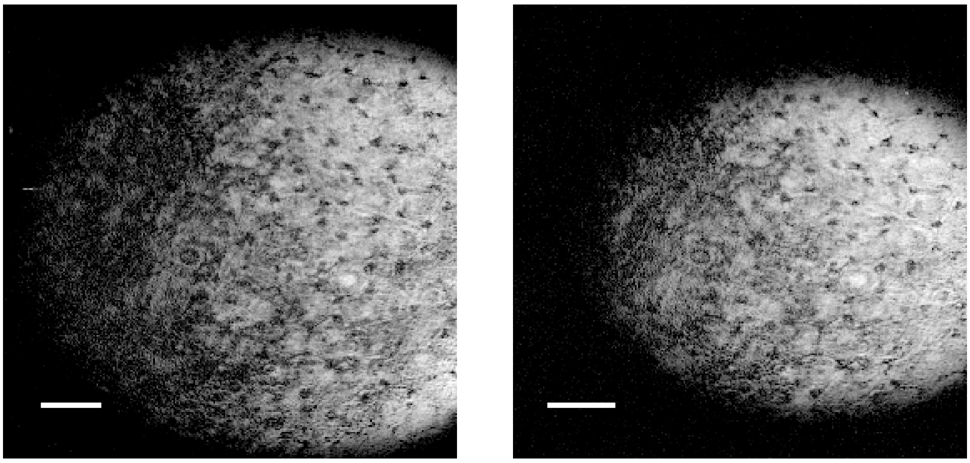

Z = 0 µm　　Z = 1.5 µm

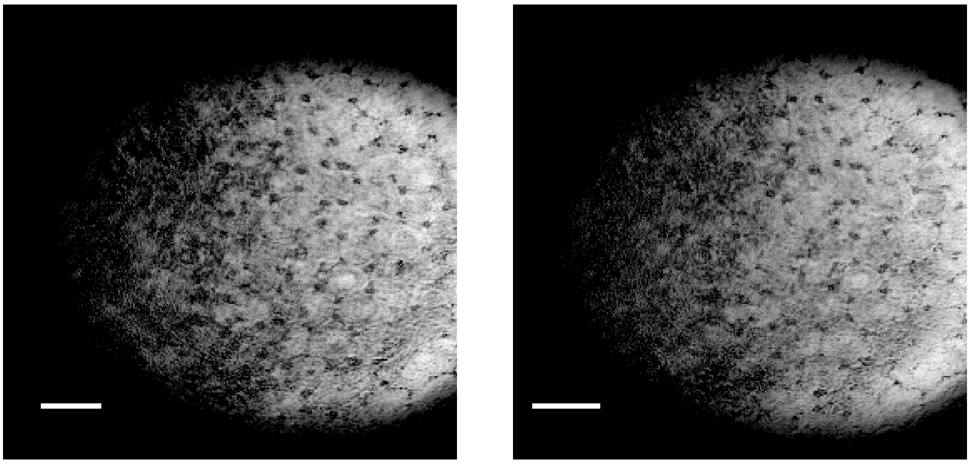

Z = 3 µm　　Z = 4.5 µm

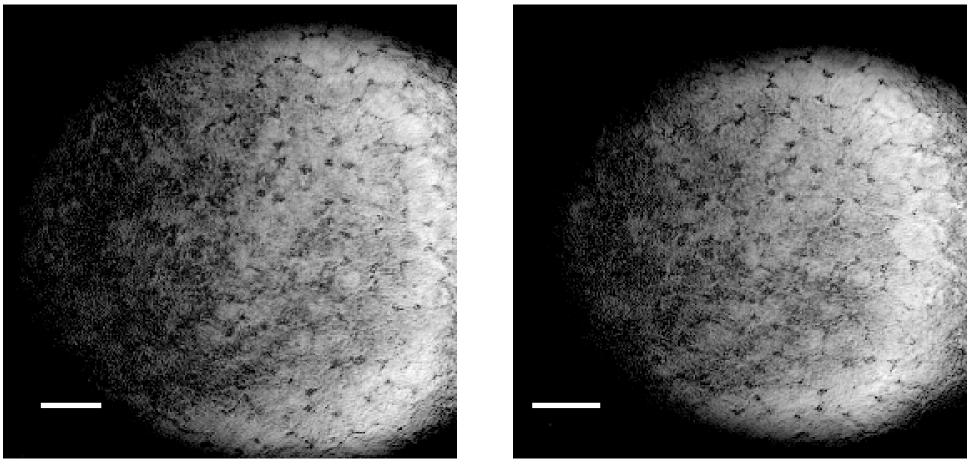

Z = 6 µm　　Z = 7.5 µm

Figure 6.4: A stack of *en face* optical sections (250 µm × 250 µm) at 1.5 µm axial steps, through cell layers of corneal epithelium. Scale bar represents 40 µm.

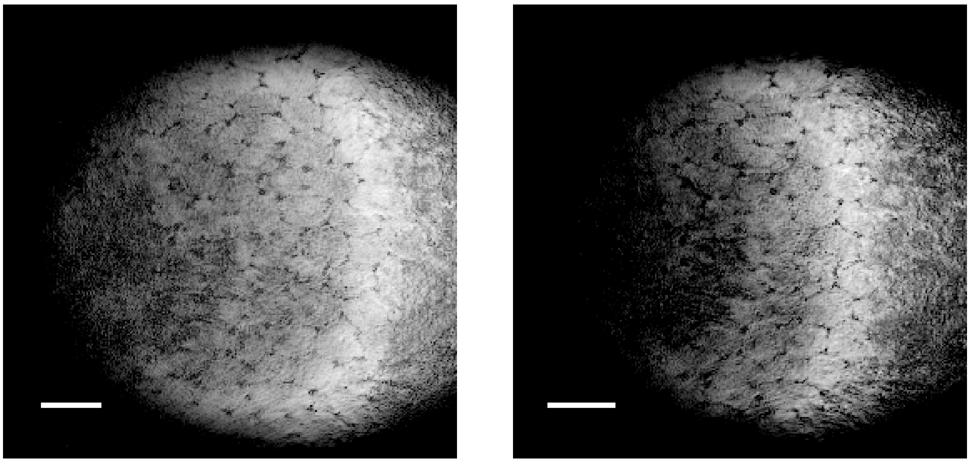

Z = 9 µm Z = 10.5 µm

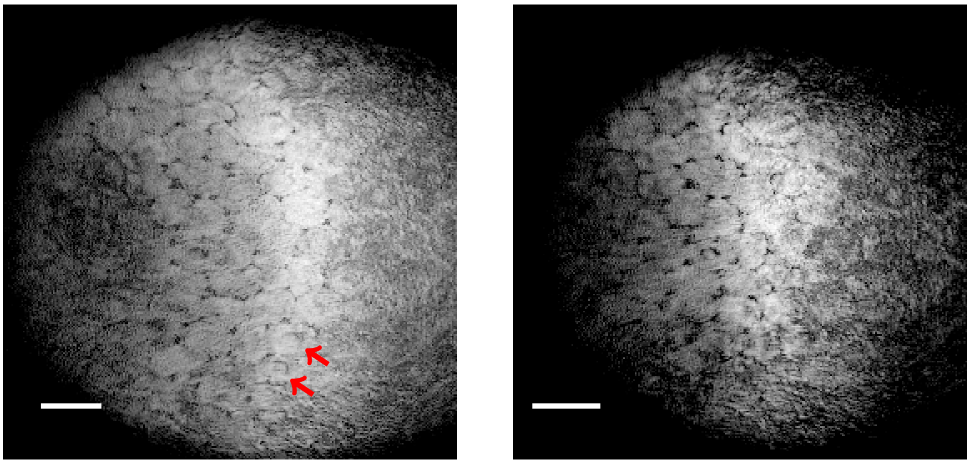

Z = 12 µm Z = 13.5 µm

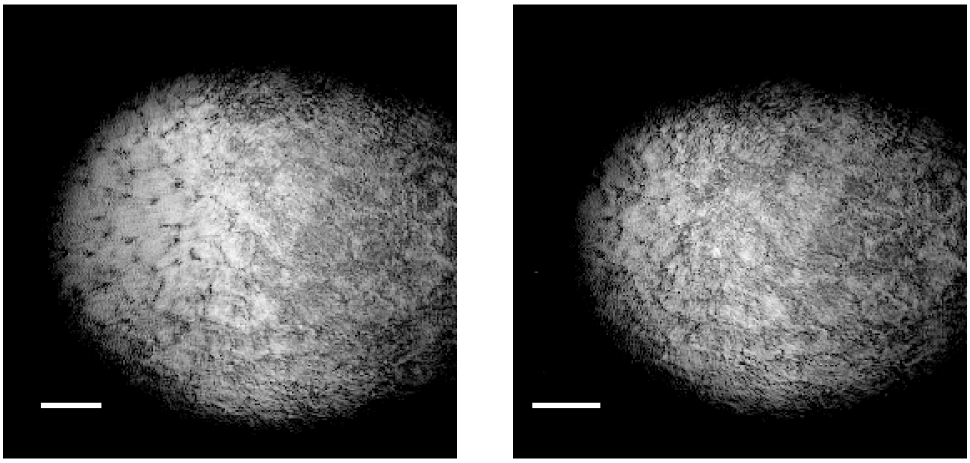

Z = 15 µm Z = 16.5 µm

Figure 6.4: (continued) Stack of *en face* optical sections (250 µm × 250 µm) at 1.5 µm axial steps, through cell layers of corneal epithelium. Single cells and their nuclei (marked with red arrows) are clearly visualized. Scale bar represents 40 µm.

Corneal stroma

Corneal stroma, which is a thick transparent layer of regularly arranged collagen fibers is visible at 18 µm below the top surface of the cornea, as shown in the *en face* optical sections in Figure 6.5. The collagen fibers make up most of the corneal stroma, and the remaining volume consists of fibroblast cells known as keratocytes.

Regularly arranged collagen fibers, which makes the cornea transparent, are clearly visualized between the depths of 18 to 22.5 µm.

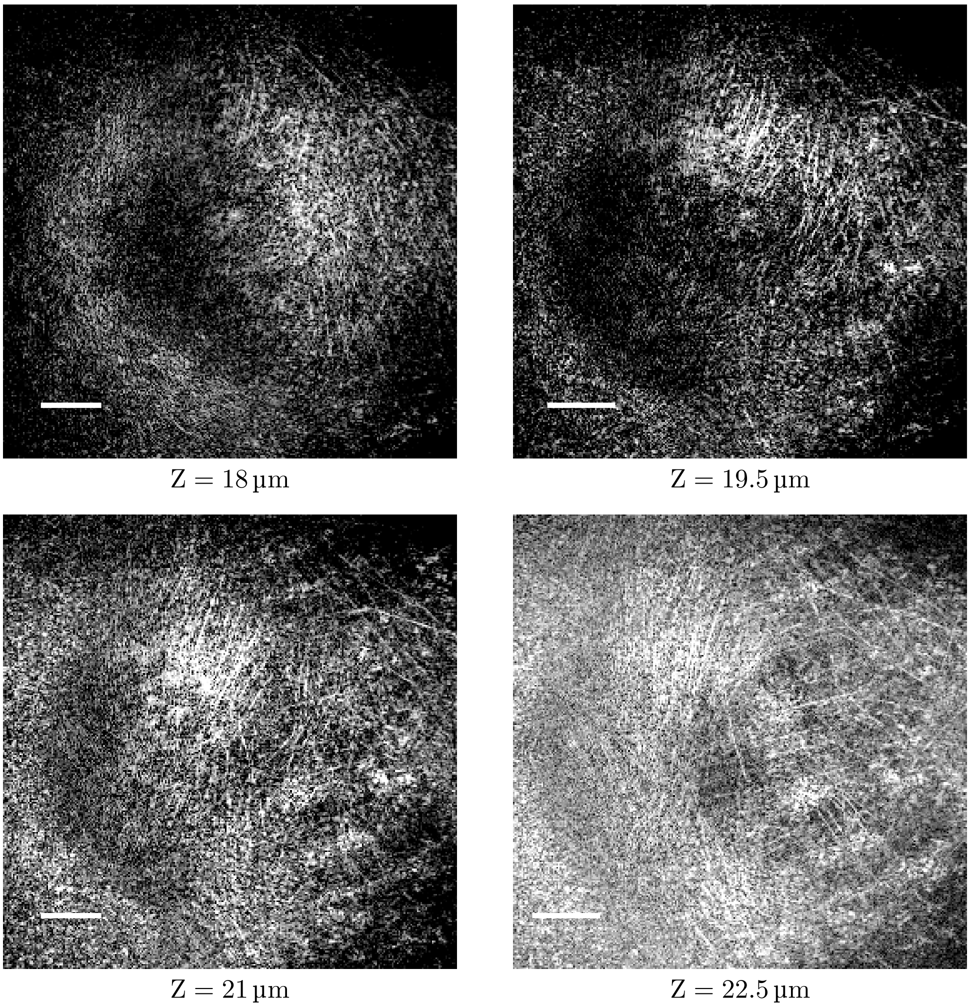

Z = 18 µm

Z = 19.5 µm

Z = 21 µm

Z = 22.5 µm

Figure 6.5: *En face* optical sections(250 µm × 250 µm) of corneal stroma. Scale bar represents 40 µm.

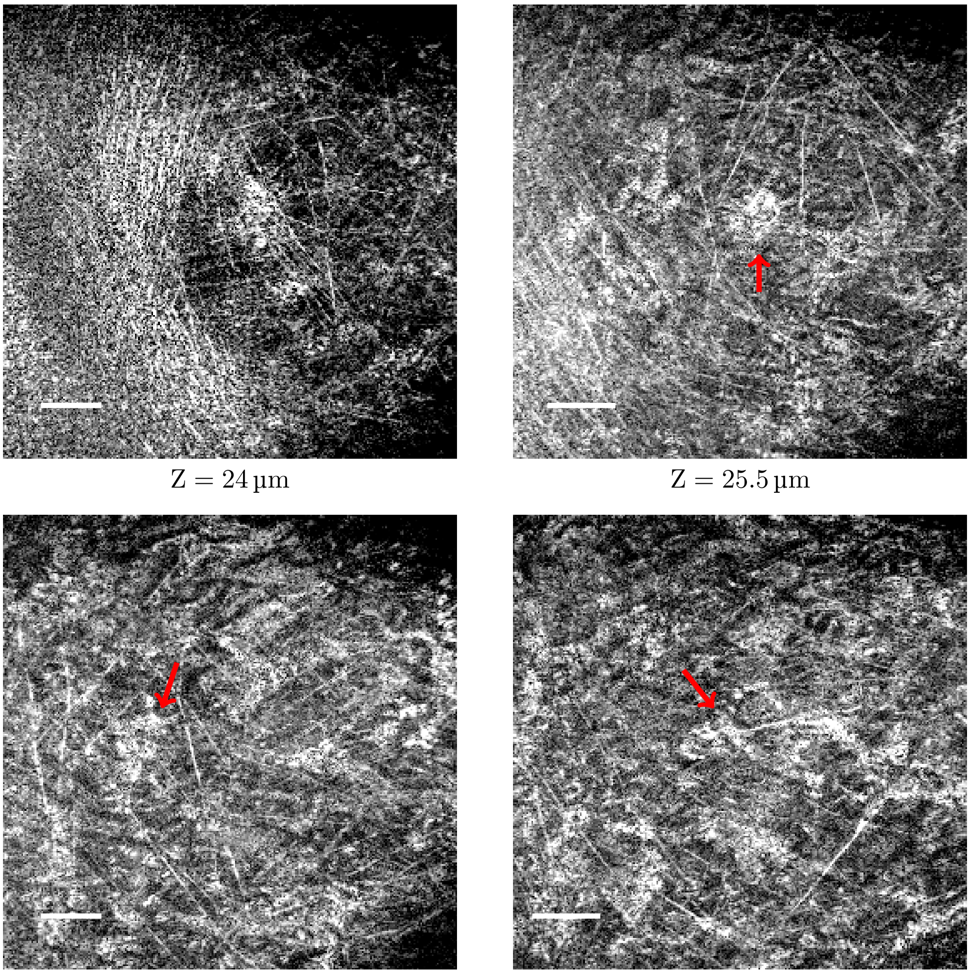

Z = 24 µm

Z = 25.5 µm

Z = 27 µm

Z = 28.5 µm

Figure 6.5: (continued) *En face* optical sections(250 µm × 250 µm) of corneal stroma. Regular arrangement of collagen fibers and keratocytes (marked with red arrows) are clearly visualized. The keratocytes are marked by red arrows, and scale bar represents 40 µm.

Corneal keratocytes are special type of fibroblast cells that synthesize extracellular matrix and collagen fibers. Keratocytes are also seen in the shown images, marked with red arrows, from the depth of 25 µm and below.

Corneal pathologies often disrupt this regular arrangement which causes excessive scattering of light and leads to vision loss. SDOCM provides better penetration depth then conventionally used confocal scanning microscopy and therefore can potentially be used as a non-invasive tool for diagnose and monitoring of these pathologies.

Three dimensional structure of corneal epithelium and stroma cell layers was reconstructed by stacking the *en face* optical sections acquired at 0.75 µm steps in depth. Reconstructed volume of size 250 µm × 250 µm × 30 µm is shown in Figure 6.6.

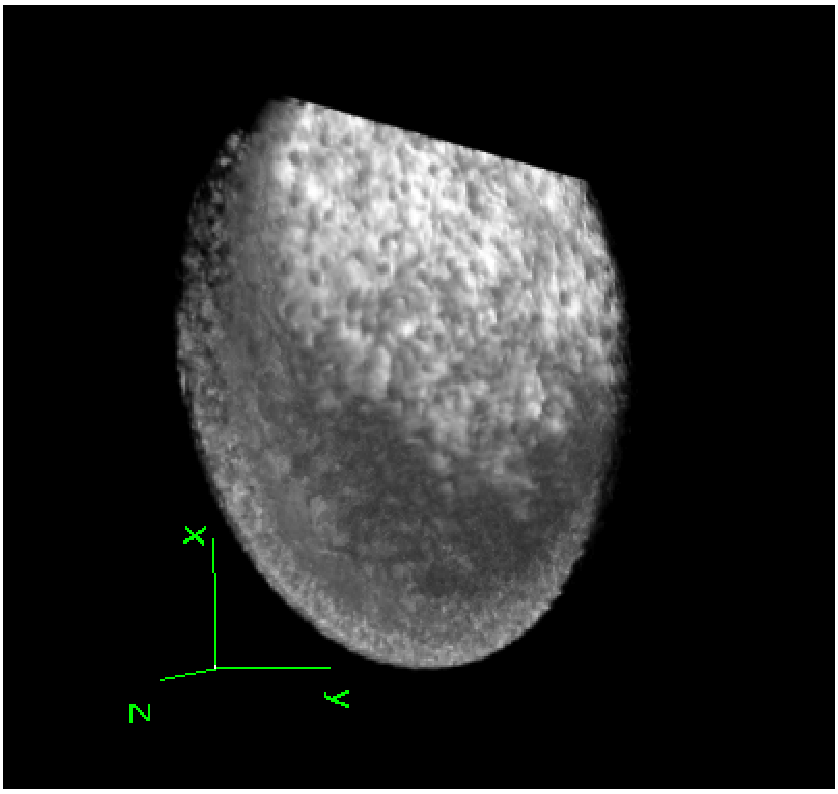

Figure 6.6: (movie) Three dimensional reconstruction of porcine corneal epithelium and stroma cell layers. Spatial dimensions of the volume are 250 µm × 250 µm × 30 µm.

6.4.2 Microanatomical Images of Neural Retina

There are eight prominent cell layers in neural retina, as can be seen in a H&E stained histology section in Figure 6.3. Microanatomical images of all but RPE cell layer obtained from an *ex vivo* porcine eye are presented in this section. Shown images are 400 µm × 400 µm across, and Z represents depth position of optical sections inside the retina from the vitreous surface.

Nerve fiber layer

The nerve fiber layer is the top most layer of retina which relays the processed visual signals to the visual cortex of brain. Nerve fiber layers are the axons of retinal ganglion cells. Figure 6.7 shows the *en face* optical sections of the nerve fiber layer.

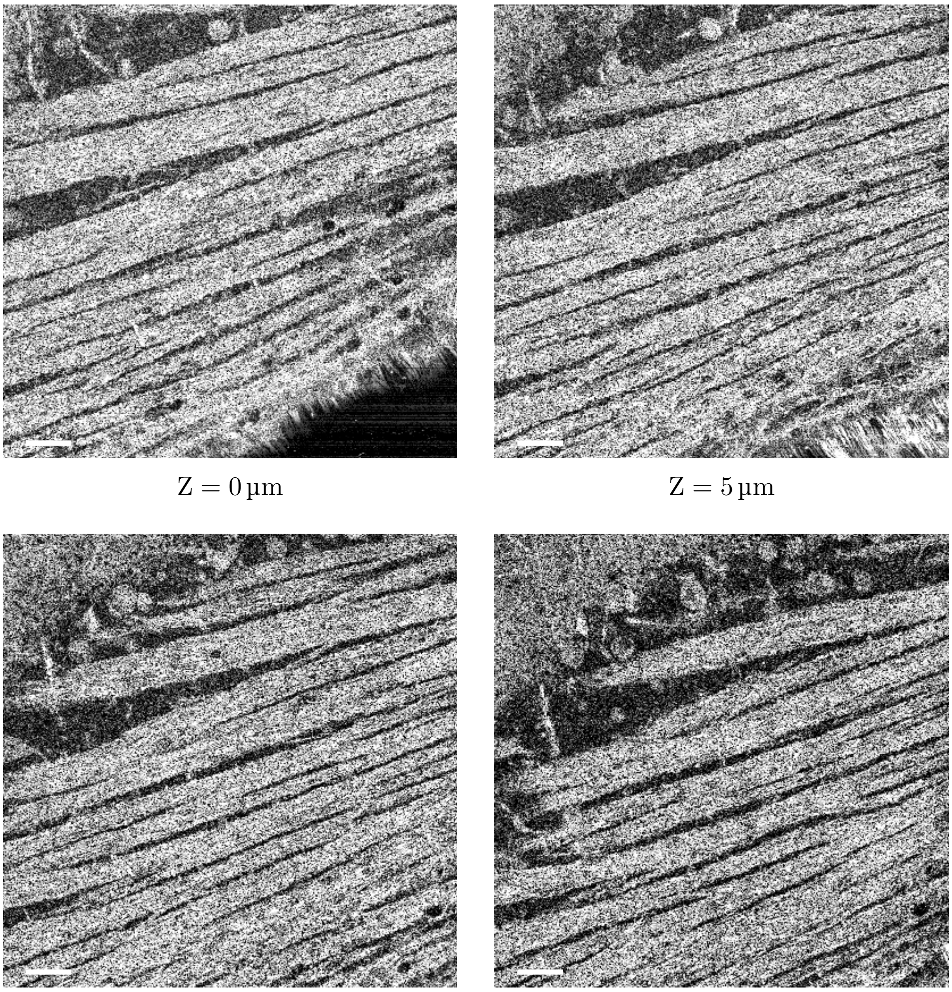

Z = 0 µm

Z = 5 µm

Z = 10 µm

Z = 15 µm

Figure 6.7: *En face* optical sections, 400 µm × 400 µm, from nerve fiber layer of an *ex vivo* porcine neural retina. Scale bar represents 40 µm.

Ganglion cell layer

Ganglion cell layer, which is just below the nerve fiber layer contains the nuclei of ganglion cells, where as their axons project outwards and synapse with nerve fiber layer. Retinal ganglion cells form the receptive field and detect edges in the image formed on the photoreceptor layer. *En face* optical sections in Figure 6.8 show ganglion cells synapsing with nerve fiber layer.

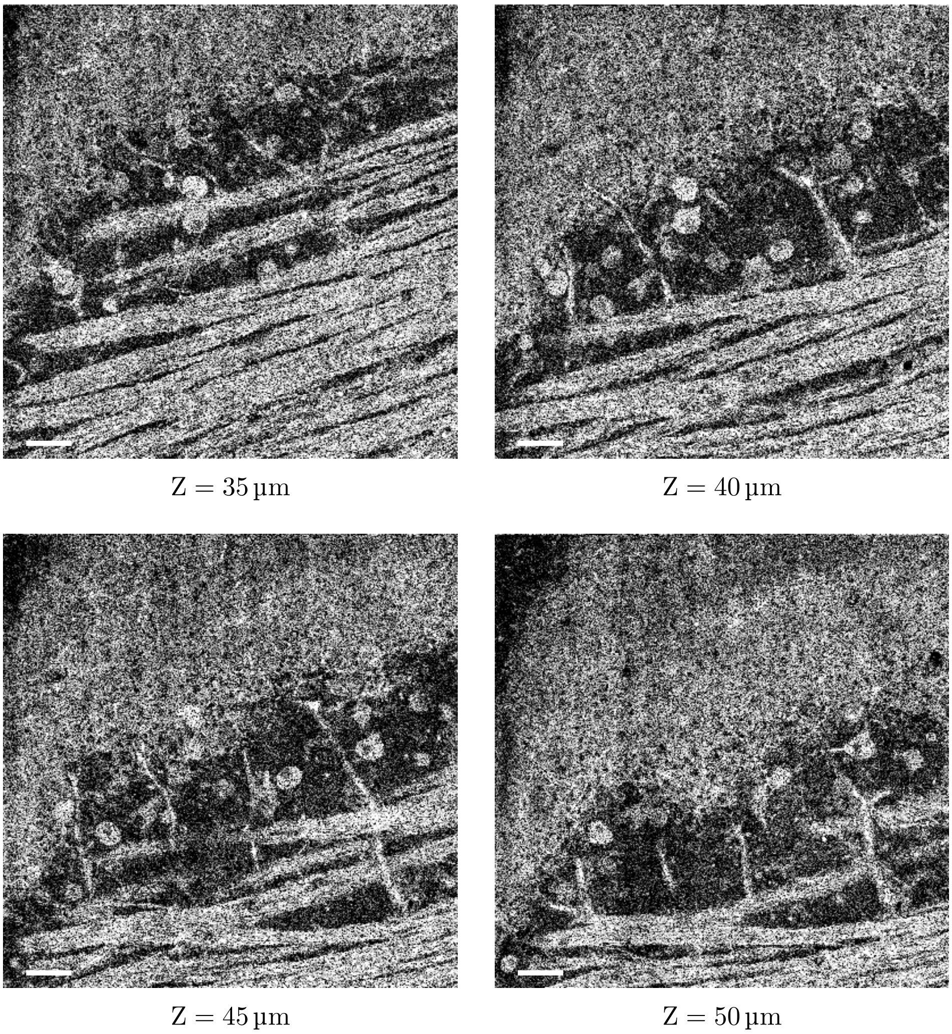
Z = 35 µm

Z = 40 µm

Z = 45 µm

Z = 50 µm

Figure 6.8: *En face* optical sections, 400 µm × 400 µm, of retinal ganglion cells from an *ex vivo* porcine neural retina. The ganglion cells can be seen synapsing with extensions of nerve fiber layer. Scale bar represents 40 µm.

Inner plexiform layer

Inner plexiform layer consists of dendrites from the ganglion cells and axons from the bipolar cells. Its a very fine network of synapses, which were not completely resolved by SDOCM, as can be seen in the optical sections from this layer in Figure 6.9. The fine processes of inner plexiform layer are also not resolved in H&E stained histology section, as shown in Figure 6.3.

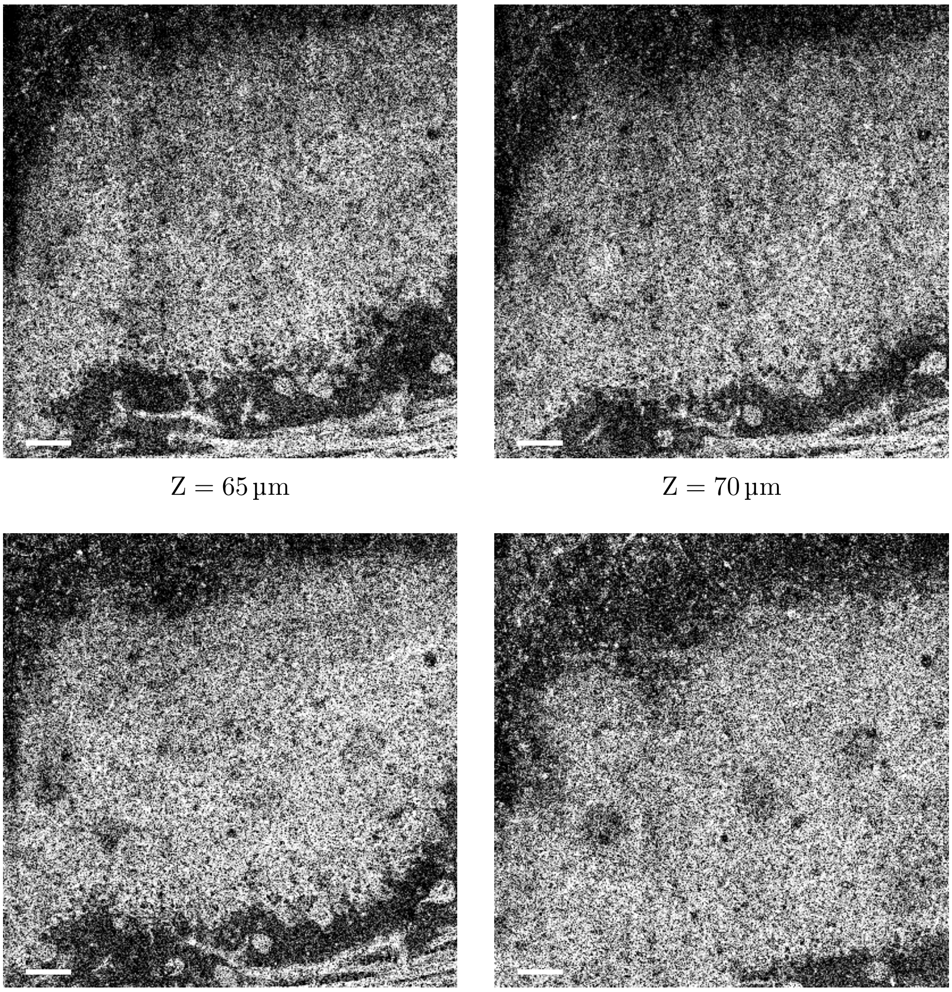

Z = 65 µm

Z = 70 µm

Z = 75 µm

Z = 80 µm

Figure 6.9: *En face* optical sections, 400 µm × 400 µm, of an inner plexiform layer from porcine neural retina. Scale bar represents 40 µm.

Inner nuclear layer

The inner nuclear layer, located just below the inner plexiform layer, consists of nuclei from amacarine and horizontal cells. Cell bodies and their processes are clearly visible in the *en face* optical sections shown in Figure 6.10.

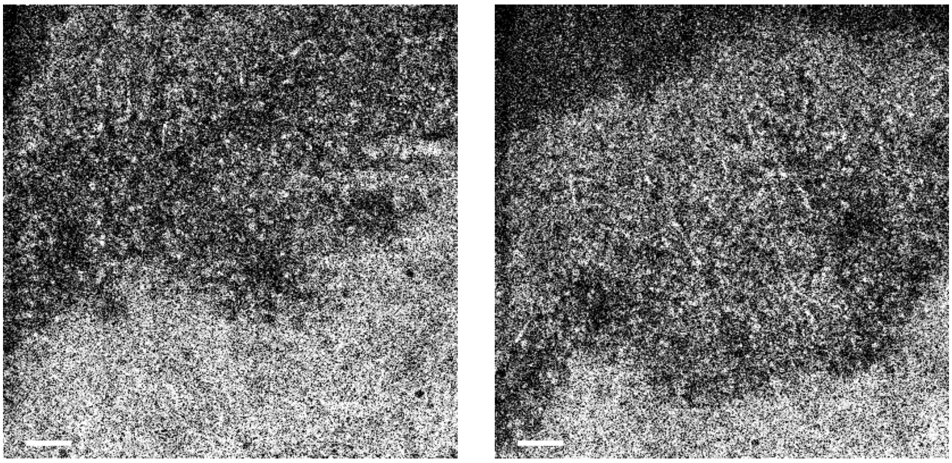

Z = 85 µm

Z = 90 µm

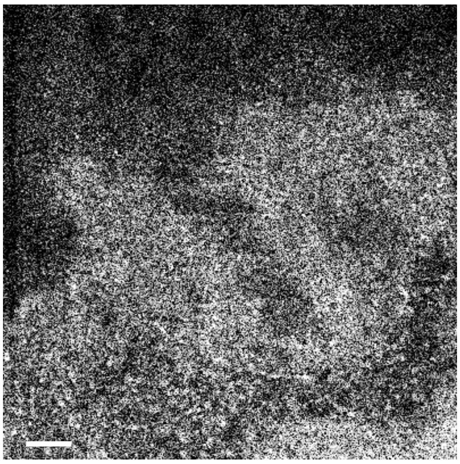

Z = 95 µm

Figure 6.10: *En face* optical sections, 400 µm × 400 µm, from an inner nuclear layer of an ex vivo porcine neural retina. Scale bar represents 40 µm.

Outer plexiform layer

In outer plexiform layer, synaptic body of the rods and cones make connections with the dendrites of amacarine and bipolar cells. These interconnections are not clearly visualized in the SDOCM images as shown in Figure 6.11. The processes from outer plexiform layer are also not visible in H&E stained histology section, as shown in Figure 6.3.

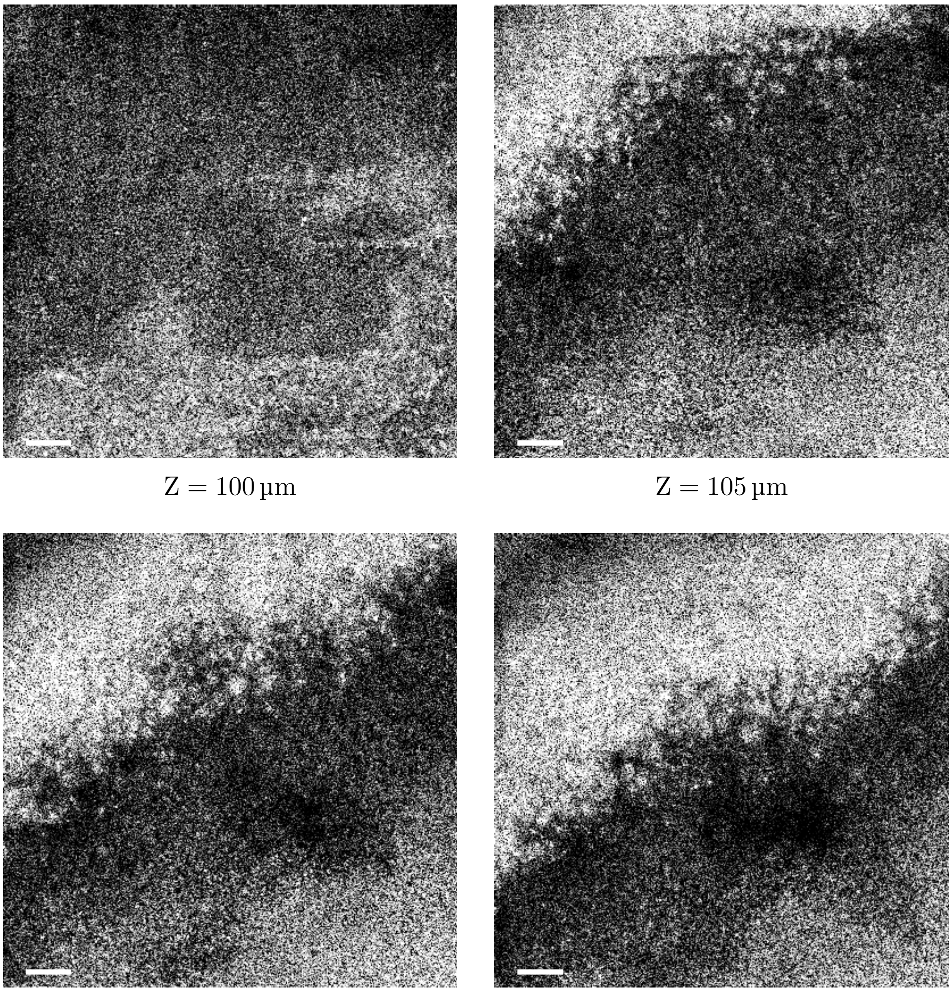

Z = 100 µm

Z = 105 µm

Z = 115 µm

Z = 120 µm

Figure 6.11: *En face* optical sections, 400 µm × 400 µm, of an outer plexiform layer from an *ex vivo* porcine neural retina. Scale bar represents 40 µm.

Outer nuclear layer

The outer nuclear layer of the neural retina consists of rods and cone nuclei. Figure 6.12 shows *en face* optical sections from outer nuclear layer, where cell bodies appear as bright circular spots against the dark background of outer plexiform layer.

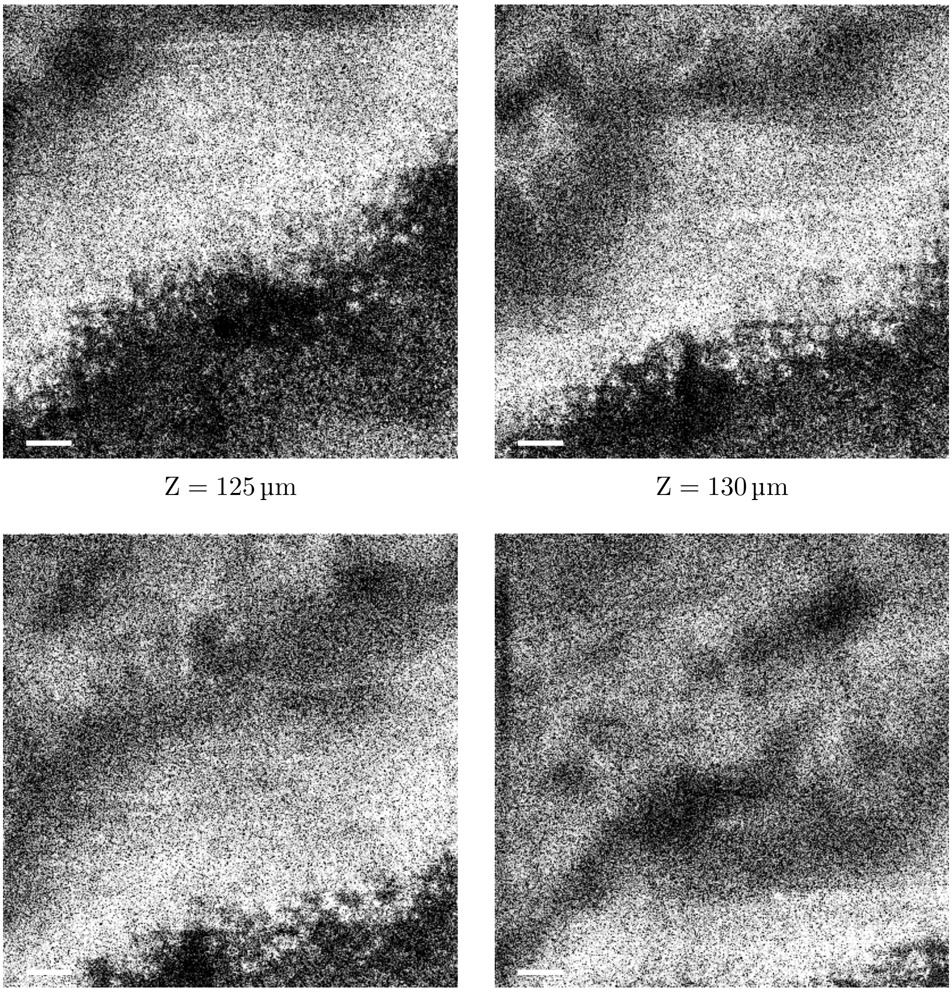

Z = 125 µm

Z = 130 µm

Z = 135 µm

Z = 140 µm

Figure 6.12: *En face* optical sections, 400 µm × 400 µm, of an outer nuclear layer from an *ex vivo* porcine neural retina. Scale bar represents 40 µm.

Photoreceptor layer

The photoreceptor layer consists of rod and cones, and the *en face* optical sections from photoreceptor cell layer are as shown in Figure 6.13. Density of cone cells is relatively lower than rod cells away from the fovea, and in the shown images cone cells appear as dark circular spots, where as rod cells appear as bright circular spots.

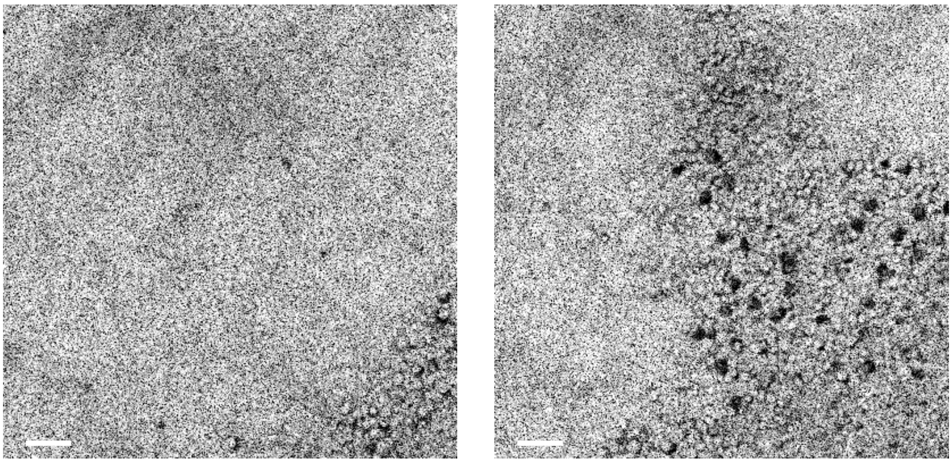

Z = 145 µm　　Z = 150 µm

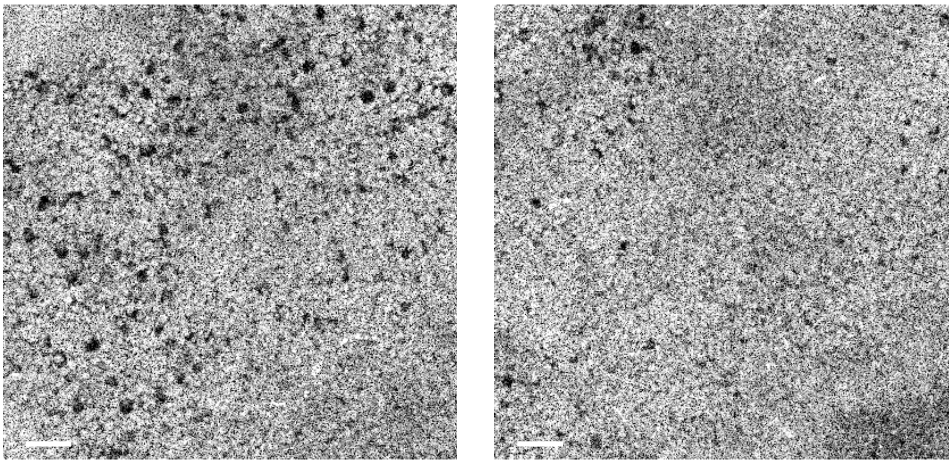

Z = 155 µm　　Z = 160 µm

Figure 6.13: 400 µm × 400 µm, *en face* optical sections of photoreceptors cell layer from an *ex vivo* porcine neural retina. Bright and dark circular spots are rods and cones cells respectively. Scale bar represents 40 µm.

Three dimensional structure of different cell layers from porcine neural retina was reconstructed using the *en face* optical sections obtained at 5 µm steps in depth, and obtained volume is as shown in Figure 6.14.

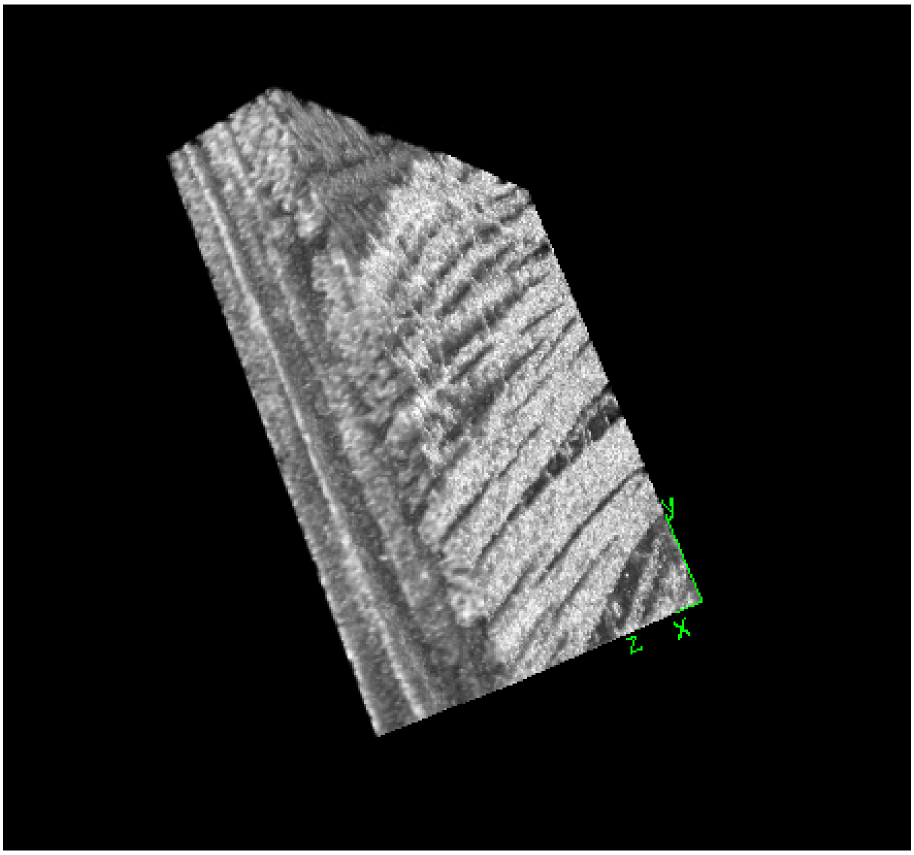

Figure 6.14: (movie) Three dimensional reconstruction of cell layers from porcine neural retina. Spatial dimensions of the volume are 400 µm × 400 µm × 160 µm.

6.5 Summary

The *en face* SDOCM images of cornea presented in this chapter clearly resolve single cells and their nuclei in the epithelium. The fibrous structure in the stroma and the keratocytes are also clearly visible. The *en face* SDOCM images from the neural retina clearly resolve individual ganglion cells, and their synaptic connections to the nerve fiber layer. Two nuclear layers, their respective plexiform layers, and photoreceptor cell layers are also clearly distinguishable. The contrast in OCM images, which helps in visualization of all these structures is generated by minuscule variations in refractive index inside the tissue, which is an intrinsic property of the tissue itself. Therefore OCM does not require any external markers for clear visualization of morphological structures on micron scale.

The morphological details obtained by SDOCM are comparable to the information typically accessible through H&E stained histology sections. Because most of the pathologies in ophthalmology are caused by atypical morphological deterioration, SDOCM can be used for detecting and monitoring sub-micrometer structural changes in eye's anatomy. Cornea is easily accessible for *in vivo* imaging, where as neural retina is behind the lens and vitreous humor, and achieving a cellular resolution is challenging because of ocular aberrations [82]. However, adaptive optics and wavefront shaping have demonstrated the improvement of transverse spatial resolution in retina [83]. The maximum NA or the transverse resolution in retina is limited by the diameter of iris. Considering the focal length of an eye as 18 mm, and maximum iris diameter as 8 mm, maximum NA that can be used for imaging retinal structures is about 0.3, sufficient enough to resolve single cells.

Although OCT is currently being used in ophthalmology for diagnosis and monitoring of various pathologies, results presented above demonstrate that OCM can be even more useful as it provides subcellular morphological details from both anterior and posterior segments of the eye. Furthermore, because of structure-function correlations in anatomy of the eye, subcellular morphological details obtained by SDOCM could potentially advance the diagnostic process, and could even lead to discovery of new pathologies.

Finally, another advantage of SDOCM is the phase contrast, which could potentially provide information about molecular diffusion and blood perfusion in the posterior segment of the eye. Combination of subcellular morphological details with functional contrast could potentially help in early diagnosis of many diseases.

Chapter 7

Quantitative Measurement of Cardiomyocyte Dynamics

7.1 Introduction

Cardiomyocytes are one of the major types of muscle cells that constitute heart. Cardiomyocytes, along with several other cell types, generate electrical impulses and produce coordinated contraction of heart, also known as cardiac cycle. The contractile elements within cardiomyocyte cells are long chains of sarcomeres, known as myofibrils. Contraction is induced by influx of Ca^{2+} ions into the cardiomyocyte cell through voltage sensitive ion channels in T-tubules. Transverse tubules or T-tubules are the specialized structures formed by inward folding of cell membrane into the cytoplasm. T-tubules forms barrier between intracellular and extracellular space, and are the major sites that convert electrical excitation into contraction force [84].

Isolated cardiomyocytes provide a good model for studying contraction mechanisms and various pathologies associated with it. Isolated cardiomyocytes can also be used for testing of pharmaceutical drugs and gene therapies. In this chapter a brief overview of methods used in measurement of cardiomyocyte dynamics are presented. *En face* images and three dimensional structure of cardiomyocyte cells with subcellular morphological details are also presented. Using the phase contrast of SDOCPM, subcellular dynamics of the cardiomyocyte cells were quantitatively measured, and obtained axial displacement profile of subcellular structures are also presented.

7.2 State of The Art

Generally, Cardiomyocyte dynamics are characterized by measuring electrical conductivity through a cell membrane, which is proportional to the force of contraction. Described below are the two widely used in-vitro electrophysiology recording methods.

7.2.1 Intracellular Patch Clamp Recordings

Intracellular patch clamp recordings are considered gold standard as they provide an accurate measurement of membrane potential and/or ionic currents of a single cell. In this technique, saline-filled glass microelectrode is impaled into the intracellular space and electrical activity of a single cell is recorded [85].

Besides being invasive, patch clamp recordings are impractical when simultaneous recording from multiple cells is required. Long-term intracellular recordings are also not possible with patch clamp method, as the intracellular fluid gets diluted with the saline filled in glass microelectrode.

7.2.2 Multisite Field Potential Recording

Multisite field potential recording technique employs a microelectrode array (MEA), which is a microchip with up to 100 or more electrodes. Cardiomyocytes are cultured directly onto the microchip and extracellular potential is recorded from multiple cells simultaneously [86].

The advantages of microelectrode array based recordings are, it provides extracellular recording from a large population of cells, and also makes long-term recordings feasible for up to several weeks.

Although, microelectrode array based recordings are non-invasive, they do require good contact between cell membrane and the electrodes. Another drawback is that, extracellular recordings cannot be performed on multi-layer cell cultures.

7.3 Materials and Methods

The imaging system used for acquiring three dimensional structures of cardiomyocyte cells and its displacement dynamics as functional contrast, is the same spectral domain optical coherence phase microscopy system as described in Chapter 4. In this section, materials and methods that are relevant to measurement of cardiomyocyte dynamics are presented.

7.3.1 Image Acquisition

In order to measure the axial displacement of cardiomyocyte cells accurately, there are two important requirements. First, the axial displacement of the cardiomyocytes should be smaller than the axial resolution of the microscope, so that the cells remain in focus through out the contraction cycle. Second, during the elapsed time between two consecutive A-scans, on same spatial location, total displacement of the cell membrane should be smaller than half of the center wavelength of the light source, so that displacement profile can be obtained by unwrapping the phase without any 2π ambiguity.

Considering the above requirements and the maximum sampling speed of the SDOCPM system, $217,000$ A-Scans/sec, two different image acquisition schemes were developed to accurately reconstruct the axial displacement profile of the cardiomyocyte cells.

Dynamic Functional Recording

In dynamic functional recording, three dimensional structure of the cardiomyocytes and its phase contrast measurements were obtained in three steps.

1. Volumetric stack of *en face* images were obtained at $0.75\,\mu\mathrm{m}$ axial steps in depth with active-low gated triggering. The active-low gated triggering was obtained by programming a software clock to the frequency of

cardiomyocyte beatings, to ensure that *en face* images through depth were acquired only during the resting period of cardiomyocytes, to avoid motion artifacts.

2. An *en face* plane was selected within the recorded volume for phase contrast measurements. *En face* image was composed by recording each B-scan 5000 times, in M-mode, at 630 B-scans/sec, to capture the displacement dynamics associated with cardiomyocytes contraction.
3. Axial displacement profile of the cardiomyocytes was obtained by unwrapping the phase over time from B-scans acquired in step 2, and axial displacement data was registered with acquired volume in step 1 as functional contrast.

Imaging parameters used in dynamic functional recording of spontaneously beating cardiomyocytes are as listen in Table 7.1.

Imaging Parameters	**Value**	**Units**
Effective N.A.	0.45	
Axial resolution	4.7	µm
Transverse resolution	0.7	µm
Image area	250 × 250	µm
No. of pixels	272 × 272	
No. of images in Z-stack	40	
Z-step	0.75	µm
B-scans per second	40	Hz
en face images per second	2.3	Hz

Table 7.1: List of imaging parameters used in the dynamic functional recording of spontaneously beating cardiomyocytes.

High-Speed Functional Volumetric Recording

Another approach to bridge the gap between available and required sampling rate was to decrease the image field, so as to increase the frame rate. With this approach, image acquisition was done in following steps.

1. A stack of *en face* optical sections were acquired at 0.75 µm axial steps in depth, and three dimensional structure of the cardiomyocytes was reconstructed.

2. An *en face* plane was selected within the recorded volume for phase contrast measurements, and with reduced Image field (40 µm × 40 µm), images were acquired at 54 sub-volume/sec.

3. Axial displacement profile of the cardiomyocytes was obtained by unwrapping the phase over time from reduced image field measurements, and registered with the volume acquired in step 1.

Imaging parameters used in dynamic functional recording of spontaneously beating cardiomyocytes are as listed in Table 7.2.

Imaging Parameters	**Value**	**Units**
Effective N.A.	0.8	
Axial resolution	2.1	µm
Transverse resolution	0.6	µm
Image area	128 × 128	µm
No. of pixels	512 × 512	
No. of images in Z-stack	40	
Z-step	0.75	µm
en face images per second	0.7	Hz
High-Speed Functional Volumetric Recording		
Image area	40 × 40	µm
No. of pixels	40 × 40	
en face images per second	54	Hz

Table 7.2: List of imaging parameters used in the high-speed functional volumetric recording of spontaneously beating cardiomyocytes.

7.3.2 Preparation of Cardiomyocytes

For the differentiation of mouse embryonic stem (mES) cells into cardiomyocytes, 129s ES cells were cultured on feeder cells in DMEM medium supplemented with 20 % ES cell fetal bovine serum (FBS) until 80 % confluent as previously described [87]. Cells were trypsinised, resuspended and counted. A defined number of 400 $cells/20\ \mu$l were used in hangingdrops and cultured for 2 days until the embryoid bodies (EBs) were formed. Single EBs were plated separately into each well of a gelatin-coated 24-well plate and cultured for 3+7 days until the cardiomyocytes start beating spontaneously.

The cardiomyocytes were prepared at Kardiovaskuläre Genetik lab of Prof. Jeanette Erdmann, University of Lübeck.

7.4 Results

7.4.1 Microanatomical Images of Cardiomyocytes

A stack of *en face* microanatomical images through a spontaneously beating cardiomyocyte, obtained with SDOCM are as shown in Figure 7.1. Shown images are 250 µm × 250 µm across and were acquired at 1.5 µm axial steps in depth. The cardiomyocytes used for this experiment were part of an embryoid body, which is a multilayer culture of different cell types.

The non-uniform brightness in first four *en face* images is caused by the uneven surface topology of the embryoid body. From the surface of the embryoid body to 6 µm in depth, single cells and their boundaries are clearly visible. These cells belong to the ectoderm layer of the embryoid body. Optical sections from depth 7.5 to 10.5 µm are from the middle of the cell bodies from top most cell layer. From 12 to 21 µm in depth, supportive structures from the mesoderm layer are visible. These network of supportive structures coordinate the synchronized beating of the cardiomyocytes. Further below in depth, from 24 to 28.5 µm, relatively larger network of supportive structures can be seen.

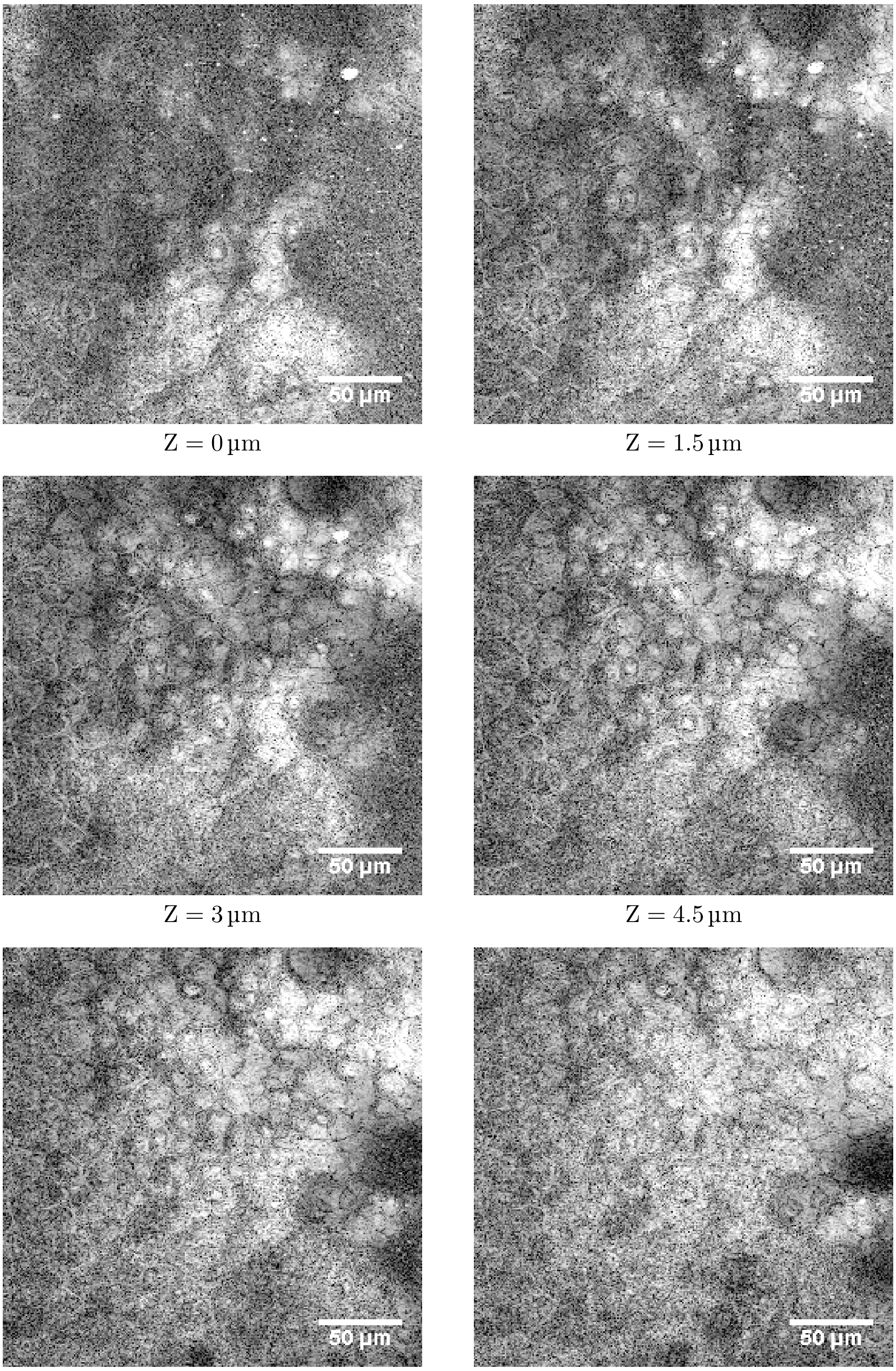

Z = 0 µm

Z = 1.5 µm

Z = 3 µm

Z = 4.5 µm

Z = 6 µm

Z = 7.5 µm

Figure 7.1: Stack of *en face* images (250 µm × 250 µm) at 1.5 µm axial steps, through a spontaneously beating cardiomyocyte. From depths of 0 to 6 µm, morphology of single cells are clearly visible on the top most layer of the embryoid body.

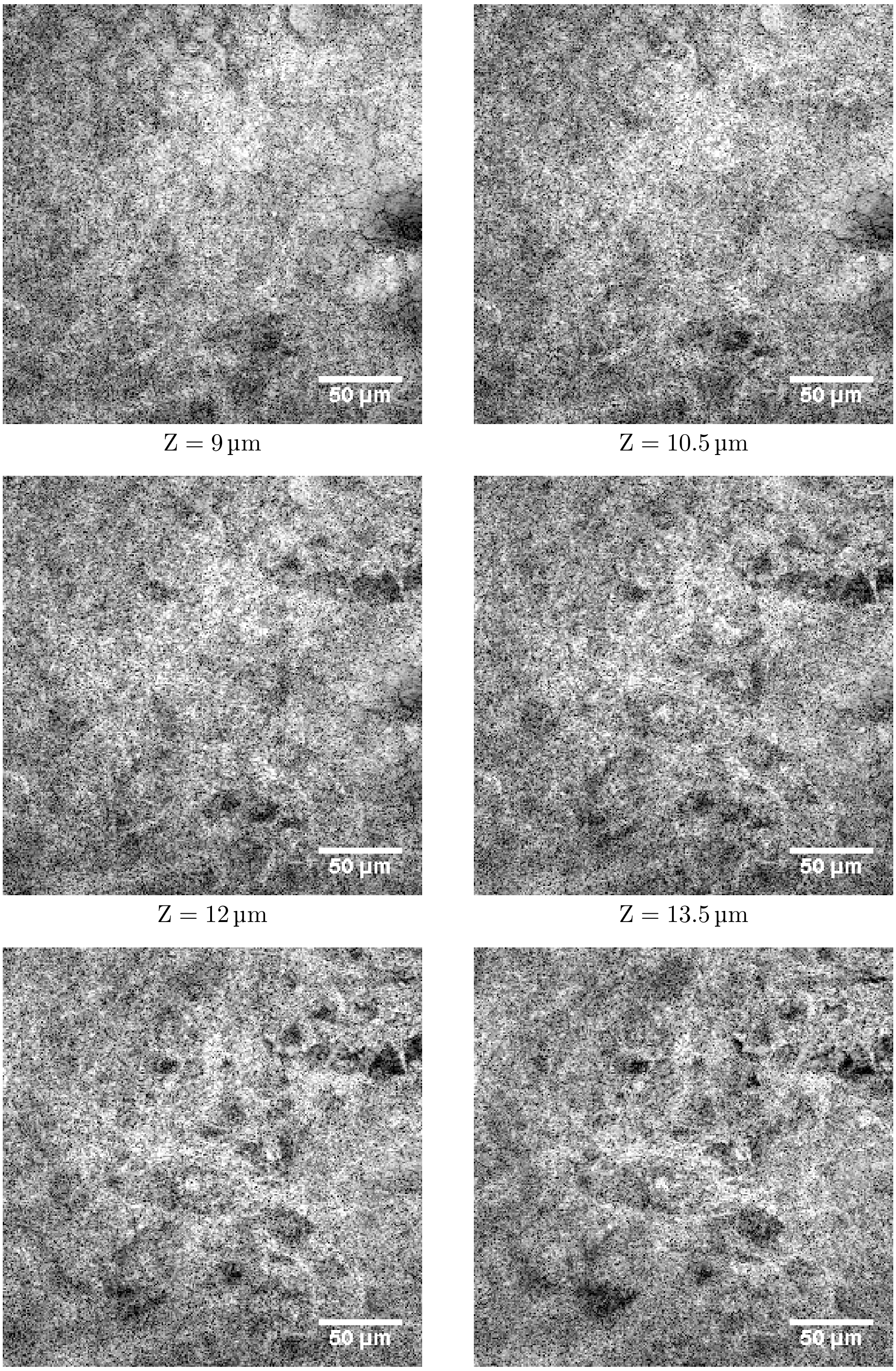

Z = 9 µm

Z = 10.5 µm

Z = 12 µm

Z = 13.5 µm

Z = 15 µm

Z = 16.5 µm

Figure 7.1: (continued) *en face* images at depths of 9 to 16.5 µm from the top surface of the embryoid body, where the fine processes and interconnections between the cells are clearly visible.

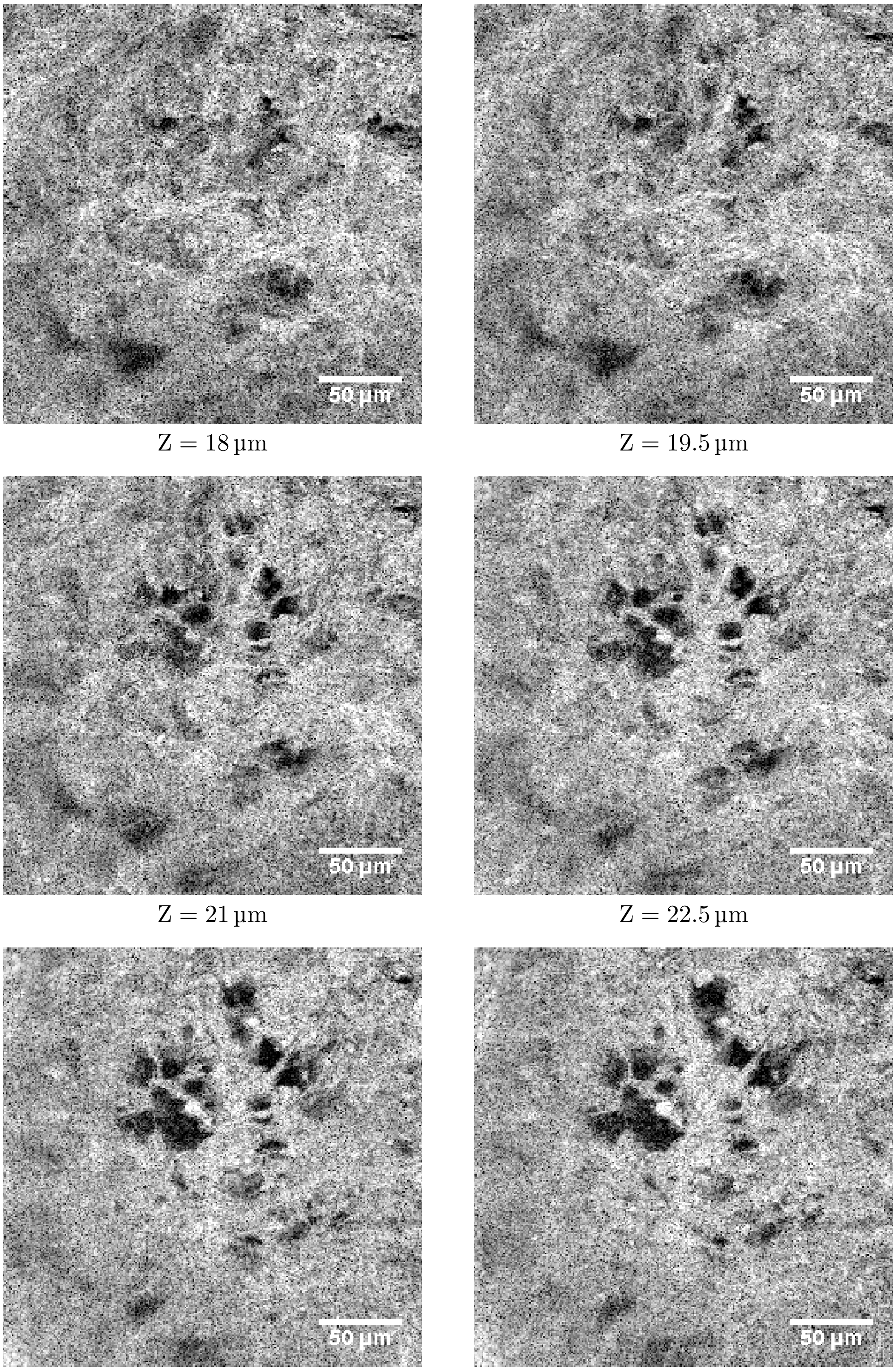

Z = 18 µm

Z = 19.5 µm

Z = 21 µm

Z = 22.5 µm

Z = 24 µm

Z = 25.5 µm

Figure 7.1: (continued) *en face* images at depths of 18 to 25.5 µm from the top surface of the embryoid body, where relatively larger extracellular matrix which provides the structural support to the embryoid body is can be seen.

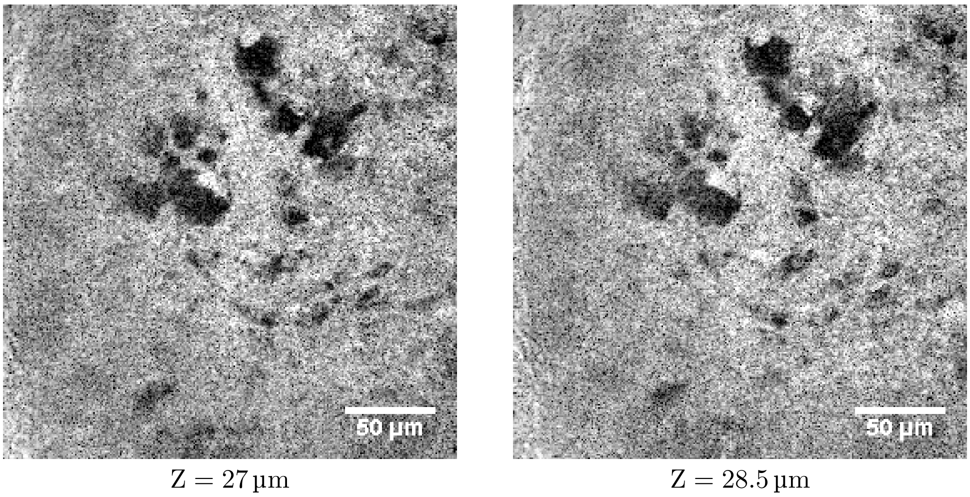

Z = 27 µm Z = 28.5 µm

Figure 7.1: (continued) *en face* images through a spontaneously beating cardiomyocytes.

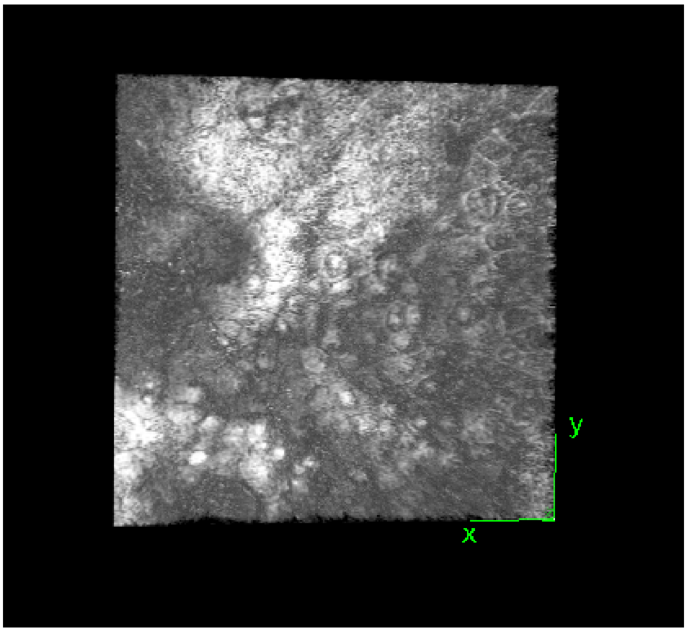

Figure 7.2: (movie) Three dimensional reconstruction of cardiomyocyte cells in the embryoid body. This 3D volume encompasses two primary germ layers of the embryoid body, i.e., ectoderm near the origin and mesoderm there after. Spatial dimensions of the volume are 250 µm × 250 µm × 30 µm.

Three dimensional structure of the embryoid body with cardiomyocytes was reconstructed by stacking the *en face* images, and obtained volume is as shown in Figure 7.2. Physical dimension of the reconstructed volume are 250 µm × 250 µm × 30 µm.

From the volume in Figure 7.2, an *en face* image plane was selected, shown in Figure 7.3, for dynamic functional recording of cardiomyocyte beatings. Selected image plane was scanned by acquiring each B-scan 350 times at 40 Hz. Therefore, by recording each B-scan over time, cardiomyocyte beatings are not synchronized through out the image field. synchronization was not possible because the cardiomyocytes were spontaneously beating with slight variation in beating frequency over time.

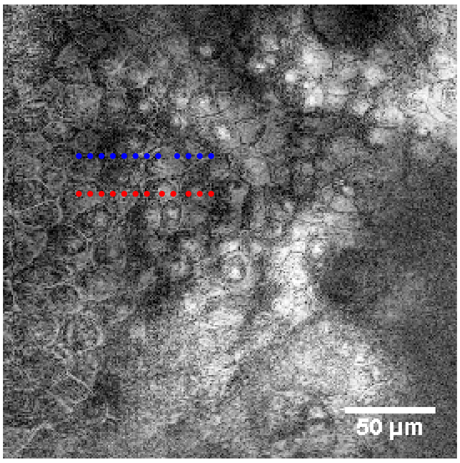

Figure 7.3: Selected *en face* optical section from the volume shown in Figure 7.2 for dynamic functional recording. Dotted lines represent spatial locations for which functional data, i.e., axial displacement over time is displayed in Figure 7.4.

7.4.2 Axial Displacement of Subcellular Structures

Axial displacement at each pixel position of image shown in Figure 7.3 was calculated by taking the phase angle of complex SDOCPM images. The phase values were unwrapped over time and then scaled into optical pathlength. Time-series of axial displacement on spatial locations marked with red and blue dots in Figure 7.3 are as shown in Figure 7.4. Shown axial displacements are caused by the spontaneous contraction of cardiomyocyte cells in the embryoid body. Arbitrary offset was added to all of the axial displacement profiles for efficient display, as the relative change in axial displacement indicates the strength of contraction at each pixel location.

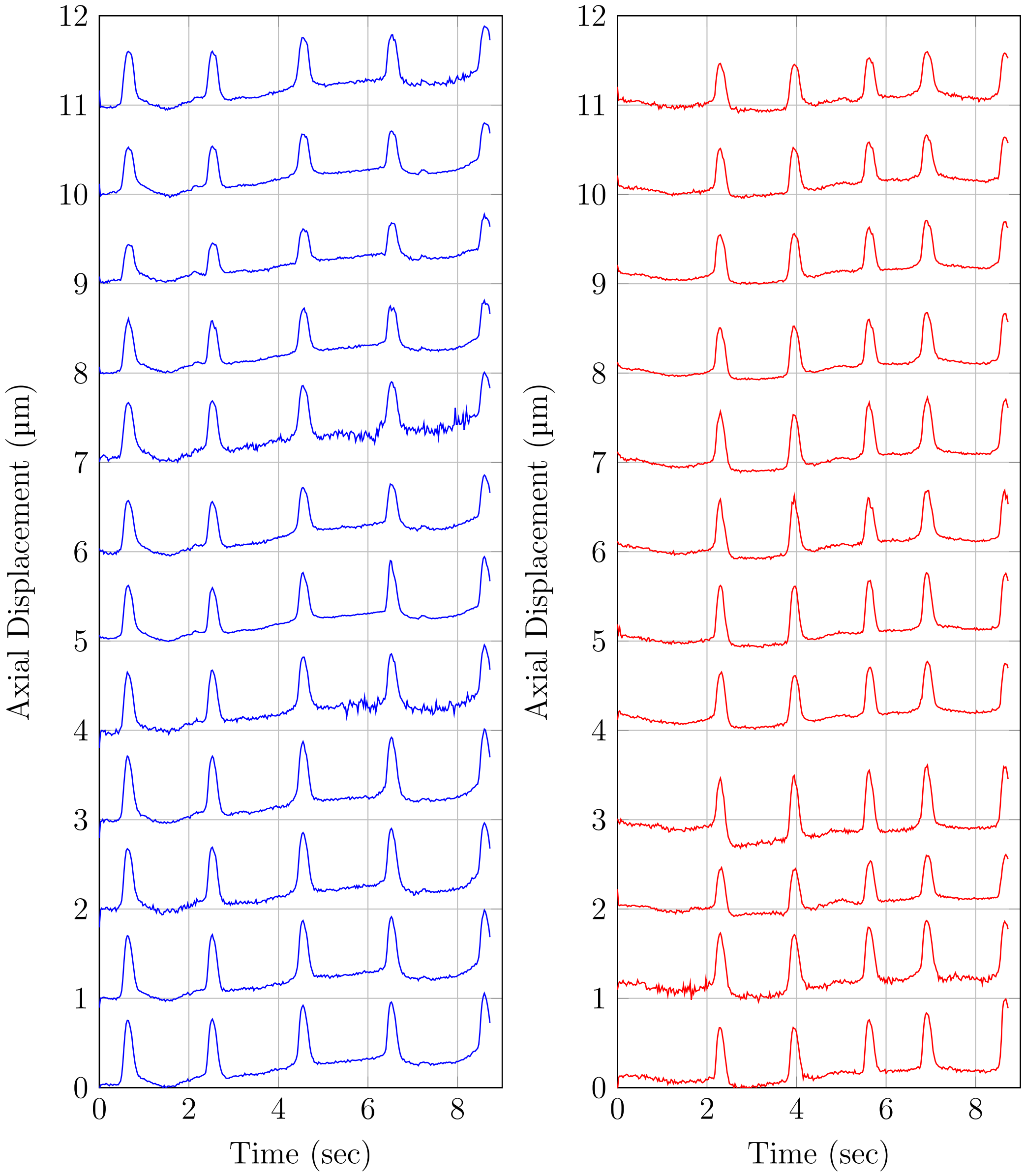

Figure 7.4: Axial displacement of cardiomyocytes cell membrane at spatial locations marked with blue and red dots in Figure 7.3. Axial displacement of the subcellular structures was on average (0.600 ± 0.008) µm. Arbitrary offset was added to all time-series, so as to accommodate them all in one axis.

Amplitude and profile of axial displacements on spatial locations across a single cell surface are slightly different. This reflects the distribution of biomass and contractile fibers that are at the heart of spontaneous beatings in cardiomyocytes [88]. The axial displacement of subcellular structures was 0.6 µm on average, and beating frequency was approximately 1 Hz.

Axial Displacement Measurement Error

Phase sensitivity of the SDOCPM system, which determines the noise floor for axial displacement measurements is 0.0027 radians, which translates to an optical pathlength of 0.11 nanometers, as described in Chapter 5. Measurement error in recorded axial displacement is can be estimated by taking the standard deviation of measured displacement values during the resting period of cardiomyocytes. For the displacement profiles shown in Figure 7.4, measurement error is 0.008 µm or 8 nanometers. It is important to note that the phase sensitivity or displacement uncertainty depends on signal-to-noise ratio (SNR), so pixels with high SNR provide the most accurate displacement profile. Therefore, measured axial displacement of subcellular structures in cardiomyocytes associated with contraction force is (0.600 ± 0.008) µm.

High-Speed Functional Volumetric Recording

Results obtained by employing the second image acquisition technique, where image field was reduced to increase the *en face* frame rate up to 58 per second, are presented in this section. Cardiomyocytes used in this experiment were also spontaneously beating and part of an embryoid body. *En face* optical sections (128 µm × 128 µm) at 1.5 µm axial steps from the surface of the embryoid body are as shown in Figure 7.5. Optical sections from the surface of the embryoid body to 9 µm in depth represent ectoderm part of the embryoid body. Optical sections from depth of 10.5 to 28.540 µm represent mesoderm layer of the embryoid body, where single cells along with fine extracellular structures are clearly visible.

For this particular dataset, transverse resolution of the SDOCPM system was 0.5 µm and therefore, fine structures connecting different cells from depths of 15 µm and below are on the order of 0.5 µm thick, demonstrating the optical sectioning capability of SDOCM.

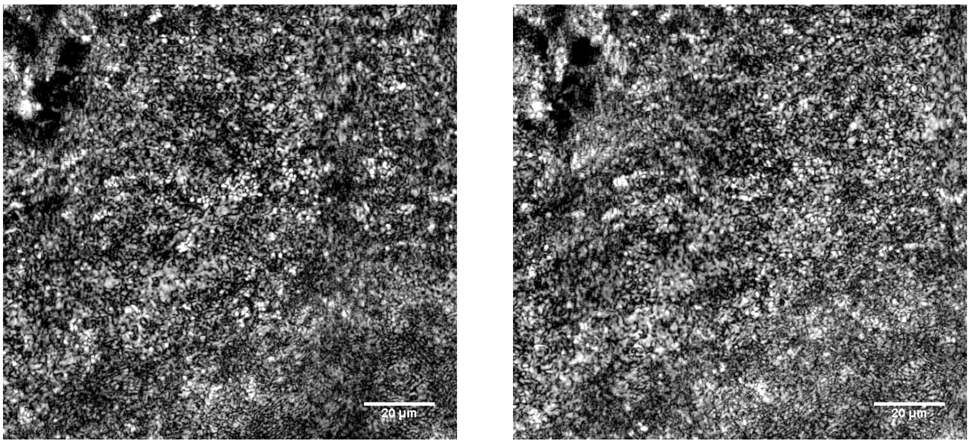

Z = 0 µm　　Z = 1.5 µm

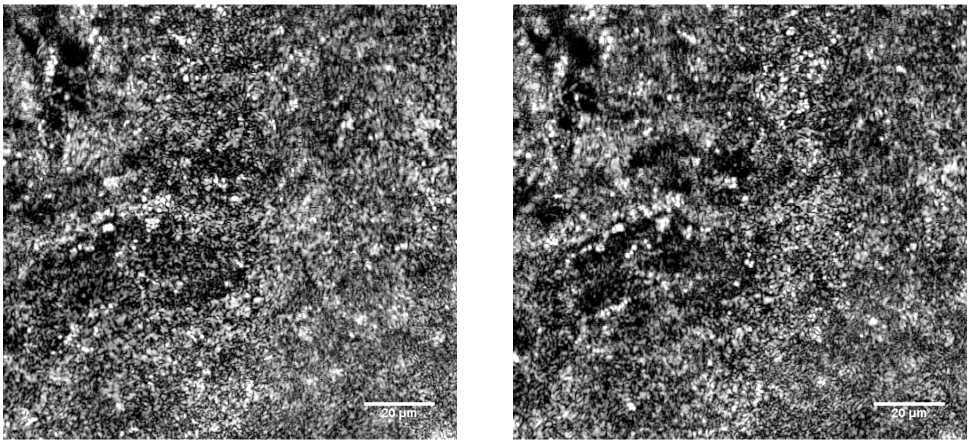

Z = 3 µm　　Z = 4.5 µm

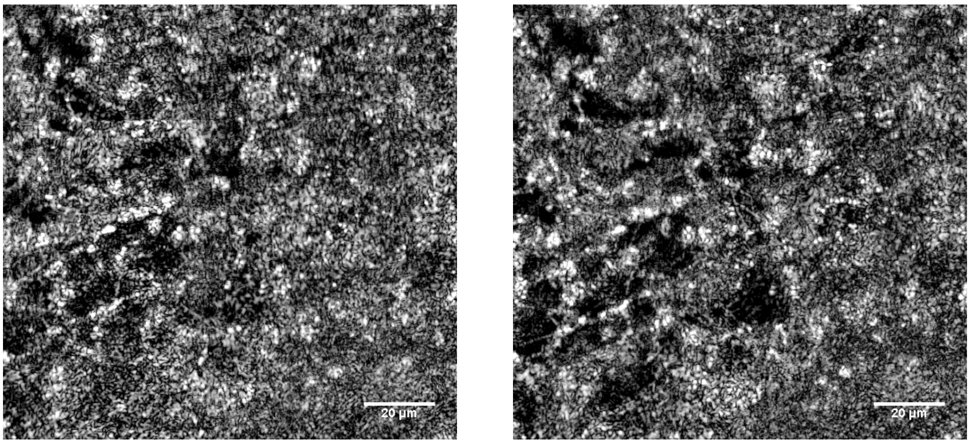

Z = 6 µm　　Z = 7.5 µm

Figure 7.4: Stack of *en face* images (128×128 μm) at 1.5 μm axial steps, through a spontaneously beating cardiomyocyte.

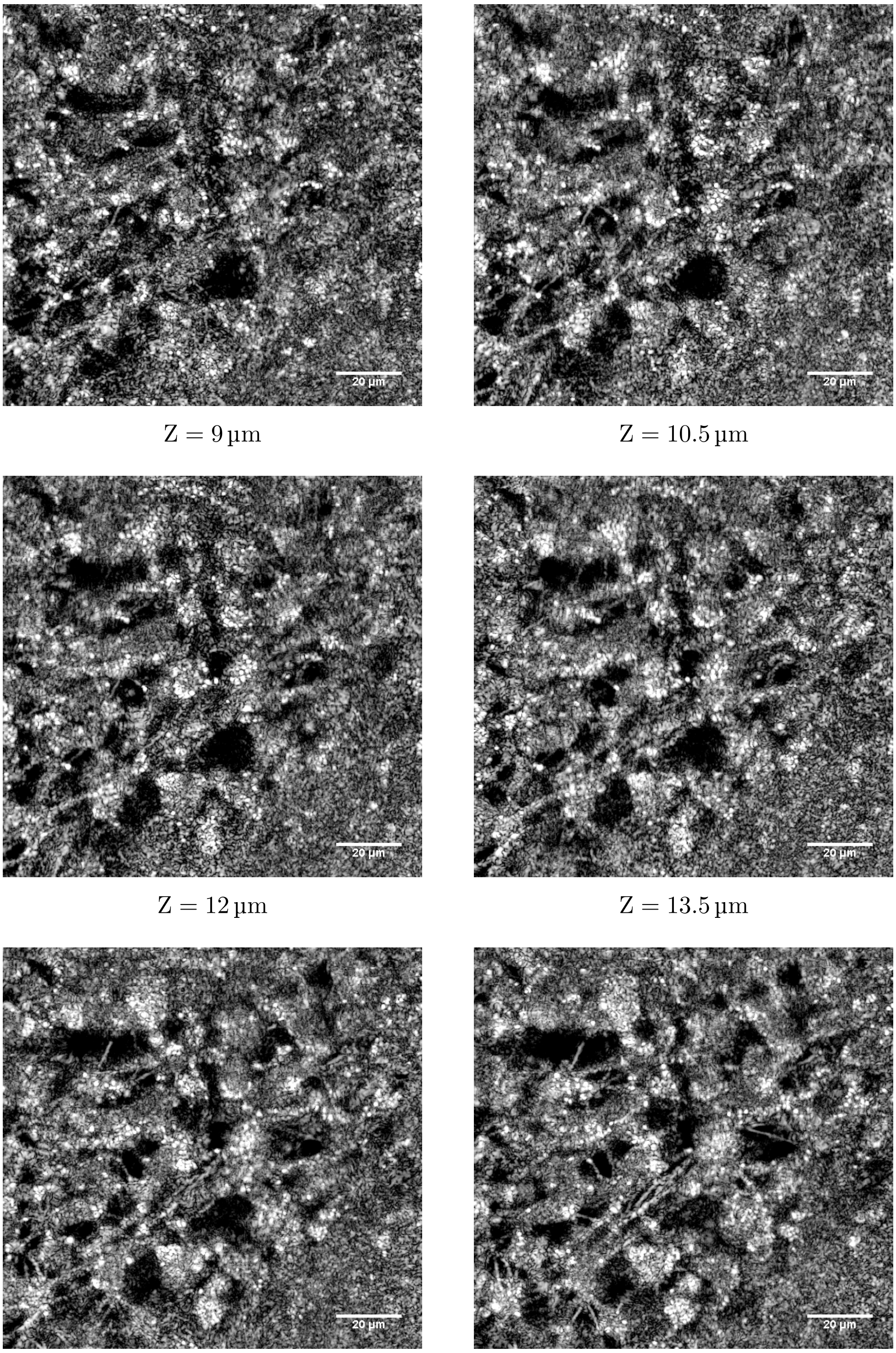

Z = 9 µm

Z = 10.5 µm

Z = 12 µm

Z = 13.5 µm

Z = 15 µm

Z = 16.5 µm

Figure 7.4: (continued) stack of *en face* images (128×128 μm) at depths of 9 to 16.5 μm from the top surface of the embryoid body.

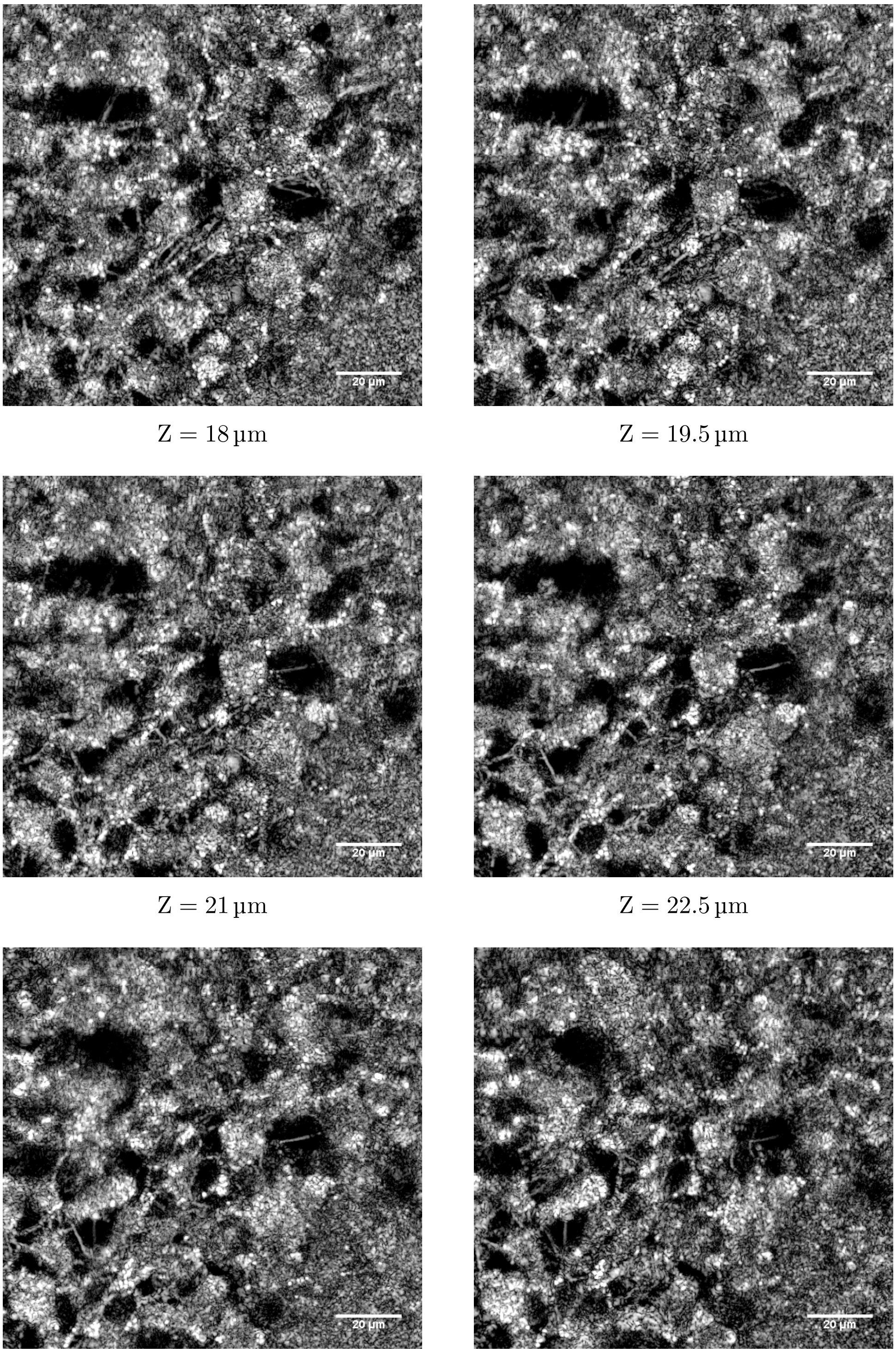

Z = 18 µm

Z = 19.5 µm

Z = 21 µm

Z = 22.5 µm

Z = 24 µm

Z = 25.5 µm

Figure 7.4: (continued) stack of *en face* images (128 × 128 μm) at depths of 18 to 25.5 μm from the top surface of the embryoid body.

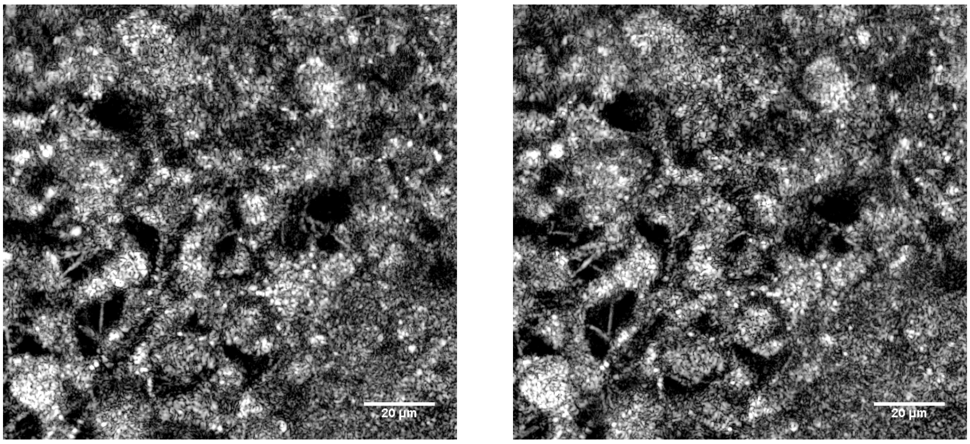

Z = 27 µm

Z = 28.5 µm

Figure 7.5: (continued) stack of *en face* images (128 µm × 128 µm) in 1.5 µm axial steps, through a spontaneously beating cardiomyocyte. Scale bar represents 20 µm.

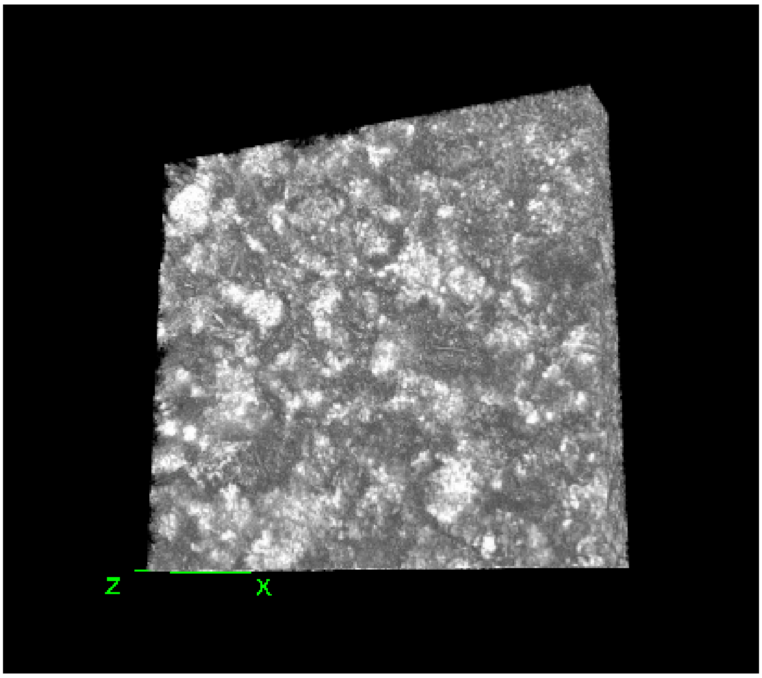

Figure 7.6: (movie) Three dimensional reconstruction of cardiomyocyte cells in the embryoid body. This 3D volume encompasses two primary germ layers of the embryoid body, i.e., ectoderm near the origin and mesoderm there after. Spatial dimensions of the volume are 128 µm × 128 µm × 30 µm.

Three dimensional volume reconstructed from the *en face* optical sections is as shown in Figure 7.6. Size of the volume is 128 µm × 128 µm × 30 µm.

Selected *en face* plane from the volume for reduced image field and high-speed acquisition is as shown in Figure 7.7. Area inside the red box, 40 µm × 40 µm, was scanned at 54 Hz to acquire the axial displacement profile of cardiomyocytes. Axial displacement of subcellular structures at spatial locations marked by red dots are plotted in Figure 7.8.

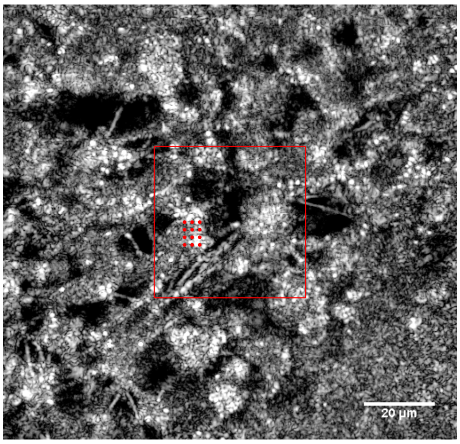

Figure 7.7: Selected *en face* optical section from the volume shown in Figure 7.6 for reduced image field functional recording. Area inside the red box, 40 µm × 40 µm, was scanned at 54 Hz to acquire the axial displacement profile of cardiomyocytes, as shown in Figure 7.8.

Axial displacement profile of the cellular structures within 40 µm × 40 µm optical section was obtained by unwrapping the phase of complex SDOCM images over time. The axial displacement profiles are as shown in Figure 7.8. Measured axial displacement of cardiomyocytes was 0.1 µm on average, and beating frequency was approximately 1 Hz. The variation in displacement amplitudes at different spatial locations, as can be seen in Figure 7.8, is caused by the variation in bio-mass of surrounding structures.

Axial Displacement Measurement Error

Axial displacement measurement error is estimated by taking the standard deviation of displacement values during the resting period of cardiomyocytes. For 40 µm × 40 µm volumetric recording at 54 Hz, the axial displacement measurement error is about 0.0067 µm or 6.7 nanometers.

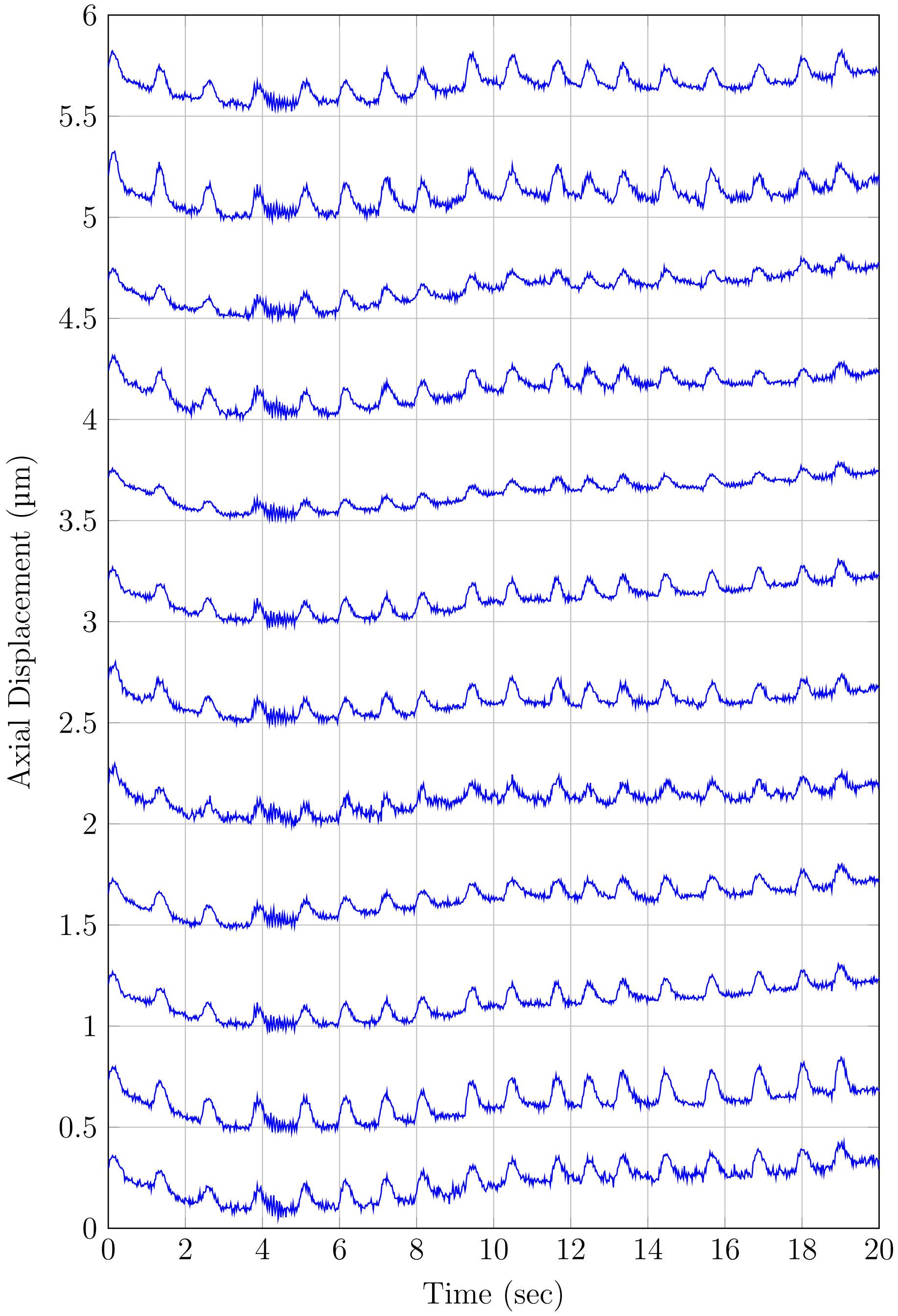

Figure 7.8: Axial displacement of subcellular structures on spatial locations marked by red dots, in Figure 7.7. Arbitrary offset was added to all of the time-series, so as to accommodate them all in one axis.

7.4.3 4D Display of Beating Cardiomyocytes

Three dimensional morphological data of beating cardiomyocytes along with a phase contrast that quantitatively measures the nano-scale axial displacements, was acquired using the implemented SDOCPM system. The 4D data was acquired at 54 sub-volume/sec and is displayed in Figure 7.9. The dimensions of the display are 40 µm × 40 µm × 50 µm over a period of one second which covers one contraction cycle of the cardiomyocytes.

The phase contrast is scaled into axial displacement in µm, whose range is represented by the shown colorbar. The contraction of cardiomyocyte cells are evident in both the amplitude and phase data. However, the propagation of contraction wave through the cellular structures is better visualized in the phase data. Furthermore, from the phase data it is evident that, there are certain spatial locations within the network of cells that have relatively higher dynamic activity before the contraction cycle begins. These spatial locations could very well be the transverse tubules of the cardiomyocyte cells, which are the sites that initiate influx of ions into the cell body [84], a prerequisite for contraction.

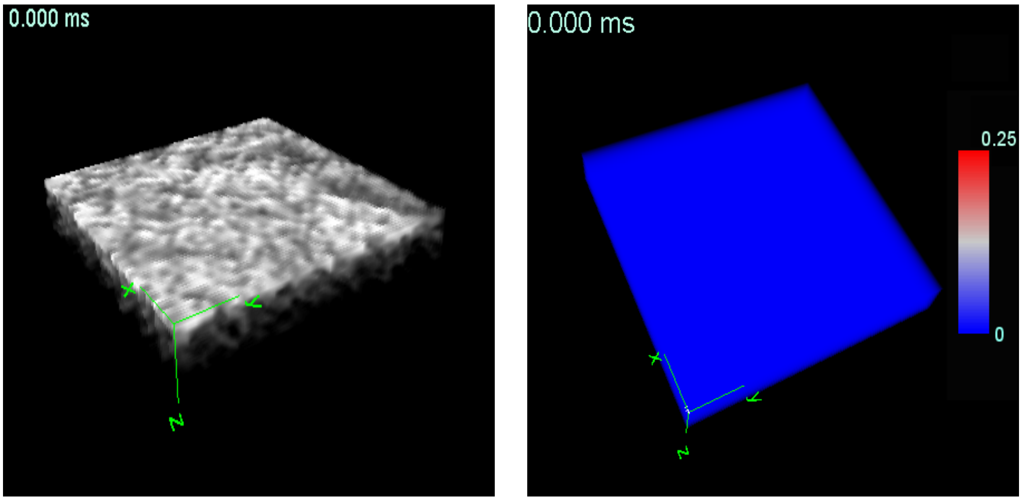

(a) (b)

Figure 7.9: (movie) 4D display of beating cardiomyocytes obtained by recording three dimensional sub-volumes (40 µm × 40 µm × 50 µm) at 54 sub-volume/second. 3D morphological structure (left) and the phase contrast sensitive to nano-scale axial displacement (right), over a period of one second, which includes one complete contraction cycle of cardiomyocyte cells. The scale bar for phase data represents axial displacement in µm.

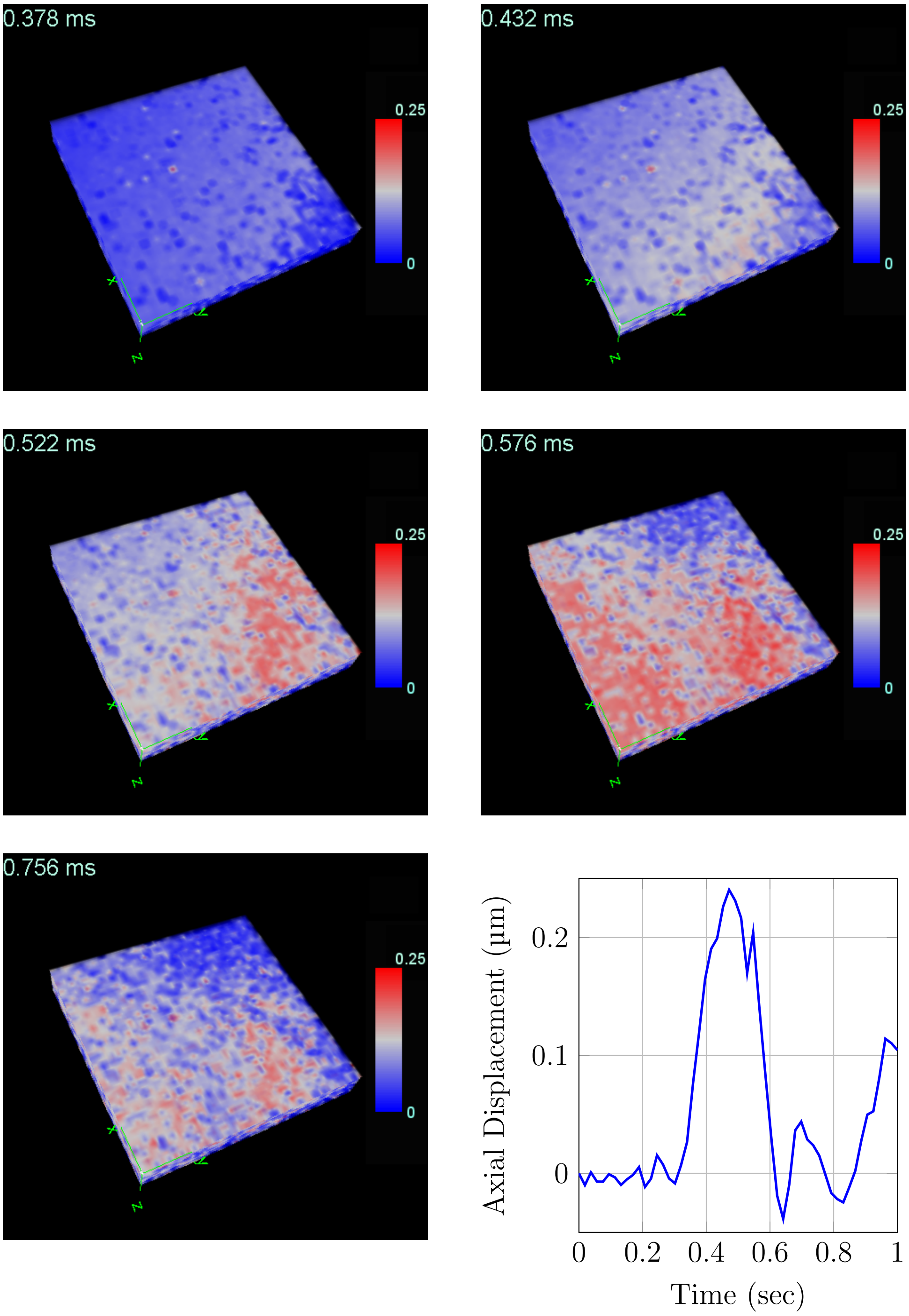

Figure 7.10: Volumetric (40 µm × 40 µm × 50 µm) phase data of beating cardiomyocytes at different time points during the contraction cycle. The progression of the contraction wave across the cellular surface over time can be clearly visualized. The colorbar in the shown images and the line plot at bottom right represents axial displacement of the cell membrane on µm scale.

Figure 7.10 shows the volumetric phase data of the spontaneously beating cardiomyocytes at different time points during the contraction cycle. The progression of contraction wave across the cellular surface over time can be clearly visualized. The line plot in Figure 7.10 shows the displacement profile of the cell membrane during the contraction cycle.

Therefore, three dimensional structural data combined with a quantitative phase contrast, at subcellular level, enables the visualization of morphology and how it engenders physiological processes. Functional imaging of physiological processes at subcellular level is important for better understanding of the function of biological tissues, and its various pathologies associated with morphological changes.

Although, the implemented SDOCPM system has a maximum sampling speed of $217,000$ A-scans/sec, the lateral field of view in the shown 4D display is limited because of high settling time of galvanometer scanners, used for raster scanning. Resonant or acousto-optics based scanners are more suitable for high-speed scanning and can increase the lateral field of view for a given A-scan sampling rate.

7.5 Summary

The *en face* images of cardiomyocytes at different depths and three dimensional reconstructions of the embryoid body presented in this chapter, demonstrate that SDOCM can resolve subcellular details with high contrast. The speckle noise is minimized because of point illumination and detection scheme, which restricts the generation of speckles. Without the presence of speckle noise, fine morphological structures such as interconnections between individual cells can be clearly visualized. In addition, phase contrast of SDOCPM allows for quantitative measurement of cellular dynamics over time, with sub-nanometer axial displacement sensitivity. The 4D display of the spontaneously beating cardiomyocyte cells enables visualization of contraction dynamics and its propagation through the subcellular structures.

In comparison with the state of the art techniques such as patch-clamp recordings and multisite field potential recordings, SDOCPM provides three significant advantages. First, the phase contrast of SDOCPM measures the dynamic properties of subcellular structures with sub-nanometer accuracy. Second, SDOCPM enables simultaneous electrophysiological recordings from a wide area that covers hundreds of cells. Third, SDOCPM is a non-invasive imaging technique which could be used for long-term studies of cardiomyocyte dynamics, without damaging the cellular integrity.

In conclusion, microanatomical images of the cardiomyocytes along with axial displacement of subcellular structures, associated with contraction dynamics are quantitatively measured with sub-nanometer accuracy. This demonstrates the unique capability of SDOCPM to combine high spatial resolution microscopy with a physiological contrast that is highly sensitive to minuscule changes in the refractive index of each voxel. Therefore, SDOCPM can be used to study both the microanatomical and physiological dynamics of tissue at cellular level.

Quantitative measurement of cellular dynamics using SDOCPM, can be used to characterize the propagation and modulation of contraction dynamics in cardiomyocytes, in relation to controlled variables such as temperature, calcium concentration, etc. Therefore, SDOCPM can be a very useful tool for electrophysiological studies that can facilitate both basic research and drug discovery for various cardiomyopathies.

Chapter 8

Quantitative Measurement of Ciliary Dynamics in Tracheal Epithelium

8.1 Introduction

Epithelium that lines the inner respiratory tract of all vertebrates plays an important role in expelling out the foreign particles, pathogens, and bacteria that are inhaled during regular breathing [89]. The sticky mucus secreted by goblet cells is layered on top of the tracheal epithelium and traps the foreign particles. The motile cilia of epithelium pushes the mucus out of the lungs by synchronous beating. The beating of cilia, which are microscopic organelles projecting from cell body, is vital for removal of pathogens or bacteria, which otherwise could cause infection or other diseases.

Besides pumping mucus out of the lungs, recent discoveries have revealed that cilia expresses sensory receptors [90], that play important roles in signal transduction pathways and maintains cellular homeostasis [91]. Ciliary dysfunction and its effects on developmental diseases is an active area of research, and some of the pathologies associated with ciliary dysfunction include respiratory infections, anosmia, and blindness, among others [92]. Therefore, an imaging technique that can provide anatomical and functional assessment of cilia is important for both our understanding of their function and the role its dysfunction plays in various pathologies.

In this chapter, anatomy of trachea is briefly described, and then microanatomical images of mouse trachea and quantitative assessment of its ciliary beating frequency, obtained with SDOCPM are presented. It is also demonstrated that the phase contrast of SDOCPM could be utilized to measure the magnitude and direction of the synchronized ciliary strokes.

8.2 Anatomy of Trachea

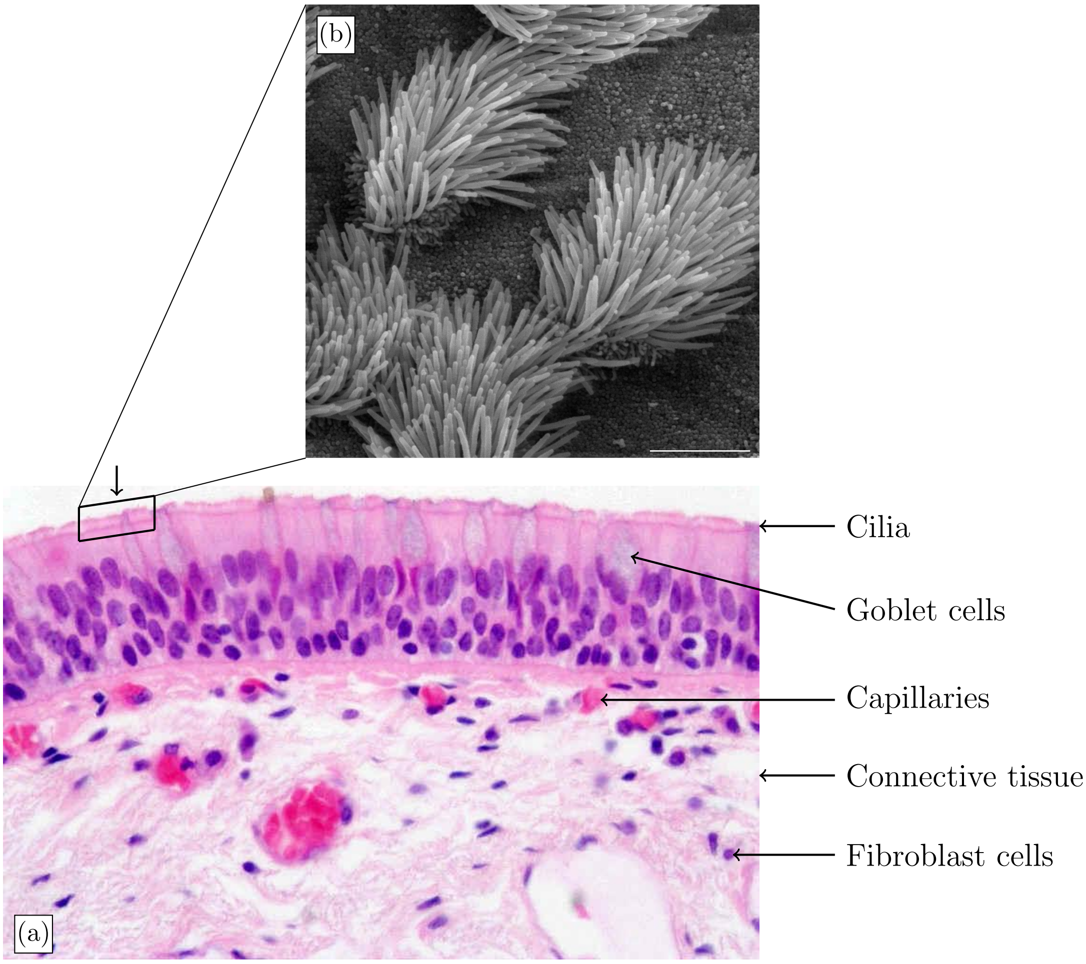

Figure 8.1: (a) H&E stained histology of trachea cross-section [77]. (b) Scanning electron microscope image of ciliated cells. scale bar represents 5 µm [93].

The trachea is a long cylindrical airway tube that connects lungs with the larynx and pharynx. Among many other functions, trachea conducts air to the lungs, warms and moisturizes the inhaled air, and protects the body from foreign bacteria. A H&E stained histological cross-section of the trachea is as shown in Figure 8.1. The trachea is lined with single layer of ciliated epithelial cells arranged in pseudostratified manner. Cilia are the hair like microscopic organelles that project from the cell bodies and induce a unidirectional flow with their synchronized beatings. The morphology of the cilia can be clearly visualized from a scanning electron microscope image shown in Figure 8.1(b). The goblet cells, which secrete mucus, are interspersed among the ciliated epithelial cells. Beneath the epithelial cell layer are basal cells, which can differentiate into other cells as part of a recovery mechanism.

The connective tissue extends from beneath the basal cell layer to the rest of the trachea thickness, which supports the cylindrical structure of the trachea. Blood circulation in the capillaries, interspersed in connective tissue, helps warm and moisten the inhaled air.

8.3 Materials and Methods

8.3.1 Preparation of Mouse Trachea

The mice were terminated via inhalation of isoflurane, trachea was extracted and placed in a Environmental Culture Dish (model # 956, CROMAPHOR Analysen-Technik GmbH, Ascheberg), which was connected to a temperature controlled Culture Dish System (model # Delta T5, Bioptechs Inc., PA, USA). The culture dish was lined with Sylgard Polymer 184 Curing Agent Silicone Elastomer (Dow Corning GmbH, Wiesbaden) and filled with HEPES (4-(2-hydroxyethyl)-1-piperazineethanesulfonic acid) buffered Ringer, whose contents are: 5.6 mM KCl; 136.4 mM NaCl; 1 mM MgCl2 x 6 H2O; 2.2 mM CaCl 2x2 H2O; 11 mM Glucose; 10 mM HEPES; pH 7.4.

After washing with the HEPES Ringer, the trachea was cut longitudinally and flattened in the culture dish with insect pins ($0.15\,\mathrm{mm} \times 12\,\mathrm{mm}$). The temperature of bathed trachea was maintained at $30 - 35°\mathrm{C}$ during the experiment. The controlled environment of the culture dish and the medium simulate normal physiological conditions to maintain the coordinated beatings of cilia, and preserve the morphology of mouse trachea for up to 5 hours.

8.3.2 Image Acquisition

The objective of the experiment was to characterize both morphological structures and functional dynamics of the tracheal epithelium using SDOCPM. While the acquisition speed is not critical for imaging morphological structures, accurate recording of the ciliary dynamics however requires faster image acquisition speeds. Therefore images of two sizes 128 µm × 128 µm and 30 µm × 30 µm were acquired at the speed of 1 and 108 sub-volume/second, respectively. The phase images obtained with high-speed recordings were processed to obtain functional contrast for ciliary dynamics. The optical setup used for trachea measurements is as described in Chapter 4, which has 217, 000 A-Scans/sec as the maximum sampling speed. The imaging protocol used to combine the morphological structures with functional contrast is as described below.

High-Speed Functional Volumetric Recording

One approach to bridge the gap between available and required sampling rate was to reduce the image field, to increase the frame rate. With this approach, image acquisition was done in following steps.

1. A stack of *en face* optical sections (128 µm × 128 µm) were acquired at 0.75 µm axial steps in depth, and three dimensional structure of the mouse trachea was reconstructed.
2. An *en face* plane was selected within the recorded volume for high-speed phase contrast measurements, and with reduced field (30 µm × 30 µm) images were acquired at 108 sub-volume/sec to fully capture the ciliary dynamics.
3. The phase images obtained with high-speed recording in step 2 were unwrapped over time, and was used to calculate the frequency of cilia beatings. Unwrapped phase was also use to calculate phase gradient maps to estimate the amplitude and direction of the synchronized ciliary strokes.

4. Functional contrast computed in step 3 was registered with the microanatomical images obtained in step 1.

The list of imaging parameters used for anatomical and functional assessment of mouse trachea are as shown in Table 8.1.

Imaging Parameters	**Value**	**Units**
Effective N.A.	0.8	
Axial resolution	2.1	µm
Transverse resolution	0.6	µm
Image area	128 × 128	µm
No. of pixels	512 × 512	
No. of images in Z-stack	50	
Z-step	0.75	µm
en face images per second	≈ 1	Hz
High-Speed Functional Volumetric Recording		
Image area	30 × 30	µm
No. of pixels	30 × 30	
en face images per second	108	Hz

Table 8.1: List of imaging parameters used in the recording of microanatomical images of mouse trachea and its ciliary dynamics with high speed volumetric recording.

8.4 Results

8.4.1 Microanatomical Images of Mouse Trachea

The *en face* optical sections of mouse trachea at 1.5 µm steps in depth, obtained by SDOCM are as shown in Figure 8.2. The images cover an area of 128 µm × 128 µm, and were acquired at 1 frame/sec. The Z value represents depth position of *en face* image in the trachea, with Z = 0 µm at the ciliated surface of the trachea. Generally, a thin layer of mucus is formed on top of the epithelium that lines inside of the trachea. However experiments were conducted on a section of trachea that is closer to lungs, and there was no mucus layer on top of the epithelium.

During the acquisition of microanatomical images, cilia of the tracheal epithelium was beating at mean frequency of 16 Hz. The synchronized beating of cilia had induced a flow stream in the culture dish carrying cell debris and other dust particles with it. Because of cilia beatings, images from Z = 0 to 6 µm appear blurred, and since the integration time of SDOCM images was significantly larger than the time period of cilia beatings, movement of individual cilium have left trails in the acquired images. In principle, it is possible to significantly slow down or stop the beating of cilia by reducing the culture dish temperature to below 10° C. However, main goal of the experiment was to characterize the dynamic properties of ciliary dynamics. The goblet cells of the epithelium which are responsible for mucus secretion can also be visualized by noticeable absence of cilia on their cell body.

Between the depths of 6 to 10.5 µm, the pseudostratified cell layer of the epithelium is can be seen. Below the epithelial cell layer, fine connective tissue that functions as scaffolding can also be clearly visualized. Further below, collagen fibers of the connective tissue get relatively larger. Between depths of 34.5 and 41.5 µm, fibroblast cells of the connective tissue are also clearly resolved. Fibroblast cells, marked with red arrows, are the specialized cell that produce the extracellular matrix that structurally supports the trachea.

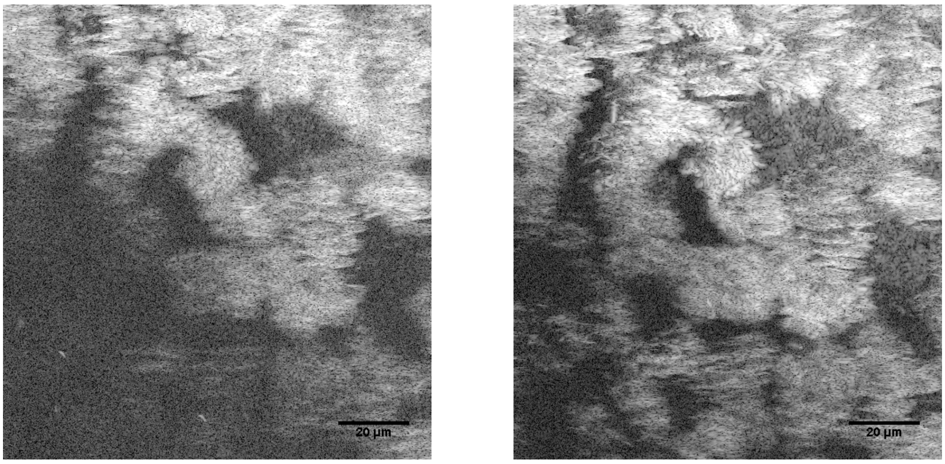

Z = 0 µm Z = 1.5 µm

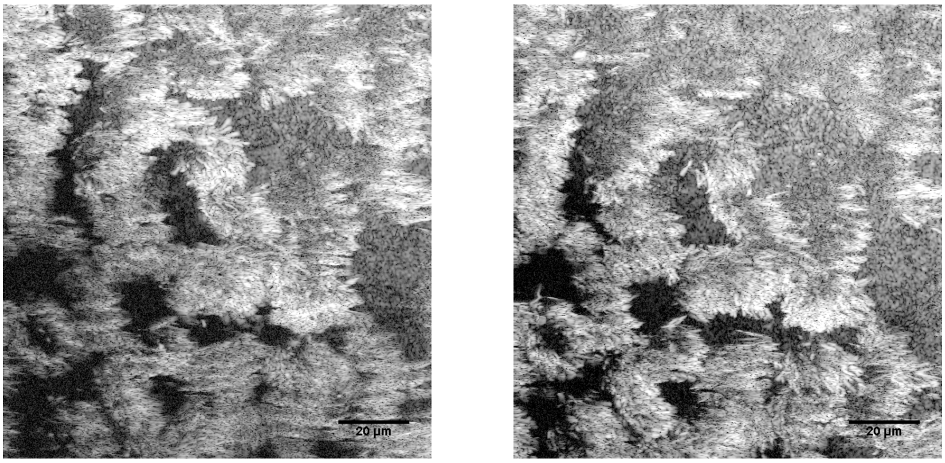

Z = 3 µm Z = 4.5 µm

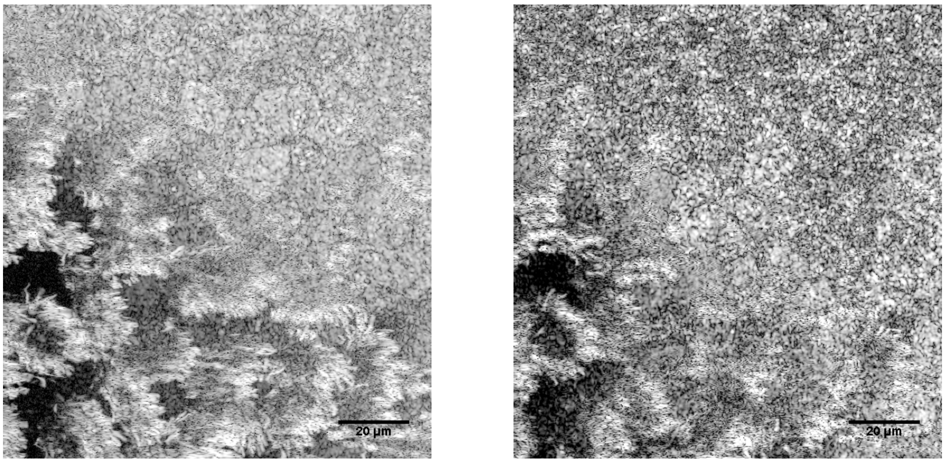

Z = 6 µm Z = 7.5 µm

Figure 8.2: Stack of *en face* SDOCM images (128 µm × 128 µm) at 1.5 µm axial steps through an *ex vivo* mouse trachea. The cilia of the epithelium appear blurred as they were beating in coordination at mean frequency of 16 Hz. Scale bar represents 20 µm.

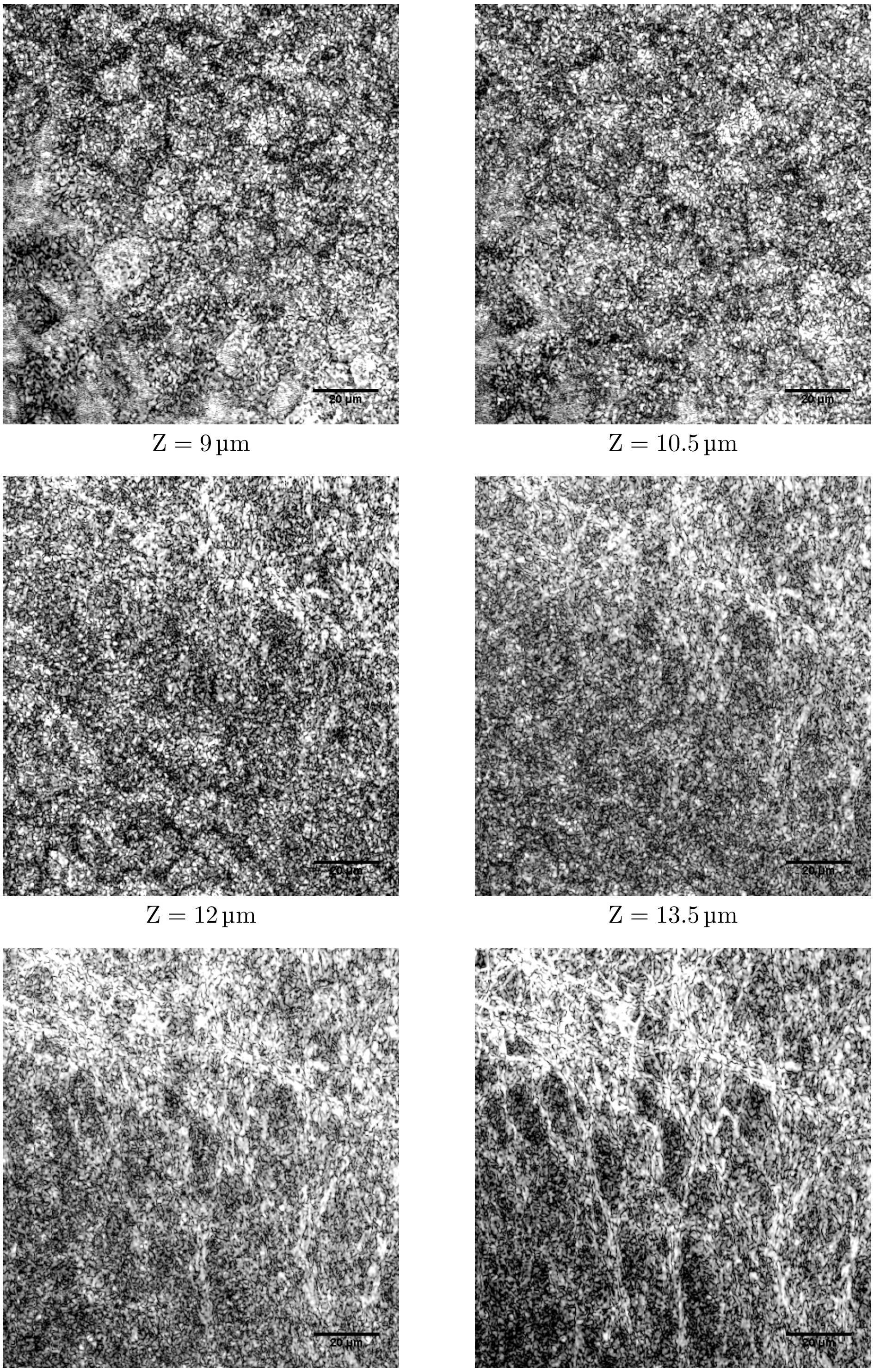

Z = 9 µm

Z = 10.5 µm

Z = 12 µm

Z = 13.5 µm

Z = 15 µm

Z = 16.5 µm

Figure 8.2: (continued) at depth of 9 µm below the cilia surface, cell bodies of the tracheal epithelium can be clearly visualized. Further in depth, fine connective tissue made up of collagen fiber is can be seen. Scale bar represents 20 µm.

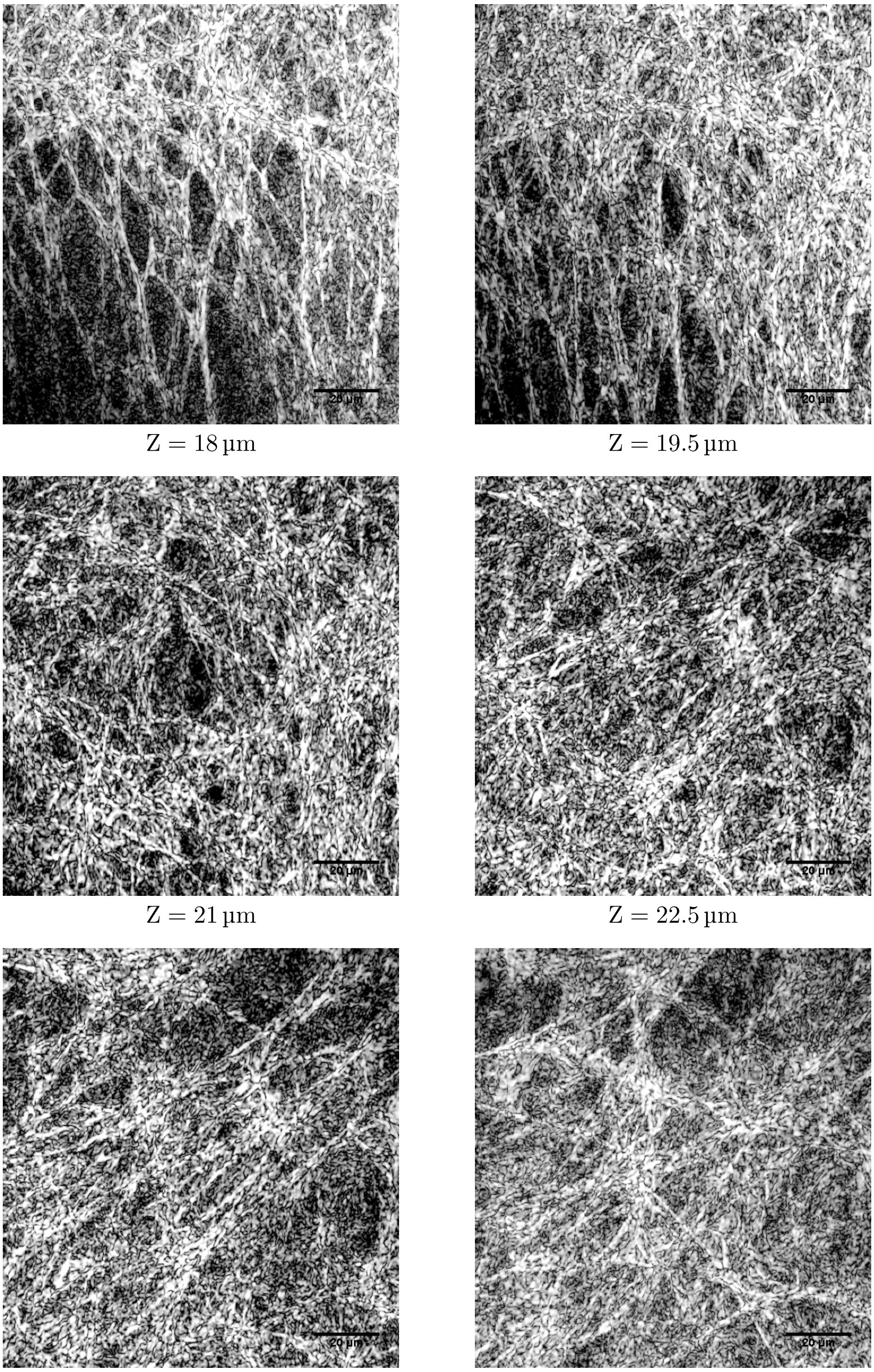

Z = 18 µm Z = 19.5 µm

Z = 21 µm Z = 22.5 µm

Z = 24 µm Z = 25.5 µm

Figure 8.2: (continued) *en face* images between the depths of 18 to 25.5 µm, where the connective tissue which structurally supports the trachea can be visualized. Scale bar represents 20 µm.

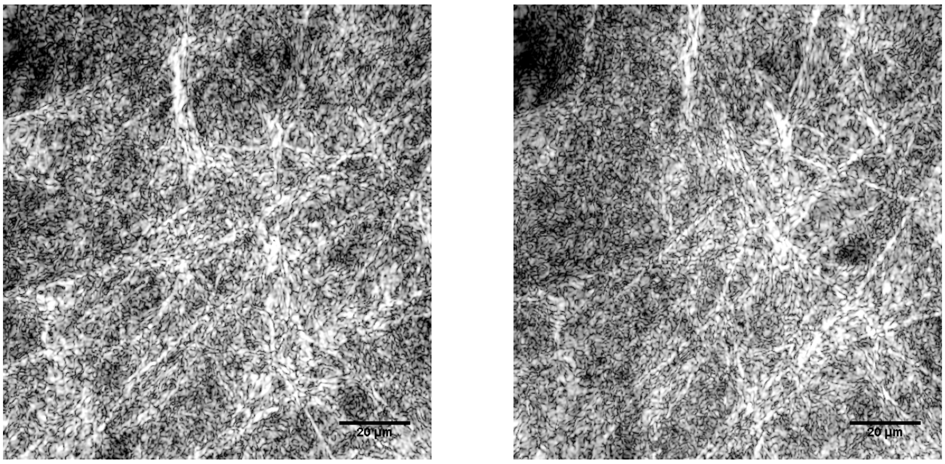

Z = 27 µm Z = 29.5 µm

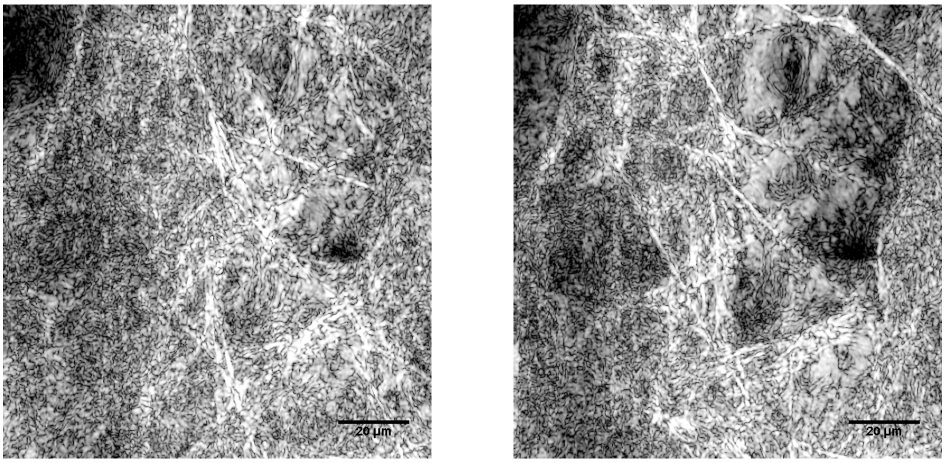

Z = 31 µm Z = 32.5 µm

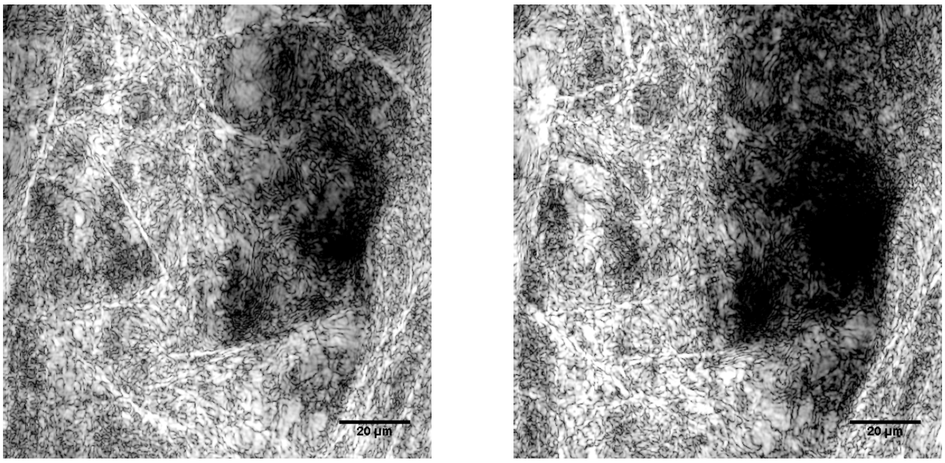

Z = 34 µm Z = 35.5 µm

Figure 8.2: (continued) *en face* images between the depths of 27 to 35.5 µm, where the collagen fibers of connective tissue are relatively larger. Fibroblast cells can also be visualized. Scale bar represents 20 µm.

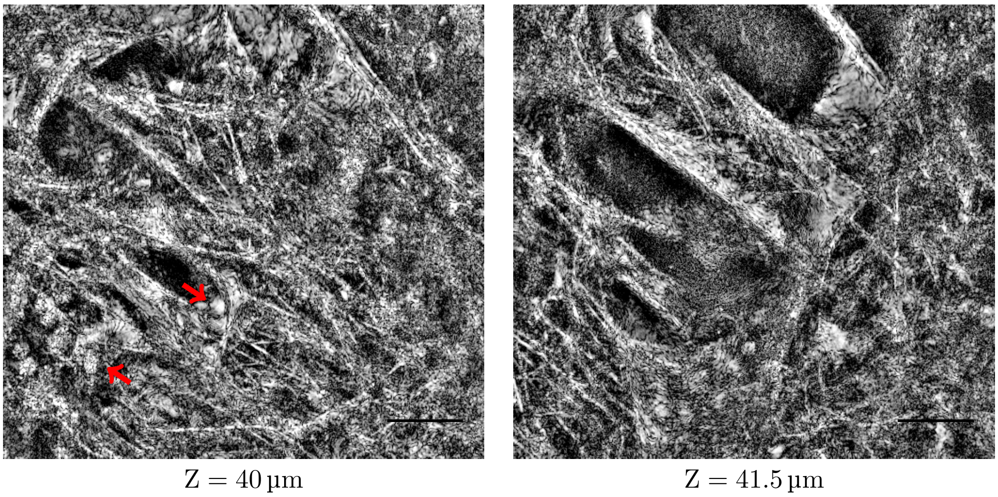
Z = 40 µm

Z = 41.5 µm

Figure 8.2: (continued) stack of *en face* SDOCM images (128 µm × 128 µm) at 1.5 µm axial steps through an *ex vivo* mouse trachea. Fibroblast cells are marked with red arrows, and scale bar represents 20 µm.

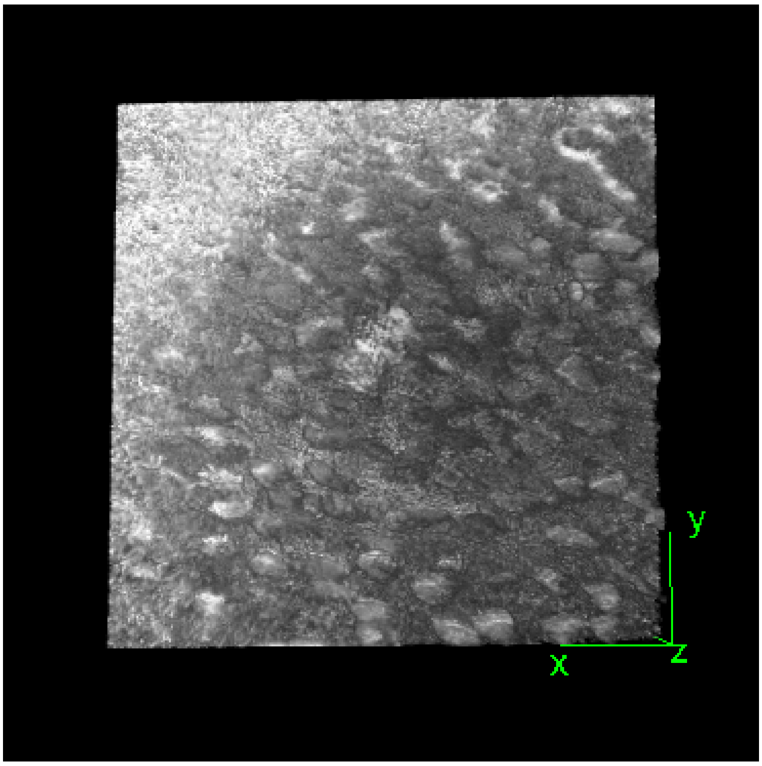

Figure 8.3: (movie) Three dimensional reconstruction of mouse trachea. Spatial dimensions of the volume are 128 µm × 128 µm × 40 µm.

By stacking the *en face* optical sections acquired at 0.75 µm steps in depth, a three dimensional microanatomical structure of the trachea was reconstructed, as shown in Figure 8.3. The dimensions of the reconstructed volume are 128 µm × 128 µm × 40 µm. The Z dimension of the volume was enlarged by linear interpolation, so that morphological structures can be clearly visualized.

8.4.2 Comparison Between Widefield Microscopy and SDOCM

The implemented SDOCPM system has an integrated widefield microscope that can acquire images up to 400 frames/second. For comparison between widefield and SDOCM, series of *en face* images at 0.75 µm steps in depth were acquired, as shown in Figure 8.4. Images show the connective tissue of mouse tracheae below the epithelium, where blood capillaries can be seen. The single blood cells within the capillaries are also clearly visualized in both wiedfield and SDOCM images. However, the fine structure of collagen fibers are only visible in SDOCM images. This demonstrates the optical sectioning capability of SDOCM, where an image is formed by collecting minimally scattered photons from the focal plane. Widefield microscope lacks optical sectioning capability and images are formed by the transillumination of the complete trachea wall, resulting in blurred images with reduced contrast.

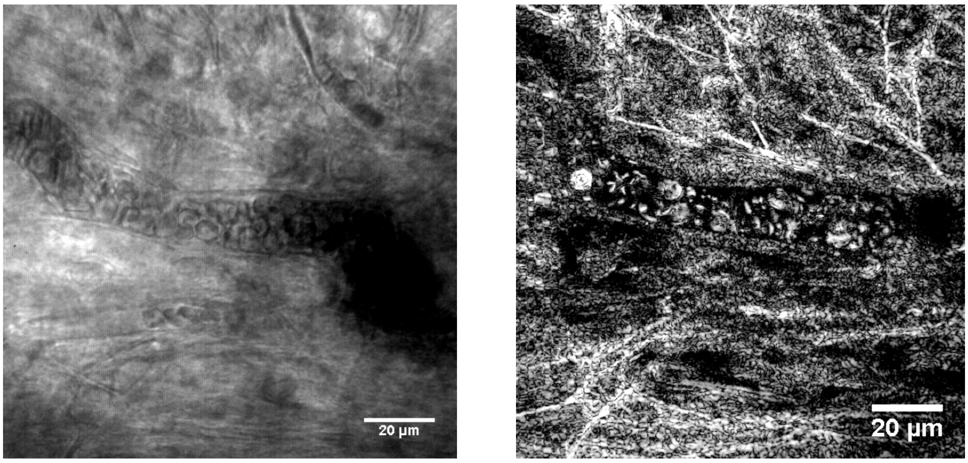

(a) Widefield images

(b) SDOCM images

Z = 36 µm

Z = 36 µm

Figure 8.4: *En face* images of connective tissue along with capillaries inside the mouse trachea, obtained with widefield microscope (a) and SDOCM (b). Images are 128 µm × 128 µm, and Z represents depth inside the trachea from the surface of ciliated cells. Scale bar represents 20 µm.

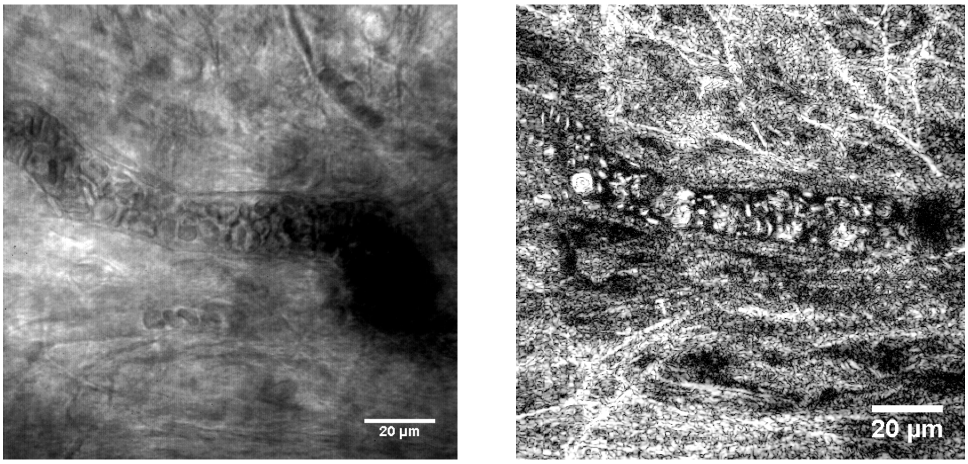

Z = 36.75 µm Z = 36.75 µm

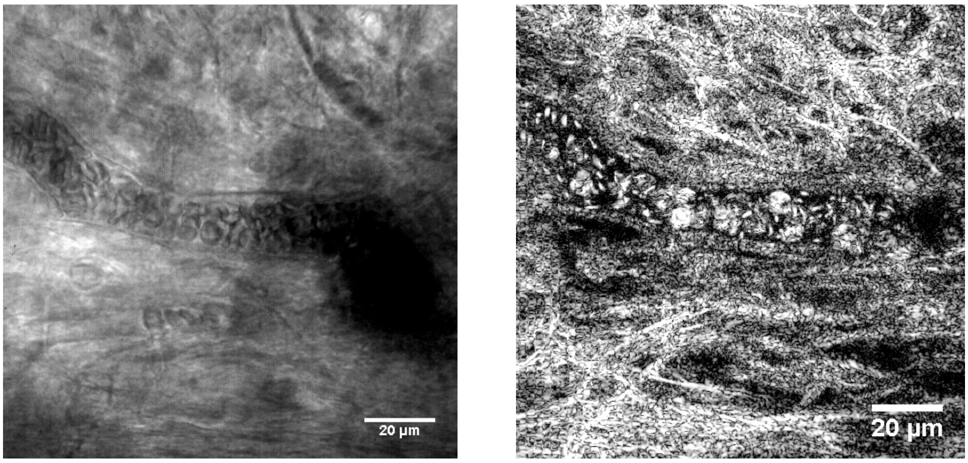

Z = 36.75 µm Z = 36.75 µm

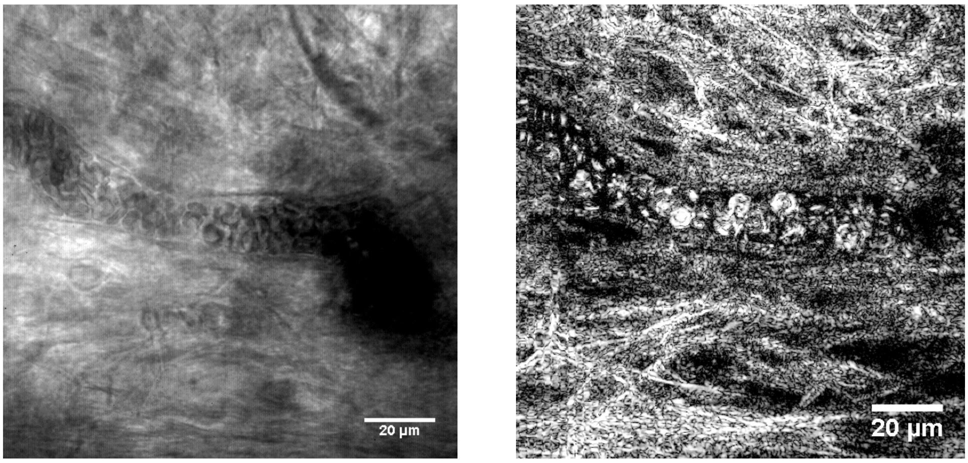

Z = 38.25 µm Z = 38.25 µm

Figure 8.4: (continued) *en face* images obtained with widefield (left) and SDOCPM (right) at consecutive depths inside the trachea. Single blood cells and collagen fibers are clearly visualized in SDOCPM images, whereas they appear blurred in widefield images.

The speckle noise in OCT reduces the image contrast and blurs the fine morphological structures of biological tissue. However, in the shown SDOCM images, fine structures such as collagen fibers and single red blood cells are clearly visualized. This is because, shorter depth of focus in combination with point illumination of the sample reduces the statistical variations that generally give rise to speckle noise [14, 15, p. 33].

The movement of motile cilia was simultaneously imaged with SDOCM and widefield microscopy, as shown in the movies in Figure 8.5. The widefield images were recorded at 100 frames/second, where as the SDOCM images were recorded at 3 frames/second. Although, SDOCM image acquisition speed was insufficient to fully capture the complete cycle of motile cilia movement, nevertheless shown images demonstrate that single cilium and their movement can be clearly visualized with SDOCM. Furthermore, with SDOCM it is possible to visualize the ciliated layer without the background cells because of its optical sectioning capability. Where as in widefield images, cell layers below the ciliated cells appears blurred, and overall reduce the image contrast and sharpness.

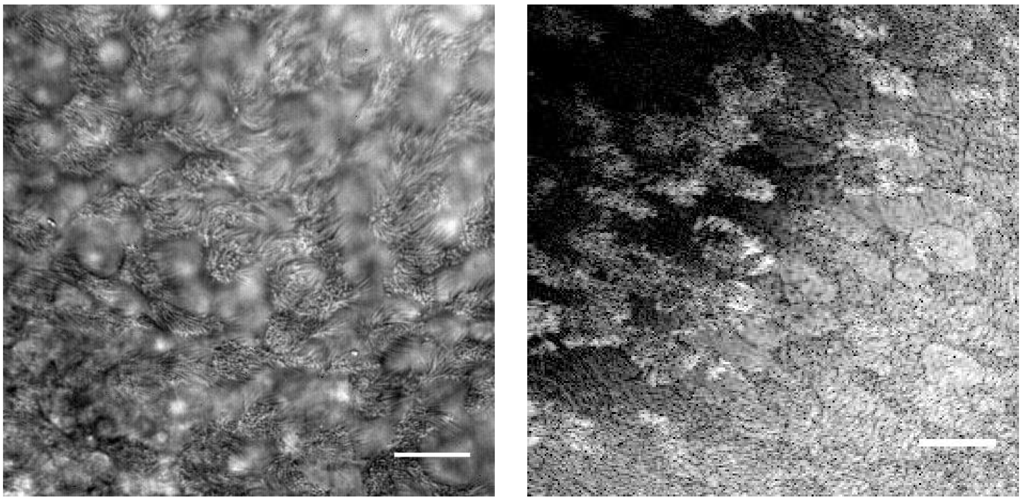
(a) (b)

Figure 8.5: (movie) Motile cilia movement of mouse trachea imaged with widefield microscope at 100 frames/sec (a), and SDOCM at 3 C-scans/sec (b). Image size is 128 µm × 128 µm and scale bar represents 20 µm.

8.4.3 4D Display of Mouse Trachea

To fully capture the ciliary dynamics of the tracheal epithelium, image field was reduced to 30 µm × 30 µm, and volumetric data was acquired over time at 108 sub-volume/second. Three dimensional structure over time, i.e., 4D display of the mouse trachea in Figure 8.6(a) shows coordinated beatings of the cilia in tracheal epithelium. Dimensions of the shown volume are 30 µm × 30 µm × 50 µm over a period of 1 second. 10 µm above the ciliated epithelium, tissue debris from the dissection of the trachea is can be seen being carried away by the flow stream in Figure 8.6(b).

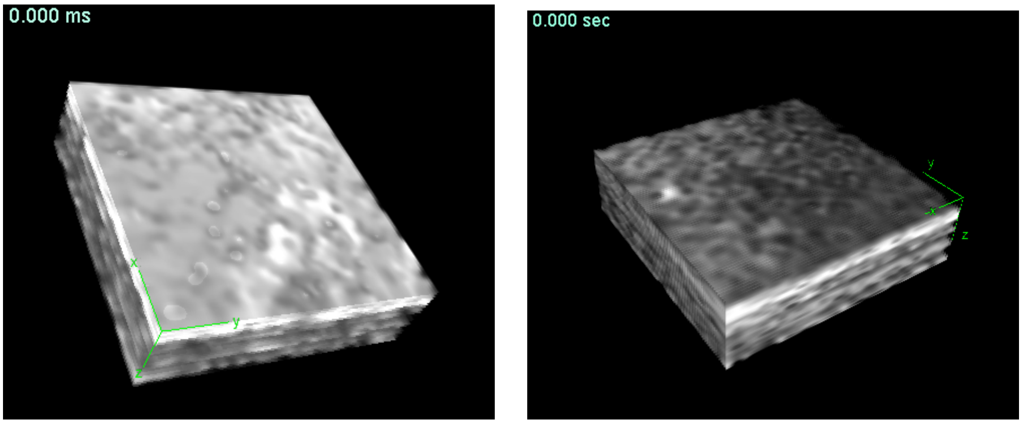

(a) (b)

Figure 8.6: (movie) 4D display of mouse trachea obtained by recording three dimensional sub-volumes (30 µm × 30 µm × 50 µm) at 108 sub-volume/second. (a) Surface of the ciliated cells where coordinated movement of motile cilia can be visualized. (b) 10 µm above the ciliated cells, same volume as in (a), cell debris being carried away by the flow induced by ciliary beatings is can be seen.

8.4.4 Quantitative Measurement of Ciliary Dynamics

Phase images obtained with high-speed volumetric recording can be used to quantitatively characterize the ciliary dynamics, such as their beating frequency, and flow rate induced by the coordinated beating. High-speed sampling of the cilia movement ensures that there are no temporal discontinuities in the phase images obtained with SDOCPM. The phase images represent relative optical pathlength values on the surface of tracheal epithelium. Changes in the optical pathlength over time or spatio-temporal changes are caused by the beating of cilia. The implemented SDOCPM system has an optical pathlength sensitivity of 0.9 nanometers for volumetric measurements, as demonstrated in Chapter 5. Therefore, spatio-temporal changes in optical pathlength caused by the coordinated beating of cilia, were measured with very high phase sensitivity, and is utilized in quantitative assessment of ciliary dynamics.

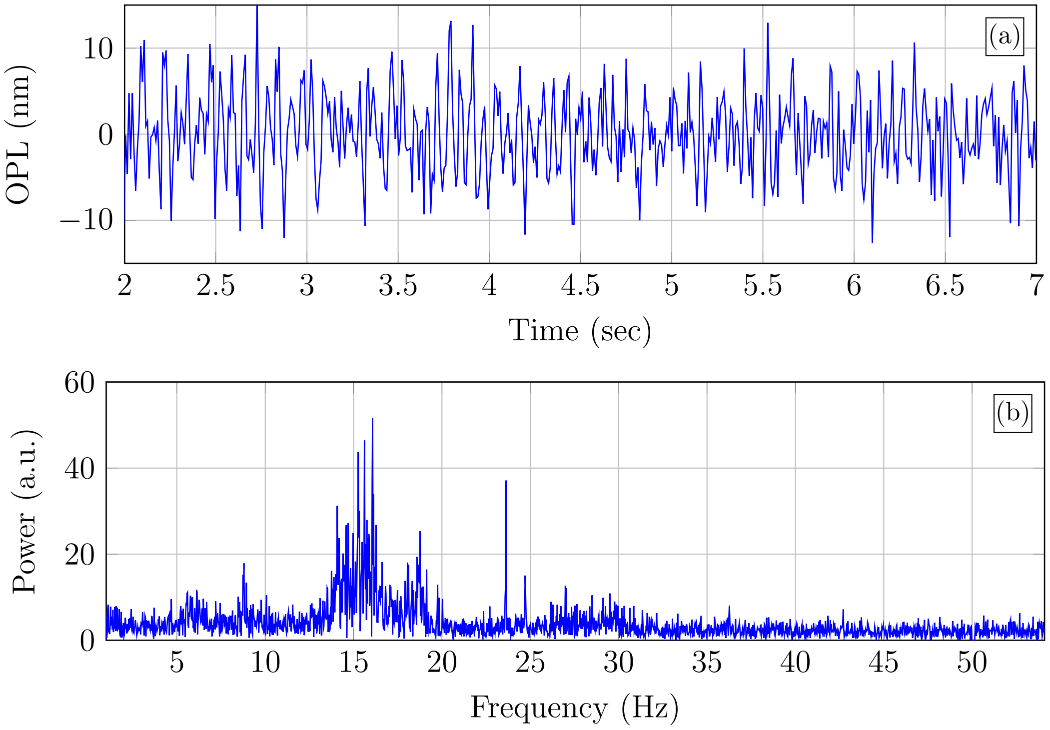

Figure 8.7: (a) Time series showing changes in optical pathlength caused by the movement of motile cilia. (b) Frequency spectrum of the time series, showing periodic nature of the cilia beatings.

Figure 8.7(a) shows changes in optical pathlength over time, caused by the coordinated beating of cilia. It was obtained by unwrapping the phase of a single pixel over time from the movie shown in Figure 8.6, and scaled into optical pathlength. The frequency spectrum of the optical pathlength time series is shown in Figure 8.7(b), which demonstrates the periodic nature of cilia beatings. The time-series was high pass filtered with a cut-off frequency of 4 Hz, to remove dc component and slow varying frequencies. Because of the complex beating cycle of motile cilia, Fourier transform of optical pathlength over time yields a range of frequency peaks. The frequency with the highest amplitude is 16 Hz, which is expected at 32°C temperature.

Optical Pathlength Gradient Mapping

Since the phase images quantitatively measure the changes in optical pathlength over time with high sensitivity, calculating its spatial gradient yields a vector field whose amplitude and direction indicates the strength and spatial orientation of cilia beatings, respectively. The optical pathlength gradient of a phase image can be represented as:

$$\nabla OPL(x,y) = \vec{u}.\mathbf{x} + \vec{v}.\mathbf{y} \tag{8.1}$$

$$\vec{u} = \frac{\delta}{\delta x}(OPL(x,y))$$

$$\vec{v} = \frac{\delta}{\delta y}(OPL(x,y))$$

Where $OPL(x,y)$ is the two-dimensional optical pathlength image, $\vec{u}$ and $\vec{v}$ are the gradient vectors along $\mathbf{x}$ and $\mathbf{y}$, which are unit vectors in X and Y spatial dimensions.

From the high-speed measurements shown in Figure 8.6, optical pathlength or phase images were obtained. Gradient of the optical pathlength images was computed and spatially averaged to obtain the resultant magnitude and direction of the sweep pattern, induced by the cilia beatings. Spatially averaged gradient vectors over a period of 2 seconds are as shown in Figure 8.8(a), where each vector represents magnitude and direction of ciliary sweep at each instance of time. To reduce the effect of noise, vector field was thresholded with half of the maximum magnitude, to obtain a concise magnitude and direction as shown in Figure 8.8(b). Obtained vector field over time is clearly biased in positive and negative X direction, with slightly higher magnitudes in negative X direction, which is consistent with the recovery and power stroke of cilia. The resultant vector in positive and negative X direction was calculated, and plotted in red color in Figure 8.8(b).

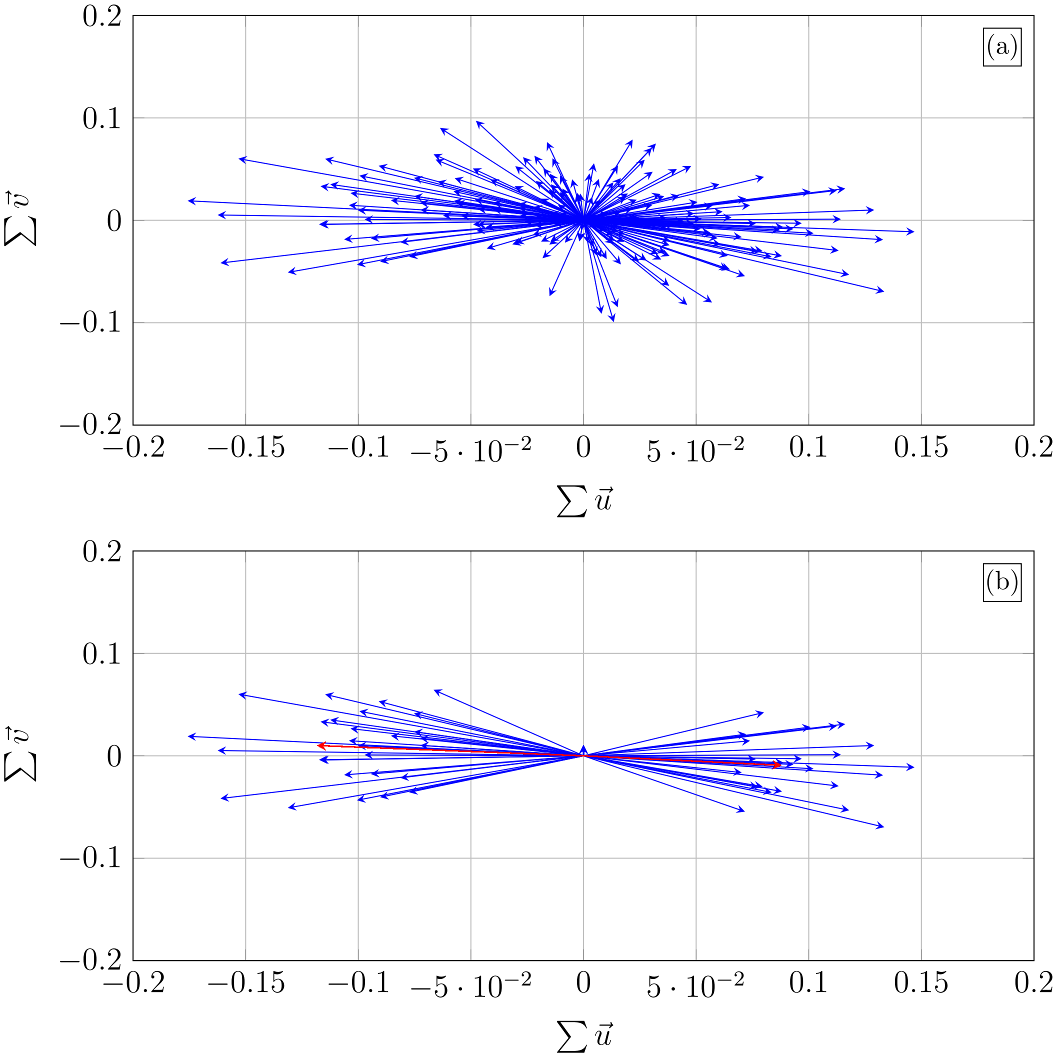

Figure 8.8: Vector representation of displacement gradient over time, where each vector represents magnitude and direction of displacement gradient at each instance of time. (a)Resultant displacement gradient vectors calculated from 200 consecutive phase images over time. (b) Resultant displacement gradient vectors after thresholding for noise reduction. Red vectors represent mean vectors in respective directions.

The magnitude and direction of the resultant flow velocity is calculated as follows:

$$|V| = \frac{\sqrt{(\sum \vec{u})^2 + (\sum \vec{v})^2}}{\Delta t} \tag{8.2}$$

$$\theta = \tan^{-1}\left(\frac{\sum \vec{v}}{\sum \vec{u}}\right) \tag{8.3}$$

The magnitude of flow velocity is 9.5 and 12.8 $\mu\mathrm{m\,s^{-1}}$ induced by the recovery and power stroke of the cilia, respectively. It is important to note that the obtained velocity magnitude $|V|$, represents the rate of change of optical pathlength transversely, which is proportional to the velocity of flow induced by cilia beatings.

8.5 Summary

The *en face* images presented in this chapter resolve anatomical structures of mouse trachea on sub-micron scale, through out its depth. Morphology of the ciliated cells and their cilium in the epithelium are clearly visualized. Basal cell layer and the connective tissue beneath the epithelium along with fibroblast cells are also clearly visualized. Generally, this kind of detailed morphological structures can only be obtained with multiphoton microscopy or by performing a biopsy on the trachea and then processing it into histological sections. Therefore, SDOCM can be used as an non-invasive histopathology tool for examining the tissue morphology at subcellular level.

The fine morphological structures of the trachea such as collagen fibers and individual red blood cells in the capillaries are clearly visualized. This is in contrast with OCT images, where speckle noise blurs the fine morphological structures. Therefore, with high numerical aperture objective and shorter depth of focus, illumination of the sample is limited to a very narrow focal volume and the measured backscattered signal is not subject to statistical variations that generate speckle noise [14, 15, p. 33].

The phase contrast of SDOCM or the SDOCPM images provide quantitative assessment of ciliary dynamics, such as ciliary beating frequency, direction and magnitude of the flow induced by coordinated beatings of cilia. From the physiological perspective, magnitude and direction of ciliary sweep provide functional assessment of the ciliated epithelium. Currently, there are no diagnostic tools or imaging technique that can provide functional assessment of ciliated epithelium *in vivo*. SDOCPM can potentially be miniaturized using a fiber-optic probe for functional endoscopic imaging. Recently OCT based methods have been demonstrated to quantitatively measure the flow dynamics in *ex vivo* trachea [94, 95]. However, some of the proposed methods rely on particle tracking velocimetry which isn't practical for *in vivo* imaging. Whereas the approach presented in this chapter utilizes the optical pathlength gradient maps to estimate flow dynamics, and does not require any extrinsic agents. Also, OCT based Doppler flow imaging techniques cannot measure flows which are perpendicular to the probing beam [96, 30]. Where as the proposed approach in this chapter estimates the dynamics of a flow which is perpendicular to the probing beam.

In conclusion, SDOCPM combines microanatomical assessment of mouse trachea with a functional contrast that quantitatively measures the flow induced by coordinated cilia beatings. An endoscopic implementation of SDOCPM could potentially be helpful in diagnosis and monitoring of various pathologies associated with mucuciliary clearance.

Chapter 9

Summary and Conclusion

9.1 Summary

This thesis has presented an implementation of spectral domain optical coherence phase microscopy (SDOCPM) that combines sub-micrometer spatial resolution with sub-nanometer optical pathlength sensitivity. The significance of this combination is that, it enables morphological and functional assessment of dynamic tissue types at sub-cellular level. Implemented SDOCPM system has maximum sampling rate of $217,000$ A-scans/sec, and can provide C-mode scans or sub-volumes at the rate of 108 sub-volumes/sec.

Almost all SDOCPM implementations reported in the literature, have used a common-path interferometer for high phase sensitivity [6, 7, 8, 9, 10, 11, 12, 13]. However, common-path interferometer topology has many drawbacks including suboptimal transverse resolution, limited depth scanning capability, and poor control on reference power which is important for high sensitivity measurements. The implemented SDOCPM system overcomes these limitations by using a symmetric Linnik interferometer and by keeping all sources of noise such as galvanometer scanners, thermal deviation, etc., in common mode between sample and reference arms. With this approach, the phase sensitivity is comparable to that of common-path interferometer topologies, and there are no limitations on the transverse resolution and detection sensitivity.

The axial and transverse response of the implemented SDOCPM system was evaluated by measuring 3D point spread function. It was demonstrated that, the axial response of SDOCPM is significantly more sensitive than the confocal scanning optical microscopy. The detection sensitivity in OCM is enhanced because weak backscattered light from tissue adds in-phase or coherently at the detector with a constant reference arm power, which provides a homodyne gain. The higher detection sensitivity of OCM also improves the penetration depth when compared with confocal scanning microscopy [63].

Microanatomical images and reconstructed 3D structures from anterior and posterior segments of the eye reveal subcellular morphological details that are comparable to histology. Given the strong structure-function correlations in human eyes [72, 73, 74], SDOCPM can potentially be used as a non-invasive tool for both diagnosis and monitoring of diseases. However, the spatial resolution at the posterior segments of eye, for *in vivo* measurements, is limited by the small aperture size of the iris. Furthermore, adaptive optics would be necessary to compensate the wavefront distortions caused by the vitreous humor.

The capability of SDOCPM to provide microanatomical and functional assessment of dynamic tissue types is demonstrated by imaging the morphological structures of cardiomyocytes and their contraction dynamics. High-speed 4D acquisition of data from spontaneously active cardiomyocytes allows spatio-temporal visualization of contraction dynamics.

The morphological structures of mouse trachea, from cilia of the epithelium to the single blood cells in the capillaries below the epithelium were imaged with sub-micrometer resolution. The phase contrast was utilized for quantitative measurement of ciliary beat frequency and the optical pathlength gradient of the phase images were used to estimate the magnitude and direction of the ciliary beatings.

Although implemented SDOCM system has maximum sampling rate of $217,000$ A-scans/sec, the volumetric acquisition speed is limited by the settling times of galvanometer scanners. Resonant or acousto-optic based scanners would be more efficient for high-speed raster scanning and will significantly increase the volumetric acquisition speeds.

9.2 Conclusion

This thesis has presented a SDOCPM system that enables high-speed 4D imaging of biological tissues with sub-micrometer transverse spatial resolution and sub-nanometer axial pathlength sensitivity. The results presented in this thesis demonstrate the capability of SDOCPM to image 3D morphological structures of biological tissues and their dynamic characteristics.

OCT has found clinical applications in many different fields, ophthalmology [17, 18, 19, 20], cardiology [97, 98], dermatology [23, 24], etc. However, there are two limitations that have been pointed out in the literature. First, the limited transverse spatial resolution makes it difficult to identify cell types and their fine processes. Second, the presence of speckle noise degrades image contrast, and obscures fine features and boundaries of morphological structures. Implemented optical coherence phase microscopy system offers solution to both of these problems. With high numerical aperture, transverse spatial resolution is improved that enables visualization of subcellular structures in biological tissues. The speckle noise is also minimized because, illumination of the sample is limited to a very narrow focal volume and the measured backscattered signal is not subject to statistical variations that generate speckle noise [14, 15, p. 33]. Therefore, Without the presence of speckle noise, fine morphological structures of biological tissues such as collagen fibers and individual cell processes are clearly visualized.

Given that most of the biological tissues are inherently dynamic in nature, their function and pathologies cannot be completely understood from the morphological structures alone. Physiological processes such as molecular diffusion, muscle contraction, respiration, perfusion, mucuciliary clearance, etc., induce localized spatio-temporal changes in refractive index. In OCM, the phase component of the coherently detected backscattered light is sensitive to minuscule changes in optical pathlength, and can be used to quantitatively measure these spatio-temporal variations of refractive index in biological tissues. Furthermore, OCM does not require any extraneous agents for functional imaging of dynamic tissue types.

The results presented in this thesis demonstrate that SDOCPM can provide anatomical and functional assessment of tissues, at sub-micrometer scale. Although, excisional biopsy and histology are the gold standard for visualization of tissue micro-structures and pathology, it has some drawbacks as well. Besides being invasive, preparation of histological slides requires fixation of tissue, dehydration and addition of staining agents, all of which could potentially alter the tissue micro-structure. Furthermore, biopsy and histology involves removing part of the tissue from a whole and functional environment, which limits the scope of examining site. SDOCPM with subcellular resolution can provide a non-invasive, *in situ* examination of tissue micro-structures without having to remove them from their functional environment. In addition to the subcellular morphological details, the phase contrast of SDOCPM could potentially be used to examine the dynamic properties of tissue. Therefore, SDOCPM can be used as a non-invasive functional biopsy tool, as it provides information about the morphological structures of tissue and their dynamic properties at subcellular level.

OCPM is a powerful imaging technique that has many advantages over confocal scanning microscopy such as higher sensitivity, higher penetration depth in scattering samples, less prone to resolution degradation with increasing depth, and a phase contrast for quantitative measurement of tissue dynamics.

OCPM also has the potential to provide depth-resolved spectroscopic contrast, as it already uses a broadband light source for sample illumination. By carefully selecting a wavelength range which includes peak absorption for certain chromophores such as haemoglobin or melanocytes, OCPM can be used to image the spectroscopic properties of biological tissues.

The scattering contrast of OCPM can also be combined with conventional imaging techniques such as florescence or multi-photon microscopy to target specific molecular signatures, and further enhance the anatomical and functional information that can be obtained from biological tissues.

Finally, OCPM can also be implemented with miniaturized fiber-optic probes that could be useful for endoscopic imaging in neurosurgery for visualization of different cell types and cancerous legions. Miniaturized OCPM probes can also be used for characterization of vulnerable plaque formations in coronary arteries, as the conventional modalities currently in use does not provide single cell resolution.

Bibliography

[1] David Huang, Eric A. Swanson, Charles P. Lin, Joel S. Schuman, William G. Stinson, Warren Chang, Michael R. Hee, Thomas Flotire, Kenton Gregory, Carmen A. Puliafito, and James G. Fujimoto. Optical coherence tomography. *Science*, 254(5035):1178–1181, 1991.

[2] Joseph A. Izatt, Michael R. Hee, Gabrielle M. Owen, Eric A. Swanson, and James G. Fujimoto. Optical coherence microscopy in scattering media. *Opt. Lett.*, 19(8):590–592, Apr 1994.

[3] A. D. Aguirre, P. Hsiung, T. H. Ko, I. Hartl, and J. G. Fujimoto. High-resolution optical coherence microscopy for high-speed, in vivo cellular imaging. *Opt. Lett.*, 28:2064–66, 2003.

[4] Yu Chen, Shu-Wei Huang, Aaron D. Aguirre, and James G. Fujimoto. High-resolution line-scanning optical coherence microscopy. *Opt. Lett.*, 32(14):1971–1973, Jul 2007.

[5] Vivek J. Srinivasan, Harsha Radhakrishnan, James Y. Jiang, Scott Barry, and Alex E. Cable. Optical coherence microscopy for deep tissue imaging of the cerebral cortex with intrinsic contrast. *Opt. Express*, 20(3):2220–2239, Jan 2012.

[6] Chulmin Joo, Taner Akkin, Barry Cense, Boris H. Park, and Johannes F. de Boer. Spectral-domain optical coherence phase microscopy for quantitative phase-contrast imaging. *Opt. Lett.*, 30(16):2131–2133, Aug 2005.

[7] Michael A. Choma, Audrey K. Ellerbee, Changhuei Yang, Tony L. Creazzo, and Joseph A. Izatt. Spectral-domain phase microscopy. *Opt. Lett.*, 30(10):1162–1164, May 2005.

[8] M.A. Choma, A. K. Ellerbee, S. Yazdanfar, and J.A. Izatt. Doppler flow imaging of cytoplasmic streaming using spectral domain phase microscopy. *J. Biomed. Opt.*, 11(2):024014, 2006.

[9] S. M. Motaghian Nezam, C. Joo, G. J. Tearney, and J. F. de Boer. Application of maximum likelihood estimator in nano-scale optical path length measurement using spectral-domain optical coherence phasemicroscopy. *Opt. Express*, 16(22):17186–17195, Oct 2008.

[10] Chulmin Joo, Emre Özkumurc, M. Selim Ünlüc, and Johannes F. de Boer. Spectral-domain optical coherence phase microscopy for label-free multiplexed protein microarray assay. *Biosensors and Bioelectronics*, 25:275–281, 2009.

[11] Andra St. Quintin, Lukas-Karim Merhi, and Marinko V. Sarunic. Spectral domain fluorescence coherence phase microscopy. *Appl. Opt.*, 50(12):1798–1804, Apr 2011.

[12] Itay Shock, Alexander Barbul, Pinhas Girshovitz, Uri Nevo, Rafi Korenstein, and Natan T. Shakeda. Optical phase nanoscopy in red blood cells using low-coherence spectroscopy. *J. Biomed. Opt.*, 17(10):101509, 2012.

[13] P. O. Bagnaninchi, Christina Holmes, and Maryam Tabrizian. Monitoring cells in engineered tissues with optical coherence phase microscopy: Optical phase fluctuations as endogenous sources of contrast. *SPIE Proceedings*, 8580(85800E), 2013.

[14] A.F. Fercher, C.K. Hitzenberger, M. Sticker, E. Moreno-Barriuso, R. Leitgeb, W. Drexler, and H. Sattmann. A thermal light source technique for optical coherence tomography. *Optics Communications*, 185(1–3):57 – 64, 2000.

[15] Timothy R. Corle and Gordon S. Kino. *Confocal Scanning Optical Microscopy and Related Imaging Systems.* Academic Press, 1996.

[16] Joseph A. Izatt, Michael R. Hee, Eric A. Swanson, Charles P. Lin, David Huang, Joel S. Schuman, Carmen A. Puliafito, and James G. Fujimoto. Micrometer-scale resolution imaging of the anterior eye in vivo with optical coherence tomography. *Arch Ophthalmol.*, 112(12):1584–1589, 1994.

[17] Strouthidis NG, Yang H, and Reynaud JF. Comparison of clinical and spectral domain optical coherence tomography optic disc margin anatomy. *Invest Ophthalmol Vis Sci*, 50(10):4709–18, 2009.

[18] Alexandre SCR, Glen P. Sharpe, Hongli Yang, Marcelo TN, Claude FB, and Balwantray CC. Optic disc margin anatomy in patients with glaucoma and normal controls with spectral domain optical coherence tomography. *Ophthalmology*, 119(4):738–747, 2012.

[19] J. Fernando Arevalo, Carlos F. Fernandez, and Aristides J. Mendoza. *Retinal Angiography and Optical Coherence Tomography.* Springer, 2009.

[20] Kang SW, Park CY, and Ham DI. The correlation between fluorescein angiographic and optical coherence tomographic features in clinically significant diabetic macular edema. *Am J Ophthalmol*, 137(2):313–332, 2004.

[21] G.J. Tearney, M.E. Brezinski, J.F. Southern, B.E. Bouma, S.A. Boppart, and J.G. Fujimoto. Optical biopsy in human pancreatobiliary tissue using optical coherence tomography. *Digestive Diseases and Sciences*, 43(6):1193–1199, 1998.

[22] Bill W. Colston, Matthew J. Everett, Luiz B. Da Silva, Linda L. Otis, Pieter Stroeve, and Howard Nathel. Imaging of hard- and soft-tissue structure in the oral cavity by optical coherence tomography. *Appl. Opt.*, 37(16):3582–3585, Jun 1998.

[23] Mark C Pierce, John Strasswimmer, B Hyle Park, Barry Cense, and Johannes F de Boer. Advances in optical coherence tomography imaging for dermatology. *J. Invest. Dermatol.*, 123:458 –463, 2004.

[24] Gambichler T., Moussa G., Sand M., Sand D., Altmeyer P., and Hoffmann K. Applications of optical coherence tomography in dermatology. *J Dermatol Sci.*, 40(2):85–94, 2005.

[25] Tuqiang Xie, Shuguang Guo, Jun Zhang, Zhongping Chen, and George M. Peavy. Polarization-sensitive oct of bovine intervertebral disk. *Journal of Biomedical Optics*, 11(6):064001, 2006.

[26] Stefan Zotter, Michael Pircher, Teresa Torzicky, Bernhard Baumann, Hirofumi Yoshida, Futoshi Hirose, Philipp Roberts, Markus Ritter, Christopher Schütze, Erich Götzinger, Wolfgang Trasischker, Clemens Vass, Ursula Schmidt-Erfurth, and Christoph K. Hitzenberger. Large-field high-speed polarization sensitive spectral domain oct and itsapplications in ophthalmology. *Biomed. Opt. Express*, 3(11):2720–2732, Nov 2012.

[27] X. J. Wang, T. E. Milner, and J. S. Nelson. Characterization of fluid flow velocity by optical doppler tomography. *Opt. Lett.*, 20(11):1337–1339, Jun 1995.

[28] Rainer Leitgeb, Leopold F. Schmetterer, Maciej Wojtkowski, Christoph K. Hitzenberger, Markus Sticker, and Adolf F. Fercher. Flow velocity measurements by frequency domain short coherence interferometry. *SPIE Proceedings*, 4619:16–21, 2002.

[29] Yonghua Zhao, Zhongping Chen, Christopher Saxer, Qimin Shen, Shaohua Xiang, Johannes F. de Boer, and J. Stuart Nelson. Doppler standard deviation imaging for clinical monitoring of in vivo human skin blood flow. *Opt. Lett.*, 25(18):1358–1360, Sep 2000.

[30] B. White, M. Pierce, N. Nassif, B. Cense, B. Park, G. Tearney, B. Bouma, T. Chen, and J. de Boer. In vivo dynamic human retinal blood flow imaging using ultra-high-speed spectral domain optical coherence tomography. *Opt. Express*, 11(25):3490–3497, 2003.

[31] Xuan Liu and Jin U. Kang. Depth-resolved blood oxygen saturation assessment using spectroscopic common-path fourier domain optical coherence tomography. *IEEE Trans Biomed Eng.*, 57(10):2572–2575, 2010.

[32] Wolfgang Drexler and James G. Fujimoto. *Optical Coherence Tomography Technology and Applications*. Springer, 2008.

[33] John E. Greivenkamp. *Handbook of Optics (Volume I), Chapter 2. Interference*. McGraw-Hill, 2009. ISBN-10: 0071498893.

[34] David J. Griffiths. *Introduction to Electrodynamics (3rd Edition)*. Addison Wesley, 1999. ISBN-10: 013805326X.

[35] A.F. Fercher, C.K. Hitzenberger, G. Kamp, and S.Y. El-Zaiat. Measurement of intraocular distances by backscattering spectral interferometry. *Optics Communications*, 117:43–48, 1995.

[36] Maciej Wojtkowski, Rainer Leitgeb, Andrzej Kowalczyk, Tomasz Bajraszewski, and Adolf F. Fercher. In vivo human retinal imaging by fourier domain optical coherence tomography. *Journal of Biomedical Optics*, 7(3):457–463, 2002.

[37] R. Leitgeb, C. Hitzenberger, and Adolf Fercher. Performance of fourier domain vs. time domain optical coherence tomography. *Opt. Express*, 11(8):889–894, Apr 2003.

[38] J. F. de Boer, B. Cense, B. H. Park, M. C. Pierce, G. J. Tearney, and B. E. Bouma. Improved signal-to-noise ratio in spectral-domain compared with time-domain optical coherence tomography. *Opt. Lett.*, 28:2067–2069, 2003.

[39] Michael Choma, Marinko Sarunic, Changhuei Yang, and Joseph Izatt. Sensitivity advantage of swept source and fourier domain optical coherence tomography. *Opt. Express*, 11(18):2183–2189, Sep 2003.

[40] F. Lexer, C. K. Hitzenberger, A. F. Fercher, and M. Kulhavy. Wavelength-tuning interferometry of intraocular distances. *Appl. Opt.*, 36(25):6548–6553, Sep 1997.

[41] S. R. Chinn, E. A. Swanson, and J. G. Fujimoto. Optical coherence tomography using a frequency-tunable optical source. *Opt. Lett.*, 22(5):340–342, Mar 1997.

[42] R. Huber, M. Wojtkowski, K. Taira, J. Fujimoto, and K. Hsu. Amplified, frequency swept lasers for frequency domain reflectometry and oct imaging: design and scaling principles. *Opt. Express*, 13(9):3513–3528, May 2005.

[43] E. A. Swanson, J. A. Izatt, M. R. Hee, D. Huang, C. P. Lin, J. S. Schuman, C. A. Puliafito, and J. G. Fujimoto. In vivo retinal imaging by optical coherence tomography. *Opt. Lett.*, 18:1864–1866, 1993.

[44] Martin F. Kraus, Benjamin Potsaid, Markus A. Mayer, Ruediger Bock, Bernhard Baumann, Jonathan J. Liu, Joachim Hornegger, and James G. Fujimoto. Motion correction in optical coherence tomography volumes on a per a-scan basis using orthogonal scan patterns. *Biomed. Opt. Express*, 3(6):1182–1199, Jun 2012.

[45] J.A. Izatt and M.A. Choma. *Optical Coherence Tomography: Technology and Applications. Chapter: Theory of Optical Coherence Tomography.* Springer, 2008. ISSN 1618-7210.

[46] N. Nassif, B. Cense, B. Park, M. Pierce, S. Yun, B. Bouma, G. Tearney, T. Chen, and J. de Boer. In vivo high-resolution video-rate spectral-domain optical coherence tomography of the human retina and optic nerve. *Opt. Express*, 12(3):367–376, Feb 2004.

[47] M. Wojtkowski, A. Kowalczyk, R. Leitgeb, and A. F. Fercher. Full range complex spectral optical coherence tomography technique in eye imaging. *Opt. Lett.*, 27(16):1415–1417, Aug 2002.

[48] Michael A. Choma, Changhuei Yang, and Joseph A. Izatt. Instantaneous quadrature low-coherence interferometry with 33 fiber-optic couplers. *Opt. Lett.*, 28(22):2162–2164, Nov 2003.

[49] Adrian Bachmann, Rainer Leitgeb, and Theo Lasser. Heterodyne fourier domain optical coherence tomography for full range probing with high axial resolution. *Opt. Express*, 14(4):1487–1496, Feb 2006.

[50] Grigory V. Gelikonov, Valentin M. Gelikonov, and Pavel A. Shilyagin. Linear wave-number spectrometer for spectral domain optical coherence tomography. *Proc. SPIE*, 6847:68470N, 2008.

[51] M. Minsky. *Microscopy Apparatus, U.S.A*, 1961.

[52] T. Wilson and T.J.R. Sheppard. *Theory and Practice of Scanning Optical Microsccopy.* Academic, London, 1984.

[53] M. Born and E. Wolf. *Principles of Otpics, 6th Edition.* Pergamon Press, 1980.

[54] E. Beaurepaire, A. C. Boccara, M. Lebec, L. Blanchot, and H. Saint-Jalmes. Full-field optical coherence microscopy. *Opt. Lett.*, 23(4):244–246, Feb 1998.

[55] Arnaud Dubois, Laurent Vabre, Albert-Claude Boccara, and Emmanuel Beaurepaire. High-resolution full-field optical coherence tomography with a linnik microscope. *Appl. Opt.*, 41(4):805–812, Feb 2002.

[56] W. Y. Oh, B. E. Bouma, N. Iftimia, S. H. Yun, R. Yelin, and G. J. Tearney. Ultrahigh-resolution full-field optical coherence microscopy using ingaas camera. *Opt. Express*, 14(2):726–735, Jan 2006.

[57] A. Ceyhun Akcay, Jannick P. Rolland, and Jason M. Eichenholz. Spectral shaping to improve the point spread function in optical coherence tomography. *Opt. Lett.*, 28(20):1921–1923, 2003.

[58] Joseph A. Izatt, Manish D. Kulkarni, Hsing-Wen Wang, Kenji Kobayashi, and Jr. Michael V. Sivak. Optical coherence tomography and microscopy in gastrointestinal tissues. *IEEE Journal of Selected Topics in Quantum Electronics*, 2(4):1017–1028, 1996.

[59] Aaron D. Aguirre, Juergen Sawinski, Shu-Wei Huang, Chao Zhou1, Winfried Denk, and James G. Fujimoto. High speed optical coherence microscopy with autofocus adjustment and a miniaturized endoscopic imaging probe. *Opt Express.*, 18(5):4222–4239, 2010.

[60] F. Zernike. Phase contrast, a new method for the microscopic observation of transparent objects. *Physica*, 9(7):686–698, 1942.

[61] Pluta M. *Advanced Light Microscopy: Specialized Methods.* Elsevier, 1989.

[62] Colin J. R. Sheppard, Min Gu, Keith Brain, and Hao Zhou. Influence of spherical aberration on axial imaging of confocal reflection microscopy. *Appl. Opt.*, 33(4):616–624, Feb 1994.

[63] A. L. Clark, A. Gillenwater, R. Alizadeh-Naderi, A. K. El-Naggar, and R. Richards-Kortum. Detection and diagnosis of oral neoplasia with an optical coherence microscope. *J. Biomed. Opt.*, 9(6):1271–1280, 2004.

[64] Chengyang Xu, Claudio Vinegoni, Tyler S. Ralston, Wei Luo, Wei Tan, and Stephen A. Boppart. Spectroscopic spectral-domain optical coherence microscopy. *Opt. Lett.*, 31(8):1079–1081, Apr 2006.

[65] Arnaud Dubois, Julien Moreau, and Claude Boccara. Spectroscopic ultrahigh-resolution full-field optical coherence microscopy. *Opt. Express*, 16(21):17082–17091, Oct 2008.

[66] Richard G. Lyons. *Understanding Digital Signal Processing, Second Edition.* Prentice Hall PTR, 1996.

[67] Dennis C. Ghiglia and Mark D. Pritt. *Two-Dimensional Phase Unwrapping: Theory, Algorithms, and Software.* John Wiley & Sons, 1998.

[68] Walt Kester. *The Data Conversion Handbook.* Elsevier/Newnes, 2005.

[69] Bernd Dörband and Henriette Müller. *Handbook of Optical Systems, Metrology of Optical Components and Systems, 5th edition.* John Wiley & Sons, 2012.

[70] S. H. Yun, G. J. Tearney, J. F. de Boer, and B. E. Bouma. Motion artifacts in optical coherence tomography with frequency-domain ranging. *Opt. Exp.*, 30:2977–2998, 2004.

[71] L. Thrane, H.T. Yura, and P.E. Andersen. Calculation of the maximum obtainable probing depth of optical coherence tomography in issue. *Proc. SPIE*, 3915:2–5, 2000.

[72] Peter Charbel Issa, Eric Troeger, Robert Finger, Frank G. Holz, Robert Wilke, and Hendrik P. N. Scholl. Structure-function correlation of the human central retina. *PLoS ONE*, 5:e12864, 2010.

[73] Arthur J. Weber and Christine D. Harman. Structure–function relations of parasol cells in the normal and glaucomatous primate retina. *Invest Ophthalmol Vis Sci.*, 46(9):3197–3207, 2005. DOI: 10.1167/iovs.04-0834.

[74] Harsha L. Rao, Linda M. Zangwill, Robert N. Weinreb, Mauro T. Leite, Pamela A. Sample, and Felipe A. Medeiros. Structure-function relationship in glaucoma using spectral-domain optical co-

herence tomography. *Arch Ophthalmol.*, 129(7):864–871, 2011. DOI:10.1001/archophthalmol.2011.145.

[75] John C Hwang, Ranjith Konduru, Xinbo Zhang, Ou Tan, Brian A Francis, Rohit Varma, Mitra Sehi, David S Greenfield, SriniVas R Sadda, and David Huang. Relationship among visual field, blood flow, and neural structure measurements in glaucoma. *Invest Ophthalmol Vis Sci.*, 53(6):3020–3026, 2012.

[76] David Shier, Jackie Butler, and Ricki Lewis. *Hole's Essentials of Human Anatomy and Physiology.* McGraw Hills, 2012.

[77] Yong gen Xu, Yong sheng Xu, Chen Huang, Yun Feng, Ying Li, and Wei Wang. Development of a rabbit corneal equivalent using an acellular corneal matrix of a porcine substrate. *Molecular Vision*, 14:2180–2189, 2008.

[78] Auran JD, Koester CJ, Kleiman NJ, Rapaport R, Bomann JS, Wirotsko BM, Florakis GJ, and Koniarek JP. Scanning slit confocal microscopic observation of cell morphology and movement within the normal human anterior cornea. *Ophthalmology*, 102(1):33–41, 1995.

[79] Florakis GJ, Moazami G, Schubert H, Koester CJ, and Auran JD. Scanning slit confocal microscopy of fungal keratitis. *Arch Ophthalmol.*, 115(11):1461–1463, 1997. DOI:10.1001/archopht.1997.01100160631019.

[80] Popper M, Morgado AM, Quadrado MJ, and Van Best JA. Corneal cell density measurement in vivo by scanning slit confocal microscopy: method and validation. *Ophthalmic Res.*, 36(5):270–276, 2004. DOI: 10.1159/000081207.

[81] David B. Fankhauser. Histology of the eye. *University of Cincinnati Clermont College*, 2008.

[82] Enrique Fernández and Wolfgang Drexler. Influence of ocular chromatic aberration and pupil size on transverse resolution in ophthalmic adaptive optics optical coherence tomography. *Opt. Express*, 13(20):8184–8197, Oct 2005.

[83] B. Hermann, E. J. Fernández, A. Unterhuber, H. Sattmann, A. F. Fercher, W. Drexler, P. M. Prieto, and P. Artal. Adaptive-optics ultrahigh-resolution optical coherencetomography. *Opt. Lett.*, 29(18):2142–2144, Sep 2004.

[84] Shintaro Nakano, Toshihiro Muramatsu, Shigeyuki Nishimura, and Takaaki Senbonmatsu. *Cardiomyocyte and Heart Failure, Current Basic and Pathological Approaches to the Function of Muscle Cells and Tissues - From Molecules to Humans.* ISBN: 978-953-51-0679-1, DOI: 10.5772/47772, 2012.

[85] Peter Molnar and James J. Hickman. *Patch-Clamp Methods and Protocols.* Human Press ISBN: 978-1-58829-698-6, 2007.

[86] S. Jacquir, S. Binczak, M. Rosse, D. Vandroux, G. Laurent, P. Athias, and JM. Bilbault. Multisite field potential recordings and analysis of the impulse propagation pattern in cardiac cells culture. *Computers in Cardiology*, 34:125–128, 2007.

[87] Victor A. Maltsev, Anna M. Wobus, Juirgen Rohwedel, Michael Bader, and Jurgen Hescheler. Cardiomyocytes differentiated in vitro from embryonic stem cells developmentally express cardiac-specific genes and ionic currents. *Circulation Research*, 75:233–244, 1994.

[88] Sean P. Sheehy, Anna Grosberg, and Kevin Kit Parker. The contribution of cellular mechanotransduction to cardiomyocyte form and function. *Biomechanics and Modeling in Mechanobiology*, 11(8):1227–39, 2012.

[89] Sleigh MA, Blake JR, and Liron N. The propulsion of mucus by cilia. *Am Rev Respir Dis.*, 137(3):726–41, 1988.

[90] Alok S. Shah, Yehuda Ben-Shahar, Thomas O. Moninger, Joel N. Kline, and Michael J. Welsh1. Motile cilia of human airway epithelia are chemosensory. *Sceince*, 325(5944):1131–1134, 2009. DOI:10.1126/science.1173869.

[91] Brent W. Bisgrove and H. Joseph Yos. The roles of cilia in developmental disorders and disease. *Development*, 133:4131–4143, 2006. DOI:10.1242/dev.02595.

[92] Sharma N., Berbari NF, and Yoder BK. Ciliary dysfunction in developmental abnormalities and diseases. *Curr Top Dev Biol.*, 85:371–427, 2008.

[93] Charles P. Daghlian. Electron microscope facility. *Dartmouth Medical School*, 2004.

[94] Amy L. Oldenburg, Raghav K. Chhetri, David B. Hill, and Brian Button. Monitoring airway mucus flow and ciliary activity with optical coherence tomography. *Biomedical Optics Express*, 3(9):1978–1992, 2012.

[95] Stephan Jonas, Dipankan Bhattacharya, Mustafa K. Khokha, and Michael A. Choma. Microfluidic characterization of cilia-driven fluid flow using optical coherence tomography-based particle tracking velocimetry. *Biomedical Optics Express*, 2(7):2022–2034, 2011.

[96] J. A. Izatt, M. D. Kulkarni, S. Yazdanfar, J. K. Barton, and A. J. Welch. In vivo bidirectional color doppler flow imaging of picoliter blood volumes using optical coherence tomography. *Opt. Lett.*, 22(18):1439–1441, 1997.

[97] Masanori Kawasaki, Brett E. Bouma, Jason Bressner, Stuart L. Houser, Seemantini K. Nadkarni, Briain D. MacNeill, Ik-Kyung Jang, Hisayoshi Fujiwara, and Guillermo J. Tearney. Diagnostic accuracy of optical coherence tomography and integrated backscatter intravascular ultrasound images for tissue characterization of human coronary plaques. *Journal of the American College of Cardiology*, 48(1):81–88, 2005.

[98] Takashi Akasaka, Takashi Kubo, Masato Mizukoshi, Atsushi Tanaka, Hironori Kitabata, Takashi Tanimoto, and Toshio Imanishi. Pathophysiology of acute coronary syndrome assessed by optical coherence tomography. *Journal of Cardiology*, 56:8–14, 2010.